Test particle analysis of high altitude ion transport and escape on Mars

by

Shannon M. Curry

A dissertation submitted in partial fulfillment
of the requirements for the degree of
Doctor of Philosophy
(Atmospheric, Oceanic and Space Sciences)
in The University of Michigan
2013

Doctoral Committee:

- Professor Michael Warren Liemohn, Chair
- Professor Edwin Anthony Bergin
- Space Scientist Jared Espley, NASA Goddard Space Flight Center
- Research Scientist Xiaohua Fang, University of Colorado, Boulder
- Professor Emeritus Andrew F. Nagy
- Professor James Arthur Slavin

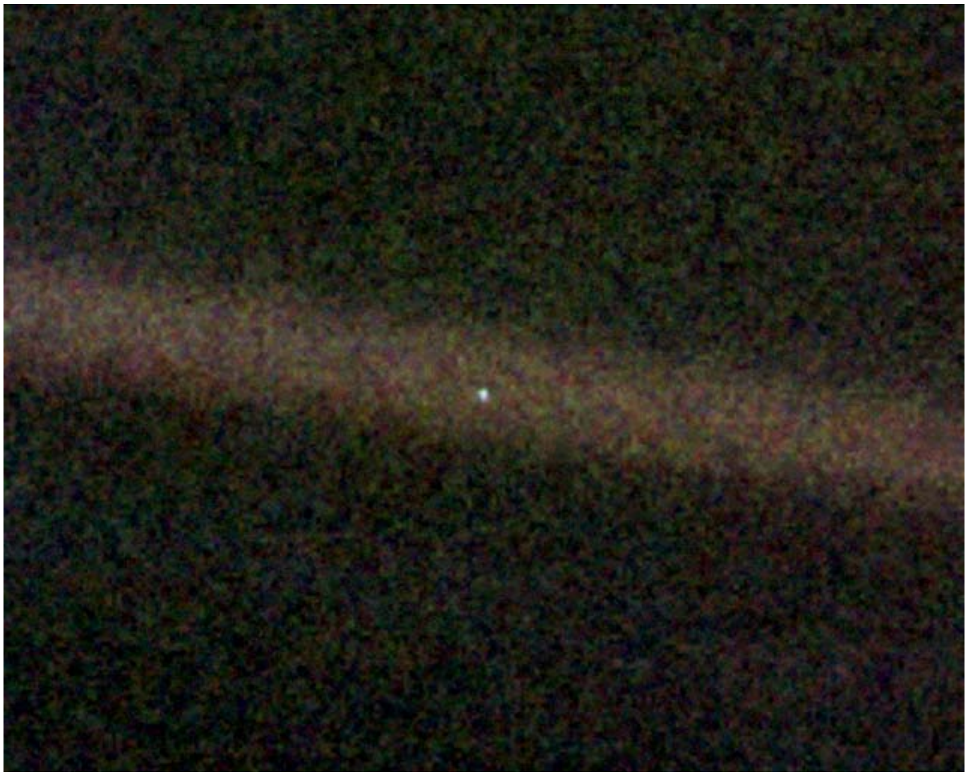

But for us, it's different. Look again at that dot. That's here. That's home. That's us. On it everyone you love, everyone you know, everyone you ever heard of, every human being who ever was, lived out their lives. The aggregate of our joy and suffering, thousands of confident religions, ideologies, and economic doctrines, every hunter and forager, every hero and coward, every creator and destroyer of civilization, every king and peasant, every young couple in love, every mother and father, hopeful child, inventor and explorer, every teacher of morals, every corrupt politician, every 'superstar', every 'supreme leader', every saint and sinner in the history of our species lived there on a mote of dust suspended in a sunbeam.

- Carl Sagan

For the pale blue dot

ACKNOWLEDGEMENTS

First and foremost, I would like to thank my academic advisor and dissertation committee chair, Professor Mike Liemohn. He has provided me with infinite encouragement and support since the moment I began working with him (despite suffering through my frequent and prolonged spells of confusion). Mike has been both a professional and personal mentor in that he genuinely enjoys sharing his vast and keen knowledge of the physical world and does so with patience, kindness and eloquence. He has provided the most positive and enjoyable working environment imaginable and I will forever be grateful for having the opportunity to work with someone of his intellect and character.

I would also like to thank my dissertation committee, Prof. James Slavin, Prof. Edwin Bergin, Prof. Andy Nagy, Dr. Xiaohua Fang and Dr. Jared Espley. Their guidance and valuable suggestions have significantly helped me navigate the academic world and have greatly improved this dissertation.

I would like to express my admiration and gratitude to Prof. Mark Moldwin, Prof. Darren McKague, Prof. Lennard Fisk, Prof. Tamas Gombosi and Prof. Derek Posselt, all of whom provided exceptional instruction and advice, as well as suffered through many of my inane questions. Prof. Sally Oey and my undergraduate adviser Prof. Austin Napier (Tufts) have also been incredibly generous with their time and have served as excellent mentors and role models for me.

Naturally, our research would not be possible (and possibly the Earth would stop turning) without the help of the administrative staff. In particular, Eidilia Thomas,

Jan Beltran, Margaret Reid, Marty Moon and Linda Chadwick have shown such kindness and patience to the students- most of us being blithely unaware of what it takes to keep a department running.

I am also indebted to the various degrees of technical support from Faye Ogasawara, Bryan White, Darren Britten-Bozzone and Melissa Terwilliger. An enormous hat tip goes to Jason Gilbert for making the AOSS LaTeX template and I would have switched to a field with less equations had it not been for http://www.codecogs.com/latex/eqneditor. I also would like to thank Brock Palen and the rest of UM's Center for Advanced Computing for their tireless efforts and help with parallel computing. Dan Welling, Yuni Lee and Fang Fang have donated a selfless amount of time helping me plot various items, whom I am indebted to. I would also like to extend my gratitude and admiration to Elizabeth Hildinger who has not only improved the quality of my technical writing, but has reminded me how enjoyable it is to be passionate about one's 'craft'.

On a personal note, I would not have gotten through qualifying exams, Michigan winters, insidious vorticity derivations or early happy hours without the enormous moral support of Catherine, Gina, Fang, Ahmed, Kevin, Dan, Jacob, Paul, Jim, Chan, Devon, Suzie (honorary), many more AOSSers and Whole Foods hot bar and expansive dessert selection. I also owe my elite Alliance membership to Rachael and Amanda (Robot/Dr.Phil and Red) and would not have inherited the glowing nickname of Pippi and all the memories of the Ruf Lab without Sid and John (Shark bait and The Republican). Despite my foul moods every time Tecplot crashes, Meng, Xing, Chuanfei, Chunpeng, Xiangyun (xyz), Zhenguang have a smile for me every time I walk down the hall, which is often the last thread of my sanity.

I have also had endless encouragement from Jennie and Alan Berliant, the Sittenfelds, the Marrs, Rick Oliver and Michael Kelley, Mike Reagan, Drew Gores, and many other family friends during trying times throughout my PhD. While the President has not directly been a part of my scientific career, I am that much more proud to be a scientist with Barack and Michelle Obama in the White House. I began my PhD in 2008 and the night Obama was elected was the night, I truly felt like we all started a new chapter and science (and our country) had very real hope ahead.

Finally, words fail me in expressing my love and gratitude for my family. To Uncle Stu, Uncle Don and Uncle Mark, thank you for 'wangling' a beer for me and talking space on the porch every summer. To Mimi, thank you for your love and support, and passing on our genetic disposition to aggressively pursue what we want. To Aunt Diane, thank you for setting an example for Lisa and me in leading a life we choose, and providing us with the opportunities to achieve our dreams. To Mom, Dad and Lisa, everything I have ever known and loved in space is only a fraction of how much I know I love you.

TABLE OF CONTENTS

CHAPTER

LIST OF FIGURES

Figure

LIST OF TABLES

Table

LIST OF APPENDICES

Appendix

ABSTRACT

Test particle analysis of high altitude ion transport and escape on Mars

by

Shannon Curry

Chair: Michael Liemohn

Because Mars has a weak magnetic field in comparison with Earth, the solar wind can directly interact with the neutral planetary environment and drive atmospheric erosion. Located in the overlap region of the atmosphere and the solar wind, the neutral constituents of the atmosphere are ionized and instantaneously affected by the fast-moving solar wind and interplanetary magnetic field. These newly-created ions are 'picked up' by the solar wind, and accelerated away from Mars by the solar wind's motional electric field. The main objective of this work is to extensively probe the high altitude ion transport and escape on Mars using a test particle model that tracks the motion and acceleration of pick-up ions through near-Mars space using virtual detectors.

The first focus of this study addresses how the escape of O^+ is influenced relative to the production mechanisms: photoionization, charge exchange and electron impact, finding that the total production and loss rates differ up to two orders of magnitude. This dissertation also investigates the influence of the hot oxygen corona and the solar cycle on the individual ion trajectories. This study found that the inclusion of the

corona roughly doubles the total escape for solar minimum conditions and directly contributing to high energy sources above 1 keV and increases the O^+ flux and total escape by an order of magnitude from solar minimum to maximum. Two other related focal points for this dissertation included examining which species dominates pick-up ion loss from Mars and quantifying how the ionospheric source influences subsequent pick-up ion acceleration. While the results indicate that O^+ dominate the loss, the ionospheric species O_2^+ and CO_2^+ were most likely to escape.

The simulations have robustly described the physics controlling high altitude ion escape by isolating the influence of ion production, the solar cycle, the ionospheric contributions, the dominant species and the background fields. The results presented are significant for the eventual interpretation of ion observations at Mars in order to quantify how much of the atmosphere is escaping, which is a critical aspect of understanding how water has evolved on Mars.

CHAPTER I

Background

1.1 Past and present atmosphere on Mars

Because Mars and Earth underwent similar processes in their formation, Mars serves as an excellent subject for comparing how the planets have evolved and why these planets are so different. Earth and Mars are believed to have formed $\sim$ 4.5 billion years ago, but life on Earth began within another billion years during the Hadean era when it had an ocean and thick atmosphere (*Sleep and Zahnle*, 2001).

Geomorphological evidence suggests that liquid water also existed on Mars when it had a much warmer, thicker atmosphere (e.g. *Squyres et al.* (2004)) that has since evolved into the much colder and thinner atmosphere of the present day. While some of this water may be frozen on or below the surface (*Carr*, 2003), a portion may have escaped to deep space as neutral or charged particles. Consequently, studying the current atmospheric production and loss of oxygen and hydrogen addresses the bigger question of how the presence of water (H_2O) has evolved on Mars (*Jakosky and Phillips*, 2002).

Given the time scales, atmospheric evolution and escape are among many challenging disciplines in space and planetary physics. Generally, atmospheric escape can be discussed in the context of thermal or non-thermal loss. Non-thermal atmospheric loss mechanisms include pick-up ion processes (*Cravens et al.*, 2002; *Luhmann et al.*, 2006; *Fang et al.*, 2008), dissociative recombination of molecular ions (*Lammer and Bauer*, 1991; *Fox*, 1993), and atmospheric sputtering (*Luhmann and Kozyra*, 1991; *Johnson*, 1994). Thermal loss processes (Jeans and hydrodynamic escape) and impact erosion (*Hunten*, 1993) have also played an important role, but the primary subject of this dissertation will be the nonthermal aspects of pick-up ion escape.

1.2 Thermal and non-thermal atmospheric escape

We begin the discussion of atmospheric loss with a brief summary of thermal escape because it is believed to contribute to at least half of the total atmospheric escape at Mars (*Cipriani et al.*, 2007; *Valeille et al.*, 2009, 2010). Thermal escape describes different ways in which neutral atoms can acquire energy to continue on a trajectory until they are lost to space, often dealing with the escape of lighter species. The neutral atoms and molecules that constitute an atmosphere are gravitationally bound to a planetary body, so the farther from the planet they are, the less that gravity exerts a force on them. Mars has a weaker gravitational field than Earth due to its smaller size ($\sim$0.1 M_{Earth}), so neutrals in the upper atmosphere require significantly less energy to escape than at Earth.

The speed of these atmospheric neutrals is determined by the average number of collisions in a neutral gas, which can be approximated by a Maxwellian distribution. As the neutral density decreases with altitude, the neutrals experience fewer collisions and the thermal velocity is no longer normally distributed. When a particle no longer experiences frequent collisions and its mean free path approaches a planetary radius, its motion becomes a ballistic trajectory [*Gombosi* (1998)]. We refer to the altitude where this transition takes place as the exobase. At especially high altitudes above the exobase when the neutrals no longer experience collisions, the velocity of lighter neutral species (hydrogen, helium) can exceed the escape speed. In these instances the neutrals are lost to space, a process referred to as Jeans escape (thermal escape).

Nonthermal escape, as its name suggests, often includes collisional processes that energize a particle above its thermal velocity (*Shizgal and Arkos*, 1996). Heavier species, such as oxygen, nitrogen, and carbon, experience Mars' gravitational field more than the lighter constituents and subsequently have a lower scale height (see Appendix C.1.4). Typically, nonthermal escape involves ionization of a neutral species via collision or energetic ejection of an electron. Examples of nonthermal escape processes include

- Dissociative recombination: when an ion recombines with an electron to become a neutral with a given recombination energy, giving the neutral enough energy to possibly escape
- Sputtering: when an accelerated ion (often a solar wind proton) enters the atmosphere and collides with a neutral causing the ion to transfer its energy to the neutral. The neutral in turn may then have enough energy to escape the atmosphere.
- **Pick-up ions: when planetary neutrals are ionized (via photoionization or collision) and accelerated, or swept away, by the solar wind convective electric field**

Thus far, collisions have been a focus of the background discussion because they dictate what type of physics and assumptions are appropriate. Thermal and nonthermal escape are processes that are based on individual particle motion, or *kinetics*. This is an important distinction and specific modeling efforts and assumptions based on kinetics will be discussed in Chapter III.

1.3 Mars-solar wind interaction

The atmospheric loss and transport of oxygen ions are especially unique in the Martian plasma environment due to the complexity of the direct solar wind interaction with the atmosphere. The solar wind around Mars can be described as a fast flowing plasma around an obstacle, in this case the non-magnetized planet of Mars. At planets with an intrinsic dipole magnetic field, such as Earth, Mercury and the gas giants, the supersonic, superalfvenic, magnetized solar wind interacts with the magnetic field of the planet and forms a magnetosphere. In the case where the planet is unmagnetized, the solar wind decelerates when it directly interacts with the dayside atmosphere and ionosphere, resulting in an *induced magnetosphere*. In both cases, a standing bow shock forms and the region between the limit of the magnetosphere (the magnetopause) and bow shock constitutes the magnetosheath. This region in particular hosts a number of complex wave and particle interaction processes due to the solar wind configuration.

The solar wind itself is an extension of the solar corona streaming radially away from the Sun throughout the solar system. It is composed of hot, fast moving ionized particles (mostly protons and electrons), and its velocity, density and composition can vary as a function of solar cycle and distance. As the Sun rotates, its magnetic field rotates with it because its dynamic pressure dominates over the magnetic pressure. Assuming an infinitely conducting plasma, the magnetic field is frozen into this coronal plasma (the frozen-in condition). As the solar wind plasma streams radially away from the corona, it carries a portion of the Sun's magnetic field. Because one end of these interplanetary magnetic fields remains rooted in the corona, which rotates with the Sun, an Archimedean or *Parker spiral* is created (shown in Figure 1.1). As the distance from the Sun increases, the angle of the Parker spiral increases until it approaches 90°, which is well beyond the orbit of Mars.

This magnetic field streaming away from the Sun is known as the interplanetary magnetic field (IMF). The strength and direction of the IMF also varies as a function of distance from the Sun and solar conditions. Without the shielding of a dipole magnetic field at Mars, the upper neutral atmosphere directly interacts with the IMF

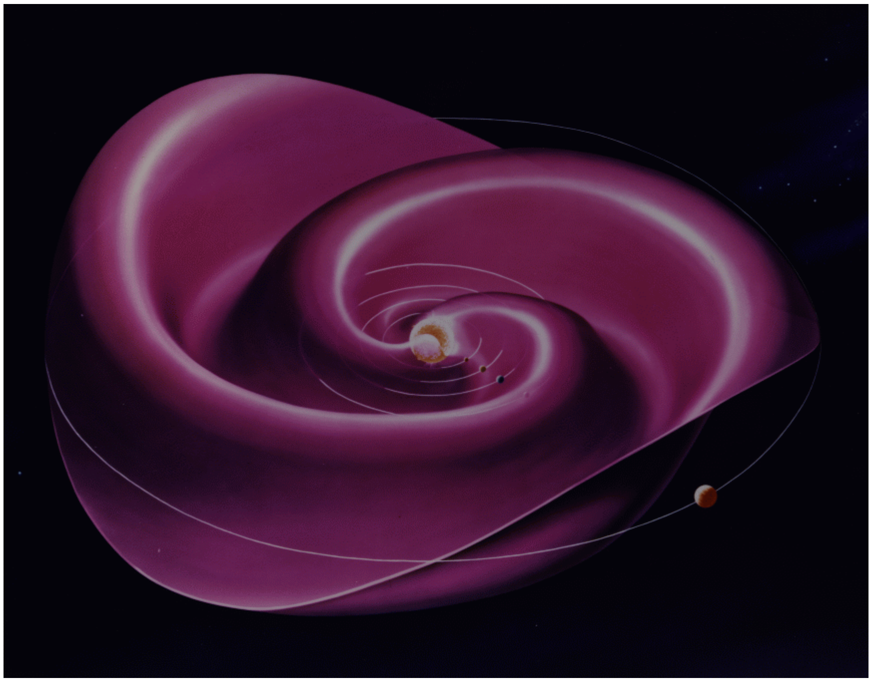

Figure 1.1: Artist's conception of the heliospheric current aheet in a Parker Spiral- (*image courtesy of http://wso.stanford.edu/gifs/HCS.html*).

(**B**) and solar wind particles.

This direct interaction of the solar wind and atmosphere is responsible for pick-up ions, which form when planetary neutrals are ionized and accelerated or swept away by the solar wind convective electric field ($\mathbf{E} = -\mathbf{U} \times \mathbf{B}$). Figure 1.2 illustrates the Mars solar wind interaction. The main source of these pick-up ions is Mars' upper atmosphere and exosphere, which contain 'hot' neutral species (often referred to as the corona). The corona includes oxygen, hydrogen, carbon, and nitrogen due to dissociative recombination of planetary molecular ions (*Fox and Ha*, 1997; *Nagy et al.*, 2004; *Chaufray et al.*, 2007; *Cipriani et al.*, 2007; *Barabash and Holmstrom*, 2002; *Valeille et al.*, 2009).

1.4 Mars in current science

The atmosphere is a critical topic in studying Mars, but the Red Planet has many fascinating features that have captivated scientists, the media and world alike:

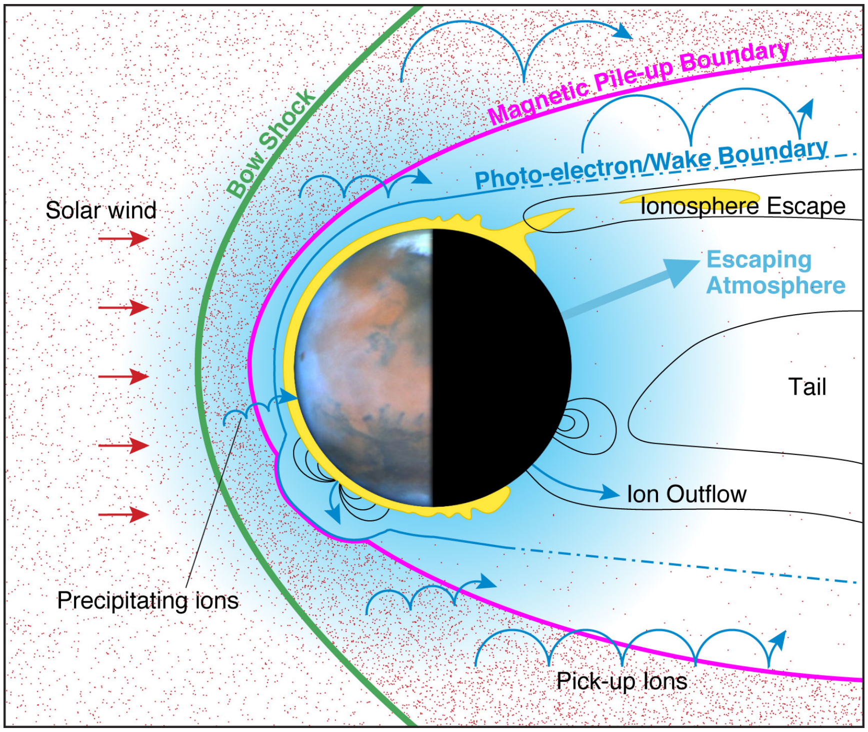

Figure 1.2: The solar wind interaction with Mars and the consequent atmospheric escape (*image courtesy of Stephen Bartlett, 2007*).

- A rocky surface with frozen carbon dioxide and a number of volcanoes, most notably Olympus Mons which is the tallest mountain known within the Solar System
- Valles Marinerus is the biggest canyon in the solar system, as long as the United States and 3 miles deep
- A dark red color comes from rust in soil rich in iron
- Crustal magnetic fields yet no intrinsic dipole magnetic field (see Appendix A)
- Two moons, Deimos and Phobos (small natural satellites) ,which scientists think may be captured asteroids
- A radius ~1/2 of Earth's but with a similar rotational period (24 hours, 36 minutes)

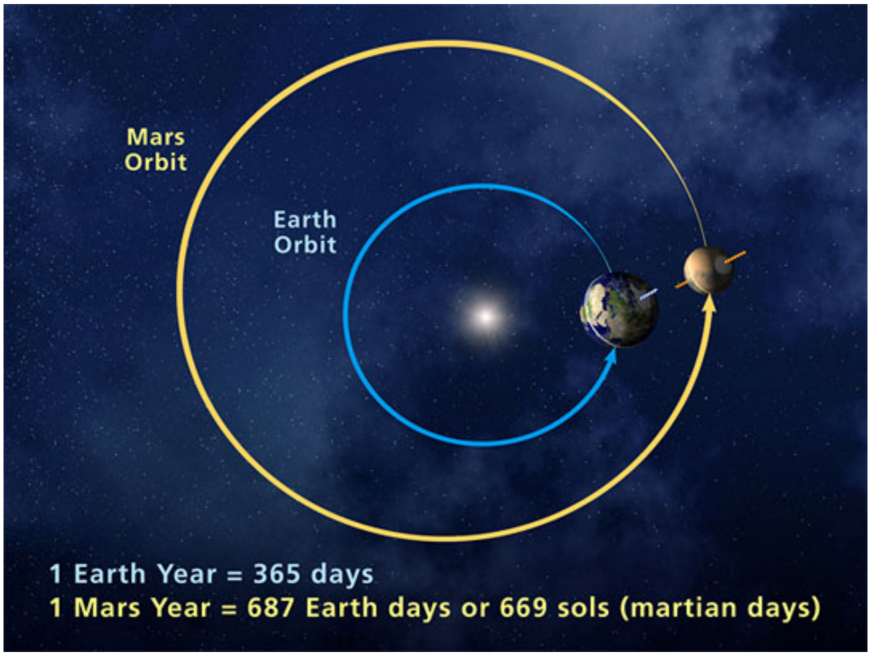

Figure 1.3: An artist's conception of the Martian year (*image courtesy of NASA, http://mars.jpl.nasa.gov/allaboutmars/extreme/martianyear/*).

- A highly eccentric orbit in comparison to Earth: perihelion = 1.381 AU and aphelion = 1.666 AU, which drives extreme differences in solstice periods and seasons
  - The Mars year is almost twice as long as Earth's, so a mission to Mars has to be very carefully timed in order to minimize the distance a spacecraft has to travel (see Figure 1.3)

Other than the moon, more space missions have been sent to Mars than any other solar system body. Rovers and orbiters have been visiting Mars since 1964 by the U.S., Russia (former Soviet Union) and Japan. A full table of missions can be seen in Table 1.1:

Table 1.1: Missions to Mars

Launch	**Name**	**Country**	**Outcome**	**Results**
1960	Korabl 4	USSR (flyby)	Failure	Didn't reach Earth orbit
1960	Korabl 5	USSR (flyby)	Failure	Didn't reach Earth orbit

Continued on next page

Table 1.1 – *Continued from previous page*

Launch	**Name**	**Country**	**Outcome**	**Results**
1962	Korabl 11	USSR (flyby)	Failure	Earth orbit only; spacecraft broke apart
1962	Mars 1	USSR (flyby)	Failure	Radio Failed
1962	Korabl 13	USSR (flyby)	Failure	Earth orbit only; spacecraft broke apart
1964	Mariner 3	US (flyby)	Failure	Shroud failed to jettison
1964	Mariner 4	US (flyby)	Success	Returned 21 images
1964	Zond 2	USSR (flyby)	Failure	Radio failed
1969	Mars 1969A	USSR	Failure	Launch vehicle failure
1969	Mars 1969B	USSR	Failure	Launch vehicle failure
1969	Mariner 6	US (flyby)	Success	Returned 75 images
1969	Mariner 7	US (flyby)	Success	Returned 126 images
1971	Mariner 8	US	Failure	Launch failure
1971	Kosmos 419	USSR	Failure	Achieved Earth orbit only
1971	Mars 2 Orbiter/Lander	USSR	Failure	Orbiter arrived but no data and Lander destroyed
1971	Mars 3 Orbiter/Lander	USSR	Success	Orbiter obtained 8 months of data
1971	Mariner 9	US	Success	Returned 7,329 images
1973	Mars 4	USSR	Failure	Flew past Mars
1973	Mars 5	USSR	Success	Returned 60 images; only lasted 9 days
1973	Mars 6 Orbiter/Lander	USSR	Partial Success	Occultation produced data but Lander failure on descent
1973	Mars 7 Lander	USSR	Failure	Missed planet; now in solar orbit.
1975	Viking 1 Orbiter/Lander	US	Success	Located landing site for Lander and first successful landing on Mars
1975	Viking 2 Orbiter/Lander	US	Success	Returned 16,000 images, atmospheric data and soil experiments
1988	Phobos 1 Orbiter	USSR	Failure	Lost en route to Mars
1988	Phobos 2 Orbiter/Lander	USSR	Failure	Lost near Phobos

Continued on next page

Table 1.1 – *Continued from previous page*

Launch	**Name**	**Country**	**Outcome**	**Results**
1992	Mars Observer	US	Failure	Lost prior to Mars arrival
1996	Mars Global Surveyor	US	Success	More images than all Mars Missions
1996	Mars 96	USSR	Failure	Launch vehicle failure
1996	Mars Pathfinder	US	Success	Technology experiment lasting 5 times longer than warranty
1998	Nozomi	Japan	Failure	No orbit insertion; fuel problems
1998	Mars Climate Orbiter	US	Failure	Lost on arrival
1999	Mars Polar Lander	US	Failure	Lost on arrival
1999	Deep Space 2 Probes (2)	US	Failure	Lost on arrival (carried on Mars Polar Lander)
2001	Mars Odyssey	US	Success	High resolution images of Mars
2003	Mars Express Orbiter/Beagle 2 Lander	ESA	Partial Success	Orbiter imaging Mars in detail but lander lost on arrival
2003	Mars Exploration Rover - Spirit	US	Success	Operating lifetime of more than 15 times original warranty
2003	Mars Exploration Rover - Opportunity	US	Success	Operating lifetime of more than 15 times original warranty
2005	Mars Reconnaissance Orbiter	US	Success	Returned more than 26 terabits of data
2007	Phoenix Mars Lander	US	Success	Returned more than 25 gigabits of data
2011	Mars Science Laboratory	US	Success	Exploring Mars' habitability

1.5 Objective

In summary, a number of missions have observed Mars and a number of simulations have modeled the atmosphere, but the contribution of the high altitude ion sources to overall atmospheric escape has not been substantially addressed to date. The main objective of this work is to extensively probe the high altitude ion transport and escape on Mars using a test particle model that tracks the motion and acceleration of pick-up ions through near-Mars space. The assumptions of the test particle model are well suited for this environment and with the current parallel processing framework, very high resolution distributions at any given virtual detector can be constructed. This work can serve as an important tool for simulating ions in the high altitude environment when observations are unavailable and can also serve as a comparison for current and future missions.

CHAPTER II

Introduction

2.1 Past studies

Non-thermal atmospheric loss mechanisms play a significant role in understanding how the presence of water has evolved on Mars. Many of these processes, including pick-up ion processes (*Cravens et al.*, 2002; *Luhmann et al.*, 2006; *Fang et al.*, 2008), dissociative recombination of molecular ions (*Lammer and Bauer*, 1991; *Fox*, 1993), and atmospheric sputtering (*Luhmann and Kozyra*, 1991; *Johnson*, 1994), are unique at Mars because the planet lacks an intrinsic dipole magnetic field. Consequently, the solar wind directly interacts with the neutral atmosphere, including the extended hot oxygen and hydrogen corona, and ionizes it to produce planetary ions, which are subsequently accelerated, or picked up, and swept away by the solar wind flow (*Luhmann and Kozyra*, 1991). The convective electric fields and interplanetary magnetic fields (IMF) transfer energy to the newly created pickup ions, slowing the solar wind flow around the planet. Thus, the processes of pickup ions and mass loading on Mars represent the complex interaction between an unmagnetized planet and the solar wind and are a critical area of research in understanding atmospheric evolution.

2.1.1 Ionization production

Pick up ions are generated in both the ionosphere and exosphere in one of three ways. Through photoionization, solar radiation ionizes the planetary neutrals. Charge exchange collisions occur with both solar wind protons and planetary ions and finally, solar wind electrons impact and ionize neutrals. These pick-up ions constitute a major source of nonthermal atmospheric loss on Mars. The most abundant ion species in the Mars plasma environment are CO_2^+, O^+, H^+ and O_2^+. The approach for Chapter IV focuses on quantifying O^+ loss and the contributing factors to O^+ escape in order to better understand the erosion of the Martian atmosphere. Specifically, this study uses a test particle approach to examine the relative contribution of different production mechanisms for upper atmospheric O^+ ions, which has not been explored in detail.

Measurements from the Phobos 2, Mars Global Surveyor (MGS), and the Mars Express (MEX) missions have provided numerous observations of the pickup ion process and subsequent escape (*Lundin et al.*, 1989; *Rosenbauer et al.*, 1989; *Barabash et al.*, 1991; *Verigin et al.*, 1991; *Lundin et al.*, 2004; *Dubinin et al.*, 2006; *Fedorov et al.*, 2006; *Barabash et al.*, 2007; *Lundin et al.*, 2009). *Barabash et al.* (2007) reported escape rates of 1.6×10^{23} ions/sec for solar minimum from the ASPERA-3 ion mass analyzer instrument on board the MEX spacecraft, showing agreement with a number of modeled results (*Ma et al.*, 2004; *Modolo et al.*, 2005; *Chaufray et al.*, 2007; *Terada et al.*, 2009; *Kallio et al.*, 2010; *Najib et al.*, 2011) . Using a different mode of the MEX ion mass analyzer, *Lundin et al.* (2009) extended the energy range of the *Barabash et al.* (2007) study and consequently increased the observed loss rate by an order of magnitude to 2.1×10^{24} ions/sec.

In addition to observations, various models and observational studies have also addressed pick up ions in the broader context of Martian atmospheric evolution. In investigating the solar wind's interaction with Mars, simulations have been extremely useful tools for probing the physics of this system. Generally, they fall into three categories: magnetohydrodynamic (MHD) models (*Liu et al.*, 1999; *Ma et al.*, 2004; *Harnett and Winglee*, 2006; *Jin et al.*, 2006; *Terada et al.*, 2009; *Najib et al.*, 2011), hybrid models (*Modolo et al.*, 2005; *Boesswetter et al.*, 2007; *Kallio et al.*, 2010; *Brecht and Ledvina*, 2010; *Kallio and Jarvinen*, 2012; *McKenna et al.*, 2012), and test particle simulations (*Luhmann and Kozyra*, 1991; *Kallio and Koskinen*, 1999; *Cravens et al.*, 2002; *Luhmann et al.*, 2006; *Fang et al.*, 2008).

MHD models describe the plasma environment as a fluid, and therefore are very efficient at self-consistently solving for the plasma parameters and magnetic field configuration around a planet. However, they assume a Maxwellian velocity distribution, and as a consequence do not account for pickup ions with extremely large gyroradii (*Liu et al.*, 1999; *Ma et al.*, 2004; *Harnett and Winglee*, 2006; *Terada et al.*, 2009; *Najib et al.*, 2011). Hybrid models represent the ions as individual particles and the electrons as a massless charged neutralizing fluid, but can be computationally taxing. As a consequence, the number of particles per cell above 300 km is very limited on the order of 5 to 30 (*Brecht and Ledvina*, 2006; *Modolo et al.*, 2005; *Boesswetter et al.*, 2007; *Kallio et al.*, 2010). It should be noted that *Brecht and Ledvina* (2010) used 16-20 particles per cell in the shock region but launched 10,000 particles per cell in the ionosphere. While self-consistent models are important for predicting plasma parameters, test-particle simulations have the capability to resolve the distribution of ions in velocity space using billions of particles which can reveal features about ion trajectories and subsequent loss. Because the constraints of a Maxwellian approach are lifted, there is no averaging of gyroradii or pitch angles, which proves critical on an unmagnetized planet with gyroradii on planetary scales (*Luhmann and Kozyra*, 1991; *Kallio and Koskinen*, 1999; *Cravens et al.*, 2002; *Luhmann et al.*, 2006; *Fang et al.*, 2008; *Andersson et al.*, 2010; *Fang et al.*, 2010a).

A study by *Brain et al.* (2010a) compared seven models in order to investigate the Mars electromagnetic environment, including O^+ escape rates. Using identical inputs for the solar wind, neutral atmosphere, ionosphere, IMF and EUV, over an order of magnitude difference for the O^+ escape rates existed among the models. The strong variations in the modeled atmospheric escape and the observations are a critical motivation for probing the factors influencing how O^+ loss is calculated in the Mars space environment.

Given the disparities in O^+ loss from observations and modeling efforts, this paper aims to investigate loss via the influence of O^+ ion production processes: photoionization, electron impact and charge exchange. Similar studies include *Zhang et al.* (1993) and *Bauske et al.* (1998), who explored ion production at Mars and Venus respectively but did not examine the influence of ion production mechanisms on total escape rates or velocity space. While *Li et al.* (2011) did explore O^+ velocity space using a test particle model, the objective was the influence of crustal fields on the spatial and energy distribution of precipitating pickup ions. Because the MTP can be run with over 10^9 particles, pickup ion distributions in velocity space are finely resolved and therefore can be used to describe specific populations of escaping O^+ (*Fang et al.*, 2008). The MTP simulation is based on the published model of *Fang et al.* (2008) and uses background MHD electromagnetic fields from *Ma et al.* (2004).

2.1.2 Solar cycle and corona

Questions surrounding the role of oxygen escape in the evolution of CO_2 and H_2O inventories in Mars' atmosphere have motivated numerous studies on atmospheric loss, particularly with respect to nonthermal processes (*Jakosky and Phillips*, 2002). Because Mars has an extended hot oxygen corona due to dissociative recombination (*Fox and Ha*, 1997; *Nagy et al.*, 2004; *Chaufray et al.*, 2007; *Cipriani et al.*, 2007; *Barabash and Holmstrom*, 2002; *Valeille et al.*, 2009), the escape of oxygen ions constitutes one of the dominant sources of nonthermal atmospheric loss [e.g. *Kallio et al.*

(2011) and references therein].

Brain et al. (2010a) conducted a global model comparison activity involving many of the current models for the Martian plasma interaction using a common set of input and boundary conditions for a nominal solar wind case. A number of diagnostics were extracted from the simulations and compared, including 1D pressure profiles, 2D slices of ion density, and global atmospheric escape rates. Among these diagnostics, *Brain et al.* (2010a) noted over an order of magnitude difference among the different models in the simulated O^+ escape rates for the selected input conditions.

A follow-on study has been underway using a common set of rate coefficients (*Brain et al.*, 3-7 Dec. 2012), neutral atmospheric profiles, and identical upstream conditions. As part of this global model comparison effort, multiple simulations were run for solar minimum and maximum conditions. Chapter V investigates the influence of the oxygen corona and solar cycle on the individual ion trajectories. Using the Mars Test Particle (MTP) simulation to solve for these kinetic effects, the O^+ trajectories can be translated into virtual detections at different spatial locations around the planet. By examining different fluxes and energy ranges for the velocity space distributions (VSD), we quantify the influence of the solar cycle and hot corona. The focus of Chapter V is to use the MTP to explore how variations in the neutral atmosphere influence O^+ acceleration and loss.

2.1.3 Ionospheric outflow and multiple species

Several processes are known to contribute to the loss of planetary ions from the Mars upper atmosphere, in particular for O^+ but also the heavier molecular ion species of CO_2^+ and O_2^+. Some studies discuss the flow of ions from the ionosphere proper (i.e., altitudes below 250 km) as the main loss process for oxygen ions from Mars [e.g., (*Lundin et al.*, 2006; *Brecht and Ledvina*, 2012), sometimes purely from the dynamical flow patterns in the transition region between the ionosphere and solar wind magnetosheath above it (*Lundin et al.*, 2004; *Penz et al.*, 2004; *Brecht and Ledvina*, 2006; *Barabash et al.*, 2007; *Pérez-de Tejada et al.*, 2009; *Kallio et al.*, 2010), but also in the context of localized acceleration mechanisms like wave heating (*Ergun et al.*, 2006; *Andersson et al.*, 2010), parallel electric fields (*Boesswetter et al.*, 2004; *Brain et al.*, 2006; *Lundin et al.*, 2006; *Dubinin et al.*, 2009), or magnetic reconnection (*Harnett*, 2009; *Brain et al.*, 2010b; *Eastwood et al.*, 2012).

While some observational studies of the escape of O^+ from Mars are careful to simply refer to high-altitude O^+ as a planetary ion (*Verigin et al.*, 1991; *Fedorov et al.*, 2006), many studies often use the term ionospheric outflow for the source of the particles measured far from the planet. *Lundin et al.* (2008, 2009) used this term for the Mars Express observations of planetary ions observed at high altitude but within the induced magnetospheric boundary (i.e., in the tail behind the planet). This is similar to the finding from Phobos-2 observations of planetary ions in the tail region (*Lundin et al.*, 1989, 1990; *Kallio and Koskinen*, 1999). However, several studies from the Phobos-2 mission data set revealed high-energy (greater than 50 keV) O^+ ions (*Afonin et al.*, 1989; *Kirsch et al.*, 1991; *McKenna-Lawler et al.*, 1993; *McKenna et al.*, 2012), presumably coming from ionization of the high-altitude exosphere (*Cravens et al.*, 2002). Similarly, *Carlsson et al.* (2006) noted that the escape rate of planetary ions is more than the ionosphere can typically supply, indicating that either there are additional acceleration processes in the topside ionosphere or that there is a significant high-altitude source.

Modeling studies, like *Brain et al.* (2010a), regularly refer to any planetary ion as 'ionospheric' in origin, regardless of the altitude of ionization. This is convenient from a variable naming standpoint within the code: solar wind ions are those that come into the simulation domain through the outer boundary while ionospheric ions are those entering through the inner boundary or produced within the simulation domain. The problem with this word usage is that the typical use the term 'ionosphere' refers only to the highly conducting layer of peak ionization coincident with the planet's thermosphere. For Mars, this is the altitude range from 100 km to perhaps 250 km altitude (*Boesswetter et al.*, 2004; *Ma et al.*, 2004; *Brecht and Ledvina*, 2010). Further confusion arises because some modeling studies use the term 'ionospheric loss' even when the model inner boundary is above the nominal ionosphere (*Kallio and Janhunen*, 2001; *Modolo et al.*, 2005; *Harnett and Winglee*, 2006). Other modeling studies have shown, however, that the source region for escaping ions is above the ionosphere, resulting from ionization of the neutral exosphere within the magnetosheath (*Luhmann and Schwingenschuh*, 1990; *Cravens et al.*, 2002; *Fang et al.*, 2008; *Curry et al.*, 2012). These later studies find that a majority of the escaping O^+ ions are produced above 300 km altitude.

Ma et al. (2004) briefly commented on the issue of the source altitude for escaping O^+, O_2^+ and CO_2^+ ions. They calculated the total influence through various altitude shells within their multispecies magnetohydrodynamic (MHD) modeling results, determining that the influence saturated in the 350-450 km altitude range. However, they did not investigate the ionization processes and transport mechanisms of the ions dominating the total escape rate. Therefore, it was left ambiguous whether the escape was dominated by ionospheric outflow or by ionization processes at higher altitudes.

Using a test particle model through the electric and magnetic fields of the *Ma et al.* (2004) simulation results, *Fang et al.* (2010b) conducted a rigorous quantification of the percentage of O^+ ions escaping to deep space as a function of their altitude of ionization. It was determined that the fraction of ions that escape among those produced at a given altitude is below 10-20% at 200 km (depending on the local time of the crustal fields), and that this fraction did not cross the 50% mark until an altitude of 400-500 km. The escape fractions reached a saturation value of 70-90% above 600 km, with some ions of high-altitude origin being directed toward the planet by the solar wind convective electric field, resulting in bombardment of the upper atmosphere (*Luhmann and Kozyra*, 1991; *Johnson*, 1994; *Kallio and Koskinen*, 1999).

Similarly, *Fang et al.* (2010a) directly compared ionospheric outflow with high-altitude ionization processes, concluding that the fluid-like flow of O^+ from low altitudes (below 200 km altitude) to deep space is negligible. This study, however, used the background MHD quantities for the ionospheric outflow initialization parameters. Furthermore, the ionospheric outflow test particles were launched from the inner boundary. This is problematic because the particles will gyrate around the local magnetic field and nearly all will cross the plane of the inner boundary on their first cycle. Therefore, the role of ionospheric outflow could have been underestimated in the *Fang et al.* (2010a) study.

In the work presented in Chapter VI-VII, the contribution of ionospheric outflow to the escaping flux of O^+, O_2^+ and CO_2^+ from Mars is investigated. In addition, the ionospheric outflow initialization parameters are systematically varied to determine the influence of each of these factors on the relative contribution of ionospheric outflow to the total loss rate.

2.2 Current science questions

While many studies have examined the nonthermal escape in the Mars space environment, none have extensively quantified the high altitude velocity space distributions (VSD) for different ion sources. A critical yet unresolved question remains: can a Mars aeronomy orbiter resolve the pick-up ion source locations and mechanisms from in situ measured VSDs and estimate atmospheric loss? Our main tool for this study is a test particle simulation that tracks the motion and acceleration of pick-up ions through near-Mars space. This simulation uses background magnetic and electric field values as specified from one of several other global numerical models.

Thus to address these unresolved issues, we systematically examine the planetary ion VSDs for different neutral atmospheric profiles, solar cycles and ion species. We also quantify the physical processes and source locations for specific VSD fine-structure features, and to put this into the context of real and virtual observations of escaping planetary ions. Specifically, we identified the following issues relating to high altitude pick-up ion transport and escape:

1. **Production processes: what is the relative role of different ion production mechanisms in controlling the distribution of planetary ions?**
2. **Solar cycle vs Corona: what atmospheric conditions, including the role of the corona and solar cycle, control the fine-structure features in observed and modeled VSDs of planetary ions?**
3. **Ionospheric sources: how does the ionosphere affect the overall escape?**
4. **Observing ion escape: what are the dominant species and how well can it be quantified?**
5. **Background fields: how do different background fields affect the spatial loss distribution, escape and VSD signatures?**

2.3 Outline

The structure of this dissertation is meant to introduce, discuss and summarize the contributions for high altitude pick-up ion transport at Mars. Chapter I presents the background for the general science questions at Mars and the context of the problem of atmospheric escape. Chapter II discusses the past studies that have addressed nonthermal loss at Mars and current science questions this dissertation undertakes.

Next, Chapter III describes the models and physics that are used to simulate pick-up ion transport and escape in the following studies.

Chapter IV then discusses the first set of results on the influence of ion production on subsequent ion loss at Mars. Chapter V builds on these results and quantifies the effect of the neutral corona and solar cycle on pick-up ion escape. Chapter VI elaborates on the low altitude, ionospheric source of ions that are critical for eventually simulating heavy species pick-up ion trajectories, such as O_2^+ and CO_2^+. Up until this point, all the of simulations has focused on O^+, so Chapter VII expands the study to O_2^+ and CO_2^+ in order to establish which species dominates the pick-up ion distributions. Finally, Chapter VIII uses a different set of background fields in order to establish how the pick-up ions respond to different field line configurations.

The contributions and conclusions for high altitude pick-up ion transport at Mars will be discussed in Chapter IX. Additional information regarding assumptions of the Mars atmosphere, numerical calculations, and modeling parameters are included in the Appendices.

CHAPTER III

Models

3.1 Modeling approach to charged particle transport

In an ideal world, modeling the Mars plasma environment would follow every particle throughout the simulation domain and calculate the cumulative effect on the electromagnetic environment: a fully self-consistent kinetic model. This model would employ the Vlasov equations and apply the collisionless Boltzmann equations to the individual charged particles and Maxwell's equations for the electromagnetic environment. While the physics for this simulation are somewhat understood, this is not currently possible due to computational requirements. As Moore's Law states, the processing speed or power roughly doubles every two years, which has a direct relationship with doubling the total number of transistors for an integrated circuit chip. As the next decades come, great model improvements will be inevitable, but for the current day, must be assessed with the constraints of our current processing capacity.

Around 1980, the first global models began to arise in order to simulate the geospace environment (magnetosphere-ionosphere-thermosphere system (*Raeder*, 2003). 2-D and then 3-D simulations began to describe plasma parameters and electric and magnetic fields as they changed in the presence of the solar wind bulk flow. Gas dynamic models (or magnetogasdynamic models) were used to understand the flow and electromagnetic field configuration around an obstacle such as a planet. Generally they assumed an ideal gas with infinite electrical conductivity could describe the average bulk flow of the solar wind around an obstacle using conservation equations (*Spreiter and Stahara*, 1980).

With the increasing use of parallel-computing, this eventually developed into a magnetohydrodynamic model. As discussed in Chapter II, the scientific community approaches modeling the Mars solar wind interaction with a magnetohydrodynamic (MHD) model, a hybrid model, or a test particle model. The current MHD models self-consistently solve fluid equations for the configuration of charged particles and magnetic fields around a planet. Current hybrid models also self-consistently solve for the plasma parameters and fields, and treat the plasma environment as a combination of individual ions and a massless neutralizing electron fluid. A more recent and third alternative for exploring the Mars plasma environment is a test particle simulation, which treats the ions as particles and follows their trajectories in a prescribed field configuration. Although this approach lacks self-consistency because the test particles do not modify the background fields, it does allow the investigation of high resolution velocity space distributions.

In an investigation of heavy pickup ions at Mars, a test particle approach is well suited to account for the effects of the finite gyroradii on a planetary scale size. The Mars Test Particle (MTP) simulation is a collisionless test particle simulation that follows the trajectories of particles of any atomic weight through the Mars space environment. Because the model is collisionless and not self-consistent, background fields for the bulk velocity, electric and magnetic field lines, and steady state low altitude ions are necessary. It should be noted that the test particle approach is valid when the difference in the velocity and density are small in comparison with MHD velocities and densities used to generate the background electric and magnetic fields (discussed further in Section 3.3.3). A flow chart of the the modeling approach used

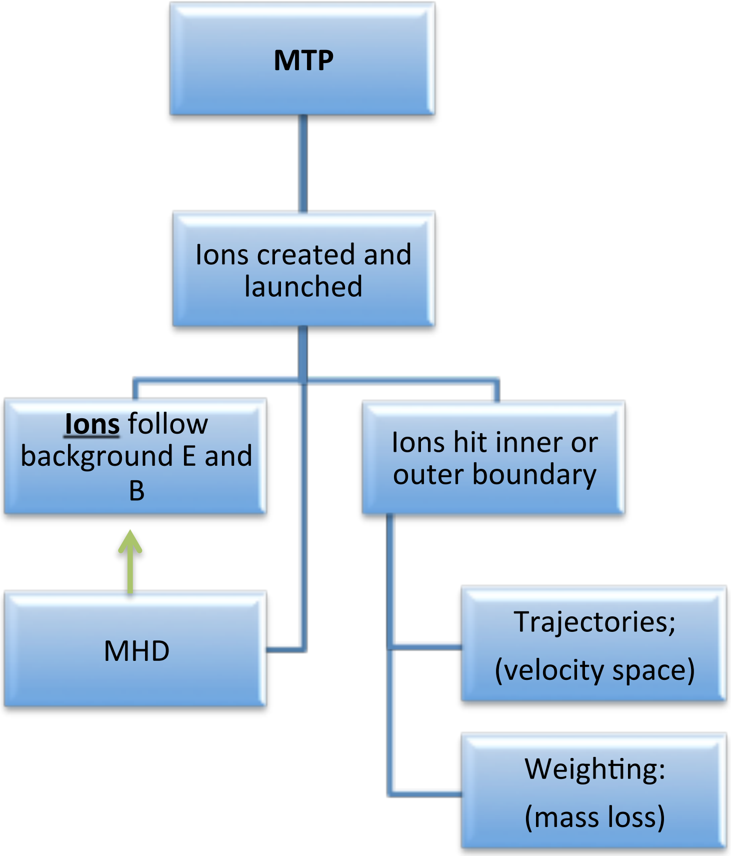

Figure 3.1: A flow chart of the MTP simulation, including the MHD input and resulting production and loss output

in this dissertation is presented in Figure 3.1.

3.2 MHD Model

The background fields for all of the results in this dissertation are based on the multi-species single fluid MHD model from *Ma et al.* (2004). They use the BATS-R-US (Block Adaptive-Tree Solar wind Roe-type Upwind Scheme) MHD model to solve the dimensionless conservative form of the MHD equations for the plasma and field parameters in the space environment around Mars. The model uses a spherical grid structure that extends from the lower boundary in the ionosphere at 100 km to an outer boundary beyond the bow shock upstream and beyond the perturbed flow downstream (nominally at 8 R_M and 24 R_M, respectively). An adaptive mesh grid allows the vertical cell sizes are 10 km near the planet in order to capture the ionospheric profile and then exponentially increases with radial distance. The MHD model solves for separate solutions of the H^+, O^+, O_2^+, and CO_2^+ mass densities.

3.2.1 Electromagnetics

A review of the electromagnetics used in the MHD assumptions will be described here. Beginning with the electric field:

$$\mathbf{E} = -\frac{\nabla p_e}{e n_e} - \mathbf{u_e} \times \mathbf{B} \tag{3.1}$$

Additionally, Maxwell's equations are used to solve the electric and magnetic field configuration:

$$\nabla \cdot \mathbf{E} = \frac{\rho_e}{\epsilon_0} \qquad \text{Gauss's law / Poisson's equation} \tag{3.2a}$$

$$\nabla \cdot \mathbf{B} = 0 \qquad \text{Absence of magnetic poles (Gauss's law for magnetism)} \tag{3.2b}$$

$$\nabla \times \mathbf{E} = -\frac{\partial \mathbf{B}}{\partial t} \qquad \text{Faraday's law} \tag{3.2c}$$

$$\nabla \times \mathbf{B} = \mu_0 \mathbf{J} + \mu_0 \epsilon_0 \frac{\partial \mathbf{E}}{\partial t} \qquad \text{Ampère's law} \tag{3.2d}$$

where ϵ_0 is the electric constant (also called the permittivity of free space), μ_0 is the magnetic constant (also called the permeability of free space), q is the charge, ρ_e

is the charge density, m is the mass, $\mathbf{J}$ is the electric current density, and $\mathbf{E}$ and $\mathbf{B}$ are the electric and magnetic fields.

Because $\mu_0\epsilon_0\frac{\partial \mathbf{E}}{\partial t}$ can be considered negligible here, we can neglect the Hall term and electron pressure gradient terms in order to express the current as:

$$\mathbf{J} = \sigma\left(\mathbf{E} + \mathbf{v} \times \mathbf{B}\right) \quad (\text{A m}^{-2}) \qquad \text{Ohm's law} \tag{3.3}$$

Now assuming conductivity is a constant, we can substitute Equation 3.2c into Equation 3.3, $\mathbf{E}$ and $\mathbf{J}$ can be eliminated to derive the magnetic induction equation (3.4).

$$\frac{\partial \mathbf{B}}{\partial t} = \frac{1}{\sigma\mu_0}\nabla^2\mathbf{B} + \nabla \times (\mathbf{v} \times \mathbf{B}) \qquad \text{magnetic induction equation} \tag{3.4}$$

3.2.2 Transport equations

The foundation of magnetohydrodynamic models (MHD) are the velocity moment equations of the Boltzmann equation (*Gombosi*, 1998); that is to say that MHD is based on the transport equations for macroscopic gases in equilibrium. The Boltzmann equation is written as:

$$\frac{\partial F(t,\mathbf{r},\mathbf{v})}{\partial t} + (\mathbf{v}\cdot\nabla)F(t,\mathbf{r},\mathbf{v}) + (\mathbf{a}\cdot\nabla_v)F(t,\mathbf{r},\mathbf{v}) = \frac{\delta F(t,\mathbf{r},\mathbf{v})}{\delta t} \tag{3.5}$$

where $F(t, \mathbf{r}, \mathbf{v})$ is the phase-space distribution function (*Gombosi*, 1998) and $\mathbf{a}$ is the acceleration, which is generally the Lorentz force in the planetary interaction with the solar wind. Note that phase space (six dimensional) describes a point at a given location and velocity, as seen in Figure 3.2 (*Schunk and Nagy*, 2000).

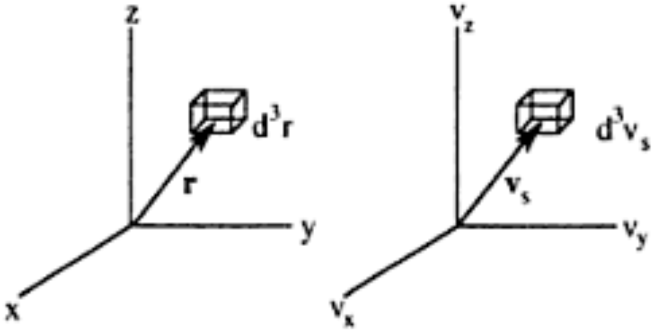

Figure 3.2: Volume element d^3r about position vector $\mathbf{r}$ in configuration space, left, and volume element d^3v_s about velocity $\mathbf{v}_s$ in velocity space (right). Note that each volume element d^3r must contain a sufficient number of particles for a complete range of velocities.

The zeroth velocity moment of the distribution function is the density,

$$n(t, \mathbf{r}) = \int\int\int_{\infty} F(t, \mathbf{r}, \mathbf{v}) d^3v \tag{3.6}$$

the first velocity moment of the distribution function is the average molecular velocity,

$$\mathbf{u}(t, \mathbf{r}) = \frac{1}{n(t, \mathbf{r})} \int\int\int_{\infty} \mathbf{v} F(t, \mathbf{r}, \mathbf{v}) d^3v \tag{3.7}$$

and finally the second velocity moment of the distribution function is the temperature, T, which measures the mean kinetic energy of the particles' random velocity, $\mathbf{c}$:

$$\mathbf{c}(t, \mathbf{r}) = \mathbf{v} - \mathbf{u}(t, \mathbf{r}) \tag{3.8}$$

$$T = \frac{p}{nk} = \frac{m}{k} \frac{1}{n(t, \mathbf{r})} \int\int\int_{\infty} c^2 F(t, \mathbf{r}, \mathbf{c}) d^3c \tag{3.9}$$

The collision frequency is important to consider because they change the momentum and energy of the individual particles (rather than the identity). Beginning with elastic binary collisions, we can take the moment equations for a single gas species with a Maxwellian distribution function, F_0:

$$F_0 = n\left(\frac{m}{2\pi kT}\right)^{3/2} \exp\left[\frac{-mc^2}{2kT}\right] \tag{3.10}$$

where we have assumed the BGK relaxation time approximation (*Gombosi*, 1998) describes how collisions drive will drive each gas component to equilibrium.

Next we consider inelastic collision, which are especially important in the context of planetary interactions with the solar wind because these collisions change the identity of the particle (i.e., via ionization or chemical reaction). The following collisions are photoionization, charge exchange and electron impact, respectively:

$$S + h\nu \rightarrow S^+ + e^- \tag{3.11}$$

$$S^+ + M \rightarrow S + M^+ \tag{3.12}$$

$$S + e^- \rightarrow S^+ + e^- + e^- \tag{3.13}$$

3.2.3 Multi-species single fluid equations

With the inclusion of the collision frequency, the *Euler equations* can be derived by neglecting the heat flow and viscous force terms. Furthermore, accounting for both terms produces the *Navier-Stokes equations.* In addition to the heat and viscosity, the MHD equations consider conductivity where a fluid comprised of neutral and charged particles is considered a conductive fluid.

Here we define an important distinction in MHD modeling: multi-species versus multi-fluid. A set of transport equations which describes the transport of the plasma as a collection of species in bulk is *multi-species single fluid* MHD ($\rho_m = \sum_S m_s n_s$). The multi-species single fluid equations assume that the gas (all ions) have the same bulk velocity and temperature, which yields one energy equation, one momentum equation and S continuity equations (S is the number of species). By further assuming the neutral species have the same temperature, T_n, the multi-species normalized transport equations (the ideal, conservative form) become:

$$\frac{\partial \mathbf{W}}{\partial t} + \nabla \cdot \mathbf{F}^T = \mathbf{Q} \tag{3.14}$$

where the state vector is $\mathbf{W}$ and flux tensor is as $\mathbf{F}$ (*Ma et al.*, 2004), which are respectively defined by:

$$\mathbf{W} = \begin{pmatrix} \rho_i \\ \\ \left(\sum_{i=1}^{4} \rho_i\right) \mathbf{u} \\ \\ \mathbf{B} \\ \\ \varepsilon \end{pmatrix} \tag{3.15}$$

$$\mathbf{F} = \begin{pmatrix} \rho_i \mathbf{u} \\ \\ (\sum_{i=1}^{4} \rho_i)\mathbf{uu} + (\mathrm{p} + \frac{1}{2}\mathrm{B}^2)\mathbf{I} - \mathbf{BB} \\ \\ \mathbf{uB} - \mathbf{Bu} \\ \\ \mathbf{u}(\varepsilon + \mathrm{p} + \frac{1}{2}\mathrm{B}^2) - (\mathbf{B} \cdot \mathbf{u})\mathbf{B} \end{pmatrix} \tag{3.16}$$

where the total energy density, ε, is defined as

$$\varepsilon = \frac{1}{2}(\sum_{i=1}^{4} \rho_i)u^2 + \frac{1}{\gamma - 1}\mathrm{p} + \frac{\mathrm{B}^2}{2} \tag{3.17}$$

$$\mathbf{Q} = \begin{pmatrix} \mathrm{S}_i - \mathrm{L}_i \\ \\ (\sum_{i=1}^{4} \rho_i)\mathbf{g} - (\sum_{i=1}^{4} \rho_i)\nu\mathbf{u} - \mathbf{u}(\sum_{i=1}^{4} \mathrm{L}_i) \\ \\ 0 \\ \\ (\sum_{i=1}^{4} \rho_i)\mathbf{u}\cdot\mathbf{g} - \frac{1}{2}\mathrm{u}^2(\sum_{i=1}^{4} \mathrm{L}_i) - (\sum_{i=1}^{4} \rho_i)\nu\mathrm{u}^2 - \frac{\mathrm{p}}{\gamma-1}(\sum_{i=1}^{4} \frac{\mathrm{L}_i}{m_i} / \sum_{i=1}^{4} \frac{\rho_i}{m_i}) \\ +\frac{\mathrm{kT}_0}{\gamma-1}(\sum_{i=1}^{4} \frac{\mathrm{S}_i}{m_i}) - 4\times 10^{-11}(\sum_{i=1}^{3} n_i)\sum_{i=1}^{4} \frac{\rho_i}{m_i}\exp[10(T_p - 6000)/T_p] \end{pmatrix} \tag{3.18}$$

Finally, these system of equations are solved to equal the source term, $\mathbf{Q}$ in 3.18 where ρ is the mass density, S_i is the production rate, and L_i is the loss rates for each species. The total thermal pressure of the plasma is represented by p, the velocity of the plasma by u, and the ion neutral collision frequency by n. T_0 is the initial temperature of the ions upon production and assumed to be equivalent to the local neutral atmosphere T_n and γ is the ratio of specific heats (assumed to be 5/3). *Ma et al.* (2004) included a final term in equation 3.18 as a 'physics-based ad hoc' term in order to empirically fit the ion temperatures (keep the temperatures close to the observed values in the ionosphere).

Notice that in the single-fluid multi-species manifestation, there are four continuity, one momentum vector, one magnetic induction, and one energy equation because the (*Ma et al.*, 2004) model follows four species (H^+, O^+, O_2^+, and CO_2^+). Because the temperature is also assumed to be a single plasma temperature, the electron and ion temperatures are assumed to be equal, prescribed by $\mathrm{T}_p/2$.

3.2.4 Multi-fluid equations

The multi-fluid equations, based on the study of (*Najib et al.*, 2011) which was developed from *Ma et al.* (2004) discussed in the previous section, now solve the transport equations for each species. As opposed to the multi-species manifestation, the multi-fluid MHD solves separate continuity, momentum, and energy equations for each species. Thus each species has its own temperature, velocity, and density.

$$\frac{\partial \rho_s}{\partial t} + \nabla \cdot (\rho_s \mathbf{u_s}) = \mathrm{S}_s - \mathrm{L}_s \tag{3.19}$$

$$\begin{aligned} \frac{\partial \rho_s \mathbf{u_s}}{\partial t} + \nabla \cdot (\rho_s \mathbf{u_s} \mathbf{u_s} + I p_s) = {} & n_s q_s (\mathbf{u_s} - \mathbf{u}_+) \times \mathbf{B} + \frac{n_s q_s}{n_e e}(\mathbf{J} \times \mathbf{B} - \nabla p_e) \\ & + \rho_s \sum_{t=neutrals} \nu_{st}(\mathbf{u_n} - \mathbf{u_s}) + S_s(\mathbf{u_n} - \mathbf{u_s}) \end{aligned} \tag{3.20}$$

$$\begin{aligned} \frac{1}{\gamma - 1}\frac{\partial p_s}{\partial t} + \frac{1}{\gamma - 1}(\mathbf{u_s} \cdot \nabla) p_s = {} & \frac{\gamma}{\gamma - 1} p_s (\nabla \cdot \mathbf{u_s}) \\ & + \sum_{t=neutrals} \frac{\rho_s \nu_{st}}{m_s + m_t}[3k(T_n - T_s) + m_t(\mathbf{u_n} - \mathbf{u_s})^2] \\ & + \frac{k}{\gamma - 1}\frac{S_s T_n - L_s T_s}{m_s} + \frac{1}{2} S_s (\mathbf{u_n} - \mathbf{u_s})^2 \\ & + \frac{n_s}{n_e}\frac{k}{\gamma - 1}\frac{S_e T_n - L_e T_e}{m_e} \end{aligned} \tag{3.21}$$

$$\frac{\partial B}{\partial t} - \nabla \times (\mathbf{u}_+ \times \mathbf{B}) = 0 \tag{3.22}$$

where once again, ρ is the mass density, S_s is the production rate, and L_s is the loss rates for each separate species including electrons. It should be noted that all of the studies throughout this dissertation use the multi-species single fluid model, rather than the multi-fluid model, in the calculations for particle motion except for a final comparison of the two in Chapter VIII.

3.2.5 Neutral Atmosphere Model: M-TGCM

The neutral atmosphere applied for this study has been either the 1D or 3D Mars Thermospheric Global Circulation Model (MTGCM) (*Bougher and Engel*, 2000; *Bougher et al.*, 2004, 2008). The MTGCM is a self consistent, finite difference primitive equation model that solves for time-dependent neutral temperatures, neutral and ion densities, as well as a neutral winds vector over the Mars globe.

Bougher et al. (2008) describes in detail the code which can solve for CO_2, CO, N_2 , and O as major species and Ar, NO, N(4S), O_2 as minor species. Additionally, MTGCM tracks CO_2^+, O_2^+, O^+, and NO^+ below 180 km using a photochemical atmosphere from *Fox and Sung* (2001) and Viking temperatures.

The M-TGCM model covers the surface to the exobase (0 - 300 km) with lower and upper atmospheric processes. The model calculates the fields from 70 - 300 km, corresponding to 33 pressure levels above 1.32 μbar during solar maximum, with 5 degree grid resolution in longitude and latitude. Beginning with the lower atmosphere below 80 km, the 'fast' radiation code was adapted from the NASA Ames MGCM to include long and shortwave radiation, aerosol heating, and the cooling in the LTE region from the CO_2 15-micron band (*Bougher et al.*, 2008). In the middle atmosphere, 80 - 120 km, the 'fast' radiation code included a correction for the non-LTE region for the near-IR heating rates. Through the middle and upper atmosphere, 80 - 300 km, a thermospheric EUV-UV heating routine (based on mostly CO_2 atmosphere) was implemented along with the NLTE CO_2 15-micron cooling.

Using the GITM framework, the sophisticated MTGCM model can now account for solar cycle, seasonal longitude (the heliocentric distance and solar declination) and dust conditions. Different neutral and ion parameters have shown strong agreement with the Mars Global Surveyor, 2001 Mars Odyssey, and Mars Reconnaissance Orbiter

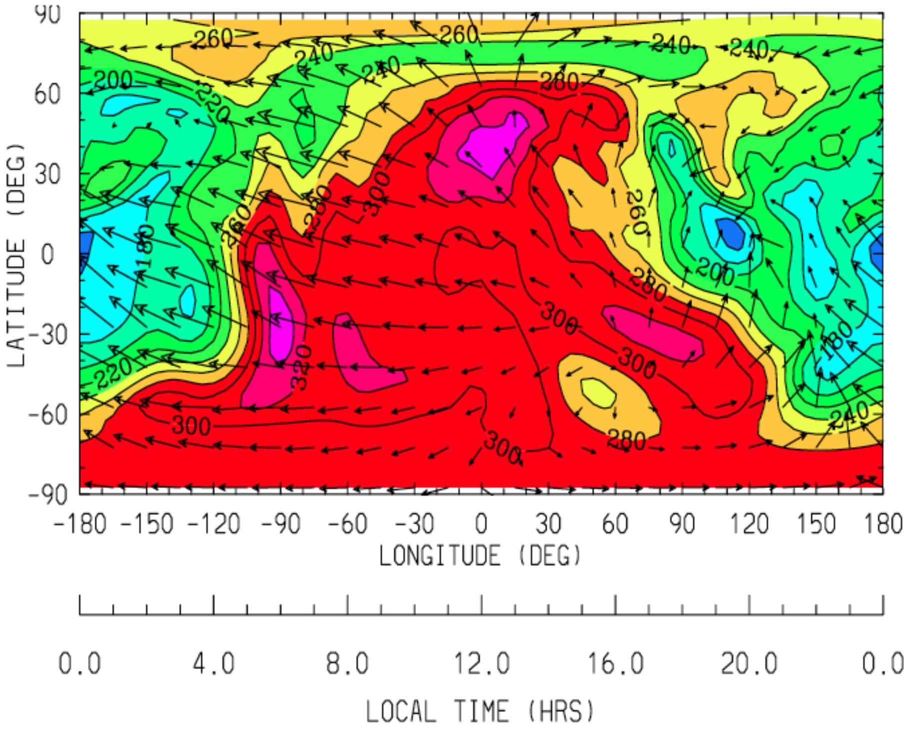

Figure 3.3: From *Bougher et al.* (2008): MTGCM simulated exospheric temperatures and superimposed horizontal neutral winds for Ls = 270, F10.7 = 175 conditions (similar to late Mars Odyssey aerobraking observations). Dayside subsolar latitude (~25 S) temperatures reach ~320 K, nightside minimum temperatures drop to ~145 K. Maximum horizontal winds reach ~550 msec^{-1} (slightly in excess of the sound speed). The average altitude for this slice is ~215 km.

datasets *Bougher et al.* (2008); *Valeille et al.* (2010). Figure 3.3 is an example of neutral horizontal winds at the exobase and temperatures during solar maximum, southern summer solstice conditions.

3.3 Mars Test Particle (MTP) simulation

Test particle modeling approaches trace charged particles (ions or electrons) motion through a background magnetic and electric field, which can be taken from an 'analytic solution' or taken from MHD or hybrid simulations (*Ledvina et al.*, 2008). As discussed in Chapter II, test particle simulations are not self consistent but are much less computationally taxing than its self-consistent counterparts (MHD, hybrid).

The Mars Test Particle (MTP) simulation is a test particle simulation that launches and tracks particles through the Mars space environment. The propagation of ions is governed by the Lorentz and gravitational force (*Fang et al.*, 2008), where the background magnetic and electric fields that the ions follow can be taken from one of the MHD models described above. The simulation follows the test particle trajectories by solving the Newton-Lorentz equation, obtaining a global picture of the angular distributions and energy spectra of pickup oxygen ions in the Martian plasma environment. The test particle approach is valid if changes in the densities and pressure from the test particles are small compared to the MHD densities used to generate the background electric and magnetic fields.

3.3.1 Particle motion / kinetic theory

In order to discuss individual particle motion and trajectories, we will review the assumptions and physics that describe the evolution of a particle at location $\mathbf{r}$. Assuming a non-relativistic charged particle in a uniform electric field without gravity or a magnetic field, the equation of motion would be:

$$\frac{d\mathbf{v}}{dt} = \frac{q}{m}\mathbf{E_0} \tag{3.23}$$

with a solution:

$$\mathbf{v} = \frac{q}{m}\mathbf{E_0}t + \mathbf{v_0} \tag{3.24}$$

Now in the presence of just a magnetic field, $\mathbf{B}_0$, the charged particles' motion can be described by:

$$\frac{d\mathbf{v}}{dt} = \frac{q}{m}(\mathbf{v} \times \mathbf{B}) \tag{3.25}$$

or

$$\begin{pmatrix} \dot{v}_x \\ \dot{v}_y \\ \dot{v}_z \end{pmatrix} = \frac{q}{m} \begin{vmatrix} \mathbf{e}_x & \mathbf{e}_y & \mathbf{e}_z \\ v_x & v_y & v_z \\ 0 & 0 & B_0 \end{vmatrix} = \frac{qB_0}{m} \begin{pmatrix} v_y \\ -v_x \\ 0 \end{pmatrix} \tag{3.26}$$

where $\mathbf{e}_x$, $\mathbf{e}_y$, and $\mathbf{e}_z$ are unit vectors with $\mathbf{e}_z$ in the direction of the magnetic field $\mathbf{B}_0$ (*Gombosi*, 1998). In order to get a frequency, we need an equation describing a simple harmonic oscillator. So taking the time derivative of equation 3.26:

$$\begin{pmatrix} \ddot{v}_x \\ \ddot{v}_y \\ \ddot{v}_z \end{pmatrix} = -\left(\frac{qB_0}{m}\right)^2 \begin{pmatrix} v_x \\ v_y \\ 0 \end{pmatrix} \tag{3.27}$$

we get a frequency for the system, which in this context is the *gyrofrequency*:

$$\Omega = \frac{|q|B_0}{m} \tag{3.28}$$

while q does not influence the sign of the gyrofrequency, it does influence the equations of motion: positively charged particles gyrate clockwise around a magnetic field pointing out of the page, while positively charged particles gyrate the counter-clockwise, as seen in Figure 3.4.

We now have three second-order differential equations solving for the components of $\mathbf{r}_0$,$\mathbf{v}_0$ (six total integration constants) in equation 3.26. We can define the parallel and perpendicular velocity of the particle: $\mathbf{v_0} = (v_\perp, 0, v_\|)$ with respect to $\mathbf{B}_0$. Now equation 3.26 becomes:

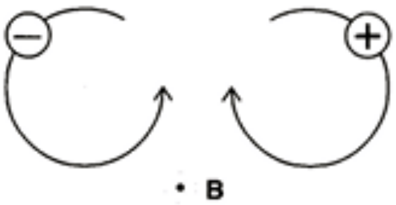

Figure 1.1 Circular trajectories of charged particles in a uniform and constant magnetic field (directed out of the page).

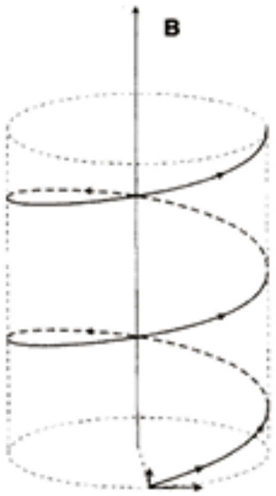

Figure 1.2 Helical trajectory of a negatively charged particle in a uniform and constant magnetic field (directed upward in the *z* direction).

Figure 3.4: Top: the circular trajectories of charged particles in a uniform and constant magnetic field (where B is out the page). Bottom: the helical trajectory of a negatively charged particle in a uniform and constant magnetic field (where B is point upward with +z) (*Gombosi*, 1998).

$$\begin{pmatrix} x - x_0 \\ y - y_0 \\ z - z_0 \end{pmatrix} = \begin{pmatrix} 0 \\ \mp v_\perp/\Omega \\ v_\parallel t \end{pmatrix} + \frac{v_\perp}{\Omega} \begin{pmatrix} \sin \Omega t \\ \pm \cos \Omega t \\ 0 \end{pmatrix} \tag{3.29}$$

This equation illustrates that a particle's motion has two components: 1) the gyration (circular motion) around the magnetic field moving at an angular velocity, Ω, and 2) a constant velocity parallel to the magnetic field line, $v_\parallel$. We can now write the position vector as

$$\mathbf{r} - \mathbf{r_0} = \mathbf{r_g} + r_c \begin{pmatrix} \sin \Omega t \\ \pm \cos \Omega t \\ 0 \end{pmatrix} \tag{3.30}$$

These describe two important terms: the guiding center $\mathbf{r}_g$ and the *gyroradius,* r_c:

$$r_c = \frac{v_\perp}{\Omega} \text{ and } \mathbf{r_g} = \begin{pmatrix} 0 \\ \mp r_c \\ v_\parallel t \end{pmatrix} \tag{3.31}$$

Finally, we will consider the scenario when gravity, a magnetic field and an electric field are uniformly imposed on the system. By defining the acceleration as $\mathbf{a} = \mathbf{g_0} + (q/m)\mathbf{E_0}$:

$$\frac{d}{dt}\begin{pmatrix} v_x \\ v_y \\ v_z \end{pmatrix} = \begin{pmatrix} a_x \\ a_y \\ a_z \end{pmatrix} \pm \Omega \begin{pmatrix} v_y \\ -v_x \\ 0 \end{pmatrix} \tag{3.32}$$

$$\tag{3.33}$$

The solution with initial conditions of $\mathbf{r_0} = (x_0, y_0, z_0)$ and $\mathbf{v_0} = (v_\perp, 0, v_\parallel)$ is now:

$$\mathbf{r} - \mathbf{r_0} = \begin{pmatrix} a_x/\Omega^2 \\ a_y/\Omega^2 \mp v_\perp/\Omega \\ v_\parallel + 1/2 a_z t^2 \end{pmatrix} + r' \begin{pmatrix} \sin(\Omega t - \delta) \\ \pm\cos(\Omega t - \delta) \\ 0 \end{pmatrix} \pm \begin{pmatrix} a_y t/\Omega \\ -a_x t/\Omega \\ 0 \end{pmatrix} \tag{3.34}$$

where

$$\mathbf{r}' = \frac{\sqrt{(v_\perp \Omega \mp a_y)^2 + a_x^2}}{\Omega^2} \tag{3.35}$$

$$\delta = \tan^{-1}\left(\frac{a_x}{v_\perp \Omega \mp a_y}\right) \tag{3.36}$$

Thus the right side of equation 3.36 describes the gyromotion of particle in three steps: the guiding center accelerating along the magnetic field line, the gyration around said guiding center with the modified gyroradius, and the guiding center itself drifting.

Section 3.3.1 is a review of kinetic theory for simplified scenarios. In reality, gyromotion is much more complex and there are no analytic solutions. A number of integration schemes can be used, but the specific methods implemented in the MTP are discussed in the following Section 3.3.2.

3.3.2 MTP numerical methods

The Mars Test Particle (MTP) simulation is originally described in much detail by *Fang et al.* (2008). It is a 3-D Monte Carlo model that randomly assigns the particles' initial position, energy and direction. The following section will discuss the specific numerics and methods for creating and tracking individual particle trajectories.

3.3.2.1 Initialization and launch

The simulation begins by launching particles time independently (generally between 1-10 billion), using a constant number of particles per source cell. *Fang et al.* (2008) demonstrated that while the escape rate converges with only 10 or 100 particles per source cell, the velocity space resolution requires far more particles per cell (i.e., thousands) in accordance with the central limit theorem: the relative error in counting statistics is proportional to one over the square root of the number of counts. For a particle code result, this places a numerical error value on any calculated quantity. Simplistically, to achieve density within 10% accuracy, then the grid cell requires 100 particles contributing to this quantity. If the grid cell only has 10 particles, then the numerical accuracy is known to only 30%. This error estimate is true in velocity space as well: to resolve the small-scale features of velocity space, each grid cell needs many particles in regions of interest in velocity space. This is where a test particle simulation is well suited: following a large number of particles through a given field to better resolve small-scale features.

$$F_E = \frac{2}{\sqrt{\pi}}\left(\frac{1}{kT_n}\right)^{\frac{3}{2}} \exp\left[\frac{E}{kT_n}\right] E \tag{3.37}$$

$$V_0 = \sqrt{\frac{2E}{m_s}} \tag{3.38}$$

The particles are given an initial energy based on a Maxwellian energy distribution,

F_E based on the neutral temperature and isotropic angular distribution, as seen in equation 3.37. T_N is the neutral temperature, V_0 is the initial velocity, E is the initial energy, k is the Boltzmann constant and m_s is the atomic mass of the species. It should be noted 2 eV is added to the initial energy which *Fang et al.* (2010b) found may be due to partially reflective of different initial ion heating (*Ergun et al.*, 2006).

3.3.2.2 Collisions

Once the particles are launched, the particles are considered collisionless because it is in the transport-dominated regime above the exobase. As discussed earlier, nonthermal and thermal loss are based on kinetic assumptions. Figure 3.5, taken from *Shizgal and Arkos* (1996), illustrates the different modeling assumptions for collisions in an atmosphere.

This places a limit on the inner boundary to stand above the Martian exobase which *Fox* (2009) and *Valeille et al.* (2010), among many others, estimated to be 180-250 km for solar minimum and maximum cases. Loss sources due to collisions of ions with the ambient neutrals are subsequently assumed to be negligible. The inner boundary for this dissertation was consistently set at 300 km, but a 200 km inner boundary would be appropriate as well (particularly at solar minimum, see Appendix C.1.4). It should be noted that the inner boundary is an important parameter in the model in that changing it will change not only the total ion production of the simulation, but will also change how 'inner loss' is perceived. Inner loss is defined throughout the following studies as the number of ions that hit the inner boundary, which represents precipitation back into the atmosphere.

3.3.2.3 Boundaries and grid

The MTP simulation grid is spherical and uses cells with 5 degree longitude by 5 degree latitude resolution and logarithmic grid spacing with respect to radial distance

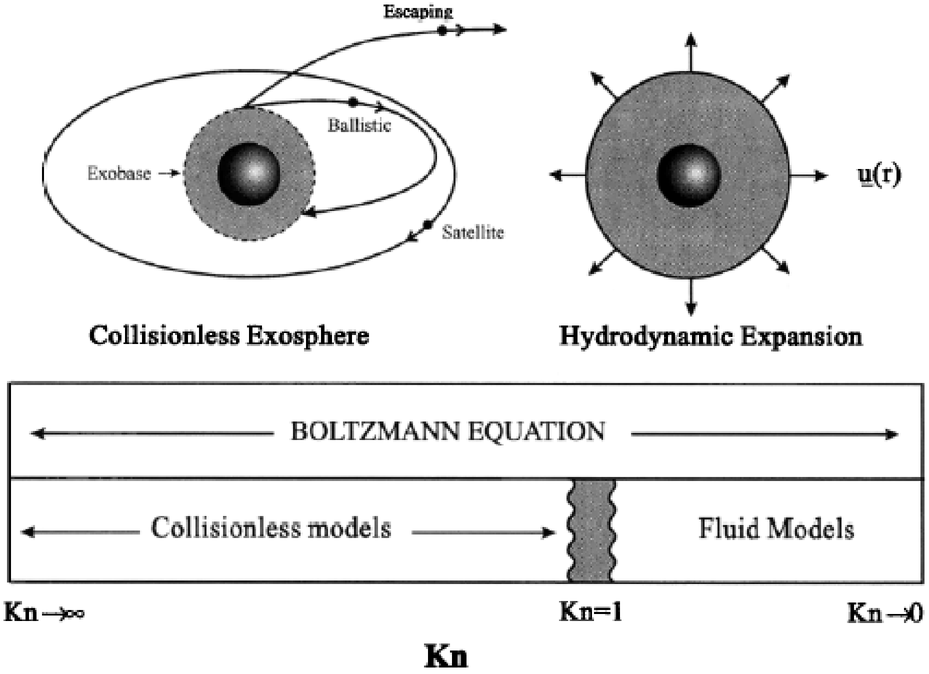

Figure 3.5: From *Shizgal and Arkos* (1996): Regimes of validity for hydrodynamics and kinetic theory versus the Knudsen number, Kn = l/H. The hydrodynamic expansion of the atmosphere with radial velocity u(r) is shown on the right. The collisionless exosphere [Chamberlain1, 1963], characterized by different particle classes is depicted on the left. Collisionless kinetic theory models are valid in the limit Kn $\rightarrow \infty$, whereas hydrodynamic models are valid when the mean free path is very small and Kn $\rightarrow$0. The Boltzmann equation of kinetic theory is valid for the whole range of Knudsen number.

(*Fang et al.*, 2008). A Cartesian coordinate system corresponding to the Mars Solar Orbital scheme (MSO) is adopted where X_{MSO} points towards the sun, Y_{MSO} is aligned with the dusk direction and Z_{MSO} completes the right hand system. As stated previously, the inner boundary is at some nominal distance at or above the exobase, and the outer boundary has been 3- 5 R_M for the studies presented in this dissertation. Future work will include a study on how the outer boundary affects the calculation of the total escape and at what radial distance out does the escape converge (i.e., from where the high-altitude production rate becomes negligible).

3.3.2.4 Trajectories and gravity

Each particle is accelerated by the background electric and magnetic field and travels until it reaches the inner boundary or the outer boundary where the positions and trajectories are recorded. A sophisticated parallelization scheme was developed by *Fang et al.* (2008) in order to support the taxing computational requirements. Each particle carries a weight determined by the ion production per unit time per cell divided by the total number of test particles (*Fang et al.*, 2008). The trajectory is determined by solving Newton's equation of motion where the pick-up ion transport is dictated by the Lorentz force and gravity. The MTP solves for the velocity and position of the particle using a staggered leap frog scheme at half time steps, where one time step is 0.05 seconds. The velocity is stepped using the Borris scheme implemented by *Birdsall and Langdon* (1985); *Fang et al.* (2008). The total acceleration on each particle is a half step acceleration by the electric field (t-1/2), a rotation in the perpendicular plane to the magnetic field, and then a half step acceleration by the electric field(t+1/2). Each step includes gravity so the individual ion motion combines a gyration around the magnetic field, the $\mathbf{E}\times\mathbf{B}$ drift, and the gravitational force towards the planet (equations 3.40-3.42).

$$\frac{d\mathbf{v}}{dt} = \frac{q}{m}\left(\mathbf{E} + \mathbf{v} \times \mathbf{B}\right) - \mathbf{G}\hat{\mathbf{r}} \tag{3.39}$$

$$\mathbf{v}^{-} = \mathbf{v}^{t-\frac{1}{2}} + \frac{\Delta t}{2}\frac{q}{m_s}\mathbf{E}^{t} - \frac{1}{2}\frac{GM_m}{r^2}\Delta t \tag{3.40}$$

$$\mathbf{v}^{+} - \mathbf{v}^{-} = \frac{\Delta t}{2}\frac{q}{m_s}\left(\mathbf{v}^{+} + \mathbf{v}^{-}\right) \times \mathbf{B} \tag{3.41}$$

$$\mathbf{v}^{+} = \mathbf{v}^{t*-\frac{1}{2}} + \frac{\Delta t}{2}\frac{q}{m_s}\mathbf{E}^{t} - \frac{1}{2}\frac{GM_m}{r^2}\Delta t \tag{3.42}$$

where **v** is the velocity vector, q is the electric charge, m_s is the mass of the species, **E** is the convective electric field, **B** is the magnetic field, G is the universal gravitational constant, and M_M is the mass of Mars. A particle travels until it reaches the inner boundary of 300 km or the outer boundary of several R_M (often varied from 3 to 5) where the positions and velocities are recorded.

3.3.2.5 Detectors

The MTP simulation tracks the full angular distribution of the particles, with no implicit averaging of the gyration or pitch angle of the particles by placing virtual detectors in any configuration around the planet. Velocity space distributions can be constructed by saving particles' trajectory and velocity.

The detectors have been placed in uniform configurations around the planet or in orbits, as seen in the top and bottom panels of Figure 3.6, respectively. The detectors record the velocity vector of the particles, which can then be visualized in directional velocity space (which we will refer to from here on as velocity space). Figure 3.7 illustrates an observation of dusk-ward moving particles. Theta is the polar angle starting from the north pole where $0° < \theta < 90°$ represents upward velocity. Phi is the azimuthal angle starting at the subsolar point and moving counterclockwise around the planet from an aerial view where $90° < \phi < 270°$ represents tailward motion and $0^\circ < \phi < 90^\circ$ and $270^\circ < \phi < 360^\circ$ correspond to a sunward motion.

3.3.3 Validity and consistency

The point of using a test particle model is to investigate the aggregate of individual particle motion and the effect that the kinetics have on velocity space and escape at different spatial locations at Mars. The MTP makes many assumptions, the first of which is that it is not self-consistent with the background electric and magnetic fields through which the particles move. While the change in particle densities and fluxes would in fact produce fields slightly different than the MHD backgrounds fields (any change in density or flux would result in a change in field, so technically all test particle models are inconsistent), it is critical to note that the difference in the fields is negligible in comparison with the total bulk velocity and density.

Figure 3.8 is a set of plots on a shell at 3 R_M of the multi-species MHD and MTP velocities as a function of local time and latitude (or co-latitude). The x and y axes are in local time (hours) and latitude (degrees), respectively, where midnight at latitude $\lambda = 0^\circ$ corresponds to the downtail point at 3 R_M along the -X_{MSO} line, and latitude $\lambda = +90^\circ$ at any local time corresponds to the north pole. The first plot is the magnitude of the bulk velocity vectors from the MHD model (u_{MHD}): the dark center downtail is the lack of bulk velocity behind the planetary obstacle in the central tail region. The second plot is the MHD velocity with the replacement of the MHD O^+ contribution by the MTP O^+ flux (u_{weight}):

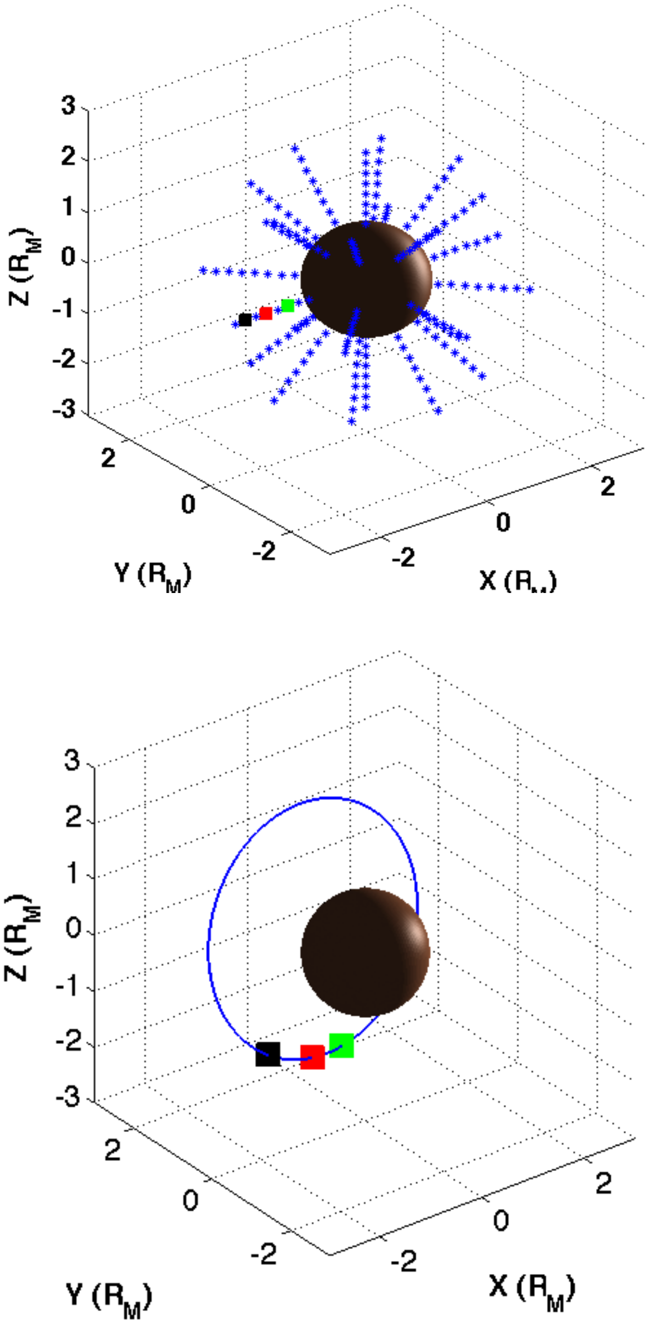

Figure 3.6: Top: virtual detectors within the MTP simulation arranged in an isotropic configuration pointing in canonical directions in MSO coordinates. Bottom: virtual detectors within the MTP simulation arranged in an orbit around the planet based on the MEX orbit

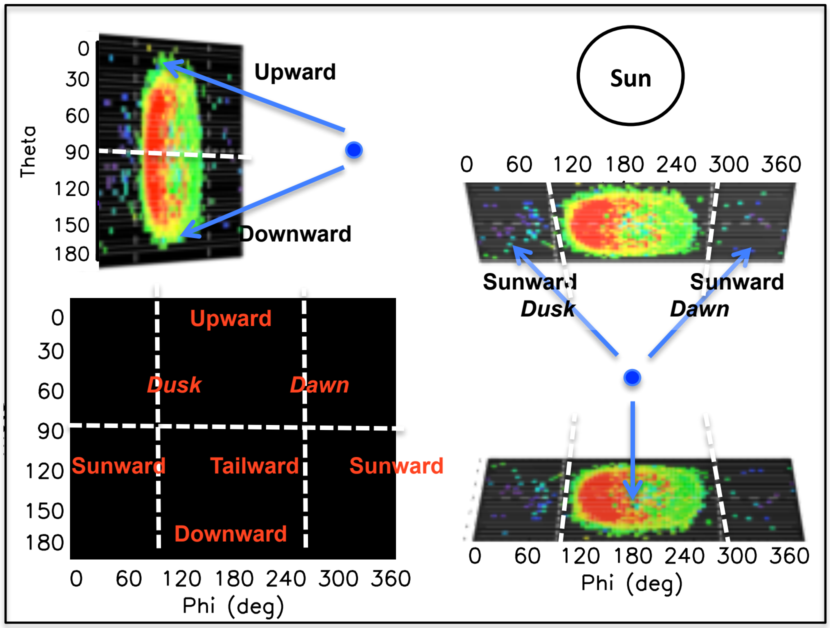

Figure 3.7: An example of the virtual detectors recording flight direction and energy: a downtail duskward observation of ions is used as an example here, where the blue dot represents an individual ion moving towards the detector in the direction of the blue arrow. The color corresponds to a nominal flux (generally the log value). Theta is the polar angle where $0^\circ < \theta < 90^\circ$ represents upward velocity and phi is the azimuthal angle where $90^\circ < \phi < 270^\circ$ represents tailward motion and $0^\circ < \phi < 90^\circ$ and $270^\circ < \phi < 360^\circ$ correspond to a sunward motion.

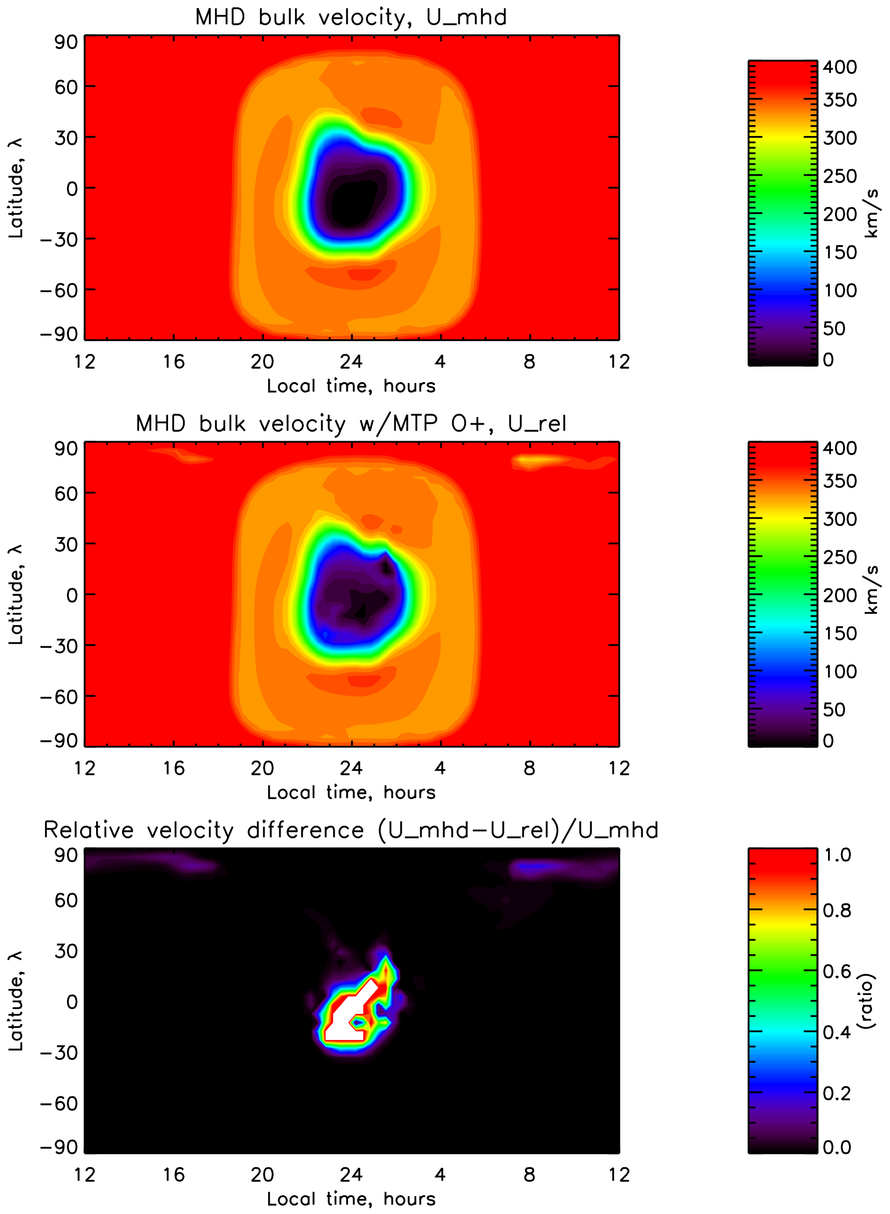

Figure 3.8: The top panel illustrates the bulk velocity, U_{MHD}, from the MHD model. The velocity is shown in the km/sec over local time and latitude projections at 3 R_M. The middle panel illustrates the MHD velocity, U_{rel}, from the MHD model *but* with the MTP O^+ velocity and density. The bottom panel illustrates the ratio of the top and middle values to illustrate a difference in the background fields and the fields the MTP produces. The ratio is shown as a decimal over the local time and latitude projections at 3 R_M.

$$u_{rel} = \frac{(n_{mhd} \cdot u_{mhd} + n_{mtp} \cdot u_{mtp})}{n_{mtp} + n_{mhd}} \tag{3.43}$$

$$\begin{aligned} \text{where } n_{mhd} &= \text{MHD density of } H^+, CO_2^+, O_2^+ \\ u_{mhd} &= \text{MHD bulk velocity (plotted at the top)} \\ n_{mtp} &= \text{MTP density of } O^+ \\ u_{mtp} &= \text{MTP velocity of } O^+ \end{aligned}$$

And finally, the bottom panel is the ratio of the relative difference between the MHD and weighted velocities (u_{ratio}):

$$u_{ratio} = \frac{u_{mhd} - u_{rel}}{u_{mhd}} \tag{3.44}$$

Note that while there is a difference in the MHD and weighted velocity (1st and 2nd plot), the relative difference (3rd plot) shows that it is minimal (below 0.1) and takes place when the velocities approach zero. The north pole shows deviations of less than or equal to 0.15. It should be noted that other self-consistent models have observed a northern polar plume (both multi-fluid MHD and hybrid, all of which our paper references). The downtail area is where the MTP velocity is greater than the MHD velocity, but both are in the same direction and would not create an extra current or distort the fields since the MHD model finds most of the O^+ is transported downtail. Furthermore, the velocities in this central downtail region are below 50 km/sec, so the denominator becomes small which increases the relative difference ratio (u_{ratio}).

Additionally, it is prudent to observe the different physical and plasma parameters for a given planetary body in order to assess what modeling assumptions are appropriate. Table 3.1 (*Ledvina et al.*, 2008) lists the following parameters for a number of

Table 3.1: Characteristics of Solar System Objects (*Ledvina et al.*, 2008)

Body	R (km)	r_c/R	λ_D/R	$\lambda_m fp$/R	c/$\omega_p i$/R	c/$\omega_p e$/R
Mercury	2400	0.041	1.4×10^{-6}	1.8×10^{4}	0.011	2.5×10^{-4}
Venus	6052	0.063	9.3×10^{-7}	2.2×10^{4}	0.0097	2.2×10^{-4}
Earth	6378	0.10	1.6×10^{-6}	6.4×10^{4}	0.014	3.1×10^{-4}
Mars	3395	0.43	6.4×10^{-6}	5.5×10^{5}	0.047	1.1×10^{-3}
Jupiter	71492	0.02	6.8×10^{-7}	1.4×10^{5}	0.0050	1.2×10^{-4}
Io	1815	0.0039	4.7×10^{-7}	2.0×10^{3}	0.010	4.9×10^{-5}
Europa	1569	0.076	5.4×10^{-6}	3.6×10^{5}	0.12	5.7×10^{-4}
Saturn	60268	0.14	1.5×10^{-6}	5.4×10^{5}	0.012	2.7×10^{-4}
Titan H+	2575	0.097	7.4×10^{-5}	1.6×10^{7}	0.28	3.8×10^{-3}
Titan O+	2575	1.6	7.4×10^{-5}	1.4×10^{9}	0.79	3.8×10^{-3}
Enceladus	250	0.062	5.2×10^{-6}	7.1×10^{3}	0.48	2.6×10^{-3}
Uranus	25559	0.74	2.8×10^{-6}	8.6×10^{5}	0.04	9.3×10^{-4}
Neptune	24764	0.95	5.4×10^{-6}	3.0×10^{6}	0.10	2.4×10^{-3}
Pluto	1150	20	7.4×10^{-5}	2.6×10^{7}	2.0	4.6×10^{-2}

solar system bodies: the radius R (km), the ratio of the ion gyroradius to the planetary radius r_c/R, the ratio of the Debye length to the planetary radius λ_D/R, the ratio of the normalized collisional mean free path to the planetary radius $\lambda_m fp$/R, the ratio of the ion skin depth to the planetary radius c/$\omega_p i$/R, the ratio of the electron skin depth to the planetary radius c/$\omega_p e$/R. At Mars, the ratio of the ion gyroradius to the planetary radius r_c/R is quite large and thus a test particle approach is fitting.

CHAPTER IV

High altitude ion production

This study quantifies the influence of ionization production mechanisms on ion escape and transport through near-Mars space. The Mars Test Particle simulation calculates the detailed ion velocity space distribution through a background magnetic and electric field model at specific locations. The main objective of this work is to extensively probe the sources of O^+ ion escape relative to the production mechanisms: photoionization, charge exchange and electron impact. Seven production methods are explored and compared, resulting in total production and loss rates differing up to two orders of magnitude. Photoionization was compared as a function of solar zenith angle and optical shadow. Charge exchange O^+ production was studied with three methods: a constant rate assuming cold ion collisions, a constant rate proportional to the reaction cross-section and upstream solar wind bulk velocity, and finally a novel approach proportional to the cross-section and both the random and bulk velocity. Finally, electron impact ionization was considered as a constant and as a function of electron temperature. Of these methods, a baseline of the most physically relevant ion mechanisms was selected. Additionally, energy distributions at specific spatial locations highlight the individual ion populations in velocity space, revealing asymmetric and non-gyrotropic features due to specific ionization methods. Analysis of the O^+ flux and loss is in agreement with observations and also indicates a strong polar plume in the northern hemisphere for a given interplanetary magnetic field orientation. We calculate the total production and escape to be 2.5×10^{25} and 6.4×10^{24} ions/sec respectively.

4.1 Approach

The Mars Test Particle (MTP) simulation is a test particle simulation that launches and tracks particles through the Mars space environment. The propagation of ions is governed by the Lorentz force (*Fang et al.*, 2008), where the background magnetic and electric fields that the ions follow are calculated by a separate MHD model from *Ma et al.* (2004). The simulation follows the test particle trajectories by solving the Newton-Lorentz equation, obtaining a global picture of the angular distributions and energy spectra of pickup oxygen ions in the Martian plasma environment. The test particle approach is valid if changes in the densities and pressure from the test particles are small compared to the MHD densities used to generate the background electric and magnetic fields. A cross check of densities throughout the MTP simulation and MHD simulation show agreement and while the MTP calculated O^+ densities are higher in some spatial locations, the MTP O^+ density is consistent with or less than the total MHD ion density.

4.1.1 MHD Model Parameters

Because the test particle simulation does not self consistently calculate the magnetic and convective electric fields, background fields from the 3-D, multispecies MHD model of *Ma et al.* (2004) are used. Omitting the Hall terms, the convective electric field is calculated by:

$$\mathbf{E} = -\mathbf{U} \times \mathbf{B}$$

where **U** is the bulk flow velocity and **B** is the magnetic field. The MHD simulation solves the dimensionless conservative form of the MHD equations for the field parameters in the plasma environment around Mars using a sophisticated, second-order accurate, numerical scheme (*Powell et al.*, 1999). The simulation domain begins from a lower boundary in the ionosphere at 100 km and reaches an outer boundary beyond the bow shock at 8 R_M upstream and 24 R_M downstream. The code uses a spherical grid structure with vertical cell sizes of 10 km near the planet that logarithmically increases with radial distance in order to capture the ionospheric profile. By solving for multiple continuity equations and combined single momentum and energy equations, separate solutions for the mass densities of H^+, O^+, O_2^+, and CO_2^+ are resolved. Combined with a broad chemistry scheme, the ionospheric profile of *Ma et al.* (2004) shows strong agreement with MGS and Viking observations. Note that the model is able to capture plasma flows around the planet including ionospheric altitudes.

The parameters used in this study are from Case 1 of *Ma et al.* (2004), which corresponds to a solar maximum condition. The IMF has a value of 3 nT using the Parker spiral structure in the XY plane at an angle of 56 degrees and the solar wind velocity and density were set at 400 km/sec and 4 cm^{-3}. A critical aspect of the induced magnetosphere at Mars is the effect of the crustal fields (see Appendix A). These regions were first observed (*Acuna et al.*, 1999) by MGS and create a shielding effect that non-magnetized planets and moons do not exhibit, thus changing the dynamics of the atmospheric evolution and erosion. The *Ma et al.* (2004) Case 1 simulation includes the crustal fields by implementing the 60 degree spherical harmonic scheme from *Arkani-Hamed* (2001) and positioned the strong crustal field region (roughly centered at 180° W) to be facing the sun. *Ma et al.* (2004) illustrated that both the ion densities at high altitudes and the bow shock location are affected by the presence of the crustal fields. *Fang et al.* (2010a) further exemplified this by varying the position of the crustal fields and finding the tailward escape rates changing by a factor of two (higher in the absence of crustal fields), consistent with *Ma and Nagy* (2007).

4.1.2 MTP Parameters

The main tool for this study is the Mars Test Particle (MTP) simulation, originally described in much detail by *Fang et al.* (2008). It is a 3-D Monte Carlo model that randomly assigns the particles' initial position, energy and direction. The simulation begins by launching 4.5 billion particles, 15,000 particles per source cell, time independently and using a Maxwellian energy distribution based on the neutral temperature and isotropic angular distribution. The MTP simulation grid is spherical and uses cells with 5 degree by 5 degree resolution and logarithmic grid spacing with respect to radial distance (*Fang et al.*, 2008). A Cartesian coordinate system corresponding to the Mars Solar Orbital scheme (MSO) is adopted where the system is centered at Mars and X_{MSO} points towards the sun, Y_{MSO} is aligned with the dusk direction and Z_{MSO} completes the right hand system. Because the IMF is a Parker spiral in the ecliptic plane away the sun, the MSO and MSE (where Z_{MSE} is aligned with the interplanetary electric field) coordinate systems are equivalent in this case. The neutral atmosphere in the simulation is spherically symmetric and constructed using the parameters from *Bougher and Engel* (2000) where H, O, and CO_2 dioxide were the main constituents. The hydrogen densities were based on rates from *Fox* (2003) and the temperature-dependent oxygen densities used the calculations of *Kim et al.* (1998). Additional CO_2 densities at solar maximum were based on model results of *Bougher and Engel* (2000) and Mariner 6 and 7 observations (*Ma et al.*, 2004).

4.2 Ion Production

4.2.1 Ionization Rates

In the equation of motion for the O^+ particle trajectories, singly ionized ions are assumed. The three dominant ionization mechanisms included in this study are photoionization of the upper neutral atmosphere, charge exchange with other ions, and electron impact from solar wind electrons:

$$O + hv \rightarrow O^+ + e^- \tag{4.1}$$

$$O + H^+ \rightarrow O^+ + H \qquad\qquad O + CO_2^+ \rightarrow O^+ + CO_2 \tag{4.2}$$

$$O + e^- \rightarrow O^+ + e^- + e^- \tag{4.3}$$

We examine seven different methods for implementing these types of O^+ ionization, listed in Table 4.1 (please refer to the number in the table for each method in the descriptions below). These methods were selected in order to compare approaches used among numerous models including (but not limited to) *Stebbings et al.* (1964); *Zhang et al.* (1993); *Bauske et al.* (1998); *Ma et al.* (2004); *Modolo et al.* (2005); *Brecht and Ledvina* (2006); *Fang et al.* (2008); *Kaneda et al.* (2009); *Terada et al.* (2009); *Brain et al.* (2010a); *Najib et al.* (2011). We consider the assumptions of each of these methods in relation to the MTP simulation and will propose the most physically sound methods for photoionization, charge exchange and electron impact as a baseline. In particular, we assess the assumptions of ionization at high altitudes with regards to optical attenuation, the role of the extended corona interacting with the solar wind protons, and temperature gradients at low versus high altitudes. In addition to evaluating ionization approaches used in other models, we also introduce novel approaches for photoionization (method 2) and charge exchange (method 5) in order to capture more realistic physical representations of ionization at high altitudes.

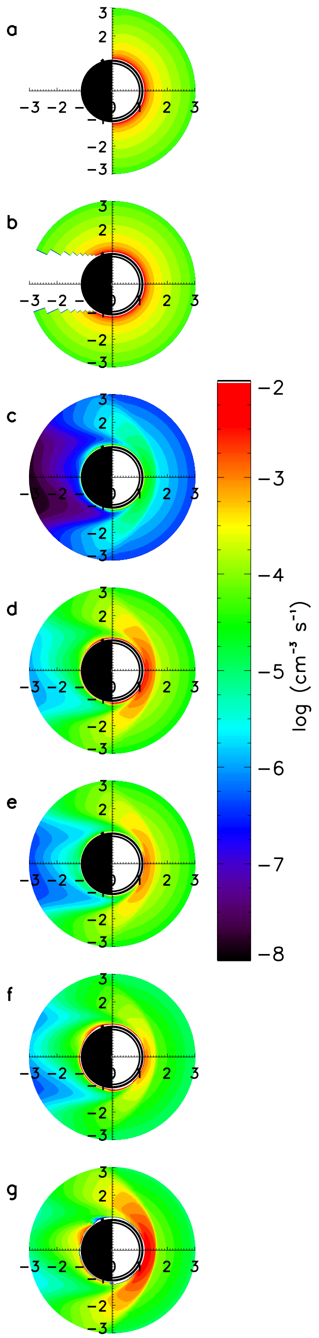

Figure 4.1: The equatorial view of the production rate shows seven sources of ionization from 300 km to 3 R$_M$ in units of $\#cm^{-3}sec^{-1}$. The production schemes are as follows: (a) photoionization using SZA, (b) photoionization using optical shadow, (c) charge exchange using *Ma et al.* (2004) constant (cold H$^+$ + O), (d) charge exchange constant from *Stebbings et al.* (1964) using upstream bulk velocity (hot H$^+$ + O), (e) charge exchange using bulk and random velocity (hot H$^+$ + O), (f) electron impact using constant temperature of 1.5 × 10^5 K, (g) electron impact using electron temperature calculated per cell. The colorbar uses a log scale from 10^{-8} to 10^{-2}. It should be noted that the empty regions in are an area of zero production.

Table 4.1: Chemical reaction rates

#	Chemical reaction	Rate Coefficient	Reference
Photoionization			
(1)	O $+h\nu \rightarrow$ O$^+ + e$	$k_1 = (2.73 \times 10^{-7})f_1$	(*Schunk and Nagy*, 2000)[1]
(2)	O $+h\nu \rightarrow$ O$^+ + e$	$k_2 = (2.73 \times 10^{-7})f_2$	current approach [2]
Charge exchange			
(3)	H$^+$+ O $\rightarrow$ H + O$^+$	$k_3 = 5.08 \times 10^{-10}$	(*Fox and Sung*, 2001) [3]
(4)	H$^+$+ O $\rightarrow$ H + O$^+$	$k_4 = v_{SW} \times 10^{-15}$	(*Stebbings et al.*, 1964) [4]
(5)	H$^+$+ O $\rightarrow$ H + O$^+$	$k_5 = v_{total} \times 10^{-15}$	current approach [5]
*	CO_2^+ + O $\rightarrow$ CO_2+ O$^+$	$k_* = 9.60 \times 10^{-11}$	(*Schunk and Nagy*, 2000)
Electron impact			
(6)	O $+e \rightarrow$ O$^+ + e + e$	$k_6 = 1.29 \times 10^{-8}$	(*Cravens et al.*, 1987) [6]
(7)	O $+e \rightarrow$ O$^+ + e + e$	k_7 =table lookup	(*Cravens et al.*, 1987) [7]

[1] Photoionization using solar zenith angle, sec^{-1}

[2] Photoionization using an optical shadow, sec^{-1}

[3] Charge exchange constant used by *Ma et al.* (2004) (cold H$^+$ + O), $cm^3 sec^{-1}$

[4] Charge exchange constant used by *Stebbings et al.* (1964) with bulk velocity (hot H$^+$ + O), $cm^3 sec^{-1}$

[5] Charge exchange using bulk and random velocity (hot H$^+$ + O), $cm^3 sec^{-1}$

[6] Electron impact using constant temperature of 1.5 × 10^5 K, $cm^3 sec^{-1}$

[7] Electron impact using calculated electron temperature per cell, $cm^3 sec^{-1}$

4.2.2 Ionization Mechanisms

For the O^+ photoionization rate of production, two methods are compared. Method (1) of Table 4.1 defines the reaction rate as a function of solar zenith angle (SZA) where the optical depth (τ) and attenuation (f_1) are determined by Equation 4.4:

$$\begin{aligned} \tau &= \frac{\sum_n \rho_n(z)\sigma_n H_n}{\cos{(SZA)}} \\ f_1 &= \begin{cases} e^{-\tau} & \text{if } SZA \leq 90^\circ \text{ (in front of the terminator)} \\ 0 & \text{if } SZA > 90^\circ \text{ (behind the terminator)} \end{cases} \end{aligned} \tag{4.4}$$

where ρ is the atmospheric density, σ is the cross section and H is the scale height for n^{th} species used (CO_2, O, H). In the equatorial plane, the attenuation would simply be a function of altitude in front of the terminator plane (closest to the sun) and would include the additional SZA attenuation behind the terminator plane, as seen in Figure 4.1a. This method is consistent with *Ma et al.* (2004), the model which supplies the background electric and magnetic fields, as well as many other models. While this assumption is valid at lower altitudes, Figure 4.1a illustrates a sharp production difference at the terminator plane.

The second method (2) for O^+ photoionization in Table 4.1 eliminates the solar zenith angle dependence and uses a constant reaction rate except in the cylindrical (geometrical) optical shadow behind the planet, as seen in Equation 4.5. This method eliminates the solar zenith angle dependence because the simulation has a lower boundary of 300 km where the atmosphere is already optically thin, as seen in Figure 4.1b. As a point of reference, the optical depth (τ) at the inner boundary 300 km above the surface in the terminator plane and subsolar point is 6.5×10^{-3} and 3.2×10^{-6} respectively. At 3 R_M, the corresponding values for τ are 4.6×10^{-4} and 2.3×10^{-7}. As discussed earlier, this is a novel method and I encourage other modelers to assess their assumptions of optical attenuation and incorporate photoionization using an optical shadow at high altitudes.

$$f_2 = \begin{cases} 0 & \text{if } y^2 + z^2 < 1 \text{ and } x < 0 \\ 1 & \text{elsewhere} \end{cases} \tag{4.5}$$

The O^+ charge exchange production rate is explored with methods 3, 4 and 5 of Table 4.1. Note the k_* charge exchange rate is the cold CO_2^+ production with neutral O but is not being modified in this study. The CO_2^+ reaction is simply added to each of the solar wind H^+ charge exchange methods (3,4,5) when describing the total charge exchange production or loss. Both the CO_2^+ and H^+ densities are provided by the *Ma et al.* (2004) simulation, which provides the background electric and magnetic fields for the MTP simulation.

Method (3) is consistent with a constant reaction rate from *Ma et al.* (2004) (originally described in *Fox and Sung* (2001)). This rate describes the interaction of cold ions and neutrals and does not account for charge exchange in the extended oxygen corona with the hot solar wind protons. As seen in Figure 4.1c, this O^+ charge exchange production rate produces very little O^+ beyond 2 R_M.

The O^+ charge exchange method (4) of Table 4.1 is a bulk velocity based constant reaction rate consistent with *Stebbings et al.* (1964). The reaction rate can be described by multiplying the $H^+ - O$ cross section by the bulk velocity as seen in Equation 4.6. Thus, the extended oxygen corona is ionized as a function of bulk velocity, seen in Figure 4.1d. The much higher rate of O^+ production is clear at the higher altitudes of 2 to 3 R_M where the hot solar wind protons ionize the corona (hot energetic charge exchange).

$$
\begin{aligned}
k_4 &= v_{SW} \times 10^{-15} \qquad (4.6)\\
&= 4.00 \times 10^{-8} (cm^3 sec^{-1})
\end{aligned}
$$

The final charge exchange process, described in method (5) in Table 4.1, accounts for the hot solar wind protons interacting with the oxygen corona as well as the dissipated energy within the induced magnetosheath. The neutrals in the corona will experience hot energetic charge exchange with the solar wind protons, but the velocity of the solar wind is no longer a constant. Because the bulk velocity transitions from super sonic to subsonic, energy is dissipated as the solar wind approaches the planetary obstacle and is transferred to the particles random velocity. The reaction rate can now be described by multiplying the H^+-O cross section by the total velocity in each cell, where the total velocity is the bulk velocity plus the random velocity, as seen in Equation 4.7. This approach has not been published in this context and is an important scheme to consider for future modeling work. The reaction rate is defined as follows:

$$
\begin{aligned}
v_{random} &= \sqrt{\frac{2kT_i}{m}}\\
v_{bulk} &= \sqrt{U_x^2 + U_y^2 + U_z^2}\\
v_{total} &= \sqrt{v_{random}^2 + v_{bulk}^2} \qquad (4.7)\\
k_5 &= v_{total} \times 10^{-15} (cm^2)
\end{aligned}
$$

where it is assumed that $T_i = T_e$ from the MHD results. Figure 4.1e illustrates the lower O^+ production as a result of the lower total velocity at the shock and in the wake of the planet. In the other two methods of charge exchange (3 and 4), the use of a constant reaction rate could over or underestimate the ionization in certain locations. It should be noted that additional charge exchange rates from *Jin et al.* (2006) are based on $T_n = 1000$ K and fall in between the k_3 and k_4 constants but were not included in this study.

Finally, the ionization due to the solar wind electron impact is explored with methods (6) and (7) from Table 4.1. Method (6) corresponds to a constant electron impact rate based on $T_e = 1.5 \times 10^5$ K, a rate which other models have assumed and a value that is reasonable for the solar wind and magnetosheath regions around Mars. The last electron impact ionization method (7) uses electron temperature dependence with rates based on the schema for O^+ impact ionization from *Cravens et al.* (1987). Figure 4.1f illustrates generally higher O^+ production than in 4.1g due to the average electron temperature being an order of magnitude higher ($\sim 10^6$ K) *except* at lower altitudes. It is critical to compare the electron temperature at low altitudes because the neutral density is much higher, which drastically changes the total O^+ production.

Figure 4.2 compares the electron impaction ionization with and without temperature dependence at 9pm local time (method 6 and 7 respectively). Panel 4.2a plots the electron temperature on the left y-axis in blue and the corresponding electron impact rate on the right y-axis in green as a function of altitude. Below 1.4 R_M, the simulated electron temperature drops three orders of magnitude, as seen by the solid navy line. The corresponding reaction rate, the green solid line, also drops with electron temperature. However, using a constant electron temperature creates a constant reaction rate which grossly overestimates the ionization at low altitudes as seen by the dashed navy and green lines respectively. Panel 4.2b plots the O^+ production rate on the left axis in black and the neutral profile of atomic oxygen in red on the right as a function of altitude. Because O^+ production is a product of the neutral density and the reaction rate (k), two very different scenarios arise below 1.4 R_M. When the constant reaction rate (dashed green line above in 4.2a) is applied to the

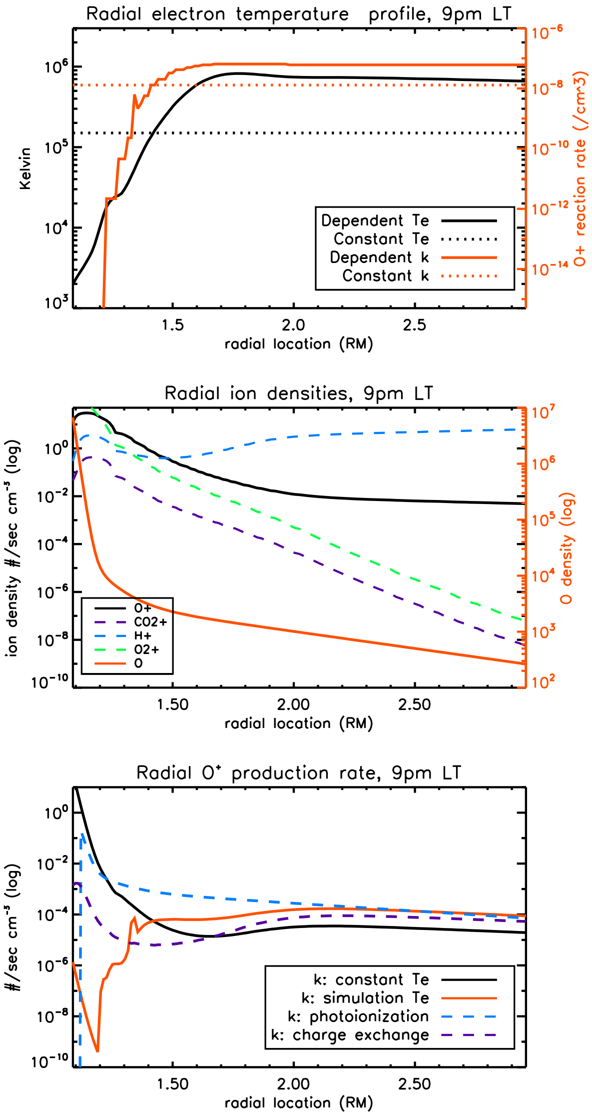

Figure 4.2: A radial slice at 9pm local time illustrates the reaction rates for electron impact ionization with a constant electron temperature of 1.5 × 10^5 K and a temperature dependent rate (methods (6) and (7) respectively). Panel a) plots the radial profile of the electron temperature (left axis) and reaction rate (right axis) where the solid navy and green lines represent the simulated electron temperature and corresponding reaction rate respectively. The dotted navy and green lines represent a constant temperature and corresponding reaction rate respectively. Panel b) illustrates the O^+ production rates for methods (6) and (7) on the left axis and the neutral O density in red on the right axis. Below 1.3 R_M, note the difference in O^+ production due to the high neutral O density. The simulated reaction rate, solid black line, is over five orders of magnitude higher than the constant reaction rate, dashed black line.

neutral density (solid red line), the O^+ production is six orders of magnitude larger, as seen in the dashed black line. In the case of the simulated electron temperature, the lower ionization rate (solid green line in 4.2a) due to the lower temperature is applied, resulting in lower production. Method 7 is much more physically accurate in that the electron density from the solar wind is not going to be constant throughout the magnetosheath and will decrease towards the planet. With fewer electrons, there will be less electron impact ionization. Subsequently, temperature dependent electron reaction rates critically affect the total production and loss, which will be discussed again in the results section.

From the seven methods outlined in Table 4.1, three have been selected as a baseline due to their consistency with the physical assumptions of the MTP simulation. The ionization methods begin with assessing photoionization as a function of solar zenith angle (method 1) and optical shadow (method 2). This study focuses on high altitudes, above 300 km, where the optical attenuation is negligibly small so using the photoionization method with just the optical shadow, method (2) is adopted for the baseline. Next, the charge exchange methods were explored using a constant reaction rate for the cold ions and neutrals consistent with *Ma et al.* (2004) (method 3− recall this is the MHD model which provides the background electric and magnetic fields), a rate using the bulk velocity to account for the hot ions interacting with the corona (*Stebbings et al.*, 1964) (method 4) and a novel approach using bulk and random velocity to account for the hot ions interacting with the corona (method 5). Because the bulk velocity is not representative of the total velocity, especially at low altitudes, the novel method (5) is adopted for the baseline. Finally, the study compares electron impact ionization with and without temperature dependence. As discussed in Figure 4.2, assuming a constant electron temperature in method (6) grossly overestimates the O^+ production rate for below 1.4 R_M. Subsequently temperature dependent electron impact ionization, method (7), is adopted for the baseline. The following Results

Section will examine the velocity space from the particles produced from these baseline ionization methods in order to probe the physics of ion motion with respect to nonthermal atmospheric loss.

4.3 Results

Figures 4.3 - 4.8 illustrate O^+ fluxes from a virtual detector as a function of energy and production mechanism (see Appendix B.1). The virtual detectors built into the MTP simulation focus on three radial directions around Mars: downtail, the northern pole and the southern pole. Specifically, the downtail location is in the equatorial plane directly behind the planet (180° away from the Sun). The north and south pole locations are in the terminator plane directly above and below the planet respectively. As discussed in the previous section, the baseline for O^+ ionization in the following plots will include photoionization using an optical shadow, charge exchange as a function of the total velocity (as seen in equation 4.7), and temperature dependent electron impact (methods 2, 5, and 7). The results are for a specific IMF orientation (away sector Parker spiral) and would largely be reversed for an opposite IMF, where features in the Northern hemisphere would occur in the Southern hemisphere. However, features due to the crustal magnetic field would not be reversed.

4.3.1 Downtail Velocity Space

Beginning with the downtail location, Figure 4.3 is a logarithmic comparison of flux versus energy in keV in units of number per cm^2 per second per steradian per keV. In Figure 4.3a, the virtual detectors are located at 1.5 and 2.5 R_M, as seen by the black and red lines respectively.

The higher flux peaks at 1.5 R_M, versus 2.5 R_M, represent the more turbulent environment inside of the induced magnetosheath. As the IMF is draped around the planet, the field lines are stretched tailward and a current sheet is created which

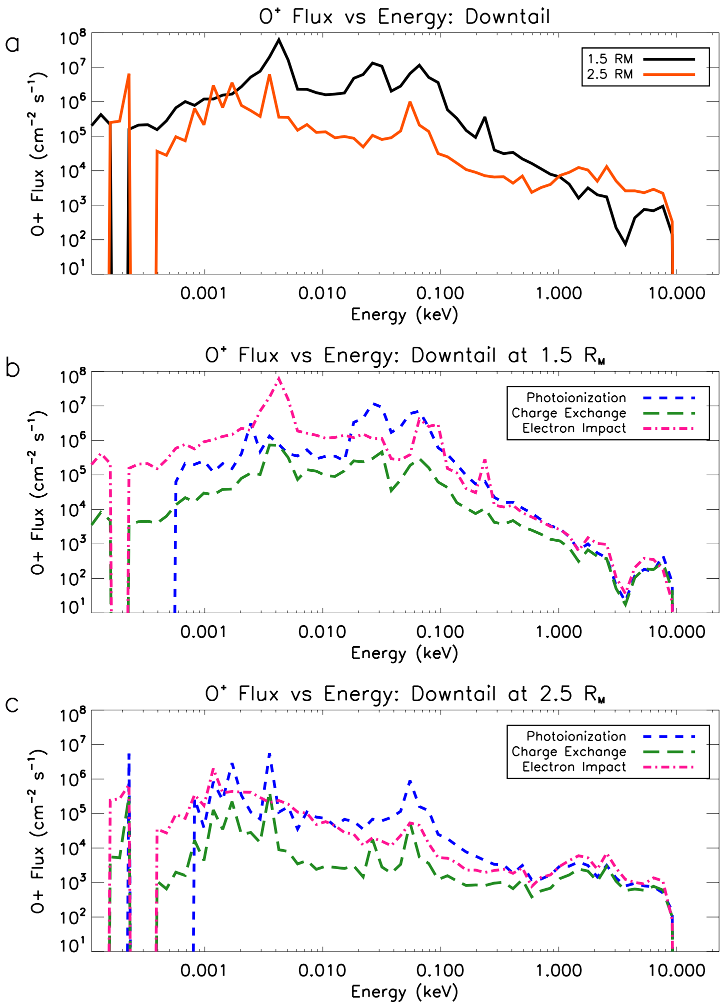

Figure 4.3: Three panels illustrate different fluxes as a function of energy at 1.5 and 2.5 R_M downtail. Panel (a) is a logarithmic comparison of flux versus energy in keV. Panel (b) and (c) the flux versus energy plot is broken down into the ionization sources at 1.5 and 2.5 R_M downtail. Note that the flux is in units of [$\text{cm}^{-2}\text{sec}^{-1}\text{ster}^{-1}\text{keV}^{-1}$], but is shortened to [$\text{cm}^{-2}\text{sec}^{-1}$].

accelerates the ions (see Figure 4.7 of *Nagy et al.* (2004)). At 1.5 R_M in Figure 4.3a, peaks can be seen around 4 eV and again between 10 to 100 eV (solid black line). Figure 4.3b decomposes the flux at 1.5 R_M into the contributions of the baseline ionization mechanisms. The first peak at 4eV is dominated by electron impact (pink line) while the peaks between 10 to 100 eV are dominated by photoionization(blue line). As seen in Figure 4.1g, there is local electron impact production downtail while Figure 4.1b shows that there is no photoionization production in the tail region due to the optical shadow. Thus any flux from photoionization has been transported and reaches medium energies (the 10 to 100 eV peaks) while the locally produced electron impact flux has a lower energy peak (4 eV). In Figure 4.3c at 2.5 R_M, there is less flux below 1 keV than at 1.5 R_M because there are less locally produced ions. At > 1 keV, the flux is higher than at 1.5 R_M because ions are transported and accelerated downtail.

The simulated downtail fluxes in Figure 4.3 show agreement with ASPERA-3 measurements. The simulated average and peak fluxes integrated over all energies at 1.5 R_M are 2.3×10^6 and 4.4×10^7 [$\mathrm{cm}^{-2}\mathrm{sec}^{-1}$], respectively. *Barabash et al.* (2007) reported average fluxes of O^+ in the downtail plasma sheet region of $\sim 2\times10^6$ [$\mathrm{cm}^{-2}\mathrm{sec}^{-1}$] and peak fluxes of 5×10^7.

While the fluxes at different energies in Figure 4.3 illustrate which ionization mechanisms are dominant, a valuable aspect of test particle simulations is the ability to resolve individual ion trajectories. Figure 4.4 illustrates a modified velocity space distribution (VSD) as a function of O^+ flight angle in the downtail region. The x−axis uses the azimuthal angle for the ions' flight direction. It is measured from the +X axis in the X-Y plane where $90^\circ < \phi < 270^\circ$ represents tailward motion and $0^\circ < \phi < 90^\circ$ or $270^\circ < \phi < 360^\circ$ corresponds to a sunward motion. The y−axis uses the polar angle measured from the +Z axis where $0^\circ < \theta < 90^\circ$ represents upward motion and $90^\circ < \theta < 180^\circ$ represents downward motion (see red dashed overlay). The colorbar

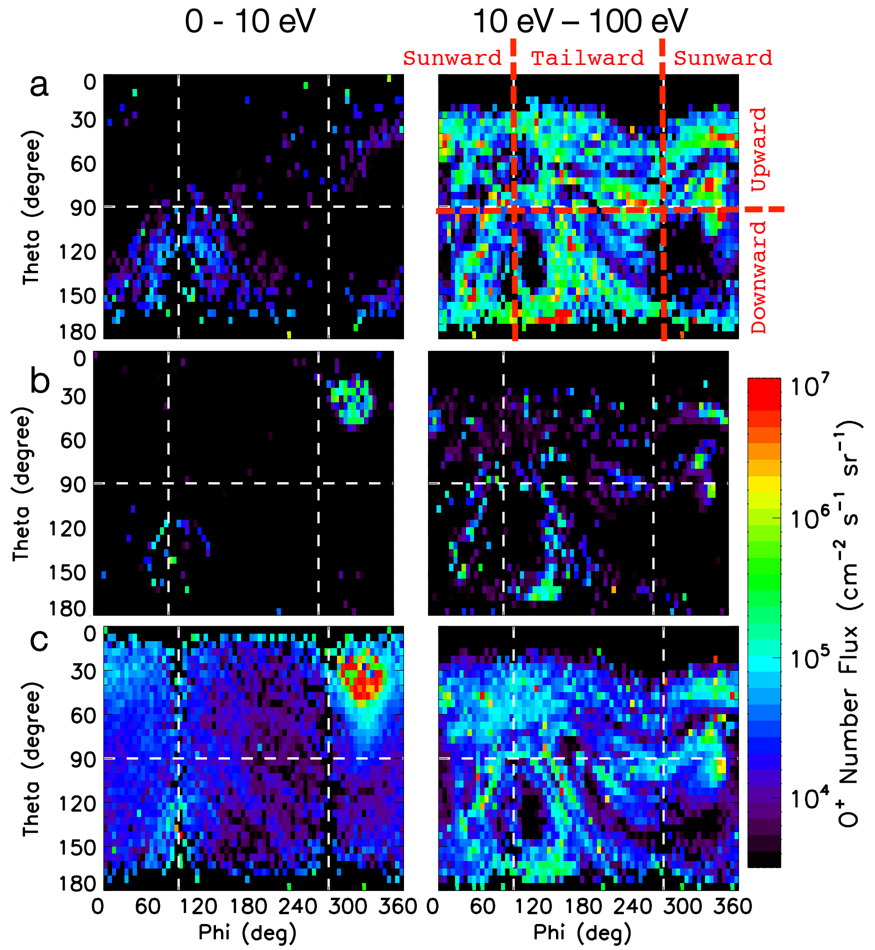

Figure 4.4: Velocity space distributions from a virtual detector downtail illustrating the contribution of different ionization source mechanisms and different energy levels at 1.5 R_M. Theta is the polar angle where $0° < \theta < 90°$ represents upward velocity and phi is the azimuthal angle where $90° < \phi < 270°$ represents tailward motion and $0° < \phi < 90°$ and $270° < \phi < 360°$ correspond to a sunward motion. Panel a) is photoionization, panel b) is charge exchange and panel c) is electron impact. The energy ranges are from 0−10 eV and 10eV−100 eV.

represents the flux in units of number per cm^2 per second per steradian as seen in the flux versus energy plots.

Figure 4.4 shows the three ionization sources at 1.5 R_M downtail: panel a) is photoionization, panel b) is charge exchange and panel c) is electron impact. The velocity space is integrated over two energy ranges (low $= 0 - 10$ eV, medium$=10 - 100$ eV). As seen in the Figure 4.3b energy versus flux plots, electron impact dominates the low energy range with a peak at 4 eV while photoionization is dominant in the medium energy range from 20 to 100 eV. Not only does Figure 4.4 reflect this but the VSDs show two distinct ion populations: the low energy range contains an electron impact population moving upward and sunward (Figure 4.4c, $0-10$ eV) while the medium energy range has asymmetric filamental structures due to photoionization moving downward (Figure 4.4a, $10-100$ eV). At 1.5 R_M, the particles are within the magnetotail and are shielded from the strong convective electric field from the solar wind and consequently have varying angles due to the bounce around the strong magnetic field, as seen in both low and medium ion populations.

4.3.2 South Pole Velocity Space

In examining flux versus energy at the southern pole locations in Figure 4.5, the same pattern for higher fluxes within the magnetosheath exists. The line plots are much smoother in the south pole due to the lack of turbulence along the draped IMF field lines (relative to the tail region) and the peak flux is about an order of magnitude less than those fluxes downtail. The ions produced in the south pole either precipitate back into the atmosphere due to the convective electric field pointing into the planet or accelerate past the planet and are transported downtail. Figure 4.5a at 1.5 R_M (solid black line) illustrates a strong peak around $80-100$ eV which dominates the energy versus flux signature, discussed in terms of velocity space further down. A particular point of interest in Figure 4.5a is the high energy 'cutoff'; at 1.5 R_M (black

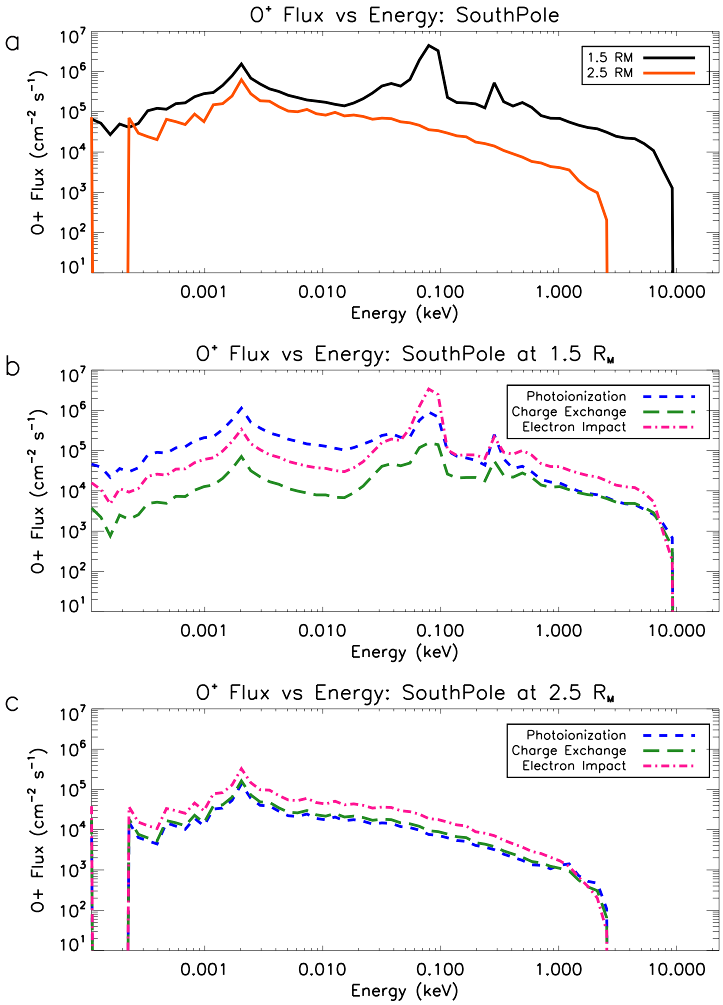

Figure 4.5: Three panels illustrate different fluxes as a function of energy at 1.5 and 2.5 R$_M$ in the south pole. Panel (a) is a logarithmic comparison of flux versus energy in keV. Panel (b) and (c) the flux versus energy plot is broken down into the ionization sources at 1.5 and 2.5 R$_M$ in the south pole. Note that the flux is in units of [cm^{-2}sec^{-1}ster^{-1}keV^{-1}], but is shortened to [cm^{-2}sec^{-1}].

line), the flux does not exceed 9.5 keV, but only reaches 2.6 keV at 2.5 R_M (red line). This lower energy cutoff at higher altitudes is due to a shorter ion trajectory from its place of origin to the detector. Recall from Figure 4.1g that electron impaction ionization has relatively high O^+ production in the terminator plane between 1.5 and 2.5 R_M. Because the convective electric field points into the planet (for this IMF configuration), ions produced between 2.5 R_M and the bow shock would not have time to accelerate before hitting the detector at 2.5 R_M. However, they are accelerated for longer distances to the virtual detector at 1.5 R_M and thus have higher energies (the path length is larger when integrating $E \cdot dl$).

Figure 4.5b and 4.5c break the ionization sources down at 1.5 and 2.5 R_M. Figure 4.5b illustrates that below 100 eV at 1.5 R_M photoionization is dominant because the O^+ ions are locally produced and the detector is no longer in the optical shadow. Above 100 eV, O^+ ions produced from electron impact in the terminator plane (again, see Figure 4.1g) are transported and swept towards the planet due to the convective electric field. In Figure 4.5c the detector is placed further from the planet at 2.5 R_M, but in a much higher area of electron impact production. Here the locally produced electron impact ions dominate the O^+ flux.

Expanding on the Figure 4.5 dominant peaks, Figure 4.6 shows VSDs when the detectors are positioned in the southern pole at 1.5 R_M. Panel a) is photoionization, panel b) is charge exchange and panel c) is electron impact. The velocity space is integrated over two energy ranges (low $= 0-30$ eV, high$=30$ eV$-$ 10 keV). Figure 4.6a illustrates that photoionization dominates the $0-30$ eV energies with more upward and tailward flux, corresponding to the 2 eV peak from Figure 4.5b. At the higher energies of 30 eV$-$ 10 keV, all three sources look similar except in Figure 4.6c where the electron impact VSD has higher flux (red filamental structure at $\phi \simeq 190^\circ$ and $\theta \simeq 90^\circ$) which corresponds to the 100 eV peak from Figure 4.5b. Thus Figure 4.6 illustrates distinct ion populations: low energy photoionization ions which were

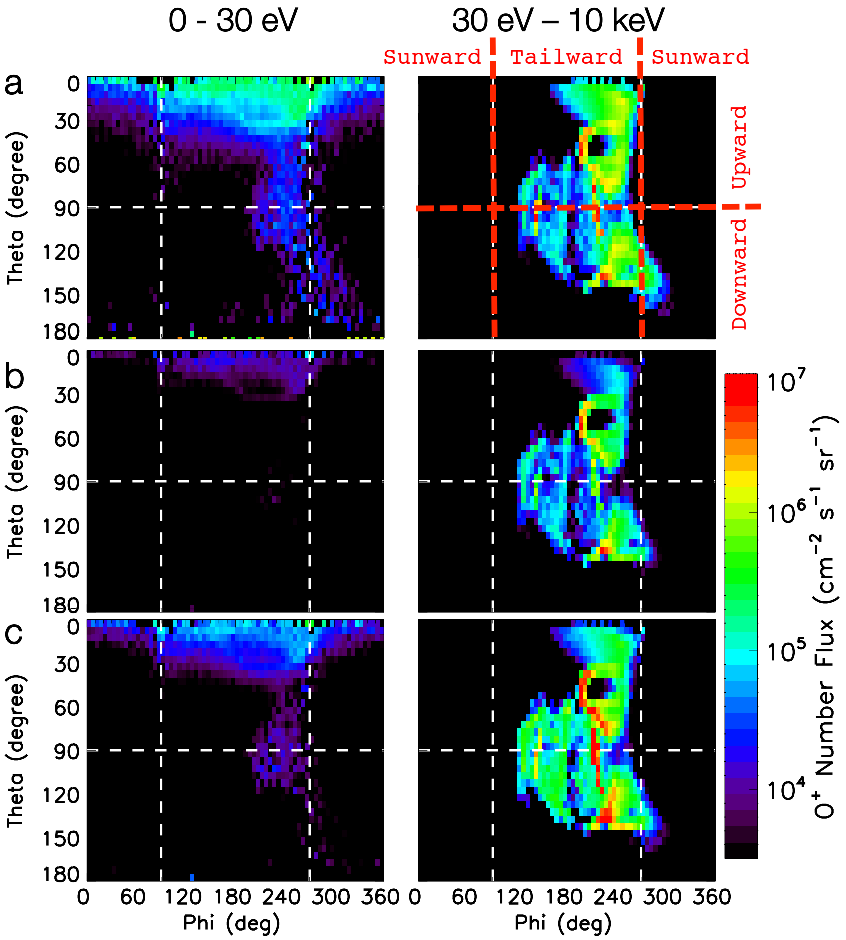

Figure 4.6: Velocity space distributions from a virtual detector over the south pole illustrating distinct populations of O^+ at 1.5 R_M. Panel a) is photoionization, panel b) is charge exchange and panel c) is electron impact. The energy ranges are from 0−30 eV and 30eV−10keV.

locally produced and electron impact ions which were created at the terminator and accelerated to higher energies under the planet.

4.3.3 North Pole−Polar features

Figure 4.7 illustrates flux versus energy in the northern pole location and highlights the northern polar plume, a phenomenon that has been predicted by numerous models but is yet to be observed (*Brecht and Ledvina*, 2006; *Fang et al.*, 2008, 2010a; *Najib et al.*, 2011). The magnitude of the flux is the lowest here compared to the downtail and south pole regions but is also the smoothest and depicts a clear track for ion acceleration. In Figure 4.7a, the sharp peak in the 3 to 20 keV range illustrates an O^+ polar plume at both 1.5 and 2.5 R_M. Figure 4.7b shows that the polar plume at 1.5 R_M is marginally dominated by photoionization. At 2.5 R_M, Figure 4.7c illustrates the flux is marginally dominated by electron impact, but clearly all of the ions regardless of their ionization source have been accelerated straight upward to high energies.

In Figure 4.8 , the velocity space signature is shown for the north pole at 1.5 R_M where panel a) is photoionization, panel b) is charge exchange and panel c) is electron impact. The velocity space is integrated over two energy ranges (low = 0−100 eV, high=100 eV− 25 keV). The low energy range includes the 2 eV peak seen in the line plots of Figure 4.7 and represents the locally produced ions. The higher energy range captures the sharp peak from 1 to 25 keV, displaying a plume structure moving directly upward, slightly dominated by photoionization. For this IMF configuration, ions are created on the dayside by photoionization, charge exchange and electron impact and are accelerated relatively evenly directly above the planet.

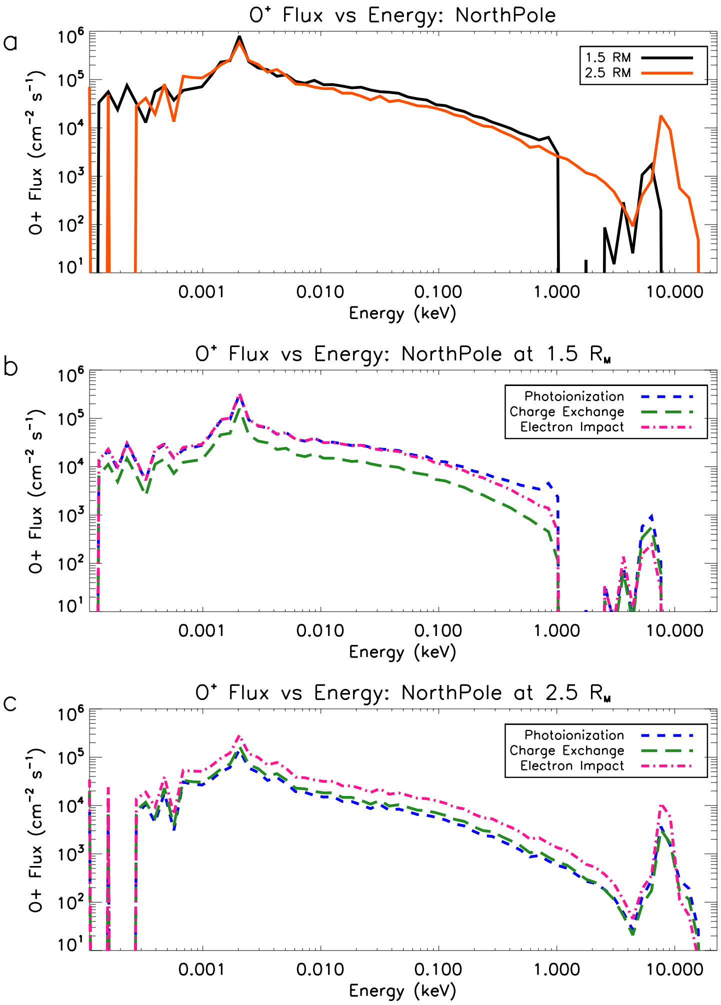

Figure 4.7: Three panels illustrate different fluxes as a function of energy at 1.5 and 2.5 R$_M$ at the north pole. Panel (a) is a logarithmic comparison of flux versus energy in keV. Panel (b) and (c) the flux versus energy plot is broken down into the ionization sources at 1.5 and 2.5 R$_M$ at the north pole. Note that the flux is in units of [cm^{-2}sec^{-1}ster^{-1}keV^{-1}], but is shortened to [cm^{-2}sec^{-1}].

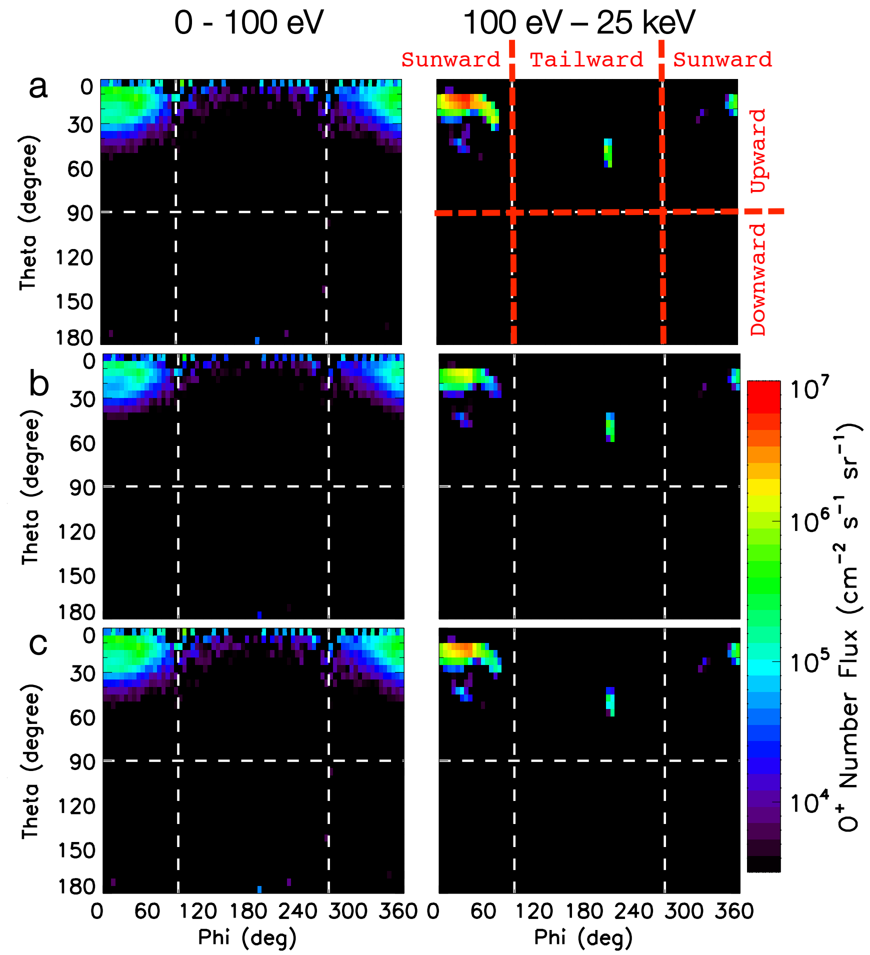

Figure 4.8: Velocity space distributions from a virtual detector over the north pole illustrating a concentrated plume of O^+ at 1.5 R_M. Panel a) is photoionization, panel b) is charge exchange and panel c) is electron impact. The energy ranges are from 0−100 eV and 100eV−25keV.

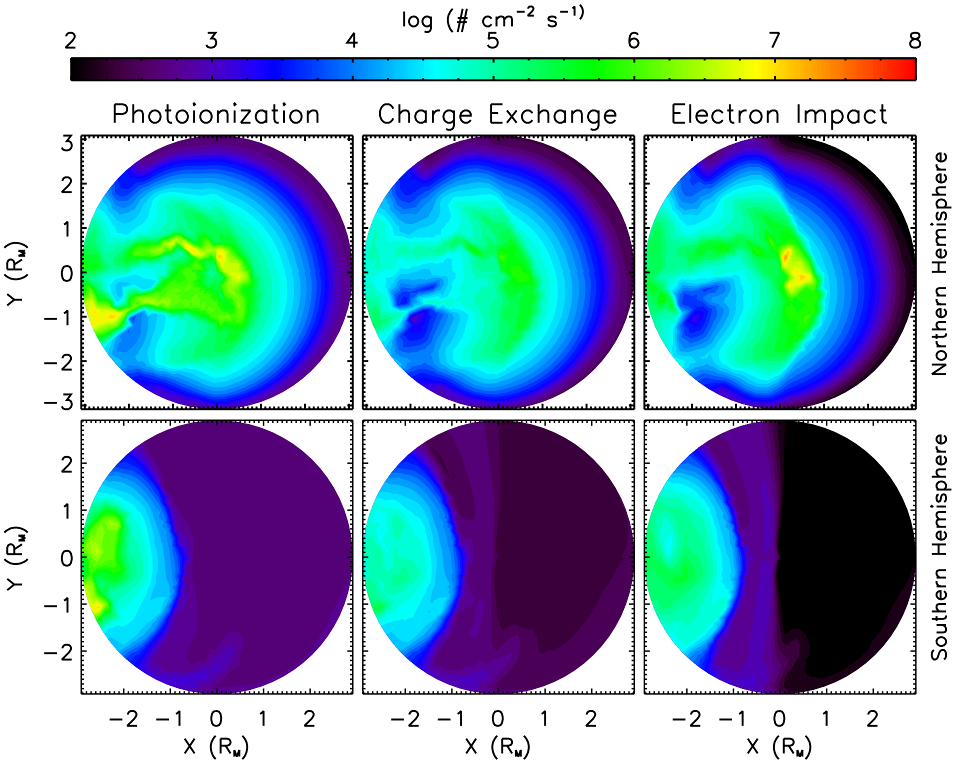

Figure 4.9: The escape of O$^+$ from the three source regions at the outer boundary shell of 3 R$_M$ in the northern and southern hemisphere with the Sun to the right. The view for both hemispheres is from over the north pole and the colorbar is in units of $cm^{-2}sec^{-1}$.

4.4 Influence on Escape

Figure 4.9 illustrates the spatial distribution of O^+ escape through a 3 R_M shell. As previously discussed, the simulation domain uses a coordinate system that corresponds to MSO directions and the escape shown is for an IMF with an away sector Parker spiral configuration. The northern and southern hemisphere loss shells are shown for each baseline ionization source (top and bottom, respectively). Note that the view is from over the north pole for all of the panels with the Sun to the right. The loss is calculated by recording a particle as it passes through the 3 R_M spherical boundary and weighting it. As described earlier, the weight is determined by the total ion production per cell divided by the total number of test particles per unit time (*Fang et al.*, 2008). The colorbar is a log scale of the flux in $\# \, cm^{-2} sec^{-1}$.

The loss shells of O^+ from Figure 4.9 clearly show a northern polar plume, which is in agreement with particle traces performed by *Fang et al.* (2008, 2010a). In the northern hemispheric loss shell, all three sources have the peak of the northern polar plume slightly sunward and display a fan of tailward loss. The northern polar plume is a result of the background convective electric field with a strong $+Z_{MSO}$ component. The southern hemisphere displays very little escape because the O^+ ions have been accelerated upward and tailward by the strong convective electric field. In the tail regions ($-X_{MSO}$ plane) of Figure 4.9, loss from photoionization and charge exchange display two separate fans on each side of the $Y_{MSO} = 0$ plane. However, electron impact ions lost through the 3 R_M shell appear to form one major stream in just the $+Y_{MSO}$ quadrant. These different tails illustrate the asymmetry that exists in the dawn-dusk direction. As a result of the Parker spiral, the E×B drift from the IMF accelerates the particles in the negative $-Y_{MSO}$ direction so there would be an expected increase in loss on the dawn side.

The O^+ escape signatures seen in Figure 4.9 are in agreement with other modeling efforts and observations. The dawn-dusk asymmetry has been observed with particle traces by *Fang et al.* (2008), hybrid models (*Kallio and Jarvinen*, 2012) and observations (*Dubinin et al.*, 2006). The preferential loss in the northern hemisphere has been reported by *Brecht and Ledvina* (2010) who noted in particular that the crustal fields in the southern hemisphere are correlated with slower ion pick up as a result of the parallel electric fields. Additionally, *Lundin et al.* (2011b) found that the averaged flux flow directions measured from ASPERA-3 suggested that the crustal fields reduced tailward transport of O^+ and as a consequence reduced escape over the southern hemisphere. Finally, the northern polar plume has been predicted in both MHD and hybrid models (*Brecht and Ledvina*, 2006; *Fang et al.*, 2008, 2010a; *Najib et al.*, 2011).

The plots of flux distributions and escape (Figures 4.3−4.9) thus far have presented one O^+ production baseline in order to highlight their influence on ion trajectories. But the method of ion production plays a critical role in total escape. Table 4.2 presents the production and loss rate contributions for each method in #/sec. The production rate is the product of the atmospheric density, the reaction rate and the volume. The loss rate is the escaping flux integrated over the 3 R_M shell, seen in Figure 4.9. We define the efficiency as the ratio of the loss rate to the production rate, illustrating how effectively O^+ ions are produced and retained in the Mars space environment for each ionization mechanism. High efficiency would correspond to a higher loss fraction per unit of production, meaning ions are more likely to escape through the 3 R_M shell. Similarly, a low efficiency ratio would suggest that the ions are less likely to escape.

Table 4.2 begins with comparing photoionization using solar zenith angle dependence (method 1) and photoionization using an optical shadow (method 2). Method (1) has lower production and loss but has a very similar efficiency ratio as method (2). Ultimately, using photoionization with an optical shadow (2) produces more O^+ ions, but a smaller percentage are lost outside of the 3 R_M shell.

Following, Table 4.2 compares charge exchange with three methods: a constant reaction rate consistent with *Ma et al.* (2004) based on cold ions and neutrals (method 3), a bulk velocity based constant reaction rate which is consistent with *Stebbings et al.* (1964) (method 4), and finally a novel method dependent on the bulk and random velocity (method 5). Methods (3), (4) and (5) have more than an order of magnitude difference in both production and loss rates based on their physical assumptions. Method (3) has smaller production and escape rates due to only accounting for cold ion neutral collisions and ignoring the hot solar wind ion collisions with the corona. Method (4) has the largest rates because it overestimates the production by assuming the solar wind flow has the same velocity throughout the simulation. Note that methods (3) and (4) have similar efficiency ratios which are quite low; this suggests that the O^+ ions produced from these methods are much less likely to escape from the 3 R_M shell. Method (5) however has production and loss rates in between (3) and (4) but has the highest efficiency ratio of 45.8 %. Using this scheme, almost half the O^+ ions produced are likely to escape.

Finally, Table 4.2 compares the electron impact with a constant temperature reaction rate (method 6) and a temperature dependent reaction rate (method 7). Method (6) yields the highest rate of production and loss rates by two orders of magnitude. As discussed in Figure 4.2, at altitudes below 1.3 R_M ($<$ 1000 km), the same reaction rate is applied to the dense neutral atmosphere which creates an enormous amount of O^+ ions. Due to this large production rate, the efficiency ratio is the smallest, 13.3%, because most of these ions are produced at low altitudes and do not get accelerated away from the planet and are unlikely to escape from the 3 R_M shell. The final method, the temperature dependent electron impact ionization (7), has a much smaller reaction rate at the low altitudes, as seen in Figure 4.2. Consequently, it has a much smaller O^+ production rate. But method (7) also has a higher efficiency ratio which suggests that ions produced from an electron temperature dependent reaction rate are more likely to escape from the 3 R_M shell.

Table 4.2: O^+ production and loss as a function of reaction rates (#/*sec*)

#	Method	Production Rates	Escape Rate	% Efficiency
(1)	Photoionization [1]	1.2×10^{25}	2.8×10^{24}	23.3 %
(2)	Photoionization [2]	1.8×10^{25}	3.8×10^{24}	21.1 %
(3)	Charge exchange [3]	6.4×10^{23}	1.0×10^{23}	15.6 %
(4)	Charge exchange [4]	3.5×10^{25}	6.2×10^{24}	17.7 %
(5)	Charge exchange [5]	1.2×10^{24}	5.5×10^{23}	45.8 %
(6)	Electron Impact [6]	1.2×10^{27}	1.6×10^{26}	13.3 %
(7)	Electron Impact [7]	5.6×10^{24}	2.0×10^{24}	35.7 %

[1] Photoionization using solar zenith angle
[2] Photoionization using an optical shadow
[3] Charge exchange constant used by *Ma et al.* (2004) (cold $H^+ + O$)
[4] Charge exchange constant used by *Stebbings et al.* (1964) with upstream bulk velocity (hot $H^+ + O$)
[5] Charge exchange using bulk and random velocity (hot $H^+ + O$)
[6] Electron impact using constant temperature of 1.5×10^5 K
[7] Electron impact using calculated electron temperature per cell

4.5 Discussion

Numerous simulations have been used to investigate the subject of nonthermal atmospheric escape in order to assess the broader context of atmospheric evolution on Mars. Over an order of magnitude difference in the net O^+ loss estimates exist among observations and simulations (*Stebbings et al.*, 1964; *Zhang et al.*, 1993; *Bauske et al.*, 1998; *Ma et al.*, 2004; *Modolo et al.*, 2005; *Brecht and Ledvina*, 2006; *Barabash et al.*, 2007; *Fang et al.*, 2008; *Kaneda et al.*, 2009; *Terada et al.*, 2009; *Brain et al.*, 2010a; *Lundin et al.*, 2011b; *Najib et al.*, 2011), providing a strong incentive to probe the assumptions and physics that influence loss. This study examines the influencing factors on the escape rate of O^+ by comparing ion production mechanisms and their effect on production, escape and velocity space in the Mars space environment.

Before discussing the results, a review of the model's assumptions, limitations and inputs is valuable. First, it is important to note that when O$^+$ densities become larger than the background MHD solar wind density, the plasma pressure balance and species weighted velocity would shift and consequently the static field assumptions of the MTP, or any test particle simulation, would no longer be appropriate due to the lack of self-consistency. As long as the MTP plasma environment can remain static and collisionless, this model serves as an excellent tool for probing pickup ion motion and escape. The MTP finds O$^+$ number densities consistent with the MHD ion density profiles except at the North Pole where the plume redirects a significant population of O$^+$. However, even here, the O$^+$ densities are two orders of magnitude smaller than the solar wind protons and therefore the test particle assumption is still valid. The MTP O$^+$ velocities are also consistent with the MHD bulk velocity except for acceleration of the O$^+$ ions to higher energies focused in center of the tail. Because the MTP accelerated downtail ion velocity is in the same direction as the MHD bulk velocity, both of which are below 50 km/sec, there would not be a significant change in the MHD fields. In addition to the static field assumptions, the inputs for all of the production and loss calculations were done for a single realization of solar EUV and solar wind and IMF conditions. The specific configuration is with solar maximum conditions, slow solar wind, and away sector Parker spiral IMF. For example, if the IMF was reversed (in the towards sector), the northern polar plume would in fact occur over the southern pole.

Using identical inputs, the Section 4.2 began with assessing each source method and comparing their physical assumptions against one another, as seen in Table 4.1 and illustrated in Figure 4.1. First, photoionization was compared as a function of solar zenith angle (method 1) and optical shadow (method 2), producing similar production and loss rates. Photoionization using an optical shadow was adopted as a baseline due to the atmosphere being optically thin in the simulation space (300 km and above). The three methods examined for O$^+$ production via charge exchange varied much more so, spanning over two orders of magnitude. The rate used by *Ma et al.* (2004) was derived from *Fox and Sung* (2001) which assumed cold ion and neutral collisions (method 3). The *Stebbings et al.* (1964) production scheme accounted for the hot ion collisions (hot energetic charge exchange) by using production rates as a function of the oxygen cross section and solar wind bulk velocity (method 4). Finally, this study expanded on the hot energetic charge exchange approach and used the same cross section but with the total velocity consisting of the random and bulk velocity (method 5), as seen in equation 4.7. Method 5 was included in the baseline because it takes into account the hot ion collisions while incorporating the changes in solar wind velocity near a planetary obstacle. I stress the novelty of this approach because of its physically based relevance as well as its influence on O^+ escape. Finally, electron impact ionization was considered as a constant with T_e =1.5 × 10^5 K (method 6) and as function of electron temperature dependence (method 7). As seen in Figure 4.2, using a reaction rate with temperature dependence does not overestimate the production at lower altitudes ($<$ 1000km), and is therefore adopted into the baseline.

In Section 4.3, virtual detectors were placed at 1.5 and 2.5 R_M in three locations in the simulation space: downtail, the south pole and the north pole. The flux versus energy plots and VSDs, Figures 4.3 − 4.8 illustrate independent ion populations at different energies for each baseline production mechanism. Downtail, the virtual detector is in the optical shadow. The lower energy ion populations are indicative of locally produced electron impact ions while the higher energies are dominated by transported photoionization ions. Peak and average fluxes over all energies show agreement with both *Barabash et al.* (2007) and *Lundin et al.* (2011b). In the south pole, the virtual detector is outside of the optical shadow and locally produced photoionization ions dominate the low energy ions. At higher energies in the south pole, electron impact ions dominate because they are transported from high production in the terminator towards the planet by the background convective electric field. The northern pole exhibits a clear polar plume at all altitudes with energies of 4 keV and higher regardless of the source.

Section 4.4 illustrates the escape shells at 3 R_M for each baseline production mechanism in Figure 4.9. Due to the northern polar plume, there is a preferential northern hemispheric loss for this specific IMF configuration (away sector Parker spiral). Each of the ionization mechanisms also exhibit different spatial channels as a result of where the ions were produced and accelerated. Accordingly, future satellite missions might further investigate the spatial distribution of ion loss for orbital considerations. Finally in Table 4.2, the production and loss rates ($\#\ \mathrm{sec}^{-1}$) are presented along with their ratio. Considering only the baseline production mechanisms (methods 2, 5, and 7), the O^+ escape ($\#\ \mathrm{sec}^{-1}$) is estimated to be 3.8×10^{24} for photoionization, 5.5×10^{23} for charge exchange and 2.0×10^{24} for electron impact, resulting in a net loss of 6.4×10^{24}.

4.6 Summary

The MTP model provides a unique and valuable approach for studying the various physical processes controlling O^+ ion creation, transport and loss through near-Mars space. The resolution provided by over four billion test particles permits the examination of pick-up ion flux distributions in spatial locations and energy ranges that have not been examined before. Because the MTP simulation does not average the gyroradii or pitch angles, it can account for ions on an unmagnetized planet with gyroradii on planetary scales.

This study has demonstrated the importance of the ion production mechanisms and their effect on velocity space and total O^+ ion escape by probing the physical assumptions of O^+ ion creation. In particular we found three unique results: (1) The use of a photoionization source with an optical shadow rather than a solar zenith angle dependence is an appropriate alternative for high altitude ion production. (2) There are several commonly used constants for the charge exchange production rate, which either neglect the hot solar wind ions interacting with the corona or do not account for the variable velocity as the solar wind approaches the planetary obstacle. A new charge exchange cross section has been introduced that is dependent on the total proton speed (bulk plus random velocity). (3) Because the electron impact ionization rate is highly dependent on temperature, a constant electron impact reaction rate drastically overestimates the low altitude O^+ ion production (<1000 km). Thus, the use of a temperature dependent rate is critical to physically model ionization at all altitudes.

I encourage MHD, hybrid and test particle simulations to explore these ionization mechanisms and stress this study is meant to be an aid for models and simulations in the broader context of examining atmospheric escape. Future work will include following the trajectories of additional species, including a source of ionospheric outflow, and providing data comparisons with ions in the Mars plasma environment.

CHAPTER V

Influence of the solar cycle and corona on ion transport

We present results from the Mars Test Particle simulation (MTP) as part of a community-wide model comparison in order to quantify the role of different neutral atmospheric conditions in planetary ion transport and escape. This study examines the effects of individual ion motion by simulating particle trajectories for three cases: solar minimum without the neutral corona, solar minimum with the inclusion of the neutral corona, and solar maximum with the inclusion of the neutral corona. The MTP simulates 1.5 billion test particles through background electric and magnetic fields computed by a global magnetohydrodynamic (MHD) model. By implementing virtual detectors in the simulation, the MTP has generated velocity space distributions of pick-up ions and quantifies the ion acceleration at different spatial locations. The study found that the inclusion of a hot neutral corona greatly affects the total O^+ production and subsequent loss, roughly doubling the total escape for solar minimum conditions and directly contributing to high energy sources above 10 keV. The solar cycle influences the amount of O^+ flux observed by the virtual detectors, increasing the O^+ flux and total escape by an order of magnitude from solar minimum to maximum. Additionally, solar maximum case induces greater mass loading of the magnetic fields, which decreases the gyroradius of the ions and redirects a significant ion population downtail to subsequently escape.

5.1 Methods

5.1.1 Models

For this study, the 3-D, multispecies MHD model of *Ma et al.* (2004) provided the background fields that incorporated the established global model comparison inputs for three different cases. The model uses a spherical grid structure that extends from the lower boundary in the ionosphere at 100 km to an outer boundary beyond the bow shock at 8 R_M upstream and 24 R_M downstream. The vertical (radial) cell sizes are 10 km near the planet in order to capture the ionospheric profile and then exponentially increases with radial distance. The MHD model solves for separate solutions of the H^+, O^+, O_2^+, and CO_2^+ mass densities.

The test particle modeling is done by the MTP simulation discussed in detail in *Curry et al.* (2012) and *Fang et al.* (2008), but modified with different neutral atmospheric profiles. The simulation tracks each particle until it hits the inner boundary at 300 km or the outer boundary at 3 R_M. Due to the assumption that the model is collisionless, the inner boundary is placed well above the nominal exobase, 180-250 km, (*Fox*, 2009) for solar minimum and maximum cases. The simulation uses a spherical grid with cell resolution of 5 degree by 5 degree and grid spacing with respect to logarithmic radial distance (*Fang et al.*, 2008). For this study, the MTP used over 1.5 billion test particles for this simulation, whose angular distribution, energy and velocity are recorded at virtual detectors and constructed into velocity space distributions. The virtual detectors can be placed anywhere in the simulation in order to record the flux, position and flight direction of the particles (see Appendix B.1).

5.1.2 Neutral Atmosphere and Ion Production

The global model comparison of *Brain et al.* (3-7 Dec. 2012) uses three common input scenarios: Case A constitutes solar minimum conditions without a corona, Case B has solar minimum conditions with a corona, and Case C follows with solar maximum conditions including a corona. All cases exclude the Martian crustal fields. The solar wind is composed of protons with a density of 2.7 cm^{-3} with a temperature of 13 eV and electron temperature of 9 eV. The bulk velocity flows radially from the sun at a speed of 485 km/sec and the IMF is consistent with a Parker spiral field of 3 nT oriented at 57 degrees configured at (-1.634, 2.516, 0.0) nT in the Mars Solar Orbital (MSO) coordinate system where $-X$ is in the direction of the bulk flow, $+Y$ is in the direction anti-parallel to Mars' orbital (instantaneous) velocity and $+Z$ completes the right-hand system. The neutral atmosphere and corona are constructed from the simulated outputs of *Bougher et al.* (2004); *Chaufray et al.* (2007); *Bougher et al.* (2008) and *Valeille et al.* (2010), seen in Figure 5.1. While a neutral hot hydrogen corona was included for Cases B and C, it is not plotted in Figure 5.1 because the MTP simulation discussed here does not trace H^+.

In this study, the MTP follows O^+ throughout the simulation, beginning with time-independent production in each cell. The total production is the product of the neutral oxygen density, the cell volume and the reaction rate for each of three production mechanisms: photoionization, charge exchange, and electron impact. For photoionization, instead of incorporating solar zenith angle dependence, an optical shadow directly behind the planet is used due the atmosphere being optically thin above 300 km. Constant photoionization rates of 8.89×10^{-8} and 2.73×10^{-7} s^{-1} for solar minimum and maximum respectively, are employed everywhere but the optical shadow.

The charge exchange production is proportional to the local bulk flow speed and the ionization cross section (cm^2), σ, in the H^+-O reaction as seen in equation 5.1.

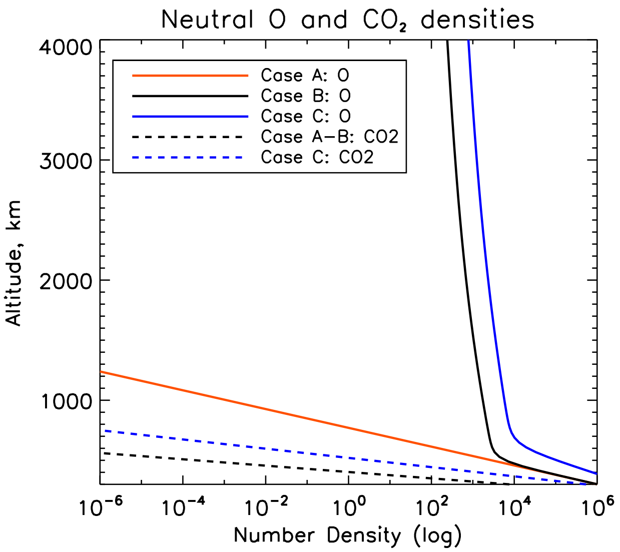

Figure 5.1: An altitude profile of the neutral atmosphere from 200 km to 3 R$_M$ for Cases A, B and C.

$$k_{ch} = v_{bulk} \times \sigma \tag{5.1}$$

Electron impact ionization is based on a logarithmic polynomial of the electron temperature consistent with *Cravens et al.* (1987).

Figure 5.2 illustrates the three ion production mechanisms for each case. The figure is an equatorial view of the production rate for each mechanism and for each case from the inner boundary of 300 km to the outer boundary of 3 R$_M$. The lack of a corona is clear in Case A, while the hot corona is ionized in Cases B and C. Due to the enhanced neutral atmosphere, the increase in production from solar minimum to maximum is relatively linear and symmetric. Because the solar wind conditions remain the same for all three cases, the neutral atmosphere and ion production are critical to examine when analyzing the trajectories and escape of O$^+$, which Chapter IV discusses in detail. In particular, high rates of ion production, often occuring inside the bow shock, can cause mass loading (*Bauske et al.*, 1998; *Shinagawa and Bougher*,

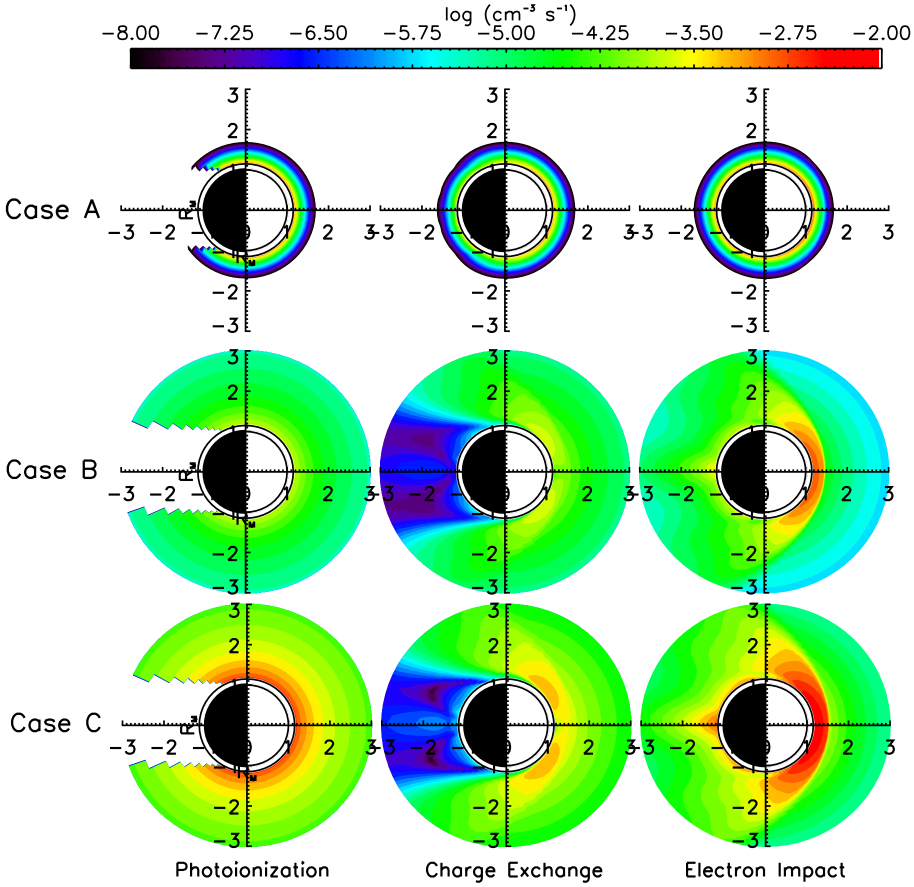

Figure 5.2: The equatorial view of the production rate for the three ion production mechanisms for each ISSI case from 300 km to 3 R_M.

1999; *Lundin et al.*, 2011a). This process occurs between a plasma in motion and a plasma at rest; at Mars, the planetary ions at rest are picked up by the solar wind and accelerated by the convective electric field. In order to preserve the conservation of momentum, the solar wind is decelerated by the increase in mass (*Dubinin et al.*, 2011). This in turn can increase the magnetic field, which subsequently affects the gyromotion of an individual particle (see equations 1 - 5 and Figure 5 and 9 from the *Ma et al.* (2004) study).

5.2 Results

Here we present flux, energy and velocity space distributions from the virtual detectors in order to highlight the influence of the corona and solar cycle on individual particle motion. As described earlier, Case A uses solar minimum conditions without a corona, Case B uses solar minimum conditions with a corona, and Case C follows with solar maximum conditions including a corona. For this study, the detectors were placed downtail (directly along the X_{MSO} line), and the north and south pole (directly along the Z_{MSO} line above and below the planet). They were radially spaced 0.2 R_M apart from 1.1 - 3.0 R_M (only a selection will be shown).

5.2.1 Influence of the Corona

A comparison of the results from Cases A and B allows us to examine the influence of the hot oxygen corona on high altitude ion motion while a comparison of Cases B and C isolates the influence of the solar cycle. Beginning with an examination of the corona, Figure 5.3 shows the number flux at 1.1, 1.5, 2. and 2.5 R_M radially downtail from the planet where the number flux is plotted as a function of logarithmic energy.

Cases A and B have very different energy-flux signatures, but follow a similar trend as the detector is moved further downtail. In each case, the peak flux increases because more ions have had a longer distance to accelerate to the virtual detector. At 1.1 R_M, the flux in Case A peaks at 1.7×10^5 between 1-3 eV and the energy limit extends up to 50 eV. The flux in Case B peaks at 2.4×10^5 between 1-3 eV but the energy limit of the flux extends just above 1 keV. As the detector observes the O^+ ions further from the planet at 2.5 R_M, the peak fluxes for both Cases A and B shift towards 7 and 12 eV respectively and both now peak at 7.3×10^5. However, the difference in the energy-flux signatures is most apparent at 2.5 R_M because the upper energy limit in Case A remains at 50 eV while in Case B it extends above 10 keV. This extended upper energy limit indicates that ions produced in the corona

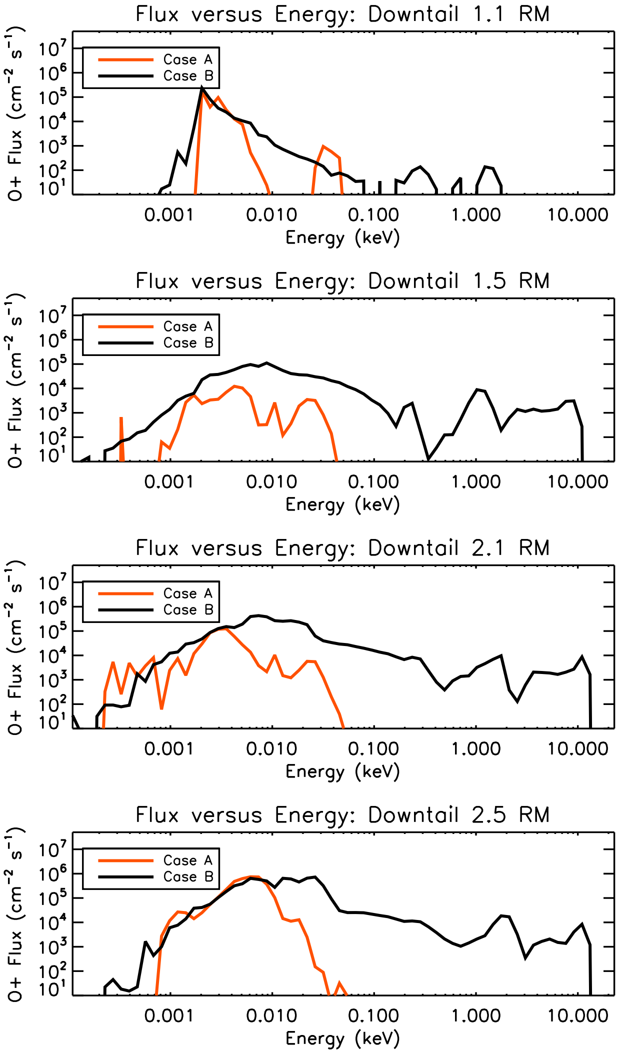

Figure 5.3: O^+ flux from virtual detectors as a function of energy for Cases A and B (log scale) in red and black respectively. Both cases are at solar minimum while only Case B includes a hot corona. The virtual detectors are positioned at 1.1 - 2.5 R_M downtail. Note that the flux is in units of [cm^{-2}sec^{-1}ster^{-1}keV^{-1}], but is shortened to [cm^{-2}sec^{-1}].

have been accelerated and transported downtail. Additionally, the total observed flux for Cases A and B at 2.5 R_M are 3.6 × 10^6 and 7.0 × $10^6 cm^{-2} sec^{-1}$ respectively, indicating that the corona roughly doubles the observed flux.

Figure 5.4 highlights the effect of the corona in velocity space at solar minimum for Case A (left) and Case B (right), where the detector is again located radially downtail from 1.1 - 2.5 R_M and integrated over an energy range of 1 eV - 25 keV. Cases A and B display similar trends in particle motion: the O^+ flux is predominantly moving upward and tailward ($+Z_{MSO}$ direction), and increasing as the detector is placed further downtail. Locally produced ions, low-energy ions with fluxes below 10^5 $cm^{-2} sec^{-1} sr^{-1} keV^{-1}$, are observed closer to the planet (1.1 - 1.5 R_M) with a broader range of flight direction angles. The range of flight direction angles, which we will refer to as flight direction coverage, is a phrase we have adopted to describe how much flux the detector observes (i.e. how much or little white space there is for a given virtual detection). At distances further downtail (2.1 - 2.5 R_M), the locally produced ions at 1.1 - 1.5 R_M have been accelerated downtail by the background convective electric field and have a more focused flight direction centered around ϕ = 180° and θ=90°.

While the overall particle motion at the downtail detectors is similar, Cases A and B exhibit very different VSD signatures and flight direction coverage. At 1.1 R_M, the fluxes for both cases are below 10^5 $cm^{-2} sec^{-1} sr^{-1} keV^{-1}$ and moving in the upward, $+Z_{MSO}$ direction (a flight direction of θ = 0-90°). At 1.5 R_M, Case A shows much more limited flight direction coverage in comparison with Case B, indicating that the hot corona contributes to the majority of the flux in this region. For Case A, the flux above 10^7 $cm^{-2} sec^{-1} sr^{-1} keV^{-1}$ does not begin to accumulate and converge until 2.5 R_M downtail because without the corona, there are fewer ions to accelerate. Case B has higher ion production due to the ionized corona and consequently begins to accumulate and directionally converge above 10^7 $cm^{-2} sec^{-1} sr^{-1} keV^{-1}$ beginning

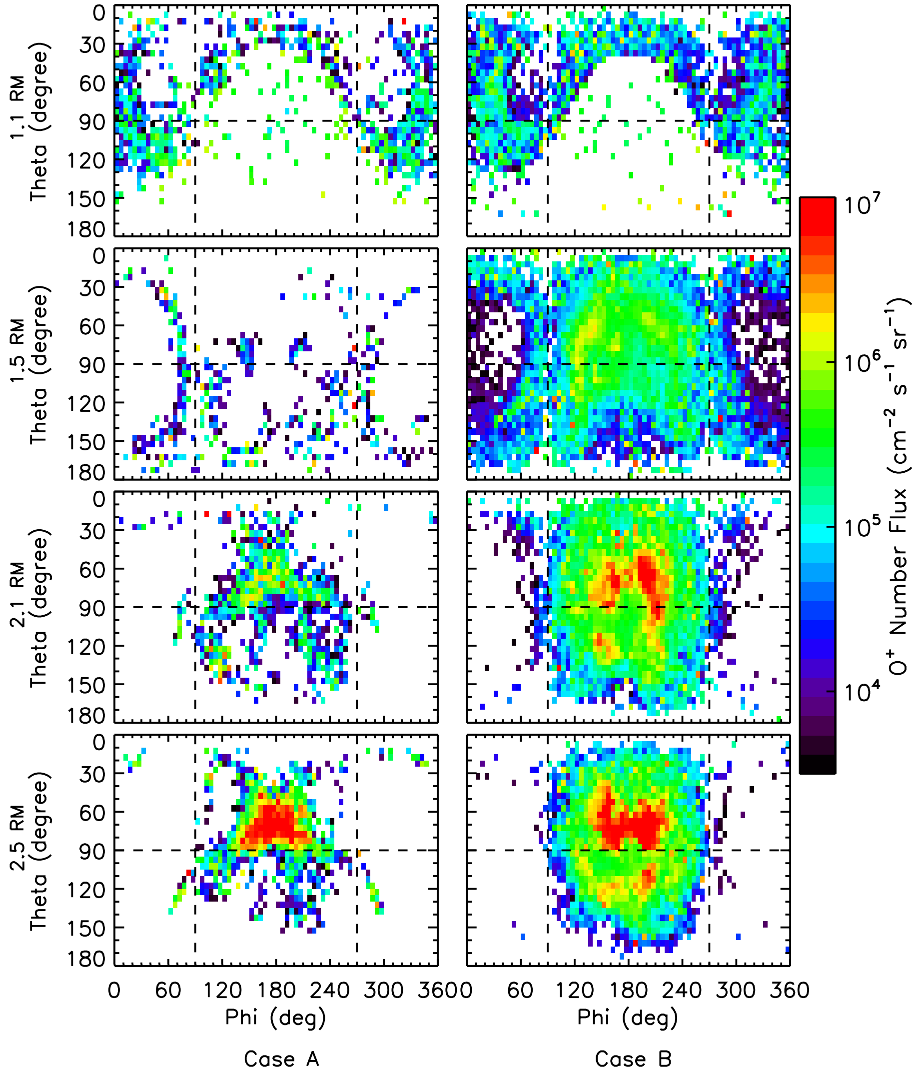

Figure 5.4: Velocity space distributions from several virtual detectors illustrating number flux shown with a logarithmic colorbar to the right in units of $cm^{-2}sec^{-1}sr^{-1}$ for Cases A - B (left and right columns). Theta is the polar angle where $0° < \theta < 90°$ represents an upward moving flight direction and $90° < \theta < 180°$ represents a downward moving flight direction, denoted by the dashed black lines. Phi is the azimuthal angle where $90° < \phi < 270°$ represents a tailward flight direction and $0° < \phi < 90°$ and $270° < \phi < 360°$ correspond to a sunward flight direction. The virtual detector is positioned at 1.1 - 2.5 R$_M$ downtail.

at 2.1 R_M. Additionally, Case B shows high flux ion distributions with much more asymmetry. These distinct high flux populations are centered around $\phi \sim$180° and $\theta \sim$90°.

5.2.2 Influence of the Solar Cycle

By comparing Cases B and C, this section explores the solar cycle's influence on O^+ velocity distributions, particularly near the magnetic pile up boundary (MPB) and bow shock (BS) regions. This dayside region is interesting because some models and observations suggest that the EUV flux has a negligible effect on the MPB and BS location (*Vignes et al.*, 2000; *Bertucci et al.*, 2005; *Modolo et al.*, 2006; *Trotignon et al.*, 2006; *Lundin et al.*, 2007). Consequently, the effect of the solar cycle on ion trajectories can be directly compared in identical locations on the dayside.

Figure 5.5 compares the fluxes for Cases B and C at virtual detectors from 1.3 to 1.9 R_M radially extending from the south pole. Cases B (solar minimum) and C (solar maximum) have similar signatures in flux versus energy, but Case B clearly shows fluxes roughly an order of magnitude below those of Case C. At 1.3 R_M, the total observed flux for Cases B and C are 1.4×10^6 and $3.6 \times 10^7 cm^{-2} sec^{-1}$, respectively. It should be noted that the total flux and the upper energy limit are higher at 1.3 R_M than at 1.9 R_M as opposed to the downtail case (Figure 5.3) where the flux increased with distance from the planet. As Chapter IV discussed, the convective electric field has a $+Z_{MSO}$ component, so particles in the southern hemisphere near the MPB travel upward towards the planet. Thus, particles produced at 2.5 R_M are accelerated for longer distances to the virtual detector at 1.3 R_M and thus have higher energies (the path length dl is larger when integrating $E \cdot dl$). The final difference in the energy-flux signatures is the slight peak at 1.5 R_M in Case C that does not exist for Case B (highlighted by the dashed black lines between 100-300 eV), a feature which will be expanded on later.

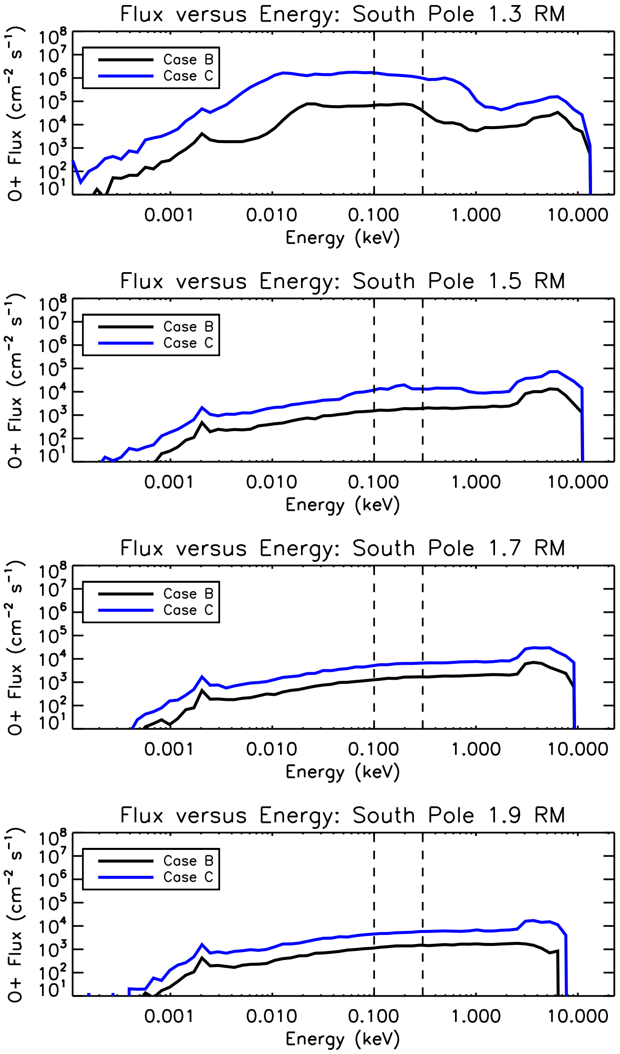

Figure 5.5: O$^+$ flux from virtual detectors as a function of energy for Cases A and B (log scale) in red and black respectively. Both cases include a corona where Case B is at solar minimum and Case C is at solar maximum. The virtual detectors are positioned at 1.3 - 1.9 R$_M$ radially over the south pole. Note that the flux is in units of [cm^{-2}sec^{-1}ster^{-1}keV^{-1}], but is shortened to [cm^{-2}sec^{-1}].

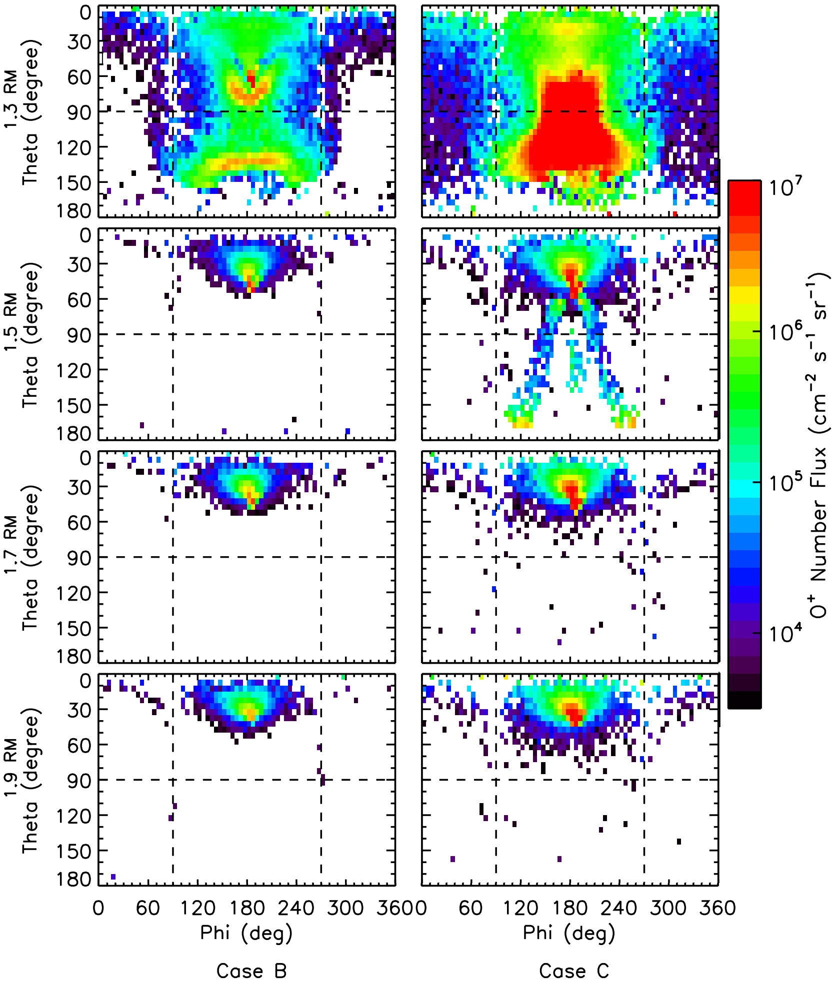

Figure 5.6: Velocity space distributions from several virtual detectors illustrating number flux shown with a logarithmic colorbar to the right in units of $cm^{-2}sec^{-1}sr^{-1}$ for Cases B - C (left and right columns). Theta is the polar angle where $0° < \theta < 90°$ represents an upward moving flight direction and $90° < \theta < 180°$ represents a downward moving flight direction, denoted by the dashed black lines. Phi is the azimuthal angle where $90° < \phi < 270°$ represents a tailward flight direction and $0° < \phi < 90°$ and $270° < \phi < 360°$ correspond to a sunward flight direction. The virtual detector is positioned at 1.3 - 1.9 R_M in the southern pole.

Figure 5.6 highlights the effect of the solar cycle by comparing the velocity space for Cases B and C at 1.3 - 1.9 R_M over the southern pole. The virtual detectors are placed directly beneath the planet and reflect velocity space for a specific IMF configuration (a Parker spiral in the away sector) with the flux integrated from 1 eV to 25 keV. From 1.9 - 1.5 R_M, both Cases B and C exhibit a high flux source moving upward and tailward centered at $\theta = \sim 30^\circ$ and $\phi = \sim 180^\circ$ ($+Z_{MSO}$, $-X_{MSO}$ components). As seen in Figure 5.5, the flux increases for both cases as the detector is moved closer to the planet and at 1.3 R_M, the high flux source broadens with more flight direction coverage as more particles are accelerated up to the detector. While Cases B and C have an extraordinarily similar flux versus energy signature in Figure 5.5, now that subtle increase in the flux near ∼200 eV at 1.5 R_M can be seen in velocity space. Case C clearly depicts two additional high flux beams at 1.5 R_M moving downward towards dawn and dusk at $\phi = \sim 90^\circ$, 270° and $\theta = \sim 170^\circ$ ($\pm Y_{MSO}$, $-Z_{MSO}$ directional components), which correspond to the small peak in flux versus energy at 200 eV. As Figures 5.7-5.9 will show, this velocity space signature is a result of the solar cycle's influence on the field line configuration that dictates the O^+ gyroradius.

First, we demonstrate this by analyzing the origin of these downward moving particles hitting the detector at 1.5 R_M. Figure 5.7 illustrates the origin (marked in rectangular cells) of any particle that was observed at 1.5 R_M with a downward flight direction of $\theta \geq 90^\circ$. In MSO Cartesian coordinates, the four panels correspond to the XY, YZ, XZ and 3D view of the cell origins. Red cells represent Case B while blue cells represent Case C. Figure 5.7 illustrates that Case C produced ions from across the dayside sector (inside the MPB) and down throughout the south pole while Case B only produced ions in the local vicinity surrounding the detector at 1.5 R_M.

Next, we need to understand why particles originating from the subsolar region were able to reach the detector in Case C while not in Case B. Figure 5.8 illustrates

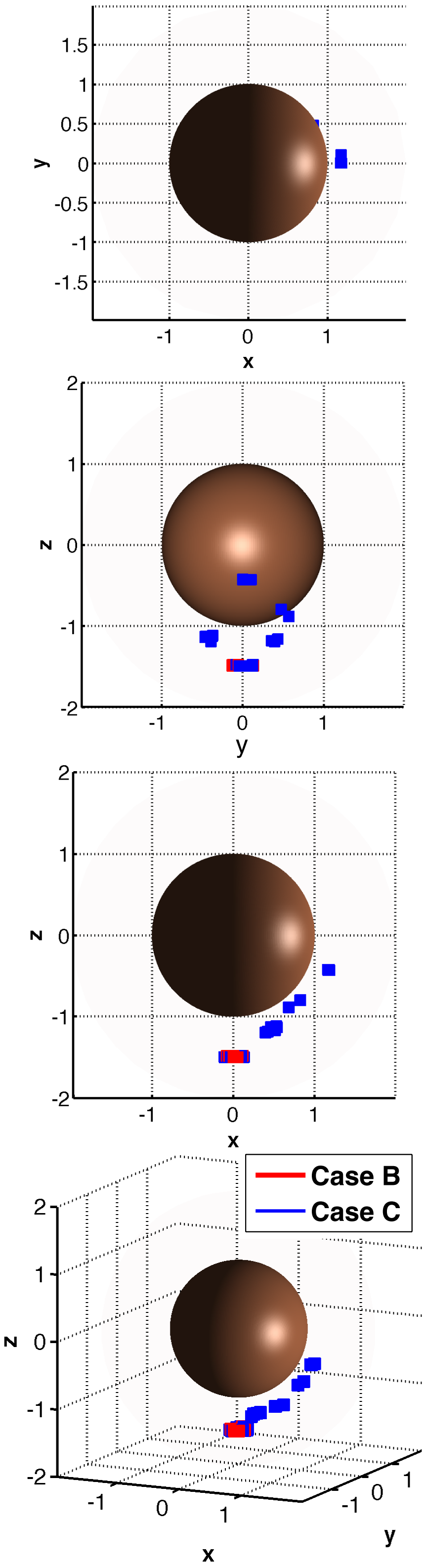

Figure 5.7: The four panels correspond to the XY, YZ, XZ and 3D view of the cell origins in MSO coordinates. Red cells represent Case B while blue cells represent Case C. The sun is in the +X sector.

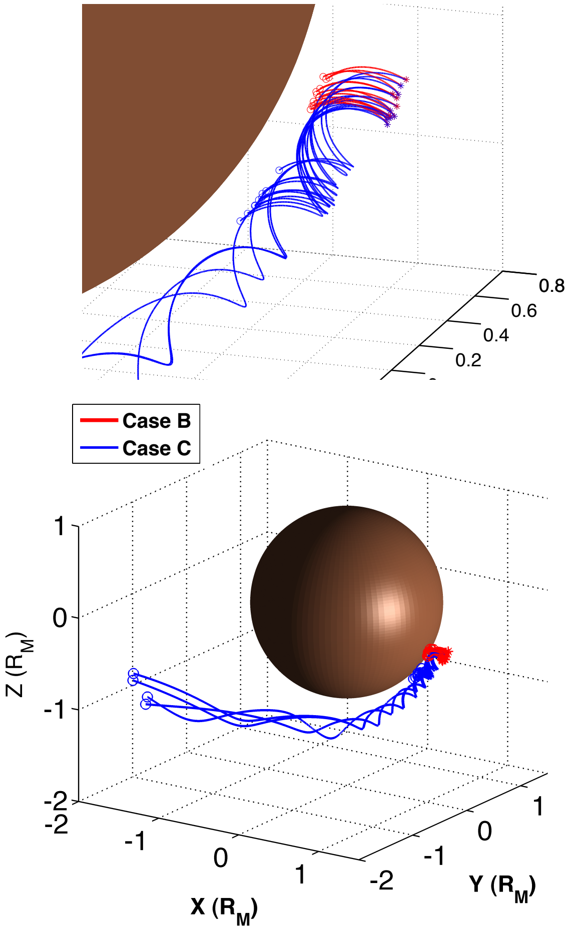

Figure 5.8: Particle traces launched from 1.26 R$_M$ and 20° below the subsolar point. Case B is in red while Case C is in blue; asterisks denote the beginning of the particle trajectory and circles denote the end of the trajectory. The top panel is a zoomed view of the particle trace and the bottom panel illustrates the trajectories in the full simulation space.

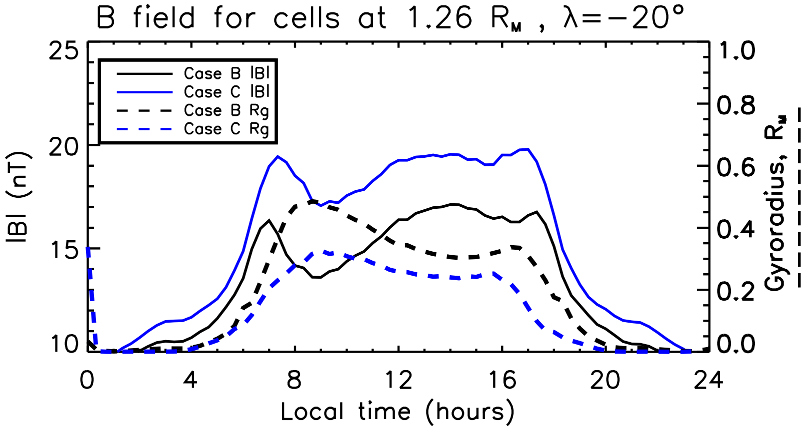

Figure 5.9: The magnetic fields and the gyroradius for solar minimum Case B (black lines) and solar maximum Case C (blue lines). The left y-axis measures the magnetic field in nT (solid lines) and the right y-axis measures the gyroradius in R$_M$ (dashed lines). The values are plotted in local time at λ=-20°.

particles that were launched from one of the origin cells, located at 1.26 R$_M$ and $\lambda = -20°$ below the subsolar point, and traced throughout the simulation. Figure 5.8 uses the same color scheme where red cells represent Case B and blue cells represent Case C. The top panel is a close view of the particle trajectories, where the asterisks denote the beginning of their flight path and the circles denote the end of their flight path. The particles in Case B begin to gyrate and soon hit the inner boundary of 300 km, representing precipitation back into the atmosphere. While some of the particles in Case C have a similar fate, the particles have a tighter gyroradius and mostly continue gyrating and accelerating under the planet. The bottom panel is a full view of the simulation to illustrate the entire trajectory of the escaping particles in Case C. These particles gyrate under the planet, hit the detector at 1.5 R$_M$ and then continue being swept tailward until they reach the outer boundary of 3 R$_M$. Because the O$^+$ ions are moving from the subsolar region downwards under the south pole, the VSD signatures reflect the two beams with a downward flight direction of $\theta \geq 90°$. Due to the larger gyroradius for Case B, particles originating near the subsolar region precipitate back into the atmosphere and do not reach the detector at 1.5 R$_M$.

This is an important point because the solar wind conditions were the same for Cases B and C and only the neutral atmosphere (see Figure 5.1) and EUV flux changed. Because the MTP simulation is not self-consistent, the background MHD fields must be static. So for the gyroradius to change in the same location, the field lines must be different for the two cases. Figure 5.9 illustrates the conditions that drive this particular velocity space signature for cells at 1.26 R_M and latitude $\lambda = -20°$, plotted over local time. The magnitude of the magnetic fields are on the left axis and plotted in the solid black and blue lines for Cases B and C, respectively. The gyroradius, defined here with the particle velocity set to the pickup drift speed of the local E/B ratio, is plotted against the right axis in dashed black and blue lines for Cases B and C.

Clearly, the magnetic field in Figure 5.9 is larger for Case C, which contributes to a smaller O^+ gyroradius. The magnetic field is larger during solar maximum because the ion production is greater and subsequently more ions mass load the solar wind. This mass loading then causes the ionospheric and solar wind thermal pressure to increase (*Ma et al.*, 2004), which subsequently drives up the magnetic field pressure and strength and causes the ions to have a smaller gyroradius. Again, this result is for a given IMF configuration (excluding crustal fields) during solar maximum on the dayside of the planet.

In summary, the solar maximum case both increases the flux through a given detector but also has a distinct signature in velocity space. When examining the south pole detector at 1.5 R_M, the 200 eV peak in Figure 5.5 corresponded to the beams of downward moving flux in velocity space in Figure 5.6. Then Figure 5.7 offered a visual representation of the origin of these ions with downward flight directions ($-Z_{MSO}$ or $\theta \geq 90°$) hitting the detector at 1.5 R_M. Figure 5.8 illustrated O^+ ions launched from one of these cells of origin and traced throughout the simulation, revealing that the ions in the solar minimum case had such large gyroradii that they would always precipitate back into the atmosphere. Recall that the MTP simulation launches the same number of particles per cell and the only difference is the enhanced O^+ production during solar maximum. If the ion density were the only parameter changed, it would only affect the weighting of the particles and the solar minimum Case B would have the same velocity space signature but with less flux. This means that the electric and magnetic fields were different between the solar minimum and maximum cases due to mass loading of the solar wind, as seen in Figure 5.9. So the solar maximum case manifested itself in the velocity space because the particles near a stronger magnetic field gyrated more tightly around the field line and were transported under the planet and downtail. The particles in a weaker magnetic field (solar minimum Case B) had a larger gyroradius on the dayside and encountered the upper atmosphere, or for this simulation, crossed the inner boundary of 300 km.

5.3 Ion Escape

The final point of comparison in examining the effect of the corona and solar cycle is the O^+ escape. While the simulation did not include the crustal magnetic fields, these idealized cases isolate the conditions affecting escape and are a useful comparison for other unmagnetized bodies. Again, it should be noted that the results are for specific IMF conditions (an away sector Parker spiral for this simulation) and represent the behavior of high altitude ions ($\geq$ 300 km).

Figure 5.10 illustrates the spatial distribution of O^+ loss (#cm^{-2}sec^{-1}) on a 3 R$_M$ shell for Cases A, B and C (top, middle, and bottom panels respectively). The axes are in local time (hours) and latitude (degrees), where midnight at $\lambda = 0°$ corresponds to the downtail point at 3 R$_M$ along the -X$_{MSO}$ line, and $\lambda = +90°$ at any local time corresponds to the north pole. Beginning with Case A, the loss is concentrated in the northern pole and downtail region, with very little O^+ loss in the southern hemisphere (at latitudes $\lambda \leq 0°$). Cases B and C exhibit more loss due to the ionized corona, with loss well above 10^2 sec^{-1} throughout the southern hemisphere, denoted by the black contour lines. Case C has the highest loss rate, focused directly downtail but with enhanced loss in the northern pole. All three cases exhibit asymmetric loss in the northern polar dawn region (local time ~8-12 hours and λ =60-90°). This asymmetry in O^+ loss at Mars has also been observed by *Dubinin et al.* (2006) and modeled by *Fang et al.* (2008); *Kallio and Jarvinen* (2012) and *Curry et al.* (2012).

In order to directly quantify and compare the O^+ escape in each case, Figure 5.11 illustrates the escape percentage at each 5 degree latitude ring on the 3 R_M shell. This percentage is the ratio of the escape at each latitude to the total escape on the 3 R_M shell for that case (see the bottom panel highlighting a given latitude). In Case A (red line), the escape from the northern pole region dominates with almost 20% of the O^+ escaping at $\lambda = +75°$. In case B (black line), the loss profile shifts and the polar and tailward loss are comparable at 13% escaping with $\lambda = +75°$ and 10% escaping at $\lambda = 0°$. Finally in Case C (blue line), the increase to solar maximum clearly shifts the dominant escape to the tailward region with over 20% of the O^+ escaping at $\lambda = 0 - 5°$. Thus the inclusion of the corona and the solar cycle contribute to the tailward and southern hemisphere escape.

Table 5.1 compares the loss rates for each case on the spherical shell at 3 R_M. Each case is listed with the following parameters: the solar cycle, the inclusion of the corona, the rate (sec^{-1}) of ion precipitation into the atmosphere at the lower boundary (inner loss), the rate (sec^{-1}) of ion escape through the outer boundary (outer loss) and the efficiency, which is the ratio of the outer loss to the total production of O^+ ions. This last parameter is particularly telling because the efficiency indicates the likelihood that particles will escape from the simulation domain.

Beginning with Case A, the outer loss is roughly half of the rate for the inner loss, which contributes to only 32.3% of the produced particles escaping. This result is physically intuitive in that the lack of high altitude O^+ ion production results in a

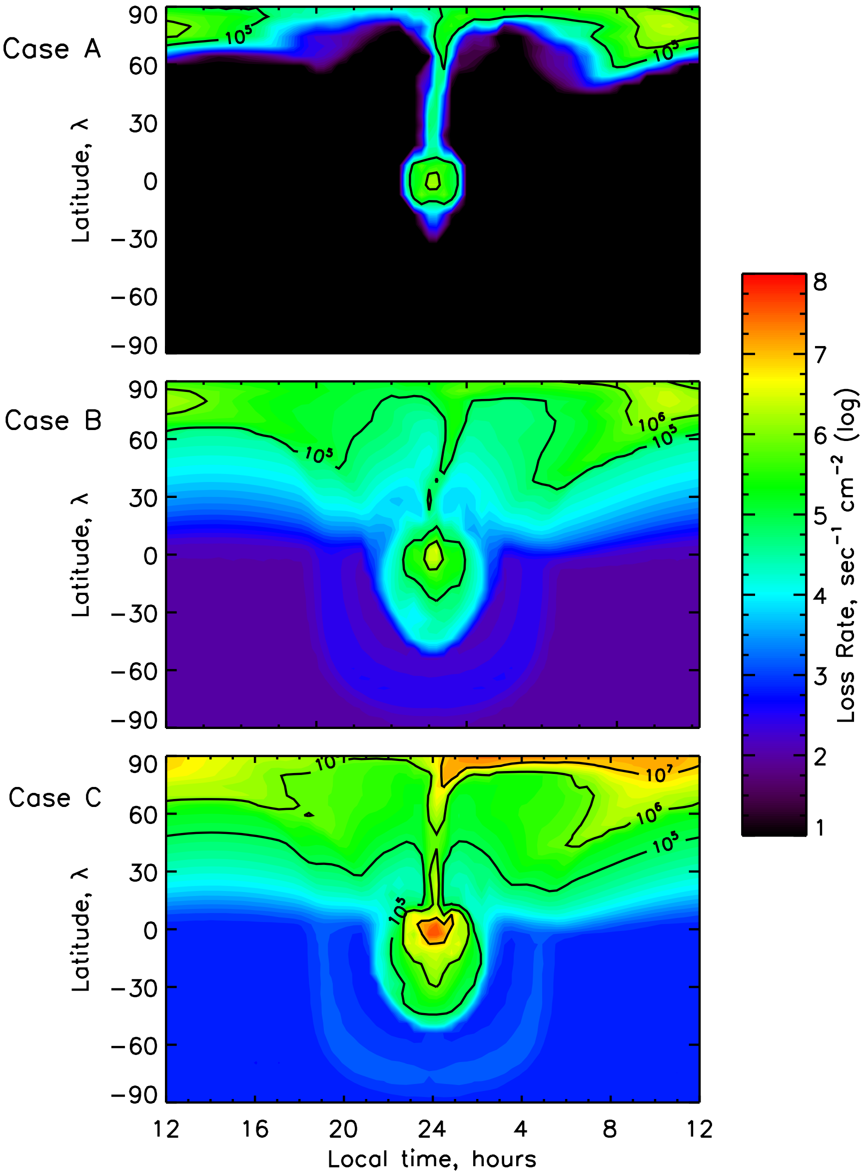

Figure 5.10: Contour plots of the O^+ loss for Case A (top), Case B (middle) and Case C(bottom). The x-axis is local time in hours and the y-axis is the latitude, in degrees, on a 3 R_M shell; a latitude of $\lambda = +90°$ corresponds to the north pole and $\lambda = -90°$ corresponds to the southern pole. The colorbar is logarithmic loss in cm^{-2} sec^{-1} from 10^1- 10^8 and are overlays for various flux levels, labeled accordingly from 10^5- 10^7 cm^{-2} sec^{-1}.

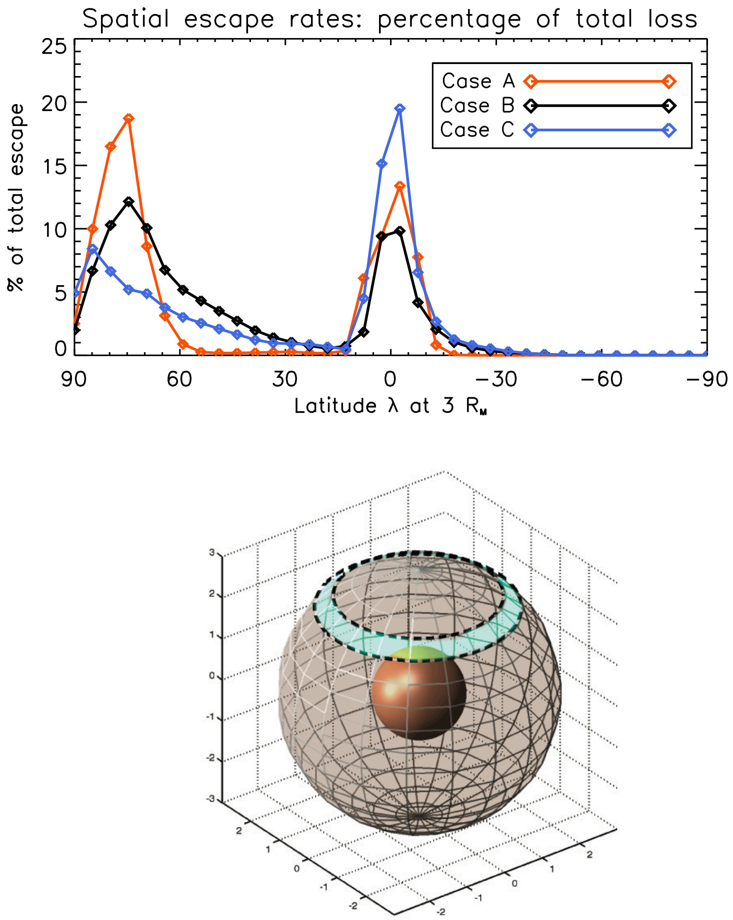

Figure 5.11: The escape is calculated at each latitude, in degrees, on a 3 R$_M$ shell; a latitude of 90° corresponds to the north pole, 0° corresponds to the equator and -90° corresponds to the southern pole. The loss at each latitude is a percentage of the total loss. The bottom panel illustrates a latitude band over which the loss is integrated on the 3 R$_M$ shell.

Table 5.1: O^+ loss rates (#sec^{-1}) and ratios

Case	Cycle	Corona	Inner Loss	Outer loss	Efficiency
Case A	Min	No	6.56×10^{23}	3.13×10^{23}	32.3%
Case B	Min	Yes	8.04×10^{23}	7.36×10^{23}	47.8%
Case C	Max	Yes	7.32×10^{24}	6.17×10^{24}	45.7%

smaller fraction of the produced O^+ escaping. Case B, which includes the corona for solar minimum, results in the inner and outer loss rates being comparable and 47.8% of the ions escaping. This is the highest efficiency among all three cases because the corona contributes to the production of high altitude ions, which are then accelerated out of the simulation domain. While Case C might be expected to have the highest efficiency due to having the highest O^+ escape, the efficiency is marginally lower. This is because the solar maximum conditions drive more ion production at lower altitudes in the denser neutral atmosphere. Subsequently Case C has a higher rate of inner loss that leads to a slightly lower efficiency at 45.7%.

The escape rates from Table 5.1 are in general agreement with both models and observations and will be discussed further in the context of the community wide model comparison (*Brain et al.*, 3-7 Dec. 2012). While many studies have estimated the O^+ loss for different solar cycle conditions, it is especially useful to compare our escape rates with rates from other studies that also exclude Mars' crustal magnetic fields. *Terada et al.* (2009) used an MHD model and found O^+ escape rates of 9.5 $\times 10^{23}$ sec^{-1} during solar minimum. *Modolo et al.* (2005) used a hybrid model, which included a hot oxygen corona, and found rates of 5.2 $\times 10^{23}$ and 2.4 $\times 10^{24}$ O^+ sec^{-1} for solar minimum and maximum respectively (an increased ratio of 4.6). *Brecht and Ledvina* (2010) also used a hybrid model and calculated the O^+ loss (sec^{-1}) at solar minimum to be 8.0 $\times 10^{24}$ and 5.2 $\times 10^{25}$ at solar maximum (an increased ratio of 6.5). The ratio of O^+ loss from solar maximum to minimum in our study is 12.4.

5.4 Summary

As discussed in Section 5.1.2 and Section 5.2, the corona and solar cycle have unique influences on the production, acceleration and escape of O^+. The three cases presented for comparison were: Case A using solar minimum conditions without a corona, Case B using solar minimum conditions with a corona, and Case C using solar maximum conditions with a corona.

Beginning with the neutral atmosphere in Section 5.1.2, Figure 5.1 highlights the different neutral profiles of atomic oxygen. The O^+ ionization rates vary as a function of this neutral profile and solar cycle, as seen in Figure 5.2. Because the O^+ escape is a subject of disagreement, the O^+ production is important to consider.

Section 5.2 quantifies the effect of the corona and solar cycle using virtual detectors to construct velocity space distributions and spatial escape maps. As discussed in Section 5.2.1, the inclusion of a hot corona dramatically increases the high energy flux downtail. Examining a series of virtual detectors downtail, Figure 5.3 shows that Case A has very little O^+ flux above 50 eV and much less flight direction coverage than Case B, whose upper energy limit extends above 10 keV and has much higher flight direction coverage. The downtail observed fluxes at 2.5 R_M are 3.6 and 7.0×10^6 cm^{-2} sec^{-1} for Cases A and B respectively, which suggests that the inclusion of a corona almost doubles the flux accelerated downtail.

Section 5.2.2 discusses the influence of the solar cycle on the observed O^+ flux and ion trajectories. At the south pole, as the detector approaches the planet, it observes high energy, accelerated ions from the ionized corona. The flux observed at the southern pole is roughly an order of magnitude higher at solar maximum than at solar minimum, as seen in Figure 5.5. Additionally, some of this flux comes down from the dayside subsolar region at solar maximum, as illustrated by Figures 5.6-5.9. These downward moving beams of ions originate from inside of the bowshock near the subsolar point, $\sim$1.2 - 1.4 R_M, and at lower latitudes ($\sim$0 through -90°). During solar maximum, the increased mass loading of the solar wind causes the magnetic pressure and field strength to increase on the dayside, which in turn decreases the ion gyroradius and allows particles to be accelerated underneath the planet and downtail. At solar minimum, the solar wind is still mass loaded, but much less so which results in a weaker magnetic field and much larger gyroradii; ions thus cannot avoid precipitating into the planetary neutral atmosphere.

Finally, section 5.3 addresses the influence of the corona and solar cycle on the overall O^+ escape. As with the case of the total flux, the inclusion of the hot corona roughly doubles the outer escape on a 3 R_M shell during solar minimum, and the solar maximum condition increases the escape almost an order of magnitude. In addition to an increase in O^+ loss, there is an increase in the efficiency of Cases B and C, indicating that the likelihood of each ion produced is more likely to escape with the inclusion of the hot oxygen corona.

These results are part of a community-wide model comparison in order to quantify the role of the solar cycle and corona with respect to the transport and escape of O^+. A particular niche of a test particle simulation includes high resolution VSDs, which the MTP constructed from 1.5 billion test particles following background electric and magnetic fields. The inclusion of a hot neutral corona greatly affects the high altitude O^+ production and subsequent acceleration to energies above 10 keV. The solar cycle contributes to an order of magnitude increase in O^+ escape between the solar minimum and maximum cases. This increase in loss is in part due to the effects of an increased dayside magnetic field, which allows more ions to avoid precipitating into the atmosphere by decreasing their gyroradius and transporting them around the planet and downtail.

CHAPTER VI

Ion outflow for heavy ion species

The Mars Test Particle model is used (with background parameters from the BATS-R-US magnetohydrodynamic code) to simulate the transport of O^+ ions in the near-Mars space environment to study the source processes responsible for ion escape. The MHD values at this altitude are used to inject an ionospheric outflow source of ions for the MTP. The resulting loss distributions (in both real and velocity space) from this ionospheric source term are compared against those from high-altitude ionization mechanisms, in particular photoionization, charge exchange, and electron impact ionization, each of which has its own source regions, albeit overlapping. For the nominal MHD settings, this ionospheric outflow source contributes only 10% to the total O^+ loss rate at solar maximum, predominantly via the central tail region. This percentage has very little dependence on the initial temperature, but a change in the initial ion density or bulk velocity directly alters this loss through the central tail. A density or bulk velocity increase of a factor of 10 makes the ionospheric outflow loss comparable in magnitude to the loss from the combined high-altitude sources. The spatial and velocity space distributions of escaping O^+ are examined and compared for the various source terms to identify features specific to each ion source mechanism. For solar minimum conditions, the nominal MHD ionospheric outflow settings yield a 27% contribution to the total O^+ loss rate, i.e., roughly equal to any one of the three high-altitude source terms with respect to escape.

6.1 Model

The MTP model is used for this study for the transport of O^+ through the Mars space environment. We recently modified this numerical tool, originally unveiled by *Fang et al.* (2008), by including three different functional forms for the pick-up ion source processes. Briefly, the MTP code launches particles with weighting terms and then calculates their motion through near-Mars space using a background electric and magnetic field description from a different model. In this study, the background field is that from the multi-species magnetohydrodynamic (MHD) calculations of *Ma and Nagy* (2007). The inner boundary of the model is set to 300 km altitude and the outer boundary is placed at 4 R_M planet-centric distance. Note that a similar test particle modeling procedure through this same MHD model was recently developed by *Li et al.* (2011).

The simulation volume is divided into ∼300,000 'source cells' (132 radial × 36 polar × 72 azimuthal) and then 5000 test particles are launched from within each of these cells. Each particle is proportionately weighted with the local ionization rate from each of the three processes, randomly assigned a starting location within the cell, and randomly assigned a velocity based on a Maxwellian distribution around the local neutral oxygen temperature. Therefore, just under 1.4 billion particles are launched for these high-altitude source terms. This high number of particles is necessary in order to resolve the fine-scale features of the high-altitude velocity space distributions of the escaping ions (see Chapter III).

The particles are weighted according to the three high-altitude pick-up ion source terms from the 'baseline' case in Chapter IV. Photoionization is taken to occur at a constant rate everywhere in the simulation domain except in the optical shadow of the planet, the charge exchange reaction rate is set proportional to the total velocity (bulk plus thermal) of the solar wind H^+ from the MHD results, and electron impact ionization uses the *Cravens et al.* (1987) temperature dependent reaction rates.

For this study, a fourth source term has been added to the calculation: ionospheric outflow. This is defined from the local MHD flux at a selected altitude shell close to the inner boundary (300 km altitude shell) of the MTP simulation (see Appendix B.1). Launching these particles from the inner MTP boundary creates unrealistically low escape rates from this process. This is because many particles launched precisely from the lower boundary will gyrate once and then strike the inner boundary, thus being 'lost' from the MTP simulation domain. This will happen even for particles with an upward drift speed if the magnetic field is oblique and/or the thermal speed is higher than the drift speed. To work around this numerical obstacle, the ionospheric outflow-weighted particles are launched within a spatial grid cell above the altitude shell at which the MHD flux values are selected. By multiplying the flux by the cell face area, an effective 'ionization rate' in units of ions/s is obtained. This rate is exactly analogous to the high-altitude pickup ion source term rates and the same volumetric random launch scenario can be applied. The only difference is that the initial velocity of the particles is based on the local MHD temperature, with an additional initial velocity component from the local MHD bulk flow vector.

Note that these ionospheric outflow particles are different from the other three 'high-altitude source' particles launched by the MTP simulation. The other particles are given a proportional weight for the three sources (photoionization, charge exchange, and electron impact), while these particles are given only the weighting of the ionospheric outflow source. The high-altitude sources could be combined into the same particle set because the initial conditions were the same within each source cell (only the weighting is different). The ionospheric outflow source, however, has a different temperature (the local plasma temperature, not the neutral temperature) and is given an initial bulk velocity (with all of the particles in a cell receiving the

MHD bulk velocity as well as a randomly-determined velocity based on a Maxwellian distribution). In addition, because the ionospheric outflow source is launched at only one altitude shell (1 radial × 36 polar × 72 azimuthal), the number of particles per cell is set to 100 times that for the other sources (which are launched in roughly 100 times more source cells). Therefore, the total number of particles is roughly the same (∼1.4 billion particles) for ionospheric outflow as for the three high-altitude source terms (i.e., a total of ∼3.8 billion particles are launched for a simulation to obtain high-resolution velocity space distributions).

The MHD simulations used for the background fields solves separate continuity equations for four ion species but a single set of momentum and energy equations. It specifies an inner boundary magnetic field with the *Arkani-Hamed* (2001) Mars crustal field model, and uses thermospheric neutral densities from Bougher et al. [2006]. The upstream boundary conditions are set to a solar wind density of 4 cm^{-3}, velocity of 400 km/s, and a nominal away-sector Parker spiral interplanetary magnetic field (IMF) of 3 nT with an angle of 56° off of the x-axis.

The MHD inputs used for the injected ionospheric outflow at 300 km altitude are given in Figure 6.1. On the dayside, the O^+ density (Figure 6.1a) is near 1000 cm^{-3}, but it plunges to values below 100 cm^{-3} (even below 1 cm^{-3}) across the nightside. The bulk velocity (Figure 6.1b) is small across most of the dayside (below 100 m/s) and is only slightly higher on average across the nightside (still below 1 km/s) except in one location, on the nightside at high southern latitudes. Viewed from upstream, this is a region directly behind the strong crustal fields, and the flow (of tens of km/s) is downward. Note that the bulk speed from the MHD results is applied regardless of direction. This allows for downward or nearly-horizontally flowing O+ to be included in the IO boundary condition. Such particles might escape, depending on the local and downstream magnetic and electric field vectors. Even if the bulk flow is downward, the temperature could be large compared to the bulk flow and some particles would be directed upward. Therefore, ionospheric outflow is initialized everywhere on the source shell, regardless of the direction of the bulk flow vector. In Figure 6.1c, it is seen that the boundary condition has dayside temperatures ranging from a few hundred Kelvin in the northern hemisphere to a few thousand K in the southern hemisphere over the region of strong crustal fields. The temperatures are higher on the nightside, reaching ∼5000 K across most of the nightside and, in the region of downwelling flow in the southern high latitude nightside, the temperature is over 10^5 K. Figure 6.1d shows the initial condition fluxes used for weighting the MTP ionospheric outflow ions. The largest fluxes ($\sim 10^8$ cm^{-2}sec^{-1}) are found on the dayside, with much smaller fluxes across the nightside. Integrated over the entire shell, the O^+ ionospheric outflow 'production rate' is 1.9×10^{25} ions/sec.

Before proceeding, the chosen methodology should be tested. Specifically, it is useful to check the O^+ gyroradius at the 300 km altitude (the MTP inner boundary). Two calculations of this quantity are shown in Figure 6.2: Figure 6.2a is a gyroradius calculation based on the MHD bulk speed and characteristic 'random' speed from the local temperature value; and Figure 6.2b is the gyroradius calculation with the velocity set to the 'pick-up **E** / **B**' velocity. Because the first MTP source grid cell has a vertical extent of 37 km, the average launch altitude of the IO test particles is 19 km above the MTP simulation's domain inner boundary. In general, the gyroradius calculated from the initial conditions (Figure 6.2a) are higher than those from pick-up acceleration (Figure 6.2b). This is because 300 km is within the magnetic pileup region (or dominated by the strong crustal fields) and the flow speed is rather low, therefore the pick-up acceleration at this altitude is small. Across the dayside, the gyroradius is below 10 km nearly everywhere. On the nightside, the gyroradius is larger, typically between 10 and 100 km, and in fact goes above 1000 km in the small region of downwelling at high southern latitudes. Note from Figure 6.1 that the largest ionospheric outflow fluxes are on the dayside. From this, it is concluded

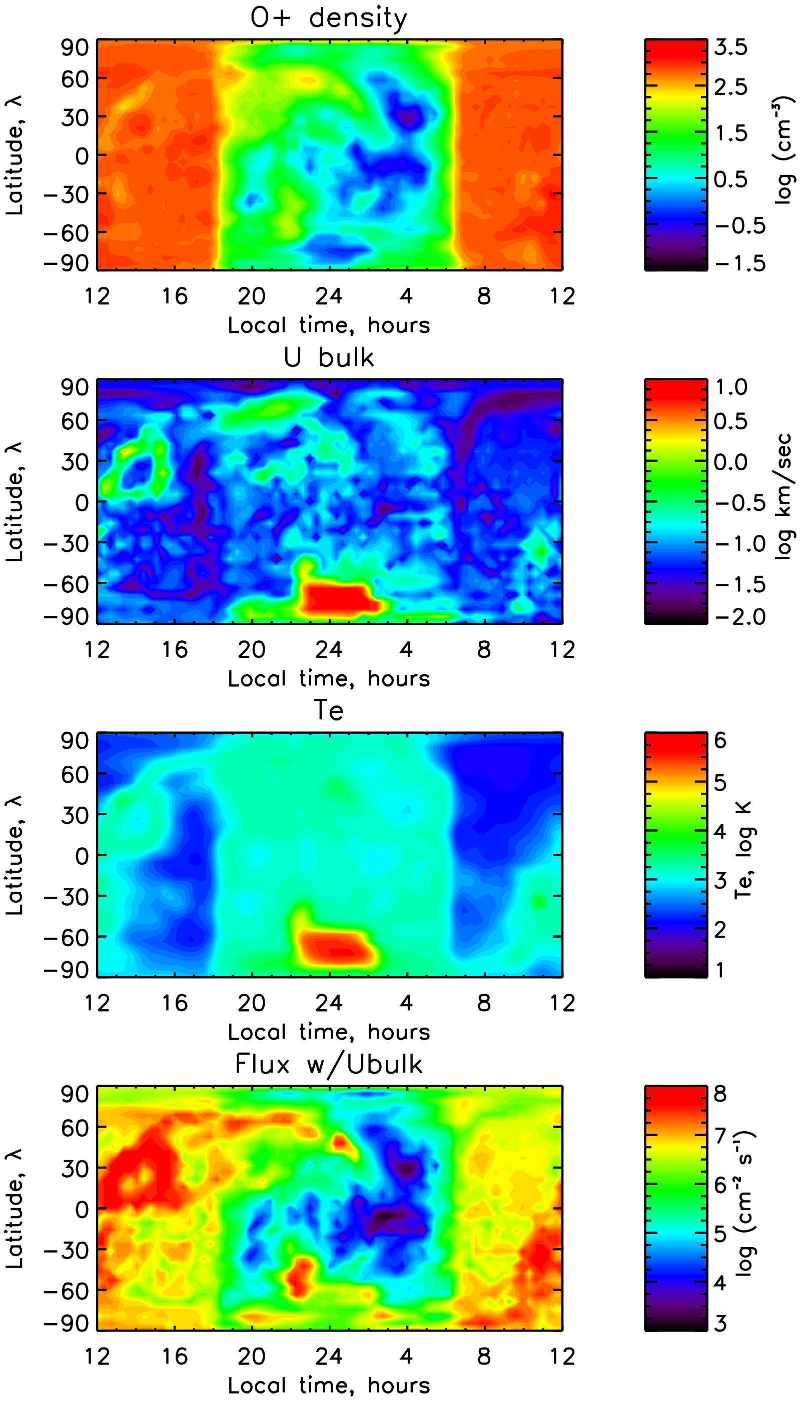

Figure 6.1: MTP ionospheric outflow boundary conditions taken at 300 km altitude in the MHD model results: (a) O^+ density; (b) bulk velocity; (c) temperature; and (d) O^+ flux. Each plot has local time as the x axis (noon on the ends, midnight in the middle) and latitude as the y axis (poles at the top and bottom, equator in the middle), with its own logarithmic color scale.

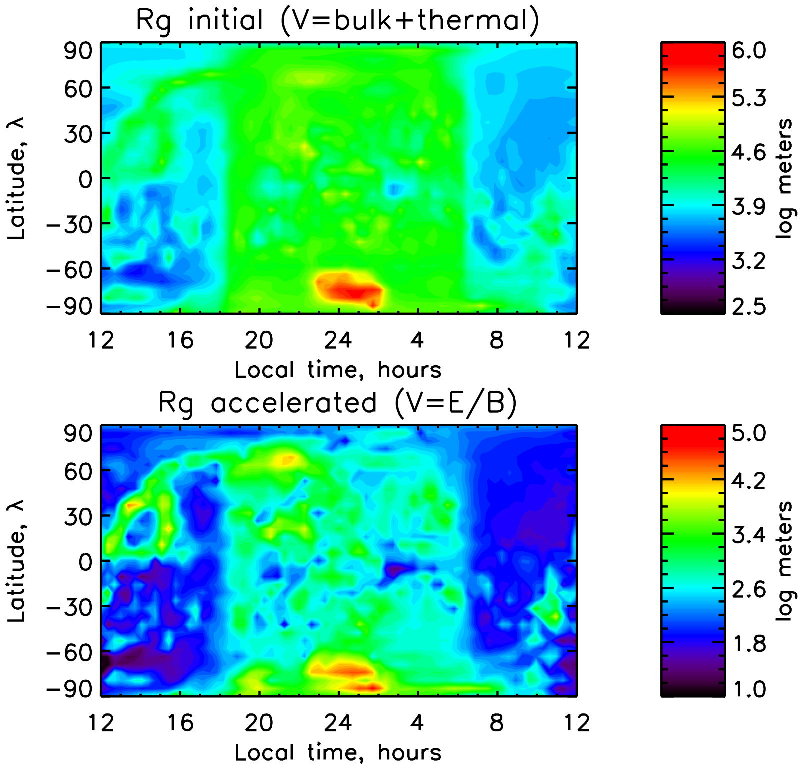

Figure 6.2: Local O^+ gyroradius at 300 km altitude from the MHD model results, with the assumed velocity from (a) the local speed calculated from the bulk and thermal velocities, and (b) the local pick-up acceleration flow from the electric and magnetic field strengths. Each plot has local time as the x axis (noon on the ends, midnight in the middle) and latitude as the y axis (poles at the top and bottom, equator in the middle), with its own logarithmic color scale.

that the assumption of launching particles at a distributed altitude source throughout the first MTP grid cell is a reasonable approach that avoids the problem of particles striking the inner boundary after their first gyration.

6.2 Results

The presentation of the results begins with an examination of the fine-scale structures in the velocity space distributions of the escaping ionospheric outflow, then progresses to spatial distributions of the escaping particles, and finally to total escape rates. A discussion of the interpretation and implications of these results is given in the following section.

6.2.1 Velocity space distributions

Figure 6.3 shows flight direction distributions at 3.9 R_M Mars-centric distance (i.e., just inside the outer boundary of the simulation domain) at two locations: (top row) along the -X axis in the central downtail direction; and (bottom row) over the northern pole in the direction of the $+Z_{MSE}$ (Mars-Sun-Electric field coordinate system) axis. The two columns show the results for the ionospheric outflow on the left and for the sum of the three high-altitude source terms on the right (photoionization, charge exchange, and electron impact ionization). The fluxes are integrated over energy. Here, flight direction refers to the polar angle (θ) and azimuthal angle (ϕ) of the velocity of the test particles striking the virtual detector. Polar angles of $\theta < 90°$ ($\theta > 90°$) indicate northward (southward) particle motion and azimuthal angle between $90° < \phi < 270°$ (or $\phi < 90°$ or $\phi > 270°$) indicate tailward (sunward) particle motion.

There are two general trends to note from the panels of Figure 6.3. The first is that the ionospheric outflow fluxes are significantly lower than those from the high-altitude sources. This is especially true for the downtail direction, where the IO fluxes are always lower than the fluxes from the high-altitude sources in every flight direction. Over the north pole, the IO flux is just as high as that from the other sources (at directional number fluxes of 10^7 ions cm^{-2} s^{-1} sr^{-1}) but it is limited to a single pixel, so the total flux at this location is dominated by the other three high-altitude source processes. The second trend of Figure 6.3 is that the IO fluxes have less flight direction coverage than those from the high-altitude sources. Usually, they extend over a portion of the flight directions covered by the high-altitude sources.

Figure 6.4 shows energy spectra of differential number flux, integrated over flight direction, for the same locations and source terms as in Figure 6.3. For a more

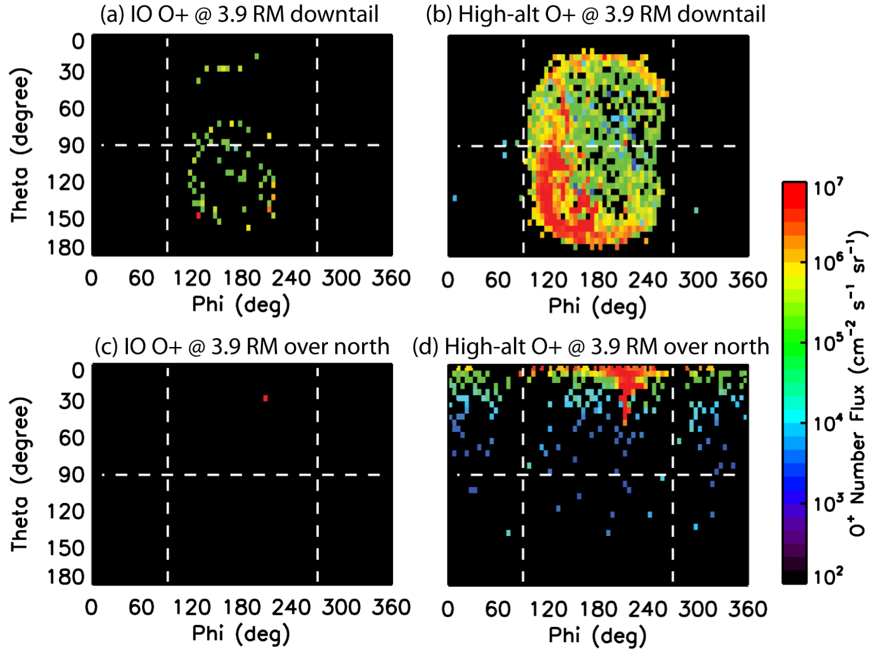

Figure 6.3: O^+ velocity space (flight direction) distributions at 3.9 R_M Mars-centric distance in the -X_{MSE} downtail direction (top row) and over the north pole in the $+Z_{MSE}$ direction (bottom row) for the ionospheric outflow source term (left column) and for the three high-altitude source terms combined (right column). The plots, summed over all particle energies, show a resolution of 5°×5° with the azimuthal angle on the x axis (sunward flow on the edges, tailward flow in the middle) and polar angle on the y axis (northward motion on the upper half, southward motion on the lower half), all on the same logarithmic color scale.

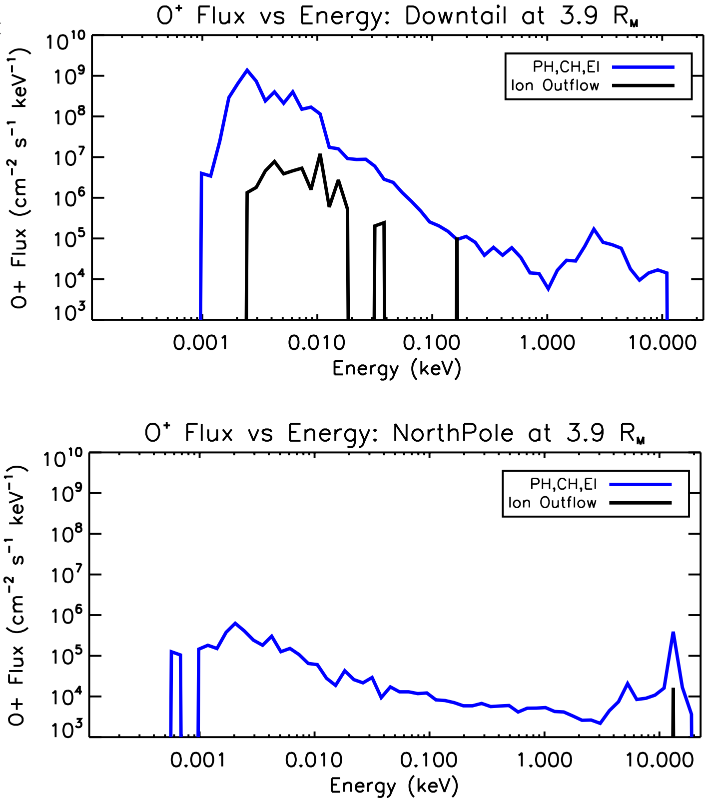

Figure 6.4: O^+ energy spectra, integrated over flight direction, at 3.9 R_M for (a) along the -X_{MSE} axis (downtail) and (b) along the $+Z_{MSE}$ axis (over the north pole). The blue curve is for the combined high-altitude source terms and the black curve is for the ionospheric outflow source term.

direct comparison, the spectra for the sources are overlaid in the same panel. It is seen that the energy of the O^+ ions from the ionospheric outflow source are highly focused in energy at this radial distance. The value of that characteristic energy, however, changes with the location of the virtual detection. In the polar plume region, ionospheric outflow yields very high energy O^+ (over 10 keV), while in the central tail, this same source term yields very low energy O^+ (centered around 10 eV). In both places, the high-altitude sources give O^+ ions across a broad spectrum of energies. The high-altitude sources have two peaks, one at low energy (below 10 eV) and another at high energy (above 1 keV), with the flux ratio of these two relative maxima changing as a function of location.

6.2.2 Ion escape spatial distributions

Integrating the velocity space distributions yields a spatial pattern of the loss of particles to deep space. Figure 6.5 shows the escaping number flux of O^+ through the 4 R_M planet-centric shell for each of the source mechanisms (Figures 6.5a-6.5d) as well as the summation of all four sources (Figure 6.5e). While they all show the same basic features of a 'polar plume' region at high latitudes (0° to +90° at all local times) connected to a central tail flow (0° near midnight), there are certain distinguishing differences between the sources.

A major difference among the spatial escape plots for each source mechanism is that the high-altitude ionization sources dominate the polar plume. The physical origin of the northern polar plume is primarily from the dayside northern hemispheric magnetosheath. The convective electric field that is associated with the reacceleration of the shocked solar wind accelerates these planetary pick-up ions. O^+ has a much larger gyroradius than H^+ due to its mass and rather than being contained within the magnetosheath like the solar wind H^+, the pick-up O^+ ions cross the bowshock and develop a high-energy beam-like velocity distribution (as seen in the previous section). The polar plume from ionospheric outflow is very narrow because the source is from the upflowing O^+ that crosses the magnetic pileup region into a region where they are affected by the large electric fields of the magnetosheath, which only happens at very high latitudes. Among the three high-altitude sources, the escaping fluxes from photoionization are a bit more structured than those from the other two processes, but in general all three ionization mechanisms yield a similar spatial pattern.

Another important difference for spatial escape is the central tail loss region, which contains most of the escaping IO particles. However, these particles still do not dominate at any particular spatial location. The IO source begins closer to the planet than the high-altitude source terms, by definition, and therefore creates a smaller, more focused, region of central tail loss. In this focused loss channel,

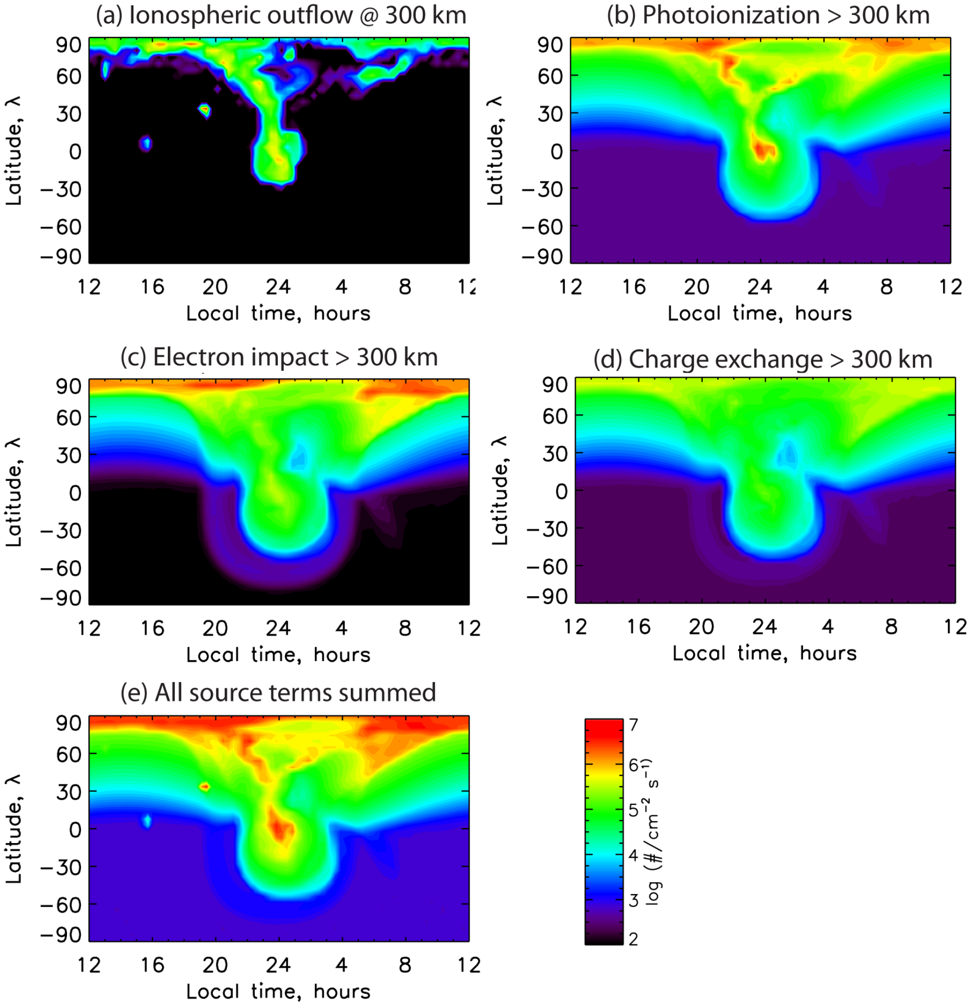

Figure 6.5: O$^+$ escape flux through a 4 R$_M$ shell for (a-d) each source process and (e) a summation of all 4 source terms. Each plot has local time as the x axis (noon on the ends, midnight in the middle) and latitude as the y axis (over the poles at the top and bottom, over the equator in the middle), all on the same logarithmic color scale.

the number flux from ionospheric outflow is comparable to that from high-altitude photoionization and larger than the fluxes from electron impact ionization or charge exchange.

To further analyze this loss, Figure 6.6 shows the average energy of the escaping O^+ particles through the 4 R_M shell. As in Figure 6.5, the average energies are shown for each source process separately (Figures 6.6a-6.6d) and then for all of them together via a weighted average (Figure 6.6e), weighted proportionately to the number fluxes in Figure 6.5. The color scale is logarithmic with black indicating an average energy of 10 eV or less and red showing an average energy of tens of keV.

Figure 6.6 illustrates that the energy of the escaping ionospheric outflow is notably different from that of the high-altitude sources. In particular, the polar plume is significantly hotter and the central tail loss region is cooler. The IO O^+ ions in the polar plume have an average energy around 10 keV, with some localized patches reaching 25 keV, while the IO ions in the central tail have an average energy below 100 eV. The average energies of the three high-altitude source terms are remarkably similar, with a polar plume average energy of ~7 keV and a central tail average energy of ~2 keV. The combined average energies in Figure 6e appear to closely resemble the high-altitude sources, reflecting the fact that the ionospheric outflow is a minor contributor to the escaping O^+ flux.

6.2.3 Total escape rate comparison

The final assessment to quantify the influence of ionospheric outflow on escape is with respect to the total O+ loss. The results are provided in Table 6.1. The IO production rate is given in the second column, integrated over the entire 300 km altitude shell. This value can be compared with the 1.2×10^{25} s^{-1} total production rate from the three high-altitude source processes. The total number of oxygen ions flowing through the inner boundary of the MTP simulation domain is over 50% larger

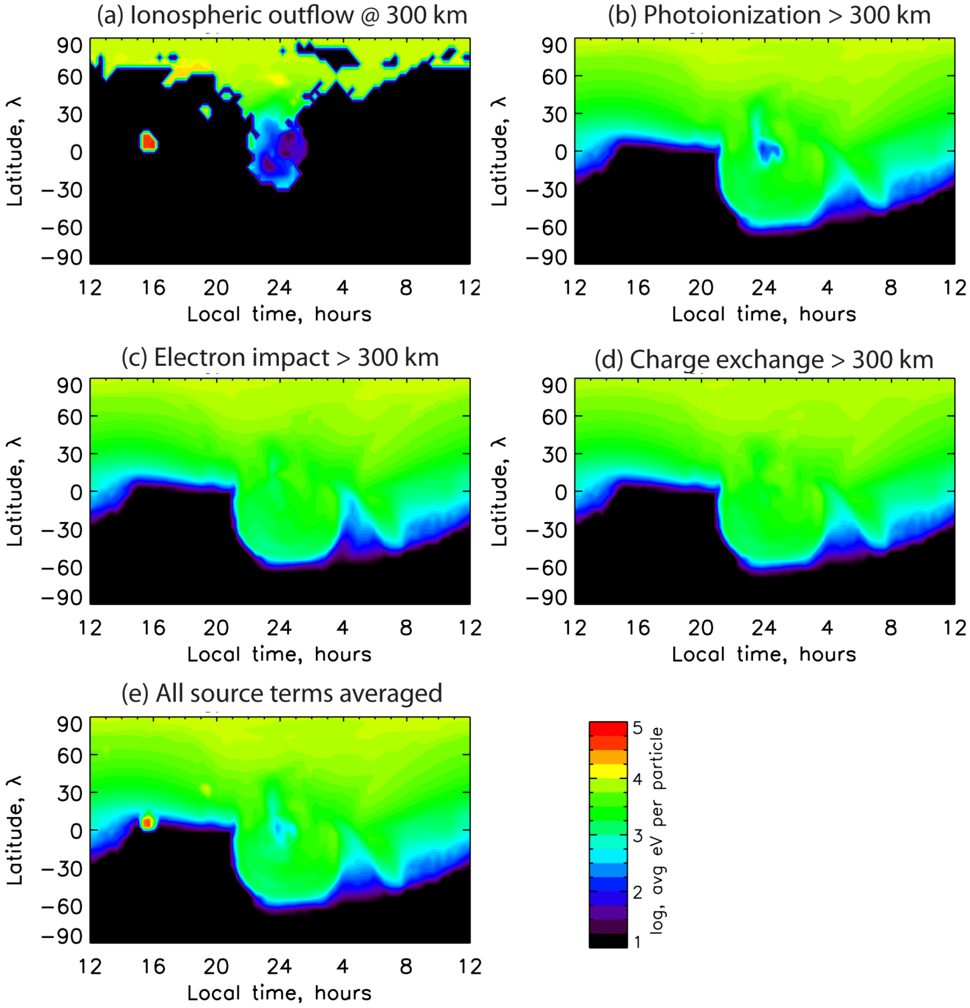

Figure 6.6: Average energies of the escaping O^+ through a 4 R_M shell for (a-d) each source process and (e) a weighted average of all 4 source terms. Each plot has local time as the x axis (noon on the ends, midnight in the middle) and latitude as the y axis (over the poles at the top and bottom, over the equator in the middle). all on the same logarithmic color scale.

Table 6.1: Ionospheric outflow as a function of initial condition parameters

Setting	IO Production	IO Inner Loss	IO Escape	IO Escape Percentage	IO Escape Efficiency
MHD values	1.9×10^{25}	1.8×10^{25}	4.5×10^{23}	9.8%	2.4%
Changing temperature in velocity initialization					
T=10^2 K	1.9×10^{25}	1.8×10^{25}	4.5×10^{23}	9.6%	2.4%
T=10^3 K	1.9×10^{25}	1.8×10^{25}	4.5×10^{23}	9.7%	2.4%
T=10^4 K	1.9×10^{25}	1.8×10^{25}	4.8×10^{23}	10.3%	2.6%
Changing bulk flow in both production rate and velocity initialization					
$U=0.5\cdot u_{local}$	9.3×10^{24}	9.0×10^{24}	2.3×10^{23}	5.2%	2.5%
$U=2\cdot u_{local}$	3.7×10^{25}	3.5×10^{25}	2.4×10^{24}	36%	6.5%
$U=10\cdot u_{local}$	1.9×10^{26}	1.4×10^{26}	4.1×10^{25}	91%	22%
Changing bulk flow in only the velocity initialization					
$U=0.5\cdot u_{local}$	1.9×10^{25}	1.8×10^{25}	4.5×10^{23}	9.7%	2.4%
$U=2\cdot u_{local}$	1.9×10^{25}	1.7×10^{25}	1.2×10^{24}	22%	6.4%
$U=10\cdot u_{local}$	1.9×10^{25}	1.4×10^{25}	4.1×10^{24}	50%	22%
Changing density in the production rate					
$n=0.5\cdot n_{local}$	9.3×10^{24}	9.0×10^{24}	2.3×10^{23}	5.1%	2.4%
$n=2\cdot n_{local}$	3.7×10^{25}	3.6×10^{25}	9.1×10^{23}	18%	2.4%
$n=10\cdot n_{local}$	1.9×10^{26}	1.8×10^{26}	4.5×10^{24}	52%	2.4%

than the total ionization rate in the MTP simulation domain.

The loss of the ionospheric outflow O^+ particles through each of the MTP simulation boundaries were also calculated (inner and outer, respectively, in the third and fourth columns of Table 6.1). For comparison, the inner and outer boundary loss rates from the three high-altitude sources combined are 7.7×10^{24} s^{-1} and 4.2×10^{24} s^{-1}, respectively. The loss through the inner boundary (i.e., bombardment of the Mars upper atmosphere) is dominated by the IO source, with a value over twice as large as that for the high-altitude sources. The situation is reversed for the outer boundary loss, with the high-altitude ionization processes contributing an order of magnitude more O^+ to the total escape rate.

The IO escape percentage and efficiency of Table 6.1 (final two columns) put the ionospheric outflow escape rate into quantitative perspective. The IO escape percent (second to last column) is the IO escape rate divided by the total loss rate through the outer boundary, while the IO escape efficiency (last column) is the escape rate divided by the production rate. It is seen that, for this scenario with the MHD moments defining the outflow source conditions at 300 km altitude, ionospheric outflow contributes less than 10% to the total escape rate. Furthermore, even though the number of O^+ ions flowing into the MTP simulation domain through the lower boundary is larger than the ionization rate within the entire MTP simulation domain, only 2.4% of those incoming ions escape through the outer boundary.

6.2.4 Parametric study of ionospheric outflow

For the results shown above, the local MHD values at 300 km altitude were used to set the ionospheric outflow rate for initializing the MTP particles. It is useful to consider the influence of the outflow initialization on the results, in particular on the total escape rate of O^+ to deep space. The three MHD quantities used in the initialization are the O^+ density, velocity, and temperature. The following subsections examine the dependence of the loss rate on each of these parameters. While the background MHD simulation results are the same, the initialization quantities for the ionospheric outflow test particles is varied. While this means that the field through which these particles move is not consistent, the results elucidate the influence of these initialization parameters on the production and escape of ionospheric outflow.

6.2.4.1 Ionospheric outflow dependence on initial temperature

Temperature is used for defining the IO by probabilistically setting the initial speed of the particle based on a Maxwellian distribution. Two additional parameters are used to assign a direction to this initial speed. As seen in Figure 6.1, the typical MHD ion temperature at 300 km altitude is around 1000 K, with extrema between 100 K and 10,000 K. For this parameter study, the temperature for the IO initialization was set to one of these three values everywhere on the shell: a low temperature of 100 K; an intermediate value of 1000 K; and a high case of 10,000 K.

The results from these numerical experiments are shown in the first grouping of rows in Table 6.1. Because the production rate (second column) only depends on density and bulk velocity, this quantity doesn't change between these simulations. However, it is interesting that the inner and outer loss rates are essentially the same regardless of the temperature setting. There is a slight increase in the IO escape rate for the 10,000 K setting, but this rise is less than 10% from the baseline escape rate.

6.2.4.2 Ionospheric outflow dependence on initial velocity

The dependence of ionospheric outflow of the initial drift velocity of the particles was also investigated. The drift velocity appears in two places in the initialization of the ionospheric outflow: first, it influences the weighting assigned to the particles because it is one of the two terms in the number flux calculation; second, it is used as an additive vector on the initial velocity for all of the IO particles in a source cell. These can be varied together or separately in the simulation. Varying only the number flux without changing the initial velocity is equivalent to changing the density, and this is discussed in the next subsection. Changing the initial velocity of the particles while keeping the total number flux the same is equivalent to changing not only the velocity but also the density inversely with the velocity. A third option is to keep the density constant and change the velocity both in the particle weighting calculation as well as in the initial condition.

Let us consider these three options in reverse order. Results with the velocity changed in both places of the outflow initialization are given in the second section of Table 6.1. The production rate changes in direct proportion to the change in velocity, and on initial inspection the loss through the inner and outer boundary also both increase with increasing initial velocity. The dependence of the loss is not the same as that for production, however, with more particles preferentially escaping through the outer boundary rather than striking the Mars upper atmosphere. This is evidenced in the IO escape efficiency (the last column), which increases with the initial velocity setting. In addition, for the case of an order of magnitude increase of the local MHD velocity, ionospheric outflow will dominate the total escape rate of O^+ to deep space.

If the MHD flux used for calculating the IO production rate is kept constant and only the particle initial bulk velocity is changed, then the results are a bit different (see the third group of rows in Table 6.1). Specifically, reducing the initial bulk velocity had essentially no effect on the results. Increasing the initial velocity of the particles, however, has a dramatic effect, with the escape rate approaching that of the high-altitude sources for an order of magnitude increase.

Table 6.2: Ionospheric Outflow as a function of launch initialization altitude

IO altitude km	IO Production s^{-1}	IO Prod. Percentage % of total	IO Inner Loss s^{-1}	IO Escape s^{-1}	IO Escape Percentage % of total	IO Escape Efficiency % of IO Prod.
300-337	1.9x10^{25}	60	1.8x10^{25}	4.5x10^{23}	10%	2%
337-374	3.0x10^{25}	71	2.2x10^{25}	8.2x10^{24}	66%	27%
374-412	3.9x10^{25}	76	2.1x10^{25}	1.8x10^{25}	81%	46%
412-450	3.9x10^{25}	76	1.7x10^{25}	2.2x10^{25}	84%	57%
450-488	3.5x10^{25}	74	1.1x10^{25}	2.4x10^{25}	85%	69%

6.2.4.3 Ionospheric outflow dependence on initial density

Results were also considered with a change in the density used for the IO initial conditions. The density only appears in the weighting factor given to the particles, which is dependent on the MHD-calculated number flux through the 300 km altitude shell. If the velocity is allowed to vary inversely with the density in order to keep this flux constant, then density has no influence on the IO escape rates. However, if the velocity is kept at the MHD-defined value, then the IO production rate varies linearly with density. The last three rows of Table 6.1 list the loss values for ionospheric outflow when using different multiples of the local MHD density in the production rate calculation. The escape efficiency remains the same, but the relative contribution of ionospheric outflow to the total escape rate rises dramatically. When the local densities are increased by a factor of 10, ionospheric outflow dominates the total escape rate (52% of the total loss through the outer boundary). The escape efficiency is the same for the three density settings because the trajectories of the particles have not changed, only their weighting.

6.2.4.4 Ionospheric outflow dependence on altitude of insertion

A final numerical experiment to consider is the dependence of the IO escape rate on the altitude at which the MHD fluxes are extracted (that is, the altitude of the ionospheric outflow source shell). All of the results to this point have been with the MHD results from 300 km altitude used for specifying particles in the first source cell of the MTP grid. Table 6.2 summarizes the results for a set of simulations in which the ionospheric outflow was specified and launched. The first column shows the altitude range of the MTP source grid where the IO particles were launched. The second column lists the total source rate for the IO process (summed over the shell), and the third column gives the relative size of this number with respect to the total source rate in the simulation (the source for the high-altitude pick-up processes is 1.2×10^{25} s^{-1}). The fourth column lists the loss rate of IO particles through the inner boundary (at 300 km altitude) and the fifth column is the loss rate through the outer boundary (at 4 R_M planet-centric distance). The final two columns give the relative value of the IO escape rate with respect to the total escape rate (the outer boundary loss from the high-altitude sources is 4.5×10^{24} s^{-1}) and with respect to the IO source rate (the second column).

It is seen that the IO source rate doubles as the source shell moves from 300 km to ∼400 km altitude. This can be from one of two things: either the MHD flows have significantly turned outward from the planet, resulting in a substantial increase in outflow rate, or the ionization rate in this altitude range is still relatively large, dominating the actual outflow from the production below 300 km.

There are also changes in the inner and outer boundary loss rate for ionospheric outflow as the source shell is elevated. The inner loss rate for the IO particles at first rises with source altitude, but then drops. This is expected because there are two competing processes: the IO source rate increases dramatically in this altitude range, but fewer particles hit the inner boundary as the initial altitude increases. The loss through the outer boundary, however, simply increases with rising source altitude, as expected. This yields a rise in escape efficiency from 2.4% to 69% across the range of IO source altitudes.

Table 6.3: Solar cycle influence on the relative contribution of ionospheric outflow

Setting	IO Production s^{-1}	IO Inner Loss s^{-1}	IO Escape s^{-1}	IO Escape Percentage % of total	IO Escape Efficiency % of IO Prod.
Solar maximum	1.9×10^{25}	1.8×10^{25}	4.5×10^{23}	9.8%	2.4%
Solar minimum	2.0×10^{23}	7.8×10^{22}	1.2×10^{23}	27%	61%

6.2.5 Solar minimum conditions

All of the results presented above are for solar cycle maximum conditions in the MHD model and in the MTP production rates. For comparison, a similar numerical experiment was conducted from an analogous solar minimum MHD simulation, with identical upstream solar wind conditions but a different neutral atmosphere and photoionization rate. Again, the MHD parameters were extracted at 300 km altitude for use as the initialization values for the IO source in the MTP model.

Table 6.3 presents the solar maximum and minimum results for total production and loss from ionospheric outflow. The IO production rate drops by two orders of magnitude between solar maximum and minimum. This is true for the high-altitude sources as well, which dropped by just over a factor of ten to 9.9×10^{23} s^{-1} at solar minimum. So, the IO source is now less than the high-altitude source of O^+ within the MTP simulation domain by nearly a factor of 5.

The loss of the IO O^+ particles at solar minimum is quite different from that at solar maximum. In particular, the partitioning of the loss between the inner and outer boundaries is reversed between the two cycle phases, with solar minimum having a larger value of loss through the outer boundary (i.e., escape) than its inner boundary loss rate. The result is a rather different IO escape efficiency, changing from 2.4% at solar maximum to 61% at solar minimum. The contribution of ionospheric outflow

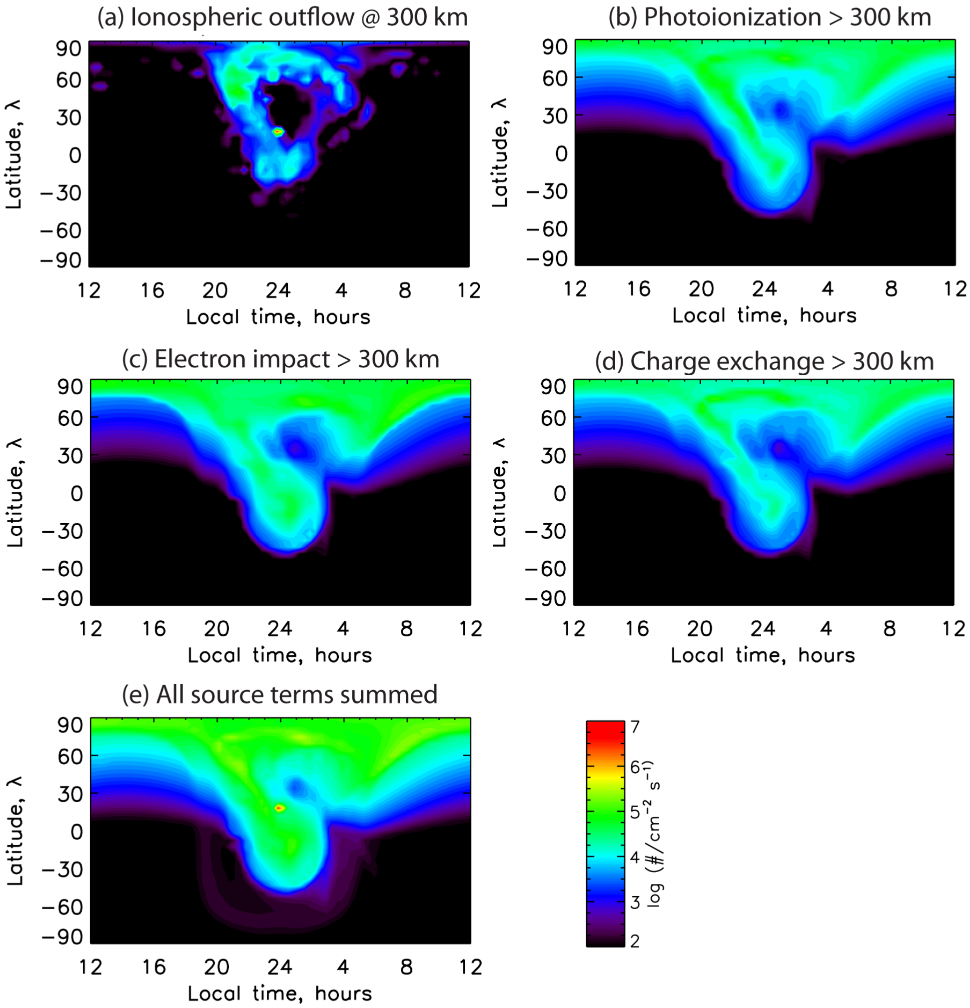

Figure 6.7: Spatial distributions of escaping O^+ number flux, like Figure 6.5, except for solar minimum instead of maximum conditions.

to the total escape rate is also much bigger (nearly 3 times larger) at solar minimum than maximum. It is still less than half of the total, but at 27% of the total escape rate it is now comparable to each of the other 3 source terms in the MTP.

Figure 6.7 shows the spatial distribution of the O^+ escape to deep space through a 4 R_M shell for the solar minimum simulation results. The fluxes are shown for each source term (Figures 6.7a-6.7d) as well as summation of all four sources (Figure 6.7e). The colorscale is the same as that in Figure 6.5. Overall, the patterns are the same as that in Figure 6.5 with a polar plume in the $+Z_{MSE}$ direction that connects through one or more ribbons to the loss channel down the central tail. The flux

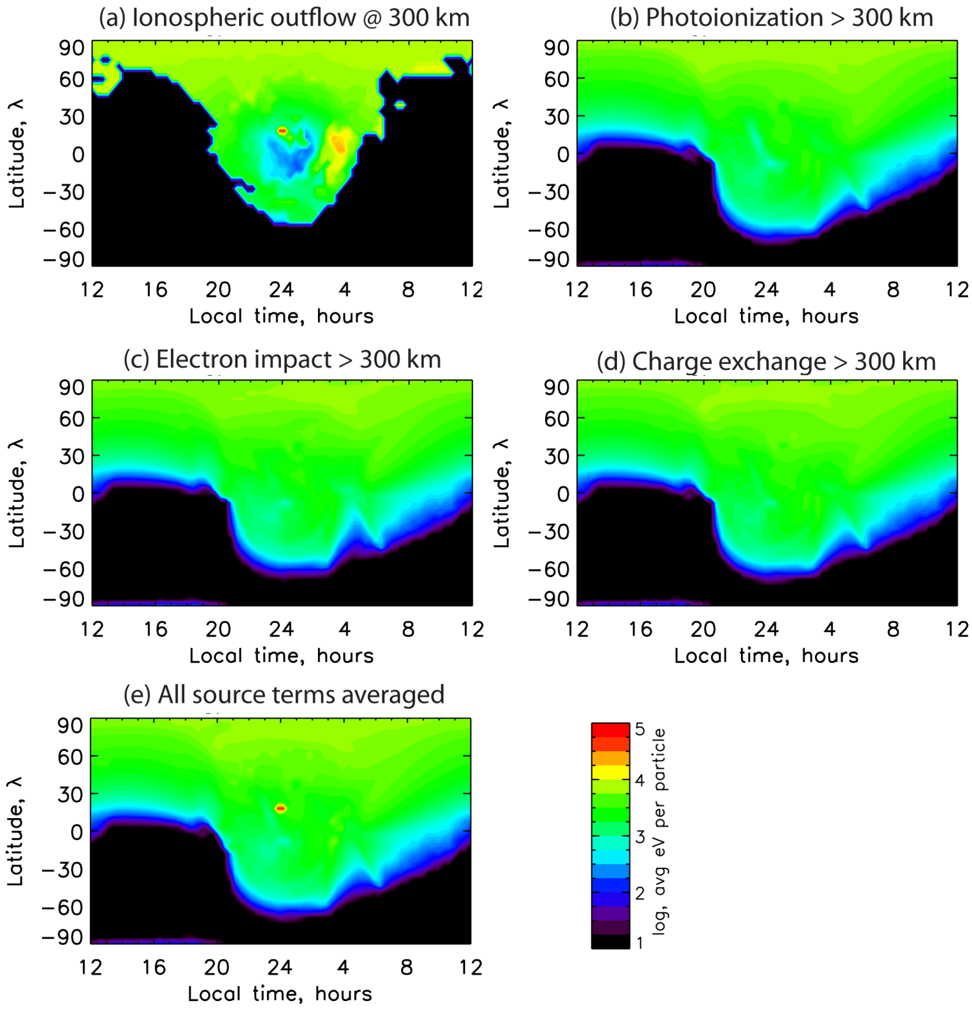

Figure 6.8: Spatial distributions of escaping O^+ average energy, like Figure 6, except for solar minimum instead of maximum conditions.

values, however, are an order of magnitude or more lower.

Similarly to the solar maximum case, Figure 6.8 presents spatial distributions of the average energy of the escaping O^+ through a 4 R_M shell for solar minimum conditions. The plots for the high-altitude sources (Figures 6.8b-6.8d) and the weighted average energy plot (Figure 6.8e) closely resemble those for solar maximum values (compare with Figures 6.6b-6.6e), with the main difference being that the average energies are slightly lower in the solar minimum case. The average energies for the IO source (Figure 6.8a) follow the same trend as those at solar maximum (compare with Figure 6.6a), but there is now a ring of keV-energy ions around the low-energy focused central tail. Some patches within this ring exceed 10 keV in average energy. Comparing this with the number flux loss distribution in Figure 6.7a, however, it is seen that these high-energy regions coincide with very low particle flux.

6.3 Discussion

As seen in the results above, using the MHD output to define the ionospheric O^+ outflow rate at 300 km altitude yields high-altitude fluxes that are significantly smaller than those from the high-altitude sources (i.e., the ionization processes creating O^+ above 300 km altitude). The O^+ escape rate for ionospheric outflow was only 10% of the total loss rate to deep space, even though the production rate was 50% higher than that for the high-altitude sources. That is, the efficiency of escape is much lower for the IO source term than it is for the high-altitude source term, to the point that ionospheric outflow is actually a small contributor to the total loss.

There are several features of the IO velocity space distribution and spatial loss patterns that are worth discussing in further detail. The first is that, at high altitudes, the IO ions are more tightly focused in flight direction than are the ions from the high-altitude sources. This is because the IO ions originate from a spatially-limited location, whereas the high-altitude sources come from a large spatial region, essentially the entire near-Mars space environment, but in particular the dayside magnetosheath. This distributed source region for the high-altitude ionization processes yields a broader spectrum of O^+ flight directions in the tail.

A related issue is the characteristic energy of the escaping IO ions. The first main feature to note regarding particle energy is that in the central tail, the IO ions are systematically lower in energy than those from the high-altitude sources. In order to reach the central tail, the IO ions remain close to the planet as they flow from the dayside to the nightside, staying below the region of large electric field in the magnetosheath where the solar wind is being reaccelerated. By avoiding this region and these large electric fields, the IO O^+ ions experience a smaller acceleration as they leave Mars and thus these ions remain at low energies, concentrated below 100 eV. Many of the high-altitude source particles, however, are created in the magnetosheath, instantly experiencing a large electric field and undergoing acceleration as they enter the central tail loss channel.

A second point to make about the characteristic energy of the escaping IO ions is that, in the polar plume (that is, $+Z_{MSE}$ in the direction of the solar wind electric field), they are found at relatively higher energies than those ions from the high-altitude production mechanisms (by roughly a factor of two). There is a simple explanation for this reversal in characteristic energy between the two escape channel locations. For loss through the polar plume, IO ions must traverse the magnetic pileup boundary while still on the dayside of Mars (in the northern MSE hemisphere, as well). They are then exposed to the high electric fields of the magnetosheath and are accelerated outward from the planet (in the southern MSE hemisphere, this acceleration is back towards the planet, causing upper atmospheric bombardment). Such particles will cross through the entire magnetosheath, experiencing the full potential difference in this spatial region. The high-altitude source processes create ions throughout the magnetosheath and will consequently have a range of peak energies within the polar plume. Therefore, those IO particles that become part of the polar plume will have a systematically higher energy than those from the high-altitude sources.

These source-term-dependent features of the escaping O^+ velocity space and spatial pattern can be used for interpreting high-altitude observations from missions like Phobos-2, Mars Express, and the upcoming Mars Atmosphere and Volatile EvolutioN (MAVEN) satellite. Certain velocity space peaks are attributable to specific source processes, thus allowing for an analysis of the physical mechanisms of escape from high-altitude ion measurements.

There was very little dependence of the IO escape rate on the initial temperature of the particles at 300 km altitude. This is because the average speed from these temperatures is well below the gravitational escape velocity at Mars. For the high temperature case, 10,000 K is still below 1 eV, which is less than half of the O^+ escape energy. So, while the escape rate increased a small amount with increasing initial temperature, these simulations show that the contribution of ionospheric outflow does not depend on the temperature of the outflow (at least not within the temperature range explored here). This is similar to the findings of *Fang et al.* (2010b), who showed that the escape probability of pickup ions is not particularly sensitive to the initial temperature setting.

When the initial velocity of the ionospheric outflow was varied, the escape rate of these particles was preferentially increased. This is not intuitive because the initial velocity could be pointed horizontally or downward, and therefore the expected result was that the efficiency should not change. It did change, though, because if the particle is directed downward, it will hit the inner boundary regardless of the initial velocity setting. Therefore, increasing the downward velocity of such particles did not increase the loss to the inner boundary. However, some particles directed upward could be redirected downward by gravity or electric field forcing. An increase in upward velocity will act to overcome any downward force and help those particles escape. Therefore, it is actually natural to expect that an increase in the magnitude of the velocity, whatever its vector direction, will result in a preferential increase in the escape rate.

Varying the density used to initialize the ionospheric outflow only changes the local upflowing number flux. This has the effect of changing the production rate but not the eventual trajectories of the test particles from this source term. Therefore, the escape efficiency is exactly the same for any setting of the initial density. However, the total production rate is directly proportional to this initial condition parameter, and therefore an increase of an order of magnitude in all of the local MHD density values yields an IO escape rate that is very similar to the total escape from the three high-altitude ionization processes.

Taking all of the results in Table 6.1 together, it shows that ionospheric outflow could be a comparable or even dominant contributor to O^+ escape relative to the high-altitude sources, but only if the density or velocity of the upflowing ions is dramatically enhanced from that calculated by the MHD model. Temperature might have a similar influence as velocity, but the parameter regime explored in this study (which was the extrema of the MHD values) wasn't enough to have much of an influence on the escape of ionospheric outflow to deep space.

The question arises as to how the density or bulk flow speed of the planetary ions could be significantly higher than the values calculated by the MHD model. The general answer is: processes not included in the MHD equation set. For instance, the MHD simulations were conducted with time-independent solar wind conditions and driven until a steady-state solution was obtained. Therefore, any transient features caused by a changing solar wind dynamic pressure or IMF are not included in the background fields for the MTP calculations. These might include Kelvin-Helmholz instabilities or reconnected magnetic plasmoids leading to temporary and localized increases in ionospheric outflow. *Brain et al.* (2010b) estimated this effect at perhaps 10% of the total escape ion escape rate at Mars. Another possibility is the presence of wave-particle interactions, preferentially heating and/or accelerating planetary ions in the topside ionosphere. Such terms are not included in the MHD results but could pose a substantial modification to the O^+ density or velocity near 300 km altitude. Espley et al. [2004] found ion cyclotron waves in the ionosphere, and *Ergun et al.* (2006) postulated that this could be a significant energy source for the planetary ions. Finally, parallel electric fields could also lead to significant O^+ energization at these altitudes. *Brain et al.* (2006) noted electron beams into the ionosphere, implying the presence of field-aligned electric potential differences, and *Lundin et al.* (2006) observed streaming planetary ions colocated with downward electron beams, indicating that such parallel electric fields are important for ion dynamics.

A caveat to remember when considering the results of the IO parameter study is that, for these simulations, the source terms are intentionally set to different values than those used in the MHD model. That is, the same background electric and magnetic field is used for all of the MTP simulations, regardless of the IO settings. This inconsistency is an issue for all test particle simulations, of course; the motion of the particles could be different from that of the model supplying the background electric and magnetic fields, and this difference could lead to significant changes in density or weighted velocity and therefore a non-negligible change in the electric and magnetic fields. The parameter study simulations conducted here add another inconsistency to the test particle results in that the particle source is also modified from that used to calculate the background fields. *Curry et al.* (2012) addressed this for the MTP model and found that the species-weighted velocity, which enters into the magnetic induction equation in the MHD model, is very close to the MHD velocity everywhere except in two places: the polar plume and the central tail region. In the plume, the difference is small, with a velocity modification of 10%. In the central tail, the difference can be large but this is because the velocity is relatively small (as the velocity approaches zero, the ratio of the velocities dramatically increases). Curry et al. [2013b] illustrated electromagnetic field differences in the dayside sheath between solar maximum and solar minimum conditions. While the two solar cycle MHD results yielded different flight trajectories of sheath-origin pick-up ions, the magnitude of the changes to the electric and magnetic fields were relatively minor. The changes to the ionospheric outflow initialization, especially when the velocity or density is increased by a factor of ten, could lead to substantial changes to the fields through which they are moving. While this means that the results are inconsistent, they are still valuable because they elucidate the general relationship between the fluid parameters near 300 km and the eventual escape of O^+ from Mars.

The results for the simulations with ionospheric outflow defined at different altitude source shells (rather than at the inner boundary of the MTP code) showed that the IO production rate significantly increased as the source shell increased with altitude. This implies that there is an ionization source within the 300-400 km altitude range and defining the IO boundary condition above 300 km double counts this source term because production in this altitude range is also included in the high-altitude ionization mechanisms within the MTP. This altitude range is above the nominal ionosphere, which is typically defined to be coexistent with the thermosphere below the exobase. Therefore, production at these altitudes should be considered as part of the high-altitude source term rather than ionospheric outflow.

A point of clarification is that the MTP inner boundary of 300 km is not necessarily the ionospheric boundary. For this study, however, all ions produced below the MTP inner boundary are given the label "ionospheric" and the flux through this inner boundary is label "ionospheric outflow." It should be noted that this is not a definition used in every study. *Ma et al.* (2004), the study from which the MHD results for the present study were taken, found that planetary ions dominate the charged particle density up to 500 km at solar maximum and 300 km at solar minimum (that is, this is the ion composition boundary, as determined from the simulation). They called this transition the upper boundary of the ionosphere. Others have called this transition the ion composition boundary, identified in both Phobos-2 and Mars Express measurements [e.g., Breus et al., 1991; Sauer et al., 1994; FrŁnz et al., 2006; Boesswetter et al., 2007]. There observational studies give a range for this transition, up to altitudes of 1000 km. This switch from planetary ion dominance to solar wind ion dominance of the density does not have to coincide with the "top" of the ionosphere. At Earth, the ionosphere is often limited to same altitude range as the thermosphere (that is, up to the exobase). Even though planetary ions can dominate the density at much higher altitudes than this, the name given to the region is changed because the dominant physical processes are different. Specifically, names like plasmasphere, auroral outflow region, and polar wind are used for the geospace regions dominated by planetary ions above the ionosphere. A generic term for this boundary between planetary and solar wind density dominance is the geopause, coined by Moore and Delcourt [1995]. While there exists some ambiguity and even confusion in naming particles and regions of space, the definition used here is that the ionosphere is coincident with the thermosphere and therefore ends with the exobase.

The solar minimum results were considerably different from those at solar maximum. The IO source increased in significance as a factor in ion escape, supplying a quarter of the total loss rate and therefore being comparable to each of the three high-altitude source processes as an originator of escaping O^+ ions. In addition, there were some notable differences in the spatial patterns of the escaping number flux and average energy of the IO particles at the 4 R_M shell. These differences can be explained by the change in the near-Mars electric field. A higher percentage of the IO source is allowed to penetrate through the magnetic pileup region and experience the large electric fields of the dayside magnetosheath. In the southern MSE hemisphere, such particles are subjected to this field and are accelerated northward into the central tail region, creating the halo of low flux but high-energy particles in Figures 6.7a and 6.8a. Note, however, that the inner boundary of the MTP simulation, and therefore the initialization altitude for ionospheric outflow, is the same for the solar maximum and minimum simulations. If the inner boundary is lowered for solar minimum to an altitude just above the exobase (say, for example, down to 250 or even 200 km), then the solar minimum IO escape efficiency might drop significantly. That is, this increased efficiency at solar minimum could be a function of initialization altitude.

6.4 Conclusions

Simulations were conducted of O^+ transport in the Mars space environment to investigate the relative contributions of ionospheric outflow to ion transport and escape. Using the combined results of an MHD model and a test particle code, high-altitude velocity space distributions and spatial patterns of escape were examined for both an IO source population (taken at 300 km altitude) and high-altitude source populations (from photoionization, charge exchange, and impact ionization above 300 km altitude).

It was found that ionospheric outflow, as defined in our simulation configuration, is a rather small contributor to the total escape of O^+. High-altitude ionization processes significantly contribute to ion loss at Mars, providing 90% of the total O^+ loss, with O^+ leakage from below 300 km contributing an order of magnitude less. At high altitudes, ionospheric outflow is defined by several key features in velocity space, most notably a focused beam in flight direction in a narrow region of space (compared to the high-altitude sources). The energy of ionospheric outflow changes dramatically depending on the pathway of escape; those that leave down the central tail are preferentially at low energies while those escaping via the polar plume are at relatively high energies.

A series of MTP simulations were conducted that systematically varied the initial conditions for ionospheric outflow (keeping the high-altitude sources and the background fields the same). It was shown that ionospheric outflow can become significant, and even dominant, if the initialization density and/or velocity is substantially increased over the nominal MHD values extracted at 300 km. This implies that ionospheric outflow could be very important if processes not included in the MHD simulation are able to alter the O^+ characteristics in the topside ionosphere. For instance, this extra energization or density enhancement process could be wave-particle interactions, parallel electric fields, large-scale turbulence (i.e., Kelvin-Helmholz oscillations), or solar wind-crustal field magnetic reconnection. These processes will preferentially influence the ionospheric outflow and escape rate relative to the high-altitude production processes, thus changing the proportion of the total loss that is attributable to lower-altitude ionization.

Finally, solar minimum conditions were also explored and found to be similar to those at solar maximum in terms of the distribution and overall features of the O^+ lost to deep space. However, the escape efficiency dramatically increases at solar minimum and ionospheric outflow can contribute a roughly equal portion to the total loss rate as each of the three high-altitude source terms.

CHAPTER VII

Multi-species high altitude ion simulations

This study focuses on using the Mars Test Particle simulation to create virtual detections of O^+, O_2^+ and CO_2^+ in an orbital configuration in the Mars space environment. These planetary pick-up ions are formed when the solar wind directly interacts with the neutral atmosphere, causing the ions to be accelerated by the background convective electric field. The subsequent mass loading and ion escape are still the subject of great interest, specifically with respect to which species dominates ion loss from Mars. This study presents energy-time spectrograms constructed from velocity space distributions for the different species from a virtual detector in an orbit around Mars. O^+ is found to be the dominant escaping ion due to its low energy (<10 eV) and high energy (>1 keV) source of transported ions. O_2^+ and CO_2^+ are only observed at these energy ranges with much lower fluxes and are generally only found in the tail between (10 eV - 1 keV). Using individual particle traces, we reveal the origin and trajectories of low energy downtail O^+ populations and high energy polar O^+ populations. Comparing them against O_2^+ and CO_2^+ reveals that the extended hot oxygen corona contributes to source regions of high and low energy accelerated ions. Additionally, we present results from different solar conditions with respect to ion fluxes and energies as well as overall escape in order to robustly describe the physical processes controlling planetary ion distributions and atmospheric escape.

7.1 Approach

In an investigation of heavy pickup ions at Mars, a test particle approach is well suited to account for the effects of the finite gyroradii on a planetary scale size. The Mars Test Particle (MTP) simulation is a collisionless test particle simulation that follows the trajectories of particles of any atomic weight through the Mars space environment. Because the model is collisionless and not self-consistent, background fields for the bulk velocity, electric and magnetic field lines, and steady state low altitude ions are necessary. The MTP uses the results of the *Ma et al.* (2004) study at solar maximum (Case 1), described below. It should be noted that the test particle approach is valid when the difference in the velocity and density are small in comparison with MHD velocities and densities used to generate the background electric and magnetic fields.

7.1.1 MHD Model

The background magnetic field, bulk plasma velocity and ion densities used in the test particle model are provided by the steady state results from the *Ma et al.* (2004) MHD study during solar maximum. *Ma et al.* (2004) does not include the Hall or polarization electric fields and calculates the background convective electric field from $\mathbf{E}$=-$\mathbf{U}\times\mathbf{B}$.

The simulation uses a local interplanetary magnetic field (IMF) configuration corresponding to a Parker spiral structure in the XY plane at an angle of 56 degrees (away sector). The IMF magnetic field strength is 3 nT and the solar wind velocity and density were set at 400 km/sec and 4 cm^{-3}. Figure 7.1 illustrates the XY plane of the steady state solution for the magnetic field and bulk flow velocity (left and right respectively).

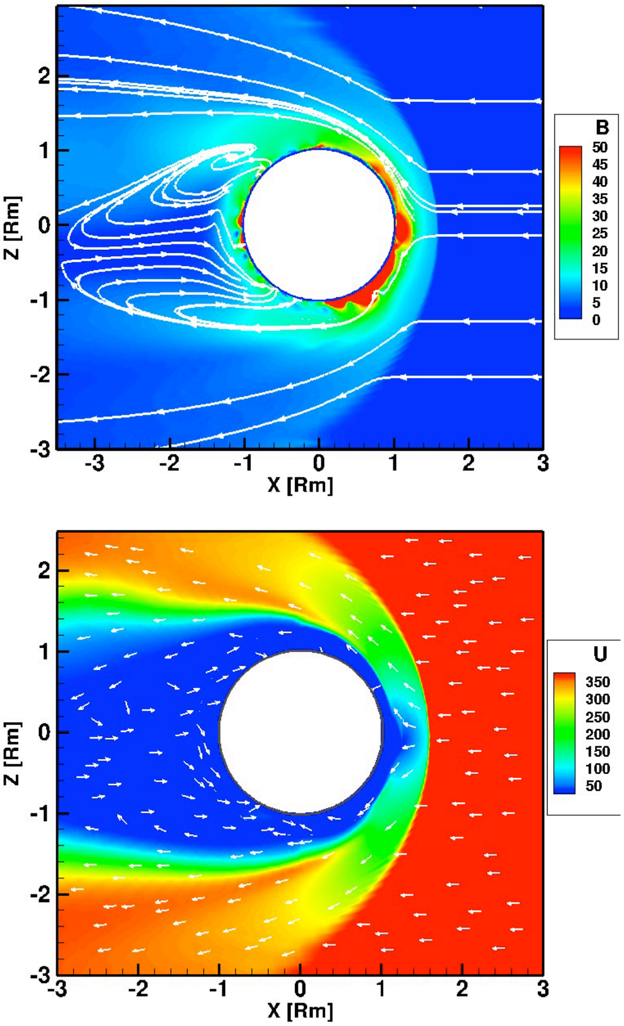

Figure 7.1: The background MHD magnetic field (top) and bulk velocity (bottom) in the equatorial plane for case 1. The colorbar show the magnitudes; the white lines marked with arrows indicate the vector direction of the magnetic field and the arrows show the direction (not the magnitude) of the velocity.

7.1.2 Mars Test Particle (MTP) simulation

The main approach for this study is the MTP simulation, the 3-D Monte Carlo model that randomly assigns the particles' initial position, energy and direction. This model is discussed in detail in Chapter III and *Fang et al.* (2008). Gravity was included and plays an important role in ion motion with the heavier species *Fang et al.* (2010a). Each step includes gravity so the individual ion motion combines a gyration around the magnetic field, the **E**×**B** drift, and the gravitational force towards the planet :

$$\frac{d\mathbf{v}}{dt} = \frac{q}{m}\left(\mathbf{E} + \mathbf{v} \times \mathbf{B}\right) - \mathbf{G}\hat{\mathbf{r}} \tag{7.1}$$

$$\tag{7.2}$$

where **v** is the velocity vector, q is the charge of an electron, m_s is the mass of the species, **E** is the convective electric field, **B** is the magnetic field, G is the universal gravitational constant, and M_M is the mass of Mars.

The MTP used over 8 billion test particles for this simulation, whose angular distribution, energy and velocity are recorded at virtual detectors and constructed into velocity space distributions. The virtual detectors can be placed anywhere in the simulation in order to record the flux, position and flight direction of the particles (see Appendix B.1).

For this study, the MTP uses a spherically symmetric neutral atmosphere based on the parameters from *Bougher and Engel* (2000) where H, O, and CO_2 dioxide were the main constituents. The neutral oxygen and hydrogen corona consist of a thermal and hot component based off of *Bougher et al.* (2004); *Chaufray et al.* (2007); *Bougher et al.* (2008); *Valeille et al.* (2010). The hydrogen profile was based on rates from *Fox* (2003) and the temperature-dependent oxygen densities used the calculations of *Kim* *et al.* (1998) (corona vs O and H). Additional CO_2 densities at solar maximum were based on the model results from *Bougher and Engel* (2000) and Mariner 6 and 7 observations (*Ma et al.*, 2004).

The neutral temperature is defined by equation 7.3 and based on the *Brain et al.* (2010a) global model comparison input conditions. The initial energy and velocity distribution for the particles is a Maxwellian centered on the neutral temperature, as seen in equation 7.3.

$$T_N = -64.56e^{-0.5*((z-115.7)/20.14)^2} + 196.95 \tag{7.3}$$
$$V_0 = \sqrt{\frac{2E}{m_s}}$$

where T_N is the neutral temperature, z is the height, $V_0$is the initial velocity, E is the initial energy and m_s is the atomic mass of the species. It should be noted 2 eV is added to the initial energy which *Fang et al.* (2010b) found may be due to partially reflective of different initial ion heating (*Ergun et al.*, 2006).

In this study, the MTP simulation records the particles' trajectory and velocity with virtual detectors which have been placed in an orbit based on the June 2007 Mars Express (MEX) orbit, sampling at the half the duty cycle.

7.2 Ion Production Schemes

The ion species and reactions included in this simulation are based on the neutral density profiles of *Bougher and Engel* (2000); *Schunk and Nagy* (2000); *Fox and Sung* (2001); *Martinis et al.* (2003); *Bougher et al.* (2008); *Fox* (2009), which are listed in Table 7.1. Nitrogen and Helium were not included because their neutral density profiles are comparatively small above 300 km. Additionally, dissociative recombination was not included for any source because the MTP simulation follows

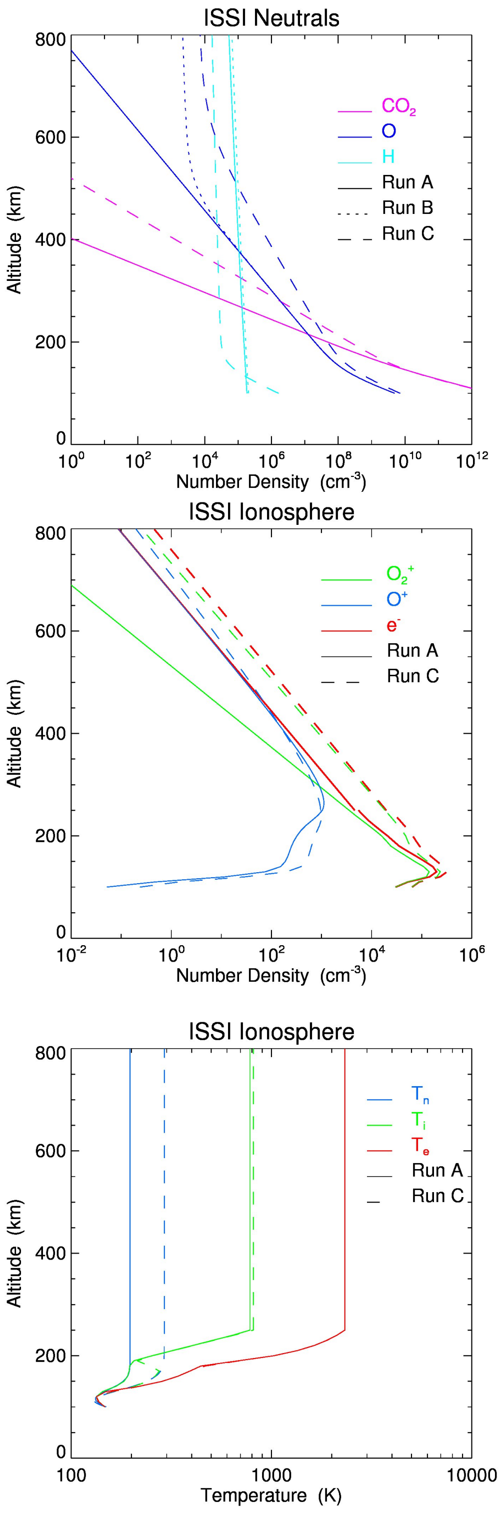

Figure 7.2: Top: The neutral atmosphere based on the ISSI Mars group study parameters for CO$_2$, O and H for Cases A, B and C for density versus altitude. Middle: the ionospheric profile for O$^+$, O$_2^+$ and e^- for Cases A-B and C. Bottom: the temperatures of the neutrals, ions and electrons for Cases A-B and C.

only ion species and the neutral atmosphere is assumed to be in equilibrium. Three physical processes are included in the MTP for ion production: photoionization, charge exchange and electron impact.

The first process for ion production is photoionization without solar zenith angle dependence, as seen in Equation 7.4 and 7.5. S represents any of the neutrals that will be ionized and traced throughout the simulation (O, O_2 or CO_2). This ionization process uses a constant reaction rate except in the cylindrical optical shadow behind the planet (the nightside) because the simulation has a lower boundary of 300 km, where the atmosphere is already optically thin. The photoionization factor, f, is therefore 1 everywhere except this optical shadow, where it would be 0. As a point of reference, the optical depth reaches a maximum at the X point with a value of X $\times 10^{-3}$.

$$\begin{aligned} S + hv \rightarrow & S^+ + e^- \\ f = & \begin{cases} 0 & \text{if } y^2 + z^2 < 1 \text{ and } x < 0 \\ 1 & \text{elsewhere} \end{cases} \end{aligned} \tag{7.4}$$

$$k_1 = f \times \text{constant}(S)\ \text{sec}^{-1} \tag{7.5}$$

For charge exchange, two reactions produce O^+. The first reaction is through $CO_2^+ + O \rightarrow CO_2 + O^+$, with a constant production rate of 9.6×10^{-11} cm^{-3} sec^{-1}. The second charge exchange reaction is based on the collision of solar wind protons and atomic oxygen $H^+ + O \rightarrow H + O^+$. The reaction rate here (k_{ch}, cm^2/sec) is proportional to the local bulk flow speed (v_{bulk}, km/sec) and the ionization cross section for $H^+ - O$ reaction (σ, cm^2), as seen in equation 5.1. As described above, the production rate for the second reaction is the product of the neutral oxygen density, the proton density, the cell volume and the reaction rate (k_{ch}).

The charge exchange process, described at length in *Curry et al.* (2012), includes two reactions for O^+ production: 1) charge exchange between solar wind protons and a neutral species and 2) charge exchange between an ion and a neutral species (the species are again denoted by S). This first type of charge exchange describes how the neutrals in the corona will experience a collision with the solar wind protons. Because the bulk velocity of the solar wind transitions from super sonic to subsonic, energy is transferred to the particles random velocity. The reaction rate can be described by multiplying the $H^+{-}S$ cross section, σ, by the total velocity, v_{total}, in each cell. Equations 7.6-7.8 denote the total velocity as the combination of the bulk velocity and the random velocity. T_e is assumed to be half the plasma temperature from the MHD results.

The second charge exchange rate characterizes the collision between an ion and a cold planetary neutral species. For example, the reaction $CO_2^+ + O \rightarrow CO_2 + O^+$ is when a planetary CO_2^+ ion and O coronal atom exchange an electron and can be described with a constant, non-temperature dependent reaction rate of 9.60×10^{-11} $\text{cm}^{-3}\text{sec}^{-1}$.

$$S + H_{SW}^+ \rightarrow S^+ + H_{SW}$$

$$v_{random} = \sqrt{\frac{2kT_e}{m}} \tag{7.6}$$

$$v_{bulk} = \sqrt{U_x^2 + U_y^2 + U_z^2} \tag{7.7}$$

$$v_{total} = \sqrt{v_{random}^2 + v_{bulk}^2} \tag{7.8}$$

$$k_2 = v_{total} \times 10^{-15}\ \text{cm}^3\text{sec}^{-1} \tag{7.9}$$

$$S_1 + S_2^+ \rightarrow S_1^+ + S_2$$

$$k_2 = \text{constant}(S)\ \text{cm}^3\text{sec}^{-1} \tag{7.10}$$

The final ionization process is electron impact ionization, which uses electron temperature dependent rates based on the schema for impact ionization from *Cravens et al.* (1987), as seen in equation 7.11.

$$
\begin{aligned}
S + e^- \rightarrow S^+ + e^- + e^- \\
k_3 = F_C(T_E) \text{ cm}^3 \text{ sec}^{-1}
\end{aligned} \tag{7.11}
$$

7.2.1 Ionospheric Source

In addition to the three ionization processes discussed above, an additional source of ions is included in the simulation: ionospheric outflow. The MTP simulation does not include the ionosphere due to the inner boundary at 300 km, but the MHD model used for the background fields begins at 100 km and uses 10 km grid resolution. Thus the number flux at 300 km represents the ionospheric outflow from 100 to 300 km in the MHD simulation. Figure 7.3 illustrates this flux from the MHD model for the O^+, CO_2^+ and O_2^+ species.

This flux is injected into the simulation at 300 km and treated as a fourth ion source carrying its own weighting per particle. The particles launched as an ionospheric outflow source have an initial energy Maxwellian now centered around the local ion temperature (where $T_i = 1/2T_p$) as opposed to a Maxwellian centered around the neutral temperature. Their initial velocity is also that of the local bulk velocity.

Each particle carries a weight determined by the total ion production per cell divided by the total number of test particles per unit time. The ion production for each species is listed in equations 7.12-7.15 where N is the ion production in ions/sec, k is the reaction rate in $\text{cm}^{-3}\text{sec}^{-1}$ (except The weight is for each independent species so the individual particle weight is per ionization source and per species, as seen in

Table 7.1: Chemical reaction rates

Chemical reaction	Rate Coefficient ($cm^3 sec^{-1}$)	Reference
Photoionization		
$CO_2 + h\nu \rightarrow CO_2^+ + e$	$k = 7.30 \times 10^{-7}$	(*Schunk and Nagy*, 2000)
$CO_2 + h\nu \rightarrow O^+ + CO + e$	$k = 7.40 \times 10^{-8}$	(*Schunk and Nagy*, 2000)
$O + h\nu \rightarrow O^+ + e$	$k = 2.73 \times 10^{-7}$	(*Schunk and Nagy*, 2000)
$H + h\nu \rightarrow H^+ + e$	$k = 8.59 \times 10^{-8}$	(*Ma et al.*, 2004)
Charge exchange		
$CO_2^+ + O \rightarrow CO_2 + O^+$	$k = 9.60 \times 10^{-11}$	(*Schunk and Nagy*, 2000)
$H^+ + O \rightarrow H + O^+$	$k = v_{total}\ (1 \times 10^{-15})$	Curry et al. 2012 [1]
$H^+ + CO_2 \rightarrow H + CO_2^+$	$k = v_{total}\ (2 \times 10^{-15})$	Curry et al. 2012 [1]
$O^+ + H \rightarrow O + H^+$	$k = 6.40 \times 10^{-10}$	(*Fox and Sung*, 2001)
$CO_2^+ + H \rightarrow CO_2 + H^+$	$k = 2.35 \times 10^{-11}$	(*Fox and Sung*, 2001)
$H^+ + H \rightarrow H + H^+$	$k = v_{total}\ (2.5 \times 10^{-15})$	Curry et al. 2012 [1]
$H^+ + O_2 \rightarrow H + O_2^+$	$k = v_{total}\ (2 \times 10^{-15})$	Curry et al. 2012 [1]
$CO_2^+ + O \rightarrow CO + O_2^+$	$k = 1.64 \times 10^{-10}$	(*Fox and Sung*, 2001)
$CO_2^+ + O_2 \rightarrow CO_2 + O_2^+$	$k = 5.50 \times 10^{-11} (300/T_i)^{0.82}$	(*Fox and Sung*, 2001)
	for $T_i \leq 1500K$	
	$1.50 \times 10^{-11} (T_i/1500)^{0.75}$	
	for $T_i > 1500K$	
$O^+ + O_2 \rightarrow O + O_2^+$	$k = 1.60 \times 10^{-11} (300/T_i)^{0.52}$	(*Fox and Sung*, 2001)
	for $T_i \leq 900K$	
	$9.00 \times 10^{-12} (T/900)^{0.92}$	
	for $T_i > 900K$	
$O^+ + CO_2 \rightarrow CO + O_2^+$	$k = 1.10 \times 10^{-9}$	(*Fox and Sung*, 2001)
	for $T_i \leq 800K$	
	$1.10 \times 10^{-9} (T_i/800)^{-0.39}$	
	for $T_i > 800K$	
Electron Impact		
$CO_2 + e \rightarrow O^+ + e + e$	table lookup	(*Cravens et al.*, 1987)
$O + e \rightarrow O^+ + e + e$	table lookup	(*Cravens et al.*, 1987)
$H + e \rightarrow O^+ + e + e$	table lookup	(*Cravens et al.*, 1987)

[1] charge exchange using bulk and random velocity (hot neutrals)

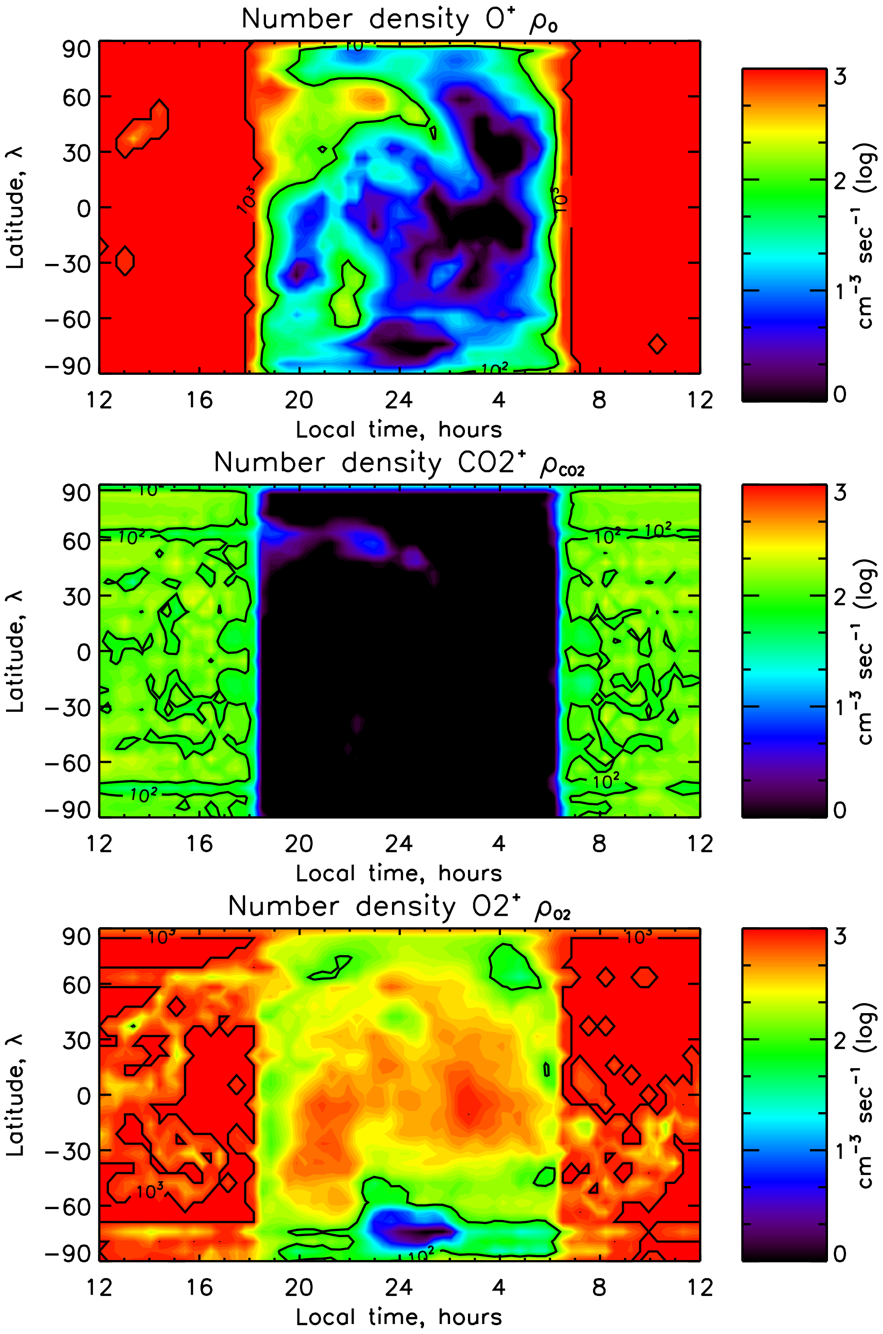

Figure 7.3: The ion flux coming through the 300 km boundary from the *Ma et al.* (2004) MHD simulation. The top panel is O^+, the middle panel is CO_2^+ and the bottom panel is O_2^+. The colorbar is a log scale of the number density flux ($cm^{-2}sec^{-1}$) and the axes represent local time (in hours, where noon is the subsolar point) and the latitude (in degrees, where 0° is the equatorial plane) of the flux coming through the 300 km boundary shell. The contours are for 10^2 - 10^3.

equation 7.16.

$$N_{ph} = f \cdot k_1 \cdot \rho_s \cdot V \tag{7.12}$$

$$N_{ch} = k_2 \cdot \rho_H \cdot \rho_s \cdot V \tag{7.13}$$

$$N_{ei} = k_3 \cdot \rho_e \cdot \rho_s \cdot V \tag{7.14}$$

$$N_{io} = v_{bulk} \cdot \rho_{ion} \cdot A \tag{7.15}$$

$$W_{ij} = N_{ij}/N_{total} \tag{7.16}$$

where i is the species (O^+, CO_2^+ and O_2^+) and j is the ionization source (ph→photoionization, ch→charge exchange, ei→electron impact, io→ionospheric outflow).

7.3 Results

7.3.1 Energy Time Spectrograms

The MTP simulation traced the ion trajectories of O^+, CO_2^+ and O_2^+ by recording the flux, energy and flight direction of each particle that passed through virtual detectors placed in an orbit around Mars. The orbit takes roughly 6.5 hours and the detector moves counterclockwise around the planet in the XZ plane if the sun is to the right. Figure 7.4 illustrates the orbit configuration of the virtual detectors in the XY, XZ, and YZ planes as well as the distance from the planet (km). The virtual detector begins the orbit in the tail region and passes under the planet as it approaches periapsis at 2.4 hours. The detector then passes across the induced magnetic boundary (IMB) at 2.7 hours and into the sheath region from roughly 2.7 - 5.9 hours, which is marked with the dashed lines. Finally, the detector crosses back over the IMB at 5.9 hours and into the tail region again from 5.9 - 6.5 hours.

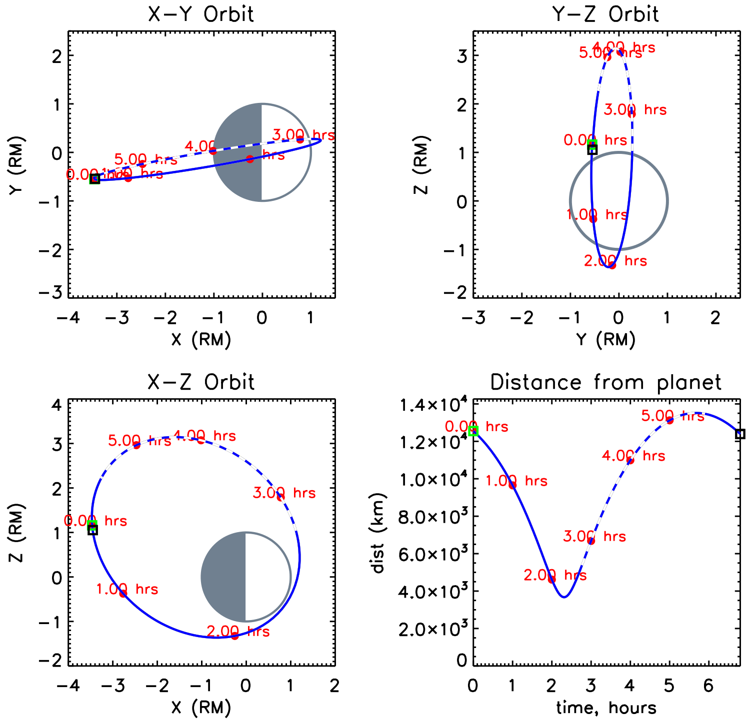

Figure 7.4: The orbit of the virtual detectors which are placed inside of the MTP simulation. The planes are the XY, XZ and YZ planes (left top and bottom, right top panels respectively) in units of R$_M$. The right bottom panel is the distance from the planets in kilometers. The red time stamps denote the time of the when the virtual detector was located in the given orbit and over 200 measurements are taken over this time. The green square denotes the beginning of the orbit and the black square denotes the end. The blue dashed sector of the orbit denotes when it is in the induced magnetosheath region.

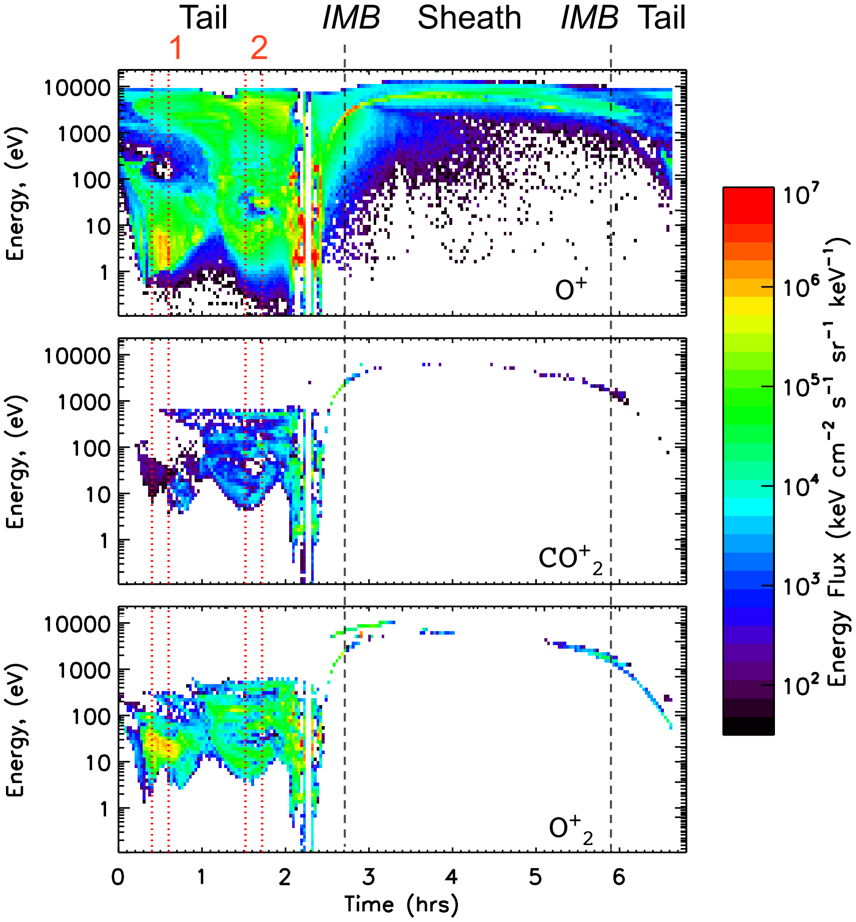

Figure 7.5: An energy-time spectrogram of O^+, CO_2^+ and O_2^+ are plotted on the top, middle and bottom panels respectively as a function of differential energy flux (keV $cm^{-2}s^{-1}sr^{-1}keV^{-1}$) for time versus energy. The IMB, which separates the sheath from the tail region, was estimated by *Lundin et al.* (2011a) and is marked with dashed black lines. The red dotted lines around 0.5 hours and 1.6 hours signify two regions of interest that will be discussed in the following sections.

An energy time spectrogram (ETS) can be constructed using the measurements from the virtual detectors, as seen in Figure 7.5, which describes the response of the pick-up ions to the **E**×**B** drift in Mars plasma environment (*Hartle et al.*, 2011). The IMB separates the sheath from the tail region and is marked with the dashed black lines estimated by *Lundin et al.* (2011a). O^+, CO_2^+ and O_2^+ are plotted on the top, middle and bottom panels respectively as a function of differential energy flux (keV $cm^{-2}s^{-1}sr^{-1}keV^{-1}$) for time versus energy.

Much of the pickup ion transport can be seen in the tail from 0 - 2.5 hours. It is immediately evident that the O^+ ions are observed at all energy ranges, especially above 1 keV, while the CO_2^+ and O_2^+ ions are observed in much narrower energy ranges. The O^+ ion observations are especially unique in the high flux regions occurring at periapsis around 2.4 hours.

As the detector moves into the dayside region from 2 to 3 hours, all three species exhibit high energy populations above 1 keV, particularly as the detector crosses the IMB and enters into the induced sheath region at ∼2.7 hours (dashed black lines). The detectors in the sheath, the region denoted in Figure 7.4 by the dashed blue and white line, observe 1 - 10 keV energies for each ion species because the convective electric field is pointing upward and tailward ($+Z_{MSO}$, $-X_{MSO}$), which accelerates the ions much further distances.

Finally the detector reaches its apoapsis at roughly 5.6 hours and enters back into the tail region at 5.9 hours. As the detector enters the tail, the observed ions lose energy and approach 100 eV again.

7.3.2 Tailward ion transport

The velocity space at a given point in the orbit is an important indicator of 1) the detailed transport and escape of the ions at that location as well as 2) how different ion species are locally accelerated. Figure 7.6 illustrates the downtail VSDs of O^+,

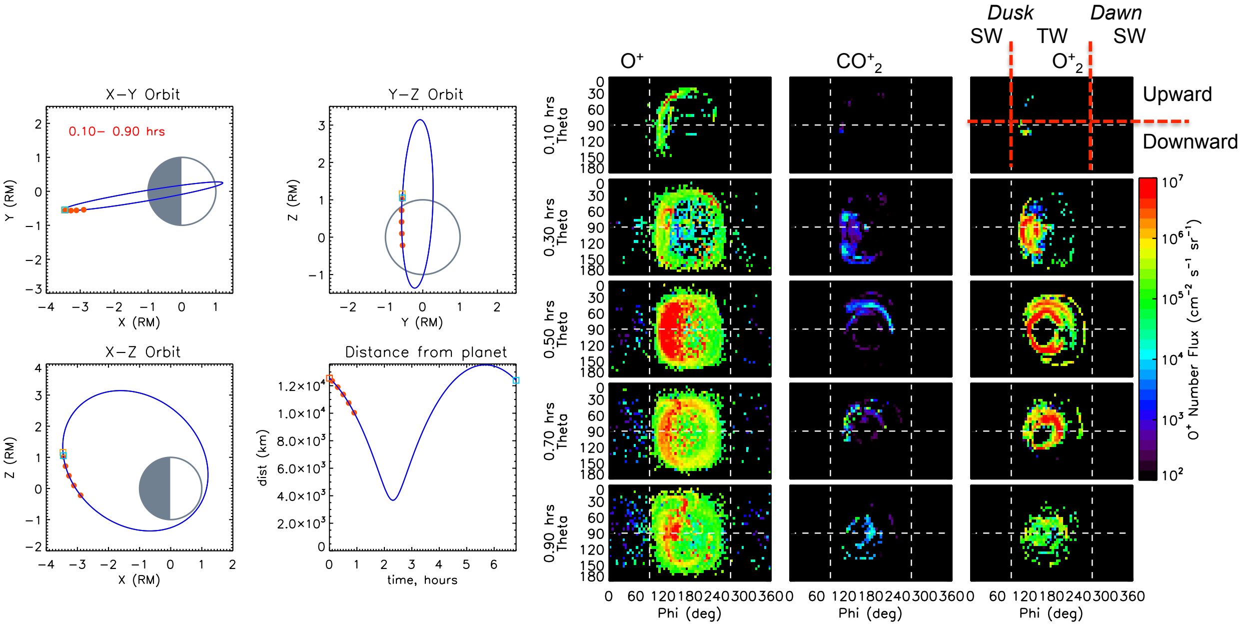

Figure 7.6: The left figure illustrates where the virtual detector was in the orbit with a red dot in the XY, XZ, and YZ planes (in R$_M$) from 0.1 - 0.9 hours in the energy-time spectrogram. In the right figure, velocity space distributions for O$^+$, CO$_2^+$ and O$_2^+$ are plotted and labeled on the top, middle and bottom panels respectively for each location from 0.1-0.9 hours (top to bottom). The velocity space distributions illustrate the ions integrated from 0-25 keV.

CO_2^+ and O_2^+ from from 0.1 - 0.9 hours, corresponding to the red dots along the orbit in the left figure.

Beginning with the trends in the downtail transport of the ions, the virtual detector moves through an area of high flux ions, peaking at roughly 0.5 hours. Initially at 0.1 - 0.3 hours, the detector observes flux mostly at 10^3 - 10^5 $cm^{-2}s^{-1}sr^{-1}$ and then observes an increase in flux for all species at 0.5 hours. Note that the virtual detector is still above the equatorial plane ($Z_{MSO} > 0$) and observes peak fluxes here because the convective electric field points upward and tailward ($+Z_{MSO}$, $-X_{MSO}$), which transports ions from the southern hemisphere upward and tailward into to the northern hemisphere. As the detector approaches $Z_{MSO} = 0$ and passes through the equatorial plane (0.7 - 0.9 hours), the observed flux decreases again.

The VSDs also illustrate a clear trend in the acceleration of different ion species. The O^+ dominates the flux downtail with counts from 10^5 - 10^7 $cm^{-2}s^{-1}sr^{-1}$. The CO_2^+ ions contribute the least flux, which is observed three orders of magnitude lower at 10^3 - 10^4 $cm^{-2}s^{-1}sr^{-1}$, but has VSD signatures that closely resemble O_2^+. This similarity in the CO_2^+ and O_2^+ signatures is a result of the lower altitude, cold neutral source of the ions ($\leq$500 km) and heavier atomic mass. The oxygen species on the other hand has a hot neutral corona due to dissociative recombination and sputtering (*Fox and Ha*, 1997; *Nagy et al.*, 2004; *Chaufray et al.*, 2007; *Cipriani et al.*, 2007; *Barabash and Holmstrom*, 2002; *Valeille et al.*, 2009) which gives it a high altitude source of O^+ ($\geq$500 km). This hot oxygen corona at Mars plays an important role in the VSDs, as discussed in depth in Chapter V.

While each species exhibits the trend of increased flux as the detector moves through the tail, the velocity space signatures vary. Because the ions are accelerated tailward, most of the downtail VSD signatures have a flight direction centered around ϕ=180° and θ=90°, but each species has distinct asymmetries. O^+ is detected at a much broader range of flight directions, which is to say that O^+ has much more flight

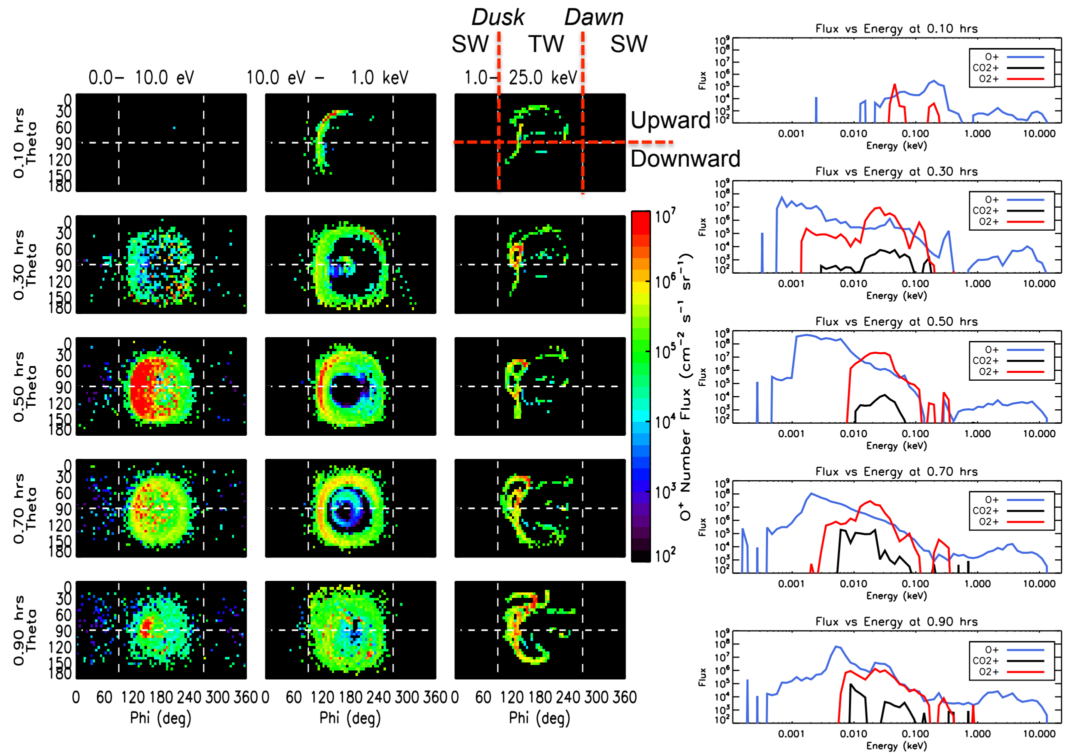

Figure 7.7: The left figure illustrates O^+ velocity space distributions illustrate from 0.1 - 0.9 hours for three energy ranges: low: 0 - 10 eV, medium: 10 eV- 1 keV, and high: 1 - 25 keV. The right panel illustrates the flux versus energy signatures O^+, CO_2^+ and O_2^+ at the same locations.

direction coverage than the heavier planetary species. We adopt the phrase *flight direction coverage* to describe how much flux the detector observes at each angle (i.e. how much or little empty space there is for a given virtual detection). This is especially visible at 0.5 hours with enhanced flux at a flight direction near dusk, ϕ=90-180°. In addition to flight direction asymmetries, the energy ranges are distinct. Referring back to Figure 7.5 at 0.5 hours (the first area of interest marked in dotted red lines), the ETS illustrates the O^+ flux peaks between 1 - 10 eV while O_2^+ peaks between 10 - 100 eV.

Figure 7.7 expands on these same trends and differences by illustrating the corresponding flux as a function of energy for O^+, CO_2^+ and O_2^+ at 0.1 - 0.9 hours on the right and the O^+ velocity space integrated over three energy ranges (low: 0 - 10 eV, medium: 10 eV- 1 keV, and high: 1 - 25 keV) on the left. As seen in Figure 7.6, the fluxes increase as the detector approaches 0.5 hours, then reach a maximum at 0.5 hours, and then decrease from 0.7 - 0.7 hours. From 0.3 - 0.9 hours, the detector observes the peak flux at roughly the same energy: 1 - 2 eV for O^+ and 11 - 12 eV for CO_2^+ and O_2^+. A critical result is this low energy O^+ flux, which dominates its energy spectrum. Although the 10 eV difference in the peak of the fluxes is not dramatic, it is important to consider the energy threshhold of an actual detector. At the peak of 0.5 hours, the total integrated O^+ and O_2^+ flux at the detector is 3.3×10^9 and 1.2×10^8 cm^{-2}s^{-1} respectively, which indicates that O^+ is dominant by over an order of magnitude. But if a detector could only see above 7 eV, the total fluxes would be 1.4×10^5 and 2.5×10^5 cm^{-2}s^{-1} and then O_2^+ would be the dominant species.

Finally, in order to visualize specific signatures in the velocity space and flux-energy for O^+, CO_2^+ and O_2^+, Figure 7.8 displays particle trajectories in MSO coordinates. The left column shows the trajectories of CO_2^+ and O_2^+ in green and blue, respectively, and the right column shows the trajectories of O^+ in red. As discussed earlier, the low energy ion flux with a dusk-ward flight direction dominated the flux, which peaked at 0.5 hours. Here we present the particle trajectories that had an energy below 10 eV and a dusk-ward flight direction ($40° < \theta < 140°$ and $90° < \phi < 120°$). Three quarter, flank and aerial views are shown in order to compare the origin and flight path of these low energy, dusk particles which were accelerated downtail.

The top row, a three quarter view (from the dawn side), best highlights the O^+ ion population originating from the southern polar region ($Z_{MSO} < -2$ R_M). CO_2^+ and O_2^+ have extremely low ion production in this region due to the lack of a high altitude corona in these corresponding neutral species, and thus there are very few ions to accelerate. The middle panel, a flank view from down tail looking sunward, shows that the majority of the ions' origins and flight paths are on the dawn side ($Y_{MSO} < 0$ R_M). This dawn-ward source of ions travels downtail and diagonally cross over what

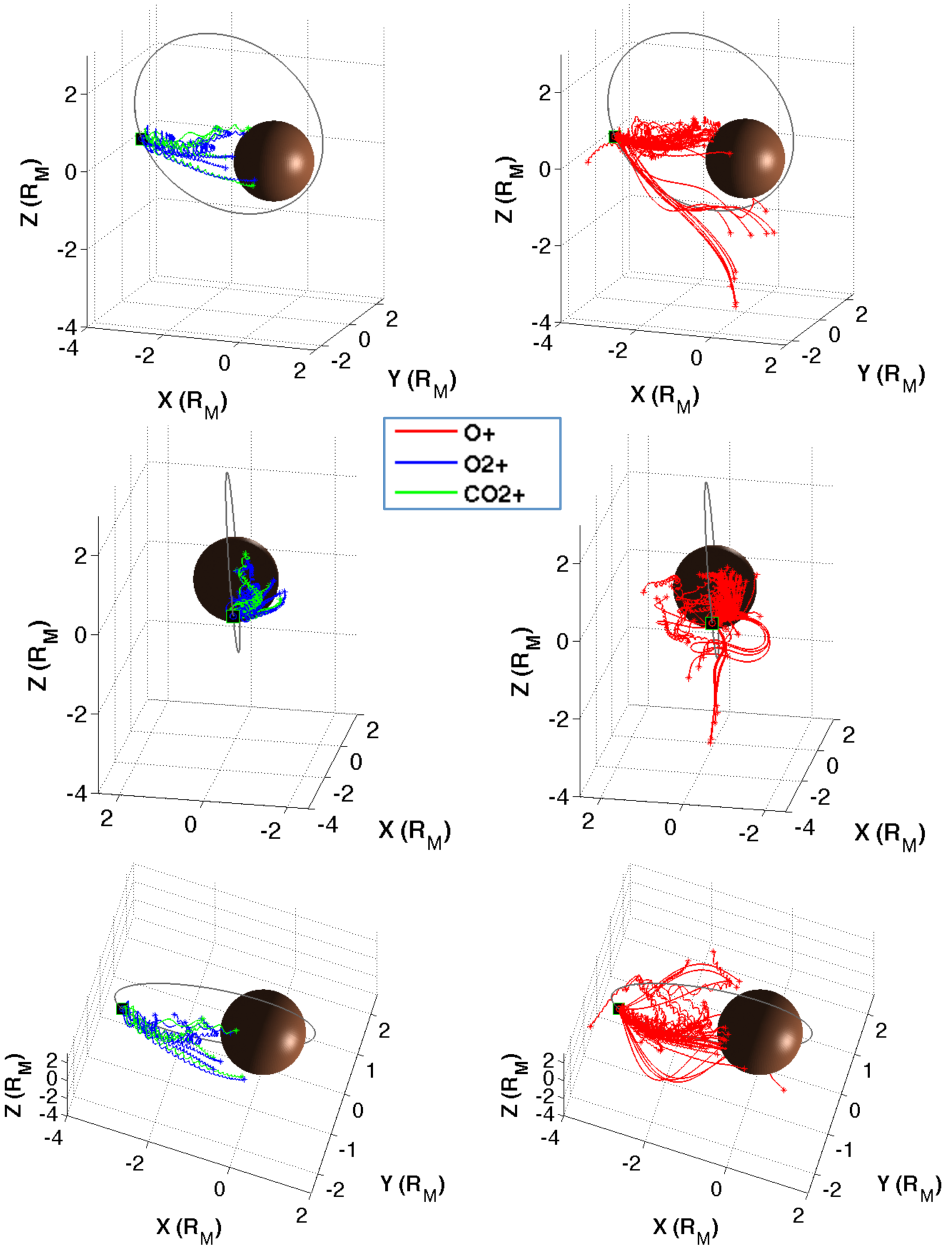

Figure 7.8: The left column shows the trajectories of CO_2^+ and O_2^+ in green and blue, respectively, and the right column shows the trajectories of O^+ in red. Three quarter, flank and aerial views are shown in order to compare the origin of the particles hitting the downtail detector at 0.5 hours.

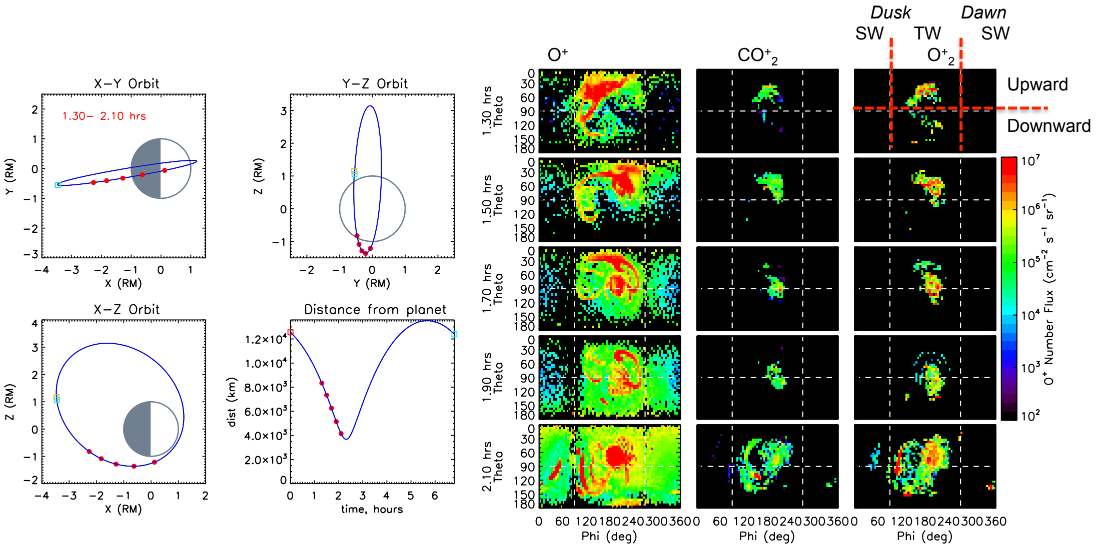

Figure 7.9: The left figure illustrates where the virtual detector was in the orbit with a red dot in the XY, XZ, and YZ planes (in R_M) from 1.3-2.1 hours in the energy-time spectrogram. In the right figure, velocity space distributions for O^+, CO_2^+ and O_2^+ are plotted and labeled on the top, middle and bottom panels respectively for each location from 1.3-2.1 hours (top to bottom). The velocity space distributions illustrate the ions integrated from 0-25 keV.

would be midnight, which gives them a dusk-ward flight direction. These ions are what make up the majority of the low energy, dusk-ward flux dominating the velocity space at 0.5 hours. The bottom panel reinforces this with an aerial view from over the north pole that shows the ions originating near the dawnward side of the planet accelerating and veering toward the midnight plane and hitting the detector with a dusk-ward flight direction. It should be noted that ions originating on the dusk side are also accelerated downtail, but veer with the solar wind magnetic field which is beginning to gain strength as the field lines 'snap' over the planet.

7.3.3 Polar VSDs

The southern polar section of the orbit approaching periapsis is the second area of interest in the ETS, Figure 7.5, and highlights the role of ion transport and escape in regions with a much denser atmosphere. Figure 7.9 illustrates VSDs in this southern polar region for O^+, CO_2^+ and O_2^+, shown with red dots along the orbit in the figure on the left from 1.3 - 2.1 hours. As discussed in the previous section, the velocity space at a given time is indicative of how the planetary ions are being transported and how different species react to the $\mathbf{E}\times\mathbf{B}$ drift as a function of their finite gyroradius.

Figure 7.9 displays a clear trend of increasing flux and flight direction coverage as the detector approaches periapsis and moves closer to the planet. From 1.3 - 1.7 hours, the total flux remains roughly the same for all three species even as the different flux populations change shape in velocity space. But by 2.1 hours, the detector is roughly 650 km from the surface resulting in all three species having high flux concentrations above 10^7 $cm^{-2}s^{-1}sr^{-1}$ and the detector having almost total flight direction coverage for O^+.

While there is a trend for the detector to observe constantly increasing flux for each species as it approaches Mars at 2.1 hours, the detector observes very different velocity space signatures for O^+, CO_2^+ and O_2^+. Unlike the downtail detections, these VSDs are asymmetric and non-gyrotropic. The CO_2^+ and O_2^+ VSDs begin at 1.3 hours with relatively focused beams of ions moving upward and tailward ($45° < \theta <130°$, $120° < \phi <240°$). Both species display a slightly dusk-ward flight direction ($90° < \phi <180°$) but shift slightly dawn-ward flight ($180° < \phi <270°$). Referring back to Figure 7.1, the velocity in the XZ plane is directly parallel to the X_{MSO} line directly under the south pole, which drives this CO_2^+ and O_2^+ ion motion.

Of all three species, O^+ has the most asymmetric features in velocity space at the southern pole. seen in Figure 7.9. First at 1.3 hours, a strong duskward, high flux population is forming with a filamental, beam-like structure. From 1.5 - 1.7 hours, this O^+ population evolves into two high flux populations: 1) a central beam with a flight direction moving tailward (ϕ=180° and θ=90°) , similar to its CO_2^+ and O_2^+ counterparts and 2) a filamental beam of ions moving upward and arcing across $90° < \phi <270°$ and $30° < \theta <60°$. At 1.9 hours, this high flux filamental structure

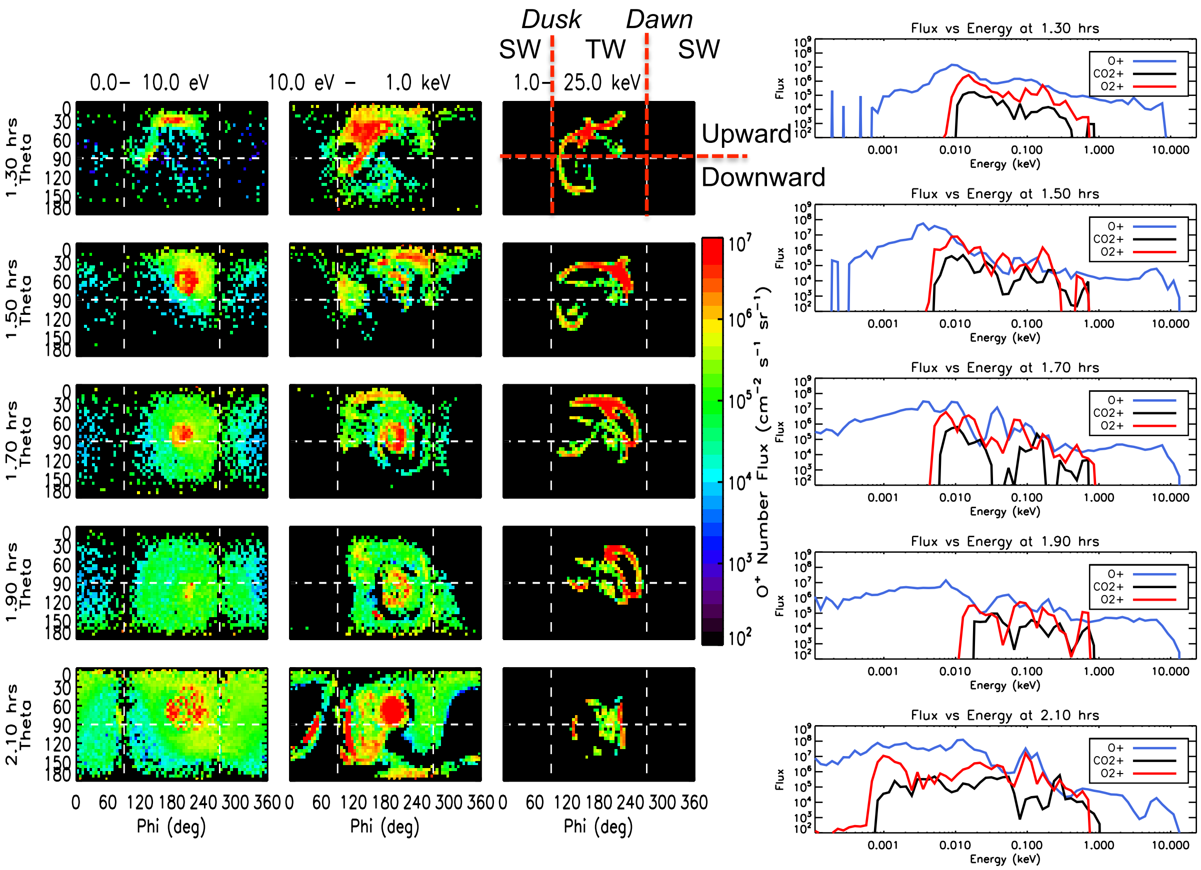

Figure 7.10: The left figure illustrates O^+ velocity space distributions illustrate from 1.3-2.1 hours for three energy ranges: low: 0 - 10 eV, medium: 10 eV- 1 keV, and high: 1 - 25 keV. The right panel illustrates the flux versus energy signatures O^+, CO_2^+ and O_2^+ at the same locations.

dominates with an upward, dawn-ward flight direction and much more flight direction coverage. Finally at 2.1 hours, the detector is flying through the hot oxygen corona (refer to the density profile in Figure 7.2) which almost saturates the detector in flight direction coverage. The CO_2^+ and O_2^+ also have higher flux and more flight direction coverage at 2.1 hours, but with specific focused populations of high flux in the downward, dusk sector.

In Figure 7.10, we highlight these distinct ion populations as function of their energy. The right panel illustrates the flux as a function of energy for O^+, CO_2^+ and O_2^+ from 1.3 - 2.1 hours. The left panel displays just the O^+, velocity space integrated over three energy ranges (low: 0 - 10 eV, medium: 10 eV- 1 keV, and high: 1 - 25 keV).

As discussed in the previous plot, the peak flux increases as the detector approaches periapsis at 2.1 hours, especially at lower energies and is responsible for the majority of the flight direction coverage. The CO_2^+ and O_2^+ are confined to this middle 10 eV - 1 keV range until the detector approaches 2.1 hours and it observes enhanced low energy flux (< 10 eV) for each species. This low energy flux corresponds to the cold planetary neutrals, which have previously been modeled and observed (*Lundin et al.*, 2009; *Terada et al.*, 2009).

Both high and low energy ranges for O^+ are evident in the energy flux plot for all detector locations, seen on the left panel of Figure 7.10. The high energy range consists of an O^+ beam moving upward and dawnward in an arc in velocity space. But comparing the high energy flux in the south pole to the energy flux signatures downtail (Figure 7.7), the higher energy flux in the southern pole is an order of magnitude higher.

Now that Figures 7.9 - 7.10 have isolated the high energy, high flux O^+ population in the south pole, Figure 7.11 illustrates a particle trace of the O^+ ions that were observed above 1 keV at each detector. The left column is a profile view (XZ) of the high energy O^+ origin and trajectories, the middle panel is a front view (YZ) of the same system and the right column is a view from underneath the planet (XY). Again, it should be noted that particles originating closer to the detectors were observed but did not have energies above 1 keV and are not shown here. Each view of these high energy O^+ ions shows specific trajectories originating on the dayside near the IMB. Now the velocity space signatures in Figure 7.10 can be traced to specific locations. From 1.5 - 1.9 hours, the Figure 7.10 VSDs show a dawnward high flux, high energy arcing beam. The corresponding detectors in Figure 7.11 show trajectories with a high number of particles at dusk (middle and right panel where $Y_{MSO} > 0$) moving to the detector near $Y_{MSO}=0$, thus having a dawnward flight direction. Additionally, this segment of the orbit observes the high altitude O^+ sources (as far as 3 - 4 R_M

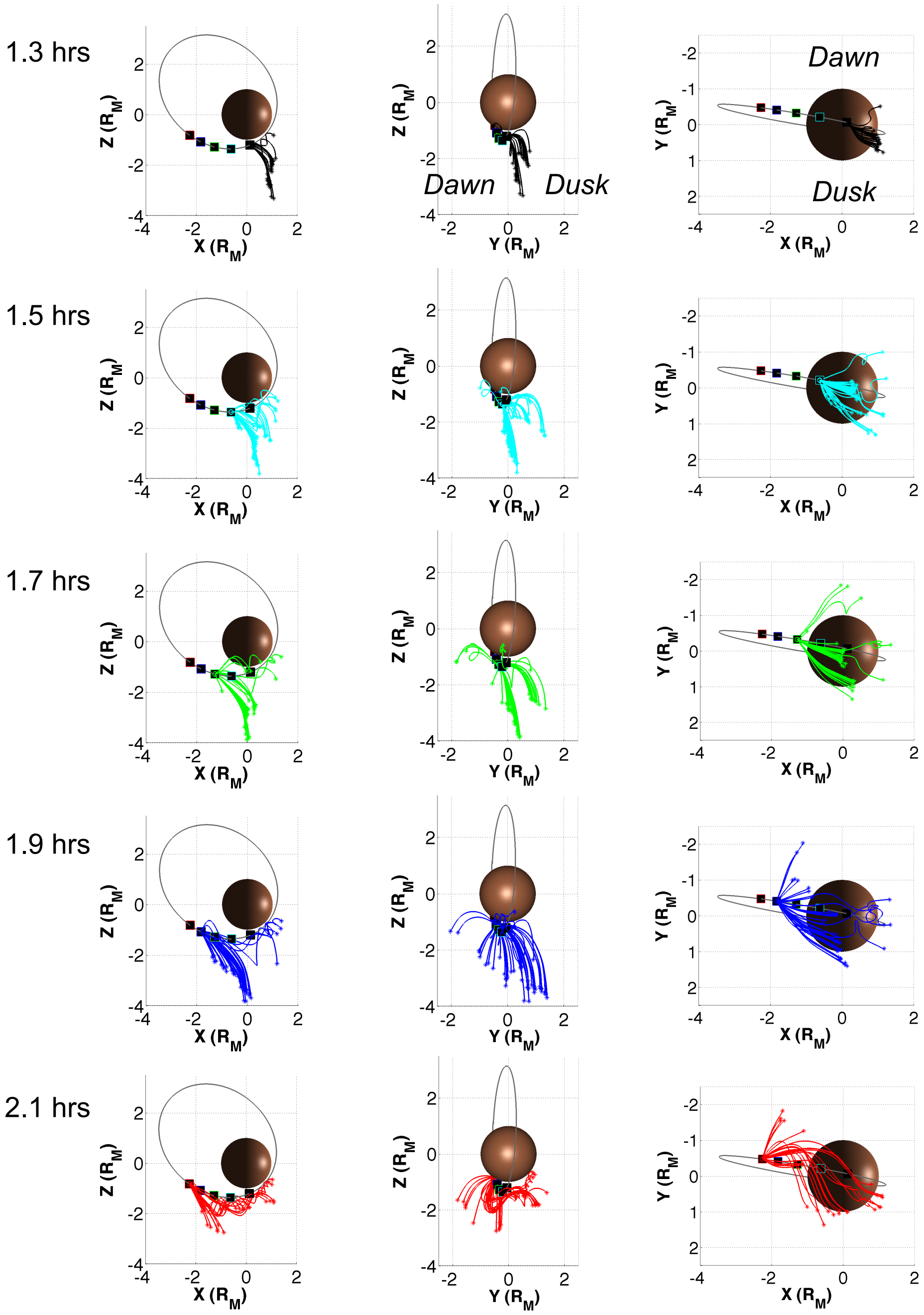

Figure 7.11: Particle traces of O^+ at each detector from 1.3 - 2.1 hours. The left column shows the trajectories of just for a profile view (XZ plane- sun to the right), the middle column shows the trajectories of O^+ face on in the YZ plane. The right column illustrates the O^+ particles from a bottom view, looking up at the south pole (XY plane- sun to the right).

below Mars). This is an important finding because CO_2^+ and O_2^+ do not have a high altitude neutral source (*Bougher et al.*, 2004, 2008) and therefore cannot generate ions which are accelerated for long enough distances to reach >5 keV energies in the southern pole. Another important point in this is the IMF configuration; if the IMF was reversed, the convective electric field would also reverse and the signatures in the southern pole would in some way translate to the northern pole (the crustal magnetic fields would interfere with a symmetric translation).

7.3.4 Ratio of ion escape

Table 7.2: O^+, CO_2^+, O_2^+ loss rates ($\#sec^{-1}$) and ratios

Species	Inner Loss	Outer Loss	Efficiency	Ratio to O^+ Outer Loss
		Solar Cycle Maximum		
O^+	2.6×10^{25}	4.6×10^{24}	15.0%	
CO_2^+	1.1×10^{24}	1.3×10^{23}	10.6%	0.03
O_2^+	1.1×10^{25}	1.1×10^{24}	9.1%	0.24
Total	3.8×10^{25}	5.8×10^{24}	15.3%	0.27
		Solar Cycle Minimum		
O^+	7.5×10^{23}	4.5×10^{23}	37.5%	
CO_2^+	2.3×10^{22}	3.0×10^{22}	56.6%	0.07
O_2^+	1.7×10^{23}	1.1×10^{23}	39.3%	0.24
Total	9.4×10^{23}	5.9×10^{23}	38.5%	0.32

As with the observed flux at the downtail and polar regions, O^+ dominates the loss rates on a 4 R_M shell, as seen by Table 7.2. The table includes the following parameters: the species, the solar cycle, the position of the crustal field, the rate (sec^{-1}) of ion precipitation into the atmosphere at the lower boundary (inner loss), the rate (sec^{-1}) of ion escape through the outer boundary (outer loss) and the efficiency, which is the ratio of the outer loss to the total production of O^+ ions. As with the previous chapters, this last parameter is particularly telling because the efficiency indicates the likelihood that particles will escape from the simulation domain.

During solar maximum, the ratio of the heavy species loss to O^+ loss is 0.27, where we define here as the combination of CO_2^+ and O_2^+. Of the heavy species, O_2^+ is dominant by an order of magnitude for both solar maximum and minimum. At solar maximum, the O^+ loss is roughly four times larger than the heavy species. Our findings for solar minimum are higher than some of the recent observations: *Barabash et al.* (2007) found the loss ratio of heavies to O^+ to be 1.4 (for ASPERA-3 observations in 2006) with observations of O^+, CO_2^+, O_2^+ to be 1.6, 0.8 and 1.5 $\times 10^{23}$, respectively. Notice that our findings predict more O^+ loss, which we determined was largely due to the low energy (<7 eV) source, which an instrument may or may not see. A similar trend follows for ASPERA-3 observations from 2007-2011 by (*Nilsson et al.*, 2011) who found the loss ratio of heavies to O^+ to be 0.90 with observations of ($CO_2^+ + O_2^+$) and O^+ to be 9.5 and 10.5 $\times 10^{23}$, respectively. One last study that most closely matched our predictions was by (*Lundin et al.*, 2009) for ASPERA-3 observations from 2008-2009 who found the loss ratio of heavies to O^+ to be 0.83 with observations of CO_2^+,O_2^+ and O^+ to be 0.35, 1.4 and 2.1 $\times 10^{24}$, respectively.

Figure 7.12 illustrates the spatial distribution of O^+, CO_2^+ and O_2^+ escape rates through a 3 R_M shell. The simulation domain uses a coordinate system that corresponds to MSO directions and the escape shown is for an IMF with an away sector Parker spiral configuration. The top and bottom panels illustrate the northern and southern hemisphere loss shells, respectively. Note that the view is from over the north pole for all of the panels with the Sun to the right. The loss is calculated by recording a particle as it passes through the 4 R_M spherical shell and displayed in number flux, with the colorbar on a log scale in # $cm^{-2} sec^{-1}$.

The loss shells of O^+ from Figure 7.12 exhibit preferential loss in the northern polar plume and tail, which is in agreement with particle traces performed by *Fang et al.* (2008, 2010a); *Curry et al.* (2012). As seen in the downtail detectors (Figures 7.6-7.8), the O^+ ions are accelerating with a duskward flight direction and can be

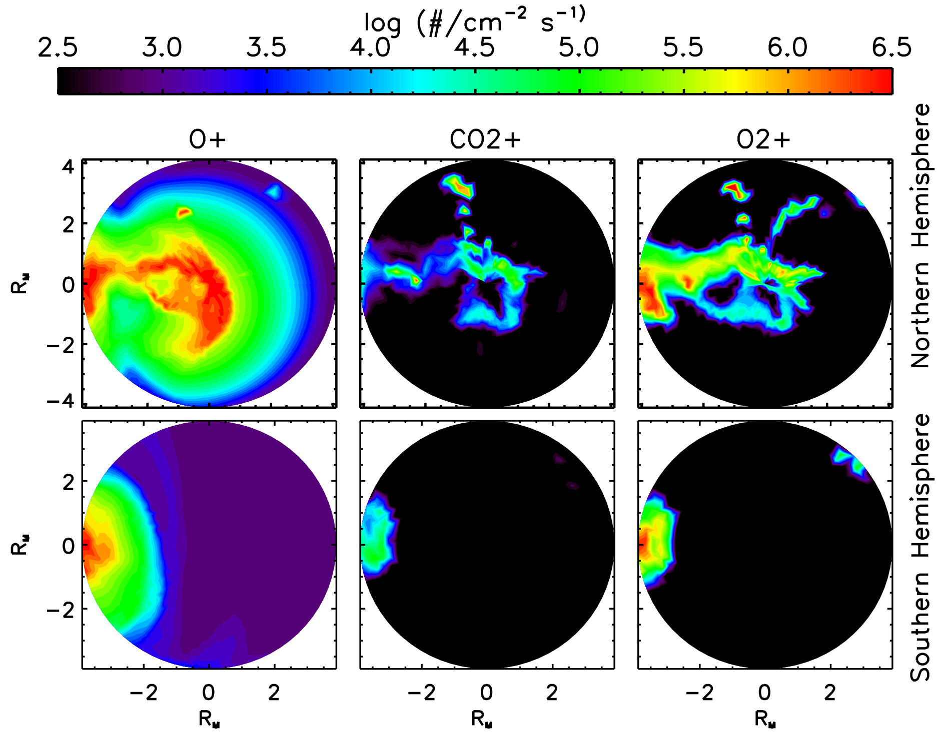

Figure 7.12: The escape of O$^+$, CO$_2^+$+O$_2^+$ on the left, middle and right panels respectively on a r R$_M$ shell. The top and bottom rows illustrate the northern and southern hemisphere with the Sun to the right. The view for both hemispheres is from over the north pole and the colorbar is in units of $cm^{-2}sec^{-1}$.

seen escaping on the 4 R_M shell with a duskward plume starting at the pole and trailing down to the tail (a 'mohawk' effect). This northern polar plume has been predicted in both MHD and hybrid models (*Brecht and Ledvina*, 2006; *Fang et al.*, 2008, 2010a; *Najib et al.*, 2011; *Curry et al.*, 2012). Interestingly, the CO_2^+ ions display a similar loss signature while the O_2^+ ions exhibit a predominantly tailward loss spatial signature.

7.4 Summary

Using the MTP simulation to create virtual detections of O^+, O_2^+ and CO_2^+ in an orbital configuration in the Mars space environment, we present results that highlight the dominant role of O^+ in ion escape at Mars. The energy-time spectrograms constructed from velocity space distributions for the different species from a virtual detector in an orbit around Mars show the ion populations changing in energy and flux as the detector moves through the tail and sheath regions. The VSDs illustrate specific low energy O^+ duskward and high energy O^+ dawnward features downtail and in the southern pole respectively. Particle traces reveal that O_2^+ and CO_2^+ do not exhibit such VSD signatures due to their low altitude cold planetary source of neutrals, as opposed to the hot extended oxygen corona that is ionized. The escape of each species also reveals particular spatial variations: O^+ dominates the polar plume while relative to each species' escape, O_2^+ and CO_2^+ are more dominant in the tail.

CHAPTER VIII

Background fields: Multi-species vs. Multi-fluid

8.1 Introduction

Initial results from the Mars Test Particle simulation (MTP) are presented here to compare a series of background fields that dictate the pick-up ion transport and escape. This study examines the effects of individual ion motion by launching particles for two MHD configurations: multi-species (*Ma et al.*, 2004) and multi-fluid (*Dong et al., 2013*, manuscript in preparation). The MTP compares the multi-species results with two regimes for the multifluid:

1. Using the bulk velocity and plasma temperature to calculate charge exchange, electron impact and ion outflow (MHD- MF_1)
2. Using each species' velocity and plasma temperature to calculate charge exchange, electron impact and ion outflow (MHD- MF_2)

It should be noted that the multi-fluid MHD model uses a 3D atmosphere whereas the MTP and multi-species MHD model use a symmetric 1D atmosphere. Thus the background ion fields are inconsistent with the particles launched, and consequently these are *preliminary results* that have not been published by either the MHD modeling authors or the MTP modeling authors. Both will undergo substantial modification and improvement before results are publicly released and should only be viewed as an initial comparison.

8.2 Models

The MTP not self-consistent in that it does not calculate the convective electric and magnetic fields and thus require input background fields. For this study, the 3-D, multispecies MHD model of *Ma et al.* (2004) and *Dong et al., 2013* [manuscript in preparation] provided the background fields that incorporated the established global model comparison inputs for three different cases: multi-species and multi-fluid (using two parameters).

The *Ma et al.* (2004) study is the multi-species MHD model described in detail in Chapter III. The multi-species model solves for separate solutions of the H^+, O^+, O_2^+, and CO_2^+ mass densities and the Hall term is neglected for these simulations. The *Dong et al., 2013* [manuscript in preparation] study employs a 3D Mars neutral atmosphere profiles from the the Mars Thermospheric Global Circulation Model (M-TGCM) and one-way couples it with the 3D BATS-R-US Mars multi-fluid MHD model. This model solves separate momentum equations for each ion species (H^+, O^+, O_2^+, and CO_2^+). This multi-fluid model calculates a one-way coupling where the M-TGCM model outputs are used as inputs for the multi-fluid MHD model. Additionally, a more adaptive grid structure is used in order to get finer resolution throughout the simulation and improve computational efficiency. This new grid structure can resolve dynamic events such as CMEs and dust storms, but is run in steady state for this model.

8.3 Results

Figure 8.1 illustrates the multi-species and multi-fluid background fields (top and bottom rows respectively), which the MTP uses to calculate the individual particle trajectories. The left column illustrates a contour of the magnetic field with white streamtraces illustrate the magnetic field direction in the XZ plane. The scale is from 0 to 40 nT and the streamtraces are presented in the traditional sense

$$\begin{aligned}&\text{if } \mathbf{u}{=}(u,v,w)\text{, then by definition}\\&\frac{dx}{u}=\frac{dy}{v}=\frac{dz}{w}\end{aligned} \tag{8.1}$$

As discussed previously, Mars lacks an intrinsic dipole magnetic field, but does have remnant crustal magnetic fields as seen in both the multi-species case (top) and multi-fluid case (bottom). The multi-species case has some asymmetry in the northern hemisphere ($Z >0$), with an enhanced magnetic region directly behind the planet (near $X \sim -2$ R_M and $Z \sim +1.5$ R_M). The multi-fluid case has even stronger asymmetries in the magnetic field strength, which occur throughout the tail and in the southern hemisphere (near $X \sim -1.5$ R_M and $Z \sim$ -2 R_M). In addition to being more asymmetric, the multi-fluid case has a stronger magnetic field amplitude from the bow shock throughout the tail. The magnetic field strength is of particular interest because it dictates the gyroradius of the individual particles. The nature of this difference is beyond the scope of this study, but will be included in continued future studies comparing background fields.

The right column illustrates a contour of the bulk velocity in the XZ plane, represented by a color scale corresponding to 0 to 400 km/sec. The black vector fields show the direction (not magnitude) of the background convective electric field. Immediately, it is clear that the multi-species case (top) has a much more symmetric velocity

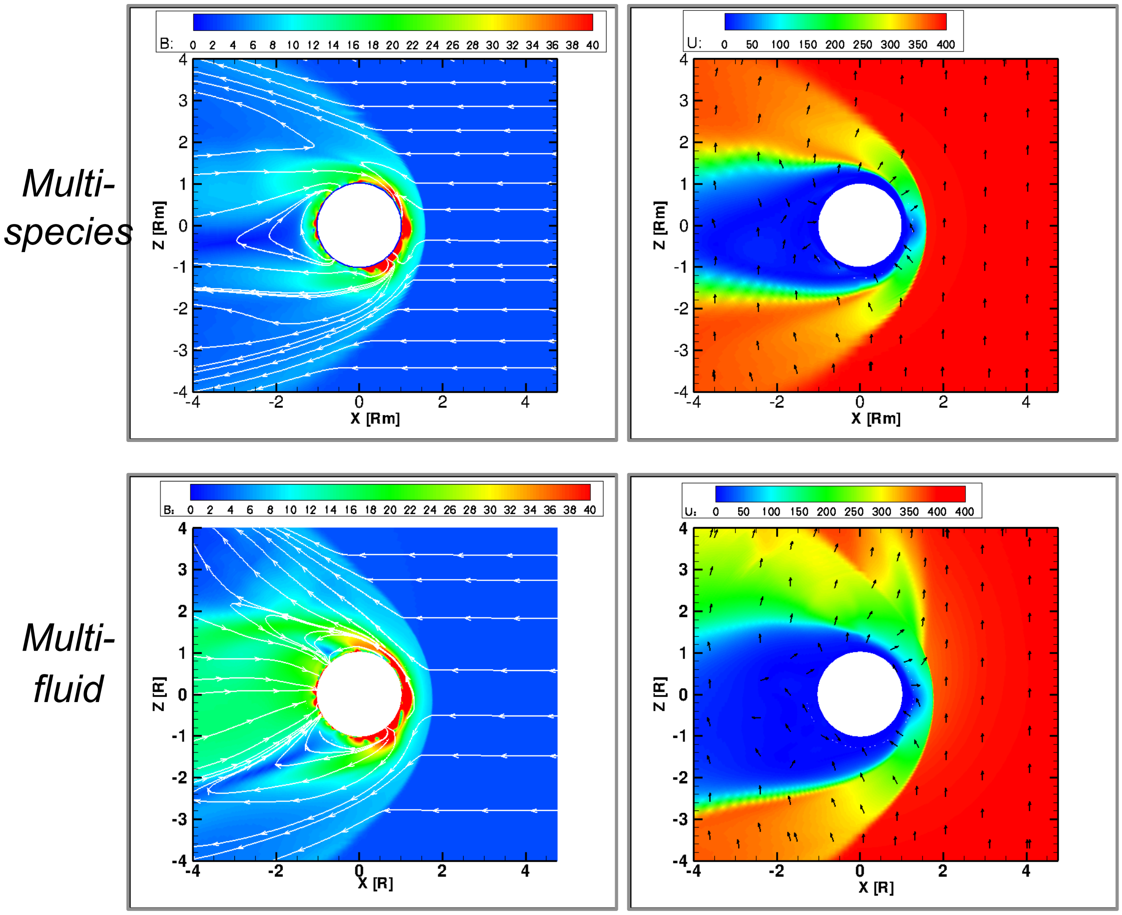

Figure 8.1: The multi-species and multi-fluid background fields (top and bottom rows respectively), which the MTP uses to calculate the individual particle trajectories. The left column illustrates a contour of the magnetic field with white streamtraces illustrate the magnetic field direction in the XZ plane where the scale is from 0 to 40 nT. The right column illustrates a contour of the bulk velocity in the XZ plane, represented by a color scale corresponding to 0 to 400 km/sec. The black vector fields show the direction (not magnitude) of the background convective electric field.

profile as opposed to the multi-fluid case (bottom), which exhibits enhanced velocity in the northern hemisphere. A number of hybrid and test particle models have predicted a 'polar plume' (*Brecht and Ledvina*, 2006; *Fang et al.*, 2008, 2010a; *Najib et al.*, 2011; *Curry et al.*, 2012), and the multi-fluid velocity profile is in agreement with these predictions with an additional spike or plume above the planet ($+Z$) and slightly sunward ($X>0$). It should be noted that the bulk velocity for the multi-fluid model is the weighted average of all of each fluid calculated (H^+, O^+, O_2^+, and CO_2^+).

Figure 8.2 illustrates the individual species bulk velocity for the multi-fluid model for H^+, O^+, O_2^+, and CO_2^+ on the same contour scale from 0 to 400 km/sec. The H^+, the lightest species (top left) stands apart from the other species in that it appears to be the most symmetric and lacks a northern polar plume. The O^+ (bottom left) velocity represents the flow due to the next lightest species, and now the polar plume is more visible. In addition to enhanced northern hemisphere flow velocity, the dayside region just below the subsolar point illustrates some very unique flow asymmetries, which again, are beyond the scope of this study but will be discussed in future investigations. Incidentally, the O_2^+ and CO_2^+ also display enhanced northern hemispheric velocity and this subsolar asymmetry. Notice that the heaviest species, CO_2^+, results in a fluid velocity near the $\sim$200 km/sec range at almost 4 R_M out from the subsolar point. The electric field vectors were not calculated for the specific flow velocities but for the weighted bulk velocity and are overlaid on the Figure 8.2 plots for the sake of comparison.

Table 8.1 compares the loss rates and loss efficiency for O^+, O_2^+, and CO_2^+ in each case as a function on ionization mechanism. The loss is calculated by the escaping flux (sec^{-1}) through a spherical shell at 4 R_M. The efficiency is the ratio of the outer loss to the total production of ions for a given species. This last parameter is particularly telling because the efficiency indicates the likelihood that particles will escape from the simulation domain.

The main result from Table 8.1 is that the multi-fluid cases with the 3D neutral atmosphere increase the escape rate for each species by almost two orders of magnitude, but increase the efficiencies only a few percent. This indicates that the production of ions increased dramatically in the multi-fluid cases, but the field lines did not necessarily enhance the escape channels for each ion species. The multi-species case shows that O^+ was the dominant escaping species while the multi-fluid cases indicate that O_2^+ was the dominant species to escape. Again, this indicates that the neu-

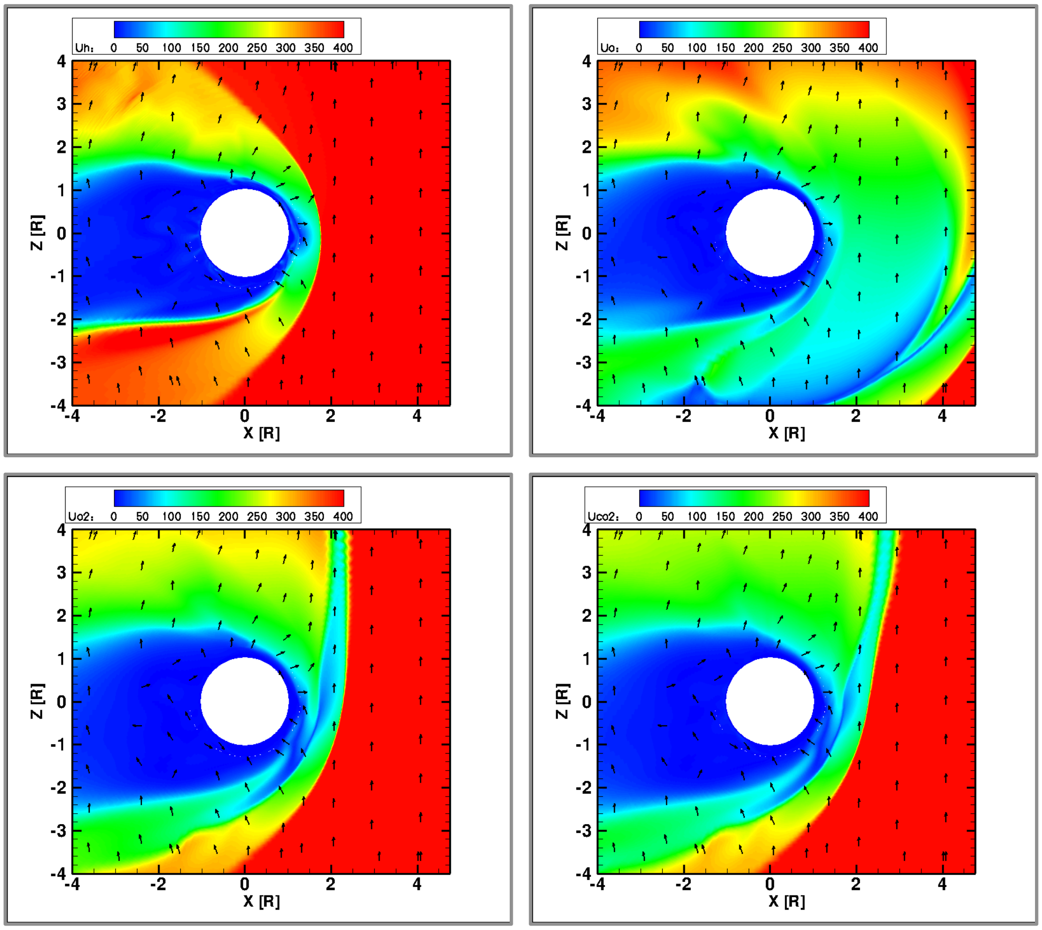

Figure 8.2: The multi-fluid background fields for H^+, O^+, O_2^+, and CO_2^+ (clockwise), which the MTP uses to calculate the individual particle trajectories. Each figure is a contour of the individual fluid species velocity the MGD model solves for in the XZ plane, represented by a color scale corresponding to 0 to 400 km/sec. The black vector fields show the direction (not magnitude) of the background convective electric field.

Table 8.1: CO_2^+, O_2^+ and O^+ loss rates ($\#sec^{-1}$) and efficiency ratio

Case	CO_2^+ Loss	O_2^+ Loss	O^+ Loss	CO_2^+ Efficiency	O_2^+ Efficiency	O^+ Efficiency
MHD- MS						
Photoionization	1.9×10^{22}	1.1×10^{21}	2.1×10^{24}	7.5%	8.3%	26.2%
Charge Exchange	4.1×10^{20}	1.6×10^{22}	6.3×10^{23}	10.4%	10.5%	67.0%
Electron Impact	2.9×10^{20}	1.5×10^{19}	1.5×10^{24}	2.0%	5.5%	48.1%
Ion Outflow	1.1×10^{23}	1.1×10^{24}	4.5×10^{23}	11.1%	9.5%	2.4%
Total	$\mathbf{1.3\times10^{23}}$	$\mathbf{1.1\times10^{24}}$	$\mathbf{4.6\times10^{24}}$	**10.2%**	**9.5%**	**15.2%**
MHD- MF$_1$						
Photoionization	1.1×10^{22}	6.4×10^{20}	1.6×10^{24}	4.3%	4.7%	20.8%
Charge Exchange	9.8×10^{19}	3.9×10^{24}	4.1×10^{24}	4.1%	6.9%	11.9%
Electron Impact	2.7×10^{23}	1.2×10^{22}	1.1×10^{26}	2.6%	4.2%	13.2%
Ion Outflow	9.6×10^{25}	3.8×10^{26}	2.7×10^{25}	18.5%	18.0%	13.3%
Total	$\mathbf{9.7\times10^{25}}$	$\mathbf{3.8\times10^{26}}$	$\mathbf{1.4\times10^{26}}$	**18.2%**	**17.7%**	**13.3%**
MHD- MF$_2$						
Photoionization	1.1×10^{22}	6.3×10^{20}	1.6×10^{24}	20.7%	4.4%	4.7%
Charge Exchange	2.0×10^{20}	3.9×10^{24}	4.1×10^{24}	11.9%	6.1%	6.9%
Electron Impact	2.8×10^{23}	1.2×10^{22}	1.1×10^{26}	12.9%	2.7%	4.0%
Ion Outflow	7.4×10^{25}	3.9×10^{26}	3.5×10^{25}	13.9%	15.5%	18.0%
Total	$\mathbf{7.5\times10^{25}}$	$\mathbf{3.9\times10^{26}}$	$\mathbf{1.5\times10^{26}}$	**13.1%**	**15.2%**	**17.7%**

tral profile was significantly different for the different MHD runs. Because further comparisons cannot distinguish the influence of the different atmospheres versus the different modeling techniques, the discussion will conclude here until further analysis can be performed; in future studies, the MTP species velocities will be compared to the multi-fluid velocities once the same neutral atmosphere and ionization scheme are in place for both simulations.

CHAPTER IX

Conclusions

9.1 Summary

With the exponential improvement of parallel computing schemes and architecture, modeling the kinetic features of the Mars space environment is more feasible than it has ever been before. As an attractive alternative to MHD and hybrid modeling, test particle modeling provides insights into individual ion motion, which often dominates the transport regime at high altitudes due to the lack of an intrinsic dipole magnetic field at Mars. Using the MTP simulation, we found the following results in response to the science questions posed:

1. **Production processes: what is the relative role of different ion production mechanisms in controlling the distribution of planetary ions?** Kinetic processes are responsible for highly non-gyrotropic and non-Maxwellian velocity space features due to specific ion production mechanisms. At higher altitudes on the dayside (>1000 km), photoionization requires simply an optical shadow as opposed to solar zenith angle dependence because the optical depth is very small. Otherwise, the application of a solar zenith angle dependence can underestimated the total production, especially for O^+ (the production is 50% higher without SZA). At lower altitudes (<1000 km), it is necessary for

charge exchange to include the random thermal velocity from the solar wind temperature in order to account for the hot neutral charge exchange reactions (the production is 88% higher). Finally at all altitudes, electron impact ionization must have temperature dependence because otherwise a constant rate could drive escape to be two orders of magnitude higher.

2. **Solar cycle vs Corona: what atmospheric conditions, including the role of the corona and solar cycle, control the fine-structure features in observed and modeled VSDs and loss of planetary ions?**

   The inclusion of a hot oxygen corona roughly doubles the overall loss and is directly responsible for the accelerated ions above 1 keV. The solar cycle also increases the overall O^+ loss by roughly an order of magnitude from solar minimum to maximum. It also results in specific VSD signatures from ions on the dayside that are able to accelerate and escape under the planet (for an away sector IMF), which at solar minimum is not observed due to less mass loading.

3. **Ionospheric sources: how does the ionosphere affect the overall escape?**

   It was found that low-altitude source of ionospheric outflow is a rather small contributor to the total escape of O^+ and the high-altitude ionization processes significantly contribute to ion loss at Mars and are responsible for 90% of the total O^+ loss. In high altitude simulated observations, ionospheric outflow is defined by several key features in velocity space, most notably a focused beam in flight direction in a narrow region of space (compared to the high-altitude sources). The energy of ionospheric outflow changes dramatically depending on the pathway of escape; those that leave down the central tail are preferentially at low energies while those escaping via the polar plume are at relatively high energies. Additionally, it was shown that ionospheric outflow can become significant, and even dominant, if the initialization density and/or velocity is substantially increased over the nominal MHD values extracted at 300 km. This implies that ionospheric outflow could be very important if processes not included in the MHD simulation are able to alter the O^+ characteristics in the topside ionosphere. For instance, this extra energization or density enhancement process could be wave-particle interactions, parallel electric fields, large-scale turbulence (i.e., Kelvin-Helmholz oscillations), or solar wind-crustal field magnetic reconnection.

4. **Observing ion escape: what are the dominant species and how well can it be quantified?**

   By simulating the ion transport of O^+, CO_2^+ and O_2^+, we established that the loss is dominated by O^+. The O^+ covers a much wider energy range, including low energy populations in the tail below 5 eV and high energy populations throughout the tail and sheath at or above 10 keV. These high and low energy populations give rise to highly asymmetric VSD features, which are in part due to the hot oxygen corona as well as the smaller gyroradius that inhibits O^+ less from precipitating back into the atmosphere. The CO_2^+ and O_2^+ have far fewer asymmetries in the simulated VSD and much narrower energy ranges from 10 eV to 1 keV.

5. **Background fields: how do different background fields affect the spatial loss distribution, escape and VSD signatures?**

   The background fields control the individual ion motion and produce drastically different loss rates but quite similar loss efficiencies, particularly for a comparison of the multi-species and multi-fluid MHD cases.

9.2 Significance

Because Mars is the closest comparison we have for Earth, the processes that led to such different atmospheric evolution are of great interest. Our focus has been on nonthermal pick-up ion transport and escape, which is a critical piece of a larger puzzle when discussing the hydrological cycle on Mars. As these results have shown, we have examined planetary ion VSDs for different neutral atmospheric profiles, solar cycles and ion species and quantified the major influences of high altitude pick-up ion escape.

This body of work is significant for interpreting both past and future observations of ions at Mars because specific VSD features are indicative of particular populations of ions for a given IMF configuration. So if a given ion distribution was observed at some location in near-Mars space, the MTP could simulate the same observation and could trace the origin and trajectory of the ions it observed. Additionally, specific VSD features could offer insights into the configuration of the IMF in the absence of magnetic field data.

This work has particular significance for Mars Atmosphere and Volatile EvolutioN (MAVEN), which is NASA's next Mars Scout for the Mars Exploration Program. MAVEN has four science objectives: 1) to determine how much of the atmosphere at Mars has been lost over time, 2) to determine the current state of the upper atmosphere and ionosphere and their interactions with the solar wind, 3) to determine the processes controlling neutral and ion escape, and 4) to determine the ratio of stable isotopes in order to extrapolate Mars' atmospheric loss over time. Because the MTP tracks individual particle motion, it is very well suited to construct virtual observations for these objectives and to provide a comparison with the actual observations.

9.3 Future work

Future work plans will include continuing to investigate the kinetics of pick-up ions at Mars but will include expanding into other fields using the foundation of modeling atmospheric loss. Specific research areas for future investigation have been identified and outlined below.

Near Term Plans

- A comparison of different background fields, including the multi-fluid model from Chapter VIII in development
- Data comparisons of VSDs with MEX and MAVEN data.
- A comparison of pick-up ion acceleration and escape for different IMF configurations, particularly with the use of simultaneous magnetometer and plasma data from MAVEN.

Future Plans

- Additional nonthermal loss processes such as plasmoid detachment and Kelvin Helmholtz instabilities.
- Investigating soft x-ray emission from charge exchange processes in the atmosphere and further quantifying energy transfer from the solar wind via charge exchange
- Adapting the MTP to both Venus and Titan. Because the model is a sophisticated, parallelized 3D simulation, there are imminent plans to expand the simulation to the Venus and Titan environments. With a large group of experts on modeling both planets at the Space Science Laboratory at the University of California, Berkeley (*Luhmann*, 1996; *Luhmann et al.*, 2006, 2012), the MTP will be highly adaptable for other science questions surrounding the transport and escape of ions.

APPENDICES

APPENDIX A

Mars crustal remnant magnetic fields

A.1 Modeling Crustal Fields

The relatively recent discovery of crustal magnetic fields on Mars indicates that the planet once had a global dynamo-generated magnetic field early in the planet's history (*http://sprg.ssl.berkeley.edu/ brain/tutorials/crust.html*). As numerous studies have shown (*Connerney et al.*, 2004; *Brain et al.*, 2010a; *Ma and Nagy*, 2007; *Fang et al.*, 2010a; *Li et al.*, 2011; *Nilsson et al.*, 2011), crustal fields protect regions of the atmosphere from the direct interaction with the solar wind as well as create magnetic cusps where the solar wind can erode the atmosphere. Thus, in order to describe the complex processes occurring near the crustal fields, numerous models have been developed to account for the crustal remnant's contribution to the observed Martian magnetic field. It should be noted that the first radial component maps presented by *Acuna et al.* (1999) were two-dimensional and did not include altitude corrections (*Arkani-Hamed*, 2001). Current approaches to modeling these crustal fields fall into two general categories.

The first approach is an empirical model (sometimes called a *local model*), which constructs a mapping of the magnetic field using low altitude, radial, MGS magnetic observations (*Purucker et al.*, 2000; *Langlais*, 2004). Empirical models often describe small regions of the Martian surface where specific crustal magnetic fields exist at a given altitude. An example of the equivalent source dipole technique from *Langlais* (2004) is described with equations A.1-A.4:

$$V = -M \cdot \nabla \frac{1}{l} \tag{A.1}$$

$$l = \left(r_d^2 + r^2 - 2 r_d r \cos\zeta\right)^{1/2} \tag{A.2}$$

where M is the magnetic moment of a dipole at (r_d, θ_d, ϕ_d) and V is the magnetic potential observed at (r, θ, ϕ). The distance between the dipole and observation is l and the angle between observation and dipole location in ζ, resulting in the magnetic field, $\vec{B}$.

$$\cos\zeta = \cos(\theta)\cos(\theta_d) + \sin(\theta)\sin(\theta_d)\cos(\phi - \phi_d) \tag{A.3}$$

$$\vec{B} = -\vec{\nabla} V = \left(-\frac{\partial}{\partial r}, \frac{\partial}{r\partial\theta}, \frac{\partial}{r\sin(\theta)\partial\phi}\right) V \tag{A.4}$$

The second approach is a spherical harmonic method, which has been explored by numerous mathematical studies (*Arkani-Hamed*, 2001; *Cain*, 2003). By using the three orthogonal vector components of the magnetic field data (such as MGS), global spherical harmonic models describe the contribution of crust to the global magnetic field as an arrangement of magnetic poles for different spatial wavelengths (dipole, quadrupole, etc...). Figure A.1-A.2 illustrate examples of the spherical harmonic method.

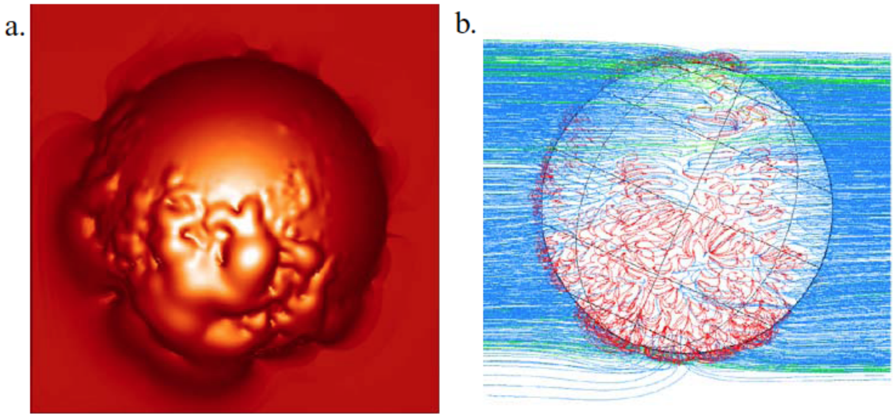

Figure A.1: From *Brain* (2007): Cartoon showing: (a) the Martian pressure balance obstacle and (b) magnetic field topology. (a) The shape of the Martian solar wind obstacle is derived from a calculation of pressure balance between upstream solar wind dynamic pressure and a combination of ionospheric thermal pressure and magnetic pressure from crustal fields. (b) The magnetic field topology results from field line tracing in a vacuum superposition of a crustal field model with a uniform background magnetic field. Field lines are colored according to their topology: closed (red), open (blue), or draped (green). Mars has the same orientation in both panels. From Brain (2002).

$$V(r, \theta, \phi) = a \sum_{n=1}^{N} pr \left(\frac{a}{r}\right)^{n+1} (g_{nm} \cos(m\phi) + h_m n \sin(m\phi)) P_n^m \cos(\theta) \tag{A.5}$$

$$\mathbf{F} = -\nabla \mathbf{V} \tag{A.6}$$

where a is the radius of a reference spherical surface, r is the distance from the center, q is the colatitude and f is the east longitude. $P_n^m \cos(\theta)$ is the Schmidt quasi-normalized associated Legendre function of degree n and order m, and g_{nm} and h_{nm} are the potential spherical harmonic coefficients. Finally N denotes the highest-degree harmonic retained in the model (*Arkani-Hamed*, 2001).

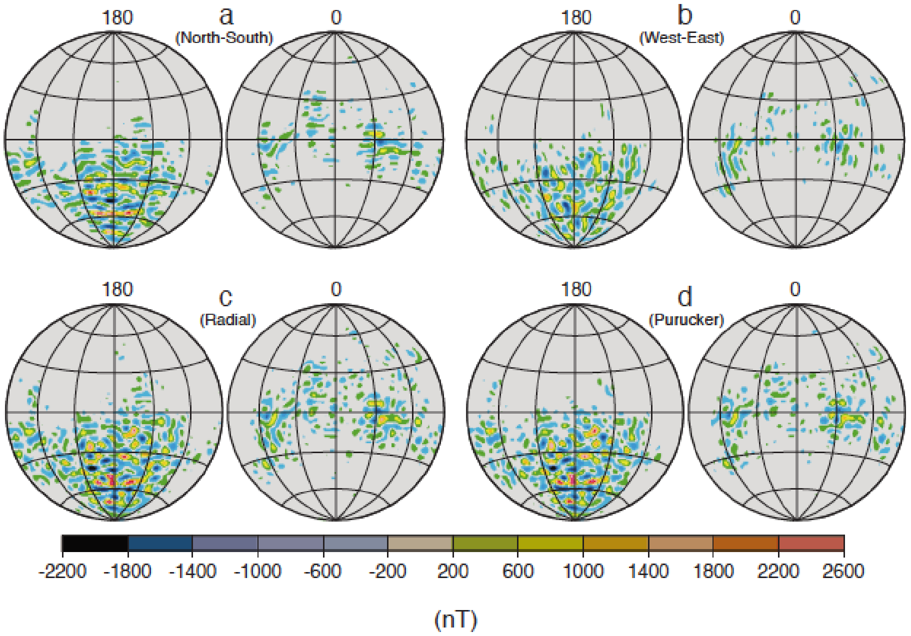

Figure A.2: From *Arkani-Hamed* (2001): Plates 1a1c show the three orthogonal components of the Martian magnetic field model (1,1,1) at the surface of Mars. Plate 1d is the downward continued version of the radial component map by Purucker et al. [2000]. I first expanded the map in terms of the spherical harmonics of degree 50 and then used the downward continuation algorithm in the spherical coordinate system.

APPENDIX B

Flux integration

B.1 Flux calculations

It is critical to establish the calculations for different types of flux because the community often does not differentiate between differential number flux, and differential energy flux, flux intensity, etc.... We begin with a hypothetical observed value of flux, F, defined as the quantity describing the number of particles passing through a given area in units of [cm^{-2}sec^{-1}]. Let us assume that as the particles pass through a given area, it has a given energy (E) and incoming direction (using the polar and azimuthal angles θ and ϕ), making it $F(\theta, \phi, E)$. Note that this is an idealized 2D surface that the particles pass through and can be moving in any direction, so unlike a detector, this surface could see particles moving towards it or away from (double sided). In the following calculations, the coordinate system will assume the given area is in a plane normal to the $+X$ axis.

The first type of flux, often useful for velocity space distributions, is referred to as *directional number flux intensity.* The conversion of flux to directional number flux intensity, F_I in units of [cm^{-2}sec^{-1}ster^{-1}], can be described as

$$F_I(\theta,\phi) = \frac{F(\theta,\phi)}{\Omega} \tag{B.1}$$

where Ω is the part of the solid angle the flux occupies, described by

$$\Omega = \int\limits_{\theta}\int\limits_{\phi} d\omega \sin\theta\cos\phi \text{ and } d\omega = \sin\theta\ d\theta d\phi \tag{B.2}$$

thus

$$\begin{aligned}
\Omega &= \int\limits_{\theta}\int\limits_{\phi} \sin^2\theta\cos\phi d\theta d\phi \\
&= \frac{1}{2}[\theta - (\sin\theta\cos\theta)]\sin\phi\Big|_{\theta_1}^{\theta 2}\Big|_{\phi 1}^{\phi 2} \\
&= \frac{1}{2}\cdot\frac{1}{2}[2\theta - 2(\sin\theta\cos\theta)]\sin\phi\Big|_{\theta_1}^{\theta 2}\Big|_{\phi 1}^{\phi 2} \\
&= \frac{1}{2}\cdot\frac{1}{2}[2\theta - (\sin 2\theta)]\sin\phi\Big|_{\theta_1}^{\theta 2}\Big|_{\phi 1}^{\phi 2} \\
&= \frac{1}{4}[2\theta - (\sin 2\theta)]\sin\phi\Big|_{\theta_1}^{\theta 2}\Big|_{\phi 1}^{\phi 2}
\end{aligned}$$

The next type of flux is referred to as *omnidirectional differential number flux*, F_O, in units of [cm^{-2}sec^{-1}ster^{-1}keV^{-1}]. This quantity is a measure of how much mass is passing through an area and can be described as

$$F_O(\theta,\phi) = \frac{F(\theta,\phi)}{\Delta E\cdot\omega} \tag{B.3}$$

where $\omega = 2\pi$ and is the average solid angle the flux occupies

and ΔE and is the energy bin

Another measure of flux is referred to as *omnidirectional differential energy flux*, F_E, in units of [keV cm^{-2}sec^{-1}ster^{-1}keV^{-1}]. This quantity is a measure of how much energy is passing through an area and can be described as

$$F_O(\theta, \phi) = \frac{F(\theta, \phi) \cdot E}{\Delta E \cdot \omega} \tag{B.4}$$

where again $\omega = 2\pi$ and is the average solid angle the flux occupies and ΔE and is the energy bin

The final measure of flux is referred to as *differential number flux per bin*, F_E, in units of [cm^{-2}sec^{-1}Ebin^{-1}], and can be described as

$$F_O(\theta, \phi) = F(\theta, \phi) \tag{B.5}$$

These calculations can result in over an order of magnitude difference and describe different physical quantities passing through a 2D space.

APPENDIX C

Variability of the Martian Exobase

C.1 Exobase Variability

C.1.1 Exobase assumptions

Due to Mars' relatively weak magnetic field compared to that of Earth (*Acuna et al.*, 1999), the interaction between the solar wind and the planetary neutral environment creates a scenario where particles can be stripped away from the atmosphere. In the upper atmosphere of Mars, the neutral gas collision frequency is high enough for the velocity to be approximated by a Maxwellian distribution. As the density decreases with altitude, the particles experience less collisions and the thermal velocity is no longer normally distributed. The exobase is the transition region where particles no longer experience collisions and their mean free path is a ballistic trajectory. Consequently, the exobase occurs at some radial distance, r_c, where the scale height is equal to the mean free path (*Gombosi*, 1998):

$$\int_{r_c}^{\infty} n(r)\sigma dr = 1 \cong \sigma n(r_c) H(r_c) = \frac{H(r_c)}{\lambda(r_c)} \tag{C.1}$$

Where n_0 is the initial density, H is the scale height and λ is the mean free path defined by (*Schunk and Nagy* (2000)):

$$H = \frac{kT}{mg} \lambda = \sqrt{\sigma n} \tag{C.2}$$

$$n(z) = n_0 exp(-\frac{z - z_0}{H}) \tag{C.3}$$

σ defines the average cross section of molecular collisions, m is the mass of the particle, g is the gravity on Mars and T is temperature. Solving for the exobase height r_c,

$$r_c = H \ln(\sigma n_0 H) \tag{C.4}$$

From equation 4, temperature and density have the strongest effect on the Martian exobase height estimation. Both of these experience fluctuations due to the solar cycle as well as seasonal effects. This paper will analytically address the impact both have on the estimating the variability of the Martian exobase altitude.

C.1.2 Exobase estimates

The structure of the Martian exosphere is layered with the heavier species, an extended corona of hot light species and then escape of the lighter constituents. Consequently, the Martian exosphere is critical in understanding the global escape of the Martian atmosphere (*Valeille et al.*, 2009). Historically, in situ measurements from Viking 1 & 2 provided limited information on the composition of the Martian corona, so numerous theoretical and analytical models have been developed in order to explore this. In particular, research on the variability of the thermosphere and exosphere has revealed the strong influence of the solar cycle on the evolution of the Martian atmosphere. *Bougher et al.* (2008) have shown that the upper atmosphere displays diurnal patterns and local variations including temperature and wind distributions, planet rotation, polar warming, and hemispheric asymmetries that require much more sophisticated modeling in 3D.

Valeille et al. (2009), among others, have quantified both the influence of the solar cycle and the Martian seasonal effects on the exosphere by characterizing the two extreme cases of net solar forcing: solar minimum at the orbital position of Aphelion (AL) and solar maximum at the orbital position of Perihelion (PH). The Martian year is described by the *heliocentric longitude* or *seasonal longitude*, L_s, in terms of the position of the Martian orbit around the Sun. L_s is equal to 0 degrees at the Martian northward equinox, 90 degrees at the Martian northern solstice (AL), 180 degrees at the Martian southward equinox, and 270 degrees at the Martian southern solstice (PH). Like the Earth, Mars has seasons due to its axial tilt and elliptical orbit which strongly influence the atmospheric temperature profile.

This paper will use a simple 1D analytic model to illustrate this variability of the exosphere and demonstrate the necessity for further research on the interaction between the upper Martian atmosphere and the solar wind and solar environment.

C.1.3 Modeling exobase

The use of a simple neutral 1D model assumes an isothermal exosphere with purely thermal escape and neglects any ion loss and subsequent MHD interactions. It also assumes a division between the collisional and collisionless domains, neglecting the momentum exchange within this region (*Valeille et al.*, 2010). Due to the complex temperature profile in the upper atmosphere of Mars, numerous models have made predictions of the thermal structure.

The atmosphere is thought to be well mixed to heights in excess of 120 km (*Fox*, 2009). Consequently, an initial altitude of 120 km was used in order to preserve the hydrostatic equilibrium assumptions from Equation 2. Temperature profiles were taken from Bougher and Nair for solar minimum and maximum modeled conditions, as seen in Figure 1. Initial values for the calculation of the Martian exobase are defined in Table 1. In situ measurements of Mars from the neutral mass spectrometers carried on Viking 1 and Viking 2 revealed that carbon dioxide is the primary constituent from 120 to 200 km. Measurements also detected trace amounts of nitrogen, argon, carbon monoxide, molecular oxygen, atomic oxygen, and nitric oxide, where the main constituents are defined as O, CO_2 and O_2.

Table C.1: Martian Exobase Input Parameters

Input	Value	Units
Gravity (g)	3.74	m/s^2
Inital Altitude (z_0)	120	km
Initial Density (n_0)	3.0 x 10^{+11}	$\#/cm^3$
Average Molecular Cross Section (σ)	2.00 x 10^{-15}	cm^2
Mass (O)	2.68 x 10^{-26}	kg
Mass (CO_2)	6.67 x 10^{-26}	kg
Mass (O_2)	5.35 x 10^{-26}	kg

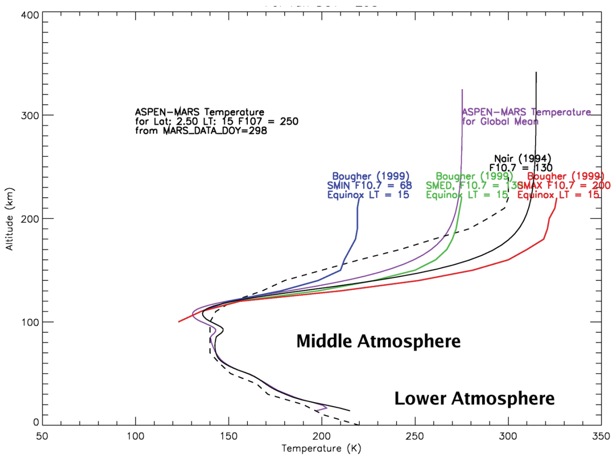

Vertical Temperature structure from ASPEN.

Figure C.1: ASPEN temperature profiles from Bougher and Nair for solar minimum and maximum modeled conditions source: *Bougher and Engel* (2000)

C.1.4 Results

Using Equation 3, the 1D analytic model calculated the exobase altitudes for the neutral atmosphere, as seen in Figure 2. Here the initial densities were varied from $n_0 = 10^{+5}$ - 10^{+13} cm^{-3} over 5 temperatures. *Bougher and Engel* (2000) modeled temperature variations ranging from roughly 150 to 350 degrees Kelvin due to solar cyclability as seen in Figure 1. These values serve as the upper and lower limits for the input temperatures used in both species and atmospheric exobase calculations. *Valeille et al.* (2009) conducted a 2D axisymmetric study of the exobase height along the Equator and estimated Martian exobase heights to be from 155 to 195 km. Figure 2 shows a minimum exobase height at 127.9 km for $T = 150$ and $n_0 = 10^{10}$ and a maximum at 208.1 km for $T = 350$ and $n_0 = 10^{13}$ (K and cm^{-3} respectively).

Figure 3 illustrates the exobase altitudes of the individual species O, CO_2 and O_2. As opposed to figure 2, here initial density input was fixed at $n_0 = 3.0$ x 10^{+11} cm^{-3} and each species is plotted as a function of $n(z)$ versus height. This can be considered as a slice of Figure 2 at $n_0 = 3.0$ x 10^{+11} cm^{-3} but over the entire span of the ranges of temperature that *Bougher and Engel* (2000) modeled. While each species will have a different scale height depending on m, the largest factor contributing to the exobase altitude is clearly temperature.

Recent Martian upper atmospheric studies have shown the seasonal variation of the zonal mean temperatures in the upper atmosphere to be ∼100 K as a result of the variation of the solar forcing (*GonzálezGalindo et al.* (2009)). The thermosphere exhibits strong seasonal temperature gradients ranging from about 60 K at aphelion to 110 K at perihelion, as seen in the top panel of Figure 4. *GonzálezGalindo et al.* (2009) developed a Martian general circulation model in order to explore the diurnal cycle perturbations from day-to-day variations of temperature, using averages from a simulation time of 1.5 Martian years. Their model reproduced the observed solar cycle variation in temperatures when using a UV heating efficiency of ∼16%, slightly

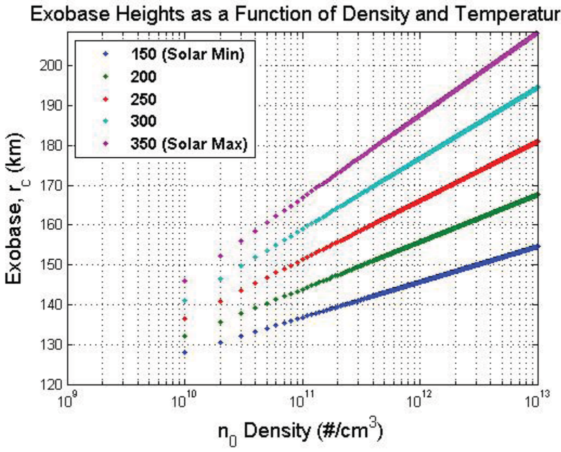

Figure C.2: Exobase altitude as a function of initial density and temperature for the neutral atmosphere for five scale height temperatures: 150-350 Kelvin. Initial densities n_0 range from 10^{+5} - 10^{+13} cm^{-3}.

lower than the theoretical value (*GonzálezGalindo et al.* (2009)). As seen in Figure 4, L_s of 270 degrees corresponds to the southern summer which is the closest point to the Sun that the Martian orbit reaches. This seasonal effect *in addition to the solar cyclability* produces an enormous temperature gradient which is has an enormous effect on the Martian exobase as seen in Figures 2 and 3.

The temperature mapping at 10^{-6} Pa corresponds to approximately 200 km. *GonzálezGalindo et al.* (2009) suggest this pressure layer is high enough to be in the thermospheric region where temperatures are constant with altitude. Because the exobase is located within the lower bounds of this isothermal region, exobase temperatures should be equal to the pressure layer at 200 km and can be used to determine the vertical variations in exobase altitude (*Hunten*, 1993).

In summary, the thermal structure of the upper Martian atmosphere is complex and subject to strong fluctuations from the solar cycle and seasonal variations. While many of the processes responsible for atmospheric loss are too complex for the scope of this study, a simple neutral 1D model illustrates the variability of the exobase relatively well. By assuming an isothermal exosphere with purely thermal escape, the scale height and mean free path can be set equal to each other to solve for the

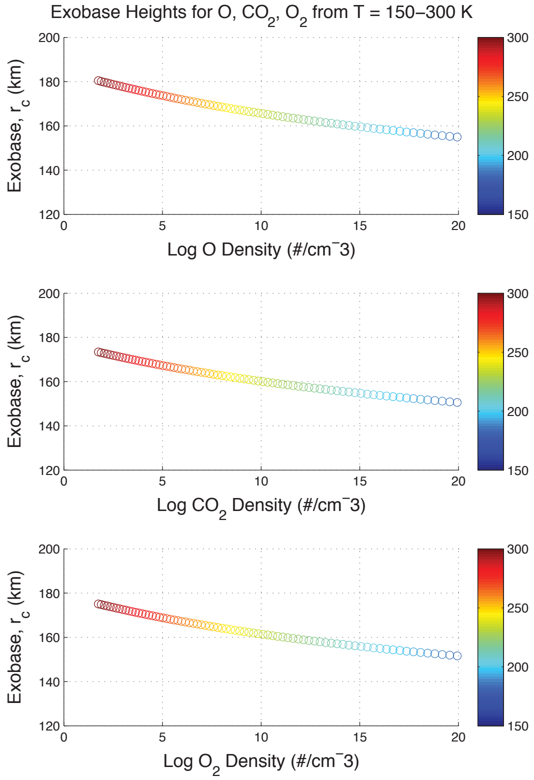

Figure C.3: Exobase altitude as a function of density and temperature for O, CO_2 and O_2. The colorscale is from 150 to 300 Kelvin for each species. n_0 is fixed at 3.0 x 10^{+11} cm^{-3} and each species is plotted as a function of $n(z)$ versus height. This can be considered as a slice of Figure 2 at n_0 but over the entire span of the ranges of temperature that *Bougher and Engel* (2000) modeled.

height of the exobase. The exobase altitudes for O, CO_2 and O_2 vary as a function of the initial density input and temperature more so than their atomic mass. But the results for the neutral atmosphere illustrate a much wider range than other predicted values. Compared to an average exobase height of 170 km calculated by *Valeille et al.* (2009), these exobase estimates generally tend to underestimate the exobase height, although the altitudes corresponding to the solar minimum and maximum exceeded the limits for the predicted values. These results do support the findings of *Hunten* (1993) who cite 160 km as the value of the Martian exobase. This variability could be due to larger ranges for initial density input or oversimplification of this 1D model

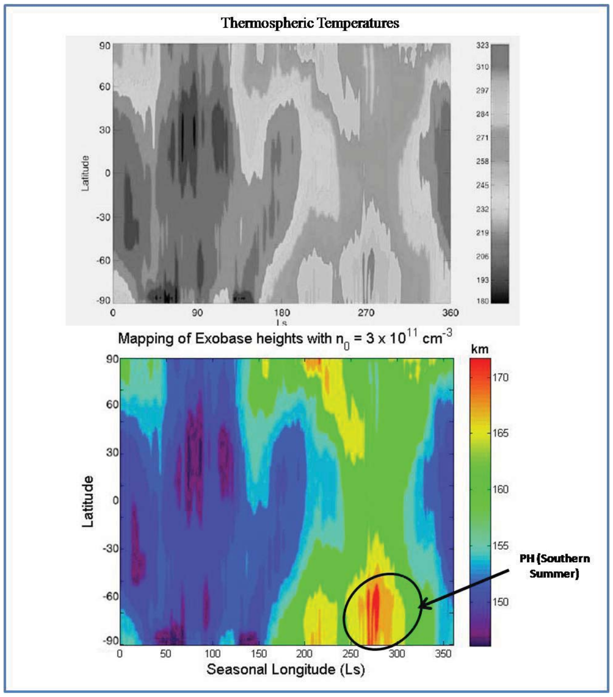

Figure C.4: Top: *GonzálezGalindo et al.* (2009) produced seasonal variations of zonal mean temperatures, at 10^{-6} Pa for solar average conditions using their Martian general circulation model. Bottom: Using the temperature mapping from *González-Galindo et al.* (2009), the 1D analytic model presented here calculates the mapping of the exobase altitudes using an initial density of 3.0 x 10^{+11} cm^{-3}.

which does not account for kinetic processes. However it should be noted that the temperature ranges are appropriate given values found from the solar cyclability as well as the orbital position of Mars. Regardless of initial density input, Figures 2 through 4 illustrate the temperature variability due to solar minimum and maximum as well as orbital position of the planet.

Given the variability of the Martian exobase, the thermal structure of the planet should be a consideration for future missions, manned or unmanned, to Mars. The density and temperature profiles, demonstrate by previous course work by *Curry*, have a dramatic effect on drag coefficients and the consequent lifetime of the instrument or spacecraft. Equally as important is the need for examining the dynamics and effects of Martian atmospheric escape. Future work in this area will directly support the NASA Mars Fundamental Research program and the Mars Exploration Program, which has selected the MAVEN mission as the next Mars Scout. One of the primary mission objectives of the MAVEN mission concept is in fact atmospheric escape. Comprehensive models including the effects of ion escape will vastly improve our understanding of the evolution of Mars and will ultimately contribute to observing the progression of both our solar system as well as the hundreds of exoplanets currently being studied.

BIBLIOGRAPHY

BIBLIOGRAPHY

Acuna, M. H., et al. (1999), Global distribution of crustal magnetization discovered by the mars global surveyor mag/er experiment, *Science*, *284*(5415), 790–793.

Afonin, V., et al. (1989), Energetic ions in the close environment of mars and particle shadowing by the planet, *Nature*, *341*, 616–618.

Andersson, L., R. E. Ergun, and A. I. F. Stewart (2010), The combined atmospheric photochemistry and ion tracing code: Reproducing the viking lander results and initial outflow results, *Icarus*, *206*(1), 120–129.

Arkani-Hamed, J. (2001), A 50-degree spherical harmonic model of the magnetic field of mars, *Journal of Geophysical Research*, *106*, 197–208.

Barabash, S., and M. Holmstrom (2002), Energetic neutral atoms at mars 4. imaging of planetary oxygen, *Journal of Geophysical Research*, *107*(A10).

Barabash, S., E. Dubinin, N. Pissarenko, R. Lundin, and C. T. Russell (1991), Pickedup protons near mars: Phobos observations, *Geophysical Research Letters*, *18*(10), 1805–1808.

Barabash, S., A. Fedorov, R. Lundin, and J. A. Sauvaud (2007), Martian atmospheric erosion rates, *Science*, *315*(5811), 501–3.

Bauske, R., A. Nagy, T. Gombosi, D. De Zeeuw, K. Powell, and J. Luhmann (1998), A three-dimensional mhd study of solar wind mass loading processes at venus: Effects of photoionization, electron impact ionization, and charge exchange, *Journal of Geophysical Research*, *103*(A10), 625–638.

Bertucci, C., C. Mazelle, and M. Acuña (2005), Structure and variability of the martian magnetic pileup boundary and bow shock from mgs mag/er observations, *Advances in Space Research*, *36*(11), 2066–2076.

Birdsall, C. K., and A. B. Langdon (1985), *Plasma physics via computer simulation*, vol. 1st edition, McGraw-Hill.

Boesswetter, A., T. Bagdonat, U. Motschmann, and K. Sauer (2004), Plasma boundaries at mars: a 3-d simulation study, *Annales Geophysicae*, *22*, 4363–4379.

Boesswetter, A., et al. (2007), Comparison of plasma data from aspera-3/mars-express with a 3-d hybrid simulation, *Annales Geophysicae*, *25*, 1851–1864.

Bougher, S. W., and S. Engel (2000), Comparative terrestrial planet thermospheres: 3. solar cycle variation of global structure and winds at solstices, *Journal of Geophysical Research*, *105*, 669–692.

Bougher, S. W., S. Engel, D. Hinson, and J. Murphy (2004), Mgs radio science electron density profiles: Interannual variability and implications for the martian neutral atmosphere, *Journal of Geophysical Research*, *109*(E3).

Bougher, S. W., P. Blelly, M. Combi, J. L. Fox, I. Mueller-Wodarg, A. Ridley, and R. Roble (2008), Neutral upper atmosphere and ionosphere modeling, *Space Science Reviews*, *139*, 107–141.

Brain, D., et al. (2010a), A comparison of global models for the solar wind interaction with mars, *Icarus*, *206*(1), 139–151.

Brain, D., et al. (3-7 Dec. 2012), Comparison of global models for the escape of martian atmospheric plasma, *Publication: Abstract P13C-1969 presented at 2012 Fall Meeting, AGU.*

Brain, D. A. (2007), Mars global surveyor measurements of the martian solar wind interaction, *Space Science Reviews*, *126*(1-4), 77–112.

Brain, D. A., D. L. Mitchell, and J. S. Halekas (2006), The magnetic field draping direction at mars from april 1999 through august 2004, *Icarus*, *182*(2), 464–473.

Brain, D. A., A. H. Baker, J. Briggs, J. P. Eastwood, J. S. Halekas, and T. D. Phan (2010b), Episodic detachment of martian crustal magnetic fields leading to bulk atmospheric plasma escape, *Geophysical Research Letters*, *37*(14).

Brecht, S., and S. A. Ledvina (2012), Control of ion loss from mars during solar minimum, *Earth, Planets and Space*, *64*(2), 165–178.

Brecht, S. H., and S. A. Ledvina (2006), The solar wind interaction with the martian ionosphere/atmosphere, *Space Science Reviews*, *126*(1-4), 15–38.

Brecht, S. H., and S. A. Ledvina (2010), The loss of water from mars: Numerical results and challenges, *Icarus*, *206*(1), 164–173.

Cain, J. C. (2003), An n = 90 internal potential function of the martian crustal magnetic field, *Journal of Geophysical Research*, *108*(E2).

Carlsson, E., et al. (2006), Mass composition of the escaping plasma at mars, *Icarus*, *182*(2), 320–328.

Carr, M. H. (2003), Oceans on mars: An assessment of the observational evidence and possible fate, *Journal of Geophysical Research*, *108*(E5).

Chaufray, J. Y., R. Modolo, F. Leblanc, G. Chanteur, R. E. Johnson, and J. G. Luhmann (2007), Mars solar wind interaction: Formation of the martian corona and atmospheric loss to space, *Journal of Geophysical Research*, *112*(E9).

Cipriani, F., F. Leblanc, and J. J. Berthelier (2007), Martian corona: Nonthermal sources of hot heavy species, *Journal of Geophysical Research*, *112*(E7).

Connerney, J., M. Acuña, N. Ness, T. Spohn, and g. Schubert (2004), Mars crustal magnetism, *Space Science Reviews*, *111*, 1–32.

Cravens, T. E., J. U. Kozyra, A. Nagy, T. Gombosi, and M. Kurtz (1987), Electron impact ionization in the vicinity of comets, *Journal of Geophysical Research*, *92*, 7341–7353.

Cravens, T. E., A. Hoppe, and S. A. Ledvina (2002), Pickup ions near mars associated with escaping oxygen atoms, *Journal of Geophysical Research*, *107*(A8), 1170–1180.

Curry, S. M., M. W. Liemohn, X. Fang, Y. J. Ma, and J. R. Espley (2012), The influence of production mechanisms on pick-up ion loss at mars, *Journal of Geophysical Research*.

Dubinin, E., M. Fränz, J. Woch, E. Roussos, S. Barabash, R. Lundin, J. D. Winningham, R. A. Frahm, and M. Acuña (2006), Plasma morphology at mars. aspera-3 observations, *Space Science Reviews*, *126*(1-4), 209–238.

Dubinin, E., M. Fraenz, J. Woch, S. Barabash, and R. Lundin (2009), Longlived auroral structures and atmospheric losses through auroral flux tubes on mars, *Geophysical Research Letters*, *36*(8).

Dubinin, E., M. Fraenz, A. Fedorov, R. Lundin, N. Edberg, F. Duru, and O. Vaisberg (2011), Ion energization and escape on mars and venus, *Space Science Reviews*, *162*(1-4), 173–211.

Eastwood, J. P., J. J. H. Videira, D. A. Brain, and J. S. Halekas (2012), A chain of magnetic flux ropes in the magnetotail of mars, *Publication: Geophysical Research Letters, Volume 39, Issue 3, CiteID L03104*.

Ergun, R. E., L. Andersson, W. K. Peterson, D. Brain, G. T. Delory, D. L. Mitchell, R. P. Lin, and A. W. Yau (2006), Role of plasma waves in mars' atmospheric loss, *Geophysical Research Letters*, *33*(14).

Fang, X., M. W. Liemohn, A. F. Nagy, Y. Ma, D. L. De Zeeuw, J. U. Kozyra, and T. H. Zurbuchen (2008), Pickup oxygen ion velocity space and spatial distribution around mars, *Journal of Geophysical Research*, *113*(A2).

Fang, X., M. W. Liemohn, A. F. Nagy, J. G. Luhmann, and Y. Ma (2010a), On the effect of the martian crustal magnetic field on atmospheric erosion, *Icarus*, *206*(1), 130–138.

Fang, X., M. W. Liemohn, A. F. Nagy, J. G. Luhmann, and Y. Ma (2010b), Escape probability of martian atmospheric ions: Controlling effects of the electromagnetic fields, *Journal of Geophysical Research*, *115*(A4).

Fedorov, A., et al. (2006), Structure of the martian wake, *Icarus*, *182*(2), 329–336.

Fox, J. L. (1993), On the escape of oxygen and hydrogen from mars, *Geophysical Research Letters*, *20*(17), 1847–1850.

Fox, J. L. (2003), Effect of h2 on the martian ionosphere: Implications for atmospheric evolution, *Journal of Geophysical Research*, *108*(A6).

Fox, J. L. (2009), Morphology of the dayside ionosphere of mars: Implications for ion outflows, *Journal of Geophysical Research*, *114*(E12).

Fox, J. L., and A. Ha (1997), Spectrum of hot o at the exobases of the terrestrial planets, *Journal of Geophysical Research*, *102*(A11), 24,005.

Fox, J. L., and K. Sung (2001), Solar activity variations of the venus thermosphere/ionosphere, *Journal of Geophysical Research*, *106*, 305–335.

Gombosi, T. (1998), *Physics of the Space Environment*, Cambridge University Press, Cambridge.

GonzálezGalindo, F., F. Forget, M. A. LópezValverde, M. Angelats i Coll, and E. Millour (2009), A groundtoexosphere martian general circulation model: 1. seasonal, diurnal, and solar cycle variation of thermospheric temperatures, *Journal of Geophysical Research*, *114*(E4).

Harnett, E. M. (2009), High-resolution multifluid simulations of flux ropes in the martian magnetosphere, *Journal of Geophysical Research*, *114*(A1).

Harnett, E. M., and R. M. Winglee (2006), Three-dimensional multifluid simulations of ionospheric loss at mars from nominal solar wind conditions to magnetic cloud events, *Journal of Geophysical Research*, *111*(A9).

Hartle, R. E., M. Sarantos, and E. C. Sittler (2011), Pickup ion distributions from three-dimensional neutral exospheres, *Journal of Geophysical Research*, *116*(A10).

Hunten, D. M. (1993), Atmospheric evolution of the terrestrial planets, *Science*, *259*(5097), 915–920.

Jakosky, B. M., and R. J. Phillips (2002), Mars volatile and climate history, *Nature*, *412*, 237–244.

Jin, H., K. Maezawa, and T. Mukai (2006), Effects of charge exchange and electron impact ionization on the formation of the magnetic pileup boundary at mars, *Journal of Geophysical Research*, *111*(A5).

Johnson, R. E. (1994), Plasma-induced sputtering of an atmosphere, *Space Science Reviews*, *69*(3-4), 215–253.

Kallio, E., and P. Janhunen (2001), Atmospheric effects of proton precipitation in the martian atmosphere and its connection to the mars-solar wind interaction, *Journal of Geophysical Research*, *106*(A4), 5617–5634.

Kallio, E., and R. Jarvinen (2012), Kinetic effects on ion escape at mars and venus: Hybrid modeling studies, *Earth, Planets and Space*, *64*(2), 157–163.

Kallio, E., and H. Koskinen (1999), A test particle simulation of the motion of oxygen ions and solar wind protons near mars, *Journal of Geophysical Research*, *104*(A1), 557–579.

Kallio, E., K. Liu, R. Jarvinen, V. Pohjola, and P. Janhunen (2010), Oxygen ion escape at mars in a hybrid model: High energy and low energy ions, *Icarus*, *206*(1), 152–163.

Kallio, E., J.-Y. Chaufray, R. Modolo, D. Snowden, and R. Winglee (2011), Modeling of venus, mars, and titan, *Space Science Reviews*, *162*(1-4), 267–307.

Kaneda, K., N. Terada, and S. Machida (2009), Solar-wind control of the hot oxygen corona around mars, *Journal of Geophysical Research*, *114*(E2).

Kim, J., A. Nagy, J. L. Fox, and T. E. Cravens (1998), Solar cycle variability of hot oxygen atoms at mars, *Journal of Geophysical Research*, *103*, 339–342.

Kirsch, E., et al. (1991), Pickup ions (e/o+/ greater than 55 kev) measured near mars by phobos-2 in february/march 1989, *Annales Geophysicae*, *9*, 761–767.

Lammer, H., and S. J. Bauer (1991), Nonthermal atmospheric escape from mars and titan, *Journal of Geophysical Research*, *96*(A2), 1819–1825.

Langlais, B. (2004), Crustal magnetic field of mars, *Journal of Geophysical Research*, *109*(E2).

Ledvina, S. A., Y. J. Ma, and E. Kallio (2008), Modeling and simulating flowing plasmas and related phenomena, *Space Science Reviews*, *139*(1-4), 143–189.

Li, L., Y. Zhang, Y. Feng, X. Fang, and Y. Ma (2011), Oxygen ion precipitation in the martian atmosphere and its relation with the crustal magnetic fields, *Journal of Geophysical Research*, *116*(A8).

Liu, Y., A. Nagy, C. Groth, D. De Zeeuw, T. Gombosi, and K. Powell (1999), 3d multifluid mhd studies of the solar wind interaction with mars, *Geophysical Research Letters*, *26*(17), 2689–2692.

Luhmann, J. G. (1996), Titan's ion exosphere wake: A natural ion mass spectrometer?, *Journal of Geophysical Research*, *101*(E12), 29,387.

Luhmann, J. G., and J. U. Kozyra (1991), Dayside pickup oxygen ion precipitation at venus and mars spatial distributions energy deposition and consequences, *Journal of Geophysical Research*, *96*, 5457–5467.

Luhmann, J. G., and K. Schwingenschuh (1990), A model of the energetic ion environment of mars, *Journal of Geophysical Research*, *95*(A2), 939.

Luhmann, J. G., S. A. Ledvina, J. G. Lyon, and C. T. Russell (2006), Venus o+ pickup ions: Collected pvo results and expectations for venus express, *Planetary and Space Science*, *54*(13-14), 1457–1471.

Luhmann, J. G., et al. (2012), Investigating magnetospheric interaction effects on titans ionosphere with the cassini orbiter ion neutral mass spectrometer, langmuir probe and magnetometer observations during targeted flybys, *Icarus*, *219*(2), 534–555.

Lundin, R., H. Lammer, and I. Ribas (2007), Planetary magnetic fields and solar forcing: Implications for atmospheric evolution, *Space Science Reviews*, *129*(1-3), 245–278.

Lundin, R., S. Barabash, M. Holmström, H. Nilsson, M. Yamauchi, M. Fraenz, and E. M. Dubinin (2008), A comet-like escape of ionospheric plasma from mars, *Geophysical Research Letters*, *35*(18).

Lundin, R., S. Barabash, M. Holmström, H. Nilsson, M. Yamauchi, E. M. Dubinin, and M. Fraenz (2009), Atmospheric origin of cold ion escape from mars, *Geophysical Research Letters*, *36*(17).

Lundin, R., S. Barabash, E. Dubinin, D. Winningham, and M. Yamauchi (2011a), Low-altitude acceleration of ionospheric ions at mars, *Geophysical Research Letters*, *38*(8).

Lundin, R., S. Barabash, M. Yamauchi, H. Nilsson, and D. Brain (2011b), On the relation between plasma escape and the martian crustal magnetic field, *Geophysical Research Letters*, *38*(2).

Lundin, R., et al. (1989), First measurements of the ionospheric plasma escape from mars, *Nature*, *341*(6243), 609–612.

Lundin, R., et al. (1990), Aspera/phobos measurements of the ion outflow from the martian ionosphere, *Geophysical Research Letters*, *17*(6), 873–876.

Lundin, R., et al. (2004), Solar wind-induced atmospheric erosion at mars: first results from aspera-3 on mars express, *Science*, *305*(5692), 1933–6.

Lundin, R., et al. (2006), Ionospheric plasma acceleration at mars: Aspera-3 results, *Icarus*, *182*(2), 308–319.

Ma, Y., A. Nagy, I. V. Sokolov, and K. C. Hansen (2004), Three-dimensional, multispecies, high spatial resolution mhd studies of the solar wind interaction with mars, *Journal of Geophysical Research*, *109*(A7).

Ma, Y.-J., and A. F. Nagy (2007), Ion escape fluxes from mars, *Geophysical Research Letters*, *34*(8).

Martinis, C. R., J. K. Wilson, and M. Mendillo (2003), Modeling day-to-day ionospheric variability on mars, *Journal of Geophysical Research*, *108*(A10).

McKenna, L., E. Kallio, R. Jarvinen, and V. Afonin (2012), Magnetic shadowing of high energy ions at mars and how this effect can be simulated using a hybrid model, *Earth, Planets and Space*, *64*(2), 247–256.

McKenna-Lawler, S., V. Afonin, Y. Yeroshenko, E. Keppler, E. Kirsch, and K. Schwingenschuh (1993), First identification in energetic particles of characteristic plasma boundaries at mars and an account of various energetic particle populations close to the planet, *Planetary and Space Science*, *41*(5), 373–380.

Modolo, R., G. Chanteur, E. Dubinin, and A. Matthews (2005), Influence of the solar euv flux on the martian plasma environment, *Annales Geophysicae*, *23*, 433–444.

Modolo, R., G. Chanteur, E. Dubinin, and A. Matthews (2006), Simulated solar wind plasma interaction with the martian exosphere: influence of the solar euv flux on the bow shock and the magnetic pile-up boundary, *Annales Geophysicae*, *24*, 3403–3410.

Nagy, A., et al. (2004), The plasma environment of mars, *Space Science Reviews*, *111*, 33–114.

Najib, D., A. F. Nagy, G. Tóth, and Y. Ma (2011), Three-dimensional, multifluid, high spatial resolution mhd model studies of the solar wind interaction with mars, *Journal of Geophysical Research*, *116*(A5).

Nilsson, H., N. J. T. Edberg, G. Stenberg, S. Barabash, M. Holmström, Y. Futaana, R. Lundin, and A. Fedorov (2011), Heavy ion escape from mars, influence from solar wind conditions and crustal magnetic fields, *Icarus*, *215*(2), 475–484.

Penz, T., et al. (2004), Ion loss on mars caused by the kelvin-helmholtz instability, *Planetary and Space Science*, *52*(13), 1157–1167.

Powell, K., P. Roe, T. Linde, T. Gombosi, and D. De Zeeuw (1999), A solution-adaptive upwind scheme for ideal magnetohydrodynamics, *Journal of Computational Physics*, *154*, 284–309.

Purucker, M., D. Ravat, H. Frey, C. Voorhies, T. Sabaka, and M. Acuña (2000), An altitude-normalized magnetic map of mars and its interpretation, *Geophysical Research Letters*, *27*(16), 2449–2452.

Pérez-de Tejada, H., R. Lundin, H. Durand-Manterola, and M. Reyes-Ruiz (2009), Solar wind erosion of the polar regions of the mars ionosphere, *Journal of Geophysical Research*, *114*(A2).

Raeder, J. (2003), Global magnetohydrodynamics: A tutorial, in *Space Plasma Simulation*, vol. 615, edited by J. Buechner, C. Dum, and M. Scholer, pp. 212–246.

Rosenbauer, H., et al. (1989), Ions of martian origin and plasma sheet in the martian magnetosphere: initial results of the taus experiment, *Nature*, *341*(6243), 612–614.

Schunk, R., and A. Nagy (2000), *Ionospheres*, Cambridge University Press, Cambridge.

Shinagawa, H., and S. W. Bougher (1999), A two-dimensional mhd model of the solar wind interaction with mars, *Earth, Planets and Space*, *51*, 55–60.

Shizgal, B., and G. Arkos (1996), Nothermal escape of the atmospheres of venus, earth and mars, *Reviews of Geophysics*, *34*(4), 483–505.

Sleep, N. H., and K. Zahnle (2001), Carbon dioxide cycling and implications for climate on ancient earth, *Journal of Geophysical Research: Planets*, *106*(E1), 1373–1399.

Spreiter, J. R., and S. S. Stahara (1980), A new predictive model for determining solar wind-terrestrial planet interactions, *Journal of Geophysical Research*, *85*(A12), 6769.

Squyres, S. W., et al. (2004), In situ evidence for an ancient aqueous environment at meridiani planum, mars, *Science*, *306*(5702), 1709–14.

Stebbings, R. F., A. C. H. Smith, and H. Ehrhardt (1964), Charge transfer between oxygen atoms and o+ and h+ ions, *Journal of Geophysical Research*, *69*(11), 2349–2355.

Terada, N., Y. N. Kulikov, H. Lammer, H. I. Lichtenegger, T. Tanaka, H. Shinagawa, and T. Zhang (2009), Atmosphere and water loss from early mars under extreme solar wind and extreme ultraviolet conditions, *Astrobiology*, *9*(1), 55–70.

Trotignon, J. G., C. Mazelle, C. Bertucci, and M. H. Acuña (2006), Martian shock and magnetic pile-up boundary positions and shapes determined from the phobos 2 and mars global surveyor data sets, *Planetary and Space Science*, *54*(4), 357–369.

Valeille, A., M. R. Combi, S. W. Bougher, V. Tenishev, and A. F. Nagy (2009), Three-dimensional study of mars upper thermosphere/ionosphere and hot oxygen corona: 2. solar cycle, seasonal variations, and evolution over history, *Journal of Geophysical Research*, *114*(E11).

Valeille, A., M. Combi, V. Tenishev, S. W. Bougher, and A. Nagy (2010), A study of suprathermal oxygen atoms in mars upper thermosphere and exosphere over the range of limiting conditions, *Icarus*, *206*, 18–27.

Verigin, M., et al. (1991), Ions of planetary origin in the martian magnetosphere (phobos 2/taus experiment), *Planetary and Space Science*, *39*(1/2), 131–137.

Vignes, D., et al. (2000), The solar wind interaction with mars: Locations and shapes of the bow shock and the magnetic pileup boundary from the observations of the mag/er experiment onboard mars global surveyor, *Geophysical Research Letters*, *27*(1), 49.

Zhang, M. H. G., J. Luhmann, A. Nagy, J. Spreiter, and S. Stahara (1993), Oxygen ionization rates at mars and venus: Relative contributions of impact ionization and charge exchange, *Journal of Geophysical Research*, *98*(2), 3311–3318.